D 2019

U.PORTO
FEUP FACULDADE DE ENGENHARIA
UNIVERSIDADE DO PORTO

MODELLING OF WIND TURBINE WAKES THROUGH AN ACTUATOR DISK

VITOR MANUEL MARTINS GONÇALVES DA COSTA GOMES

TESE DE DOUTORAMENTO APRESENTADA
À FACULDADE DE ENGENHARIA DA UNIVERSIDADE DO PORTO EM
ENGENHARIA MECÂNICA

Universidade do Porto

Faculdade de Engenharia

Modelling of Wind Turbine Wakes through an Actuator Disk

Vitor Manuel Martins Gonçalves da Costa Gomes

(MSc in Mechanical Engineering)

Dissertation submited to the Universidade do Porto
in partial satisfaction of the requirements for the
degree of Doctor in Mechanical Engineering.

November 2019

Contact information:
Vitor Manuel Martins Gonçalves da Costa Gomes
Address: Rua Dr. Roberto Frias s/n, 4200-465 Porto
email: vitor.costa.gomes@fe.up.pt

This document was typeset with LaTeX.

Abstract

The ability to accurately predict a wind farm's production largely depends on the wake model's estimation of the effect each wind turbine has on the surrounding flow downstream wind turbines. The industry standard tools can struggle with the increasing size of both modern wind turbines and wind farm projects, as well as the surrounding flow complexity. The goal of this work is to produce a model that is not encumbered by said issues, and is capable of greater accuracy when modelling the complex turbulent flows involved. This was achieved by developing it within a finite-volume CFD code, solving the elliptic RaNS equations with k-ε turbulence model.

The model is based on Froude's actuator disk concept and on one dimensional momentum theory. The rotor is discretized in such a way that it results in a smooth distribution of body forces, regardless of the rotor's position and mesh resolution. To estimate the thrust exerted by an individual wind turbine on the flow, momentum theory is combined with a thrust coefficient curve and with solution data from the current flow solver iteration, resulting in an algorithm that continuously updates the equivalent free-stream velocity approximation for that wind turbine. When converged, the approximation error is quite low, with a maximum of 2% at low wind speeds and peak thrust coefficient.

With the proposed model, the CFD code can simulate complex ABL flows including large wind farms, seamlessly updating each individual wind turbine's thrust as the CFD code iterates, until it converges on a final combined flow/wind farm operation solution. This enabled the model to be applied to two off-shore wind farm cases where considerable wake effects are at play, both within the dense wind turbine array as well as at large distances, between wind farms in an off-shore cluster. Although directional uncertainty proved to be a considerable obstacle, high quality operational data permitted the model to estimate wind farm production within a reasonable margin of error.

Along the development and documented use of the model some issues were identified with the present formulation. These are mostly tied to excess diffusivity and velocity prediction in the vicinity of the actuator disk and near-wake. Modifications to the model were tested, attempting to improve the force distribution at the actuator disk.

This page intentionally left blank

Resumo

A qualidade da estimativa de produção de um parque eólico depende da capacidade do modelo de esteira para prever o efeito do aerogerador no escoamento e na produção dos aerogeradores em seu redor. As capacidades das ferramentas utilizadas na indústria da energia eólica são insuficientes face ao crescimento das dimensões dos equipamentos e da complexidade do escoamento em que se inserem. O objectivo deste trabalho é obter um modelo que não sofra das limitações dessas ferramentas, garantindo maior precisão na modelação do escoamento turbulento. Para esse efeito o modelo foi baseado em um código CFD que resolve as equações RaNS na sua versão elíptica, associado a um modelo de turbulência k-ε.

O modelo proposto é baseado no disco actuante de Froude e na teoria mono-dimensional de quantidade de movimento. O rotor do aerogerador é discretizado de forma a resultar numa distribuição suave de forças de volume, independentemente da sua posição e da resolução da malha computacional. O impulso exercido pelo aerogerador no escoamento é estimado combinando a teoria de quantidade de movimento, a curva de coeficiente de impulso axial e a iteração mais recente da solução do código CFD, dando origem a um algoritmo que continuamente actualiza a aproximação à velocidade de escoamento livre. Atingida a convergência, o erro de aproximação é baixo, atingindo um valor máximo de 2% para velocidades de vento baixas e coeficientes de impulso máximos.

O modelo de esteira proposto permite simular um escoamento atmosférico complexo com vários aerogeradores em operação, actualizando continuamente os respectivos impulsos até convergir numa solução combinada para o escoamento atmosférico e operação do parque eólico. Para validação o modelo foi aplicado a dois parques eólicos *off-shore*, onde os efeitos de esteira são relevantes dentro do próprio parque, assim como entre parques vizinhos. A incerteza associada às medições de direcção do vento dificultou a comparação entre medições e simulações, mas na disponibilidade de dados operacionais de alta qualidade o modelo de esteira estimou as perdas associadas a esteiras dentro de margens de erro moderadas.

Decorridos já o desenvolvimento e aplicação do modelo, foi possível identificar problemas na sua formulação actual, principalmente associados ao excesso de transporte difusivo na proximidade do aerogerador e à previsão de velocidade no mesmo e no início da esteira. Foram testadas modificações ao modelo, focadas na melhoria da distribuição de impulso no disco actuante.

This page intentionally left blank

Acknowledgements

First and foremost, I must thank Prof. José Manuel Laginha Mestre da Palma for the guidance, knowledge and the continued support given as a mentor and a colleague, over the nearly 10 years we have worked together.

I must express my gratitude to my colleague Alexandre Silva Lopes for all the ideas and advice he gave and for making our office a pleasant work place, be it to throw ideas around or for general banter. Also to all with whom I collaborated along the years, particularly those whose company I shared on a daily basis (for long or short periods) such as Carlos Rodrigues, João Viana Lopes, Tiago Paiva and Roman Chertovski.

To the people at *Renewable Energy Systems* and *Natural Power*, in particular to Peter Stuart and Claude Abiven, for all the interest and valuable input given on the subject throughout our long standing collaboration.

To the EERA-DTOC project, central to this body of work, and to all its participants for the challenging and engaging environment. Special mentions to Charlotte Hasager, project coordinator, and to Kurt Hansen, for all the work done in the processing and transformation of the massive SCADA datasets into usable information.

A most special mention to Joana: your support did not fail me at the worst of times, and now I owe you my best. To my family and friends, for their continued encouragement, their positivity when mine had all but run out and also for generally avoiding the stress-inducing words ”is it done yet”.

This page intentionally left blank

Contents

This page intentionally left blank

List of Figures

List of Tables

Nomenclature

List of Acronyms

1-D	One dimensional	
2-D	Two dimensional	
3-D	Three dimensional	
ABL	Atmospheric Boundary Layer	
AD	Actuator Disc	
AEP	Annual Energy Production	
ALM	Actuator Line Model	
AOA	Angle of Attack	[°]
AOI	Area of Interest	
BEM	Blade element momentum theory	
BL	Boundary Layer	
CFD	Computation Fluid Dynamics	
DNS	Direct Numerical Simulation	
E	East	
IEC	International Electrotechnical Commission	
LES	Large Eddy Simulations	
LIDAR	Light Detection and Ranging	
N	North	
NE	Northeast	

NW	Northwest	
Ny	Nysted wind farm	
PIV	Particle Image Velocimetry	
RaNS	Reynolds averaged Navier-Stokes	
RsII	Rødsand II wind farm	
S	South	
SCADA	Supervisory control and data acquisition	
SE	Southeast	
SW	Southwest	
W	West	
WF	Wind Farm	
WT	Wind Turbine	

Symbols - Greek

α	Flow's Angle of Attack on a wind profile	[°]
α_{WT}	Free-stream velocity under-relaxation factor	
β	Pitch angle of the wing profile on a rotor blade	[°]
δ_{ij}	Kronecker delta	
η_i, η_j, η_k	Tri-linear extrap. factors to CV centres in Cartesian coords.	
γ	WT rotor conicity angle	[°]
μ	Molecular dynamic viscosity	[kg m^{-1} s^{-1}]
μ_T	Turbulent dynamic viscosity	[kg m^{-1} s^{-1}]
ω	Rotor angular velocity	[rad s^{-1}]
ω	Turbulence Frequency	[s^{-1}]
ρ	Fluid density	[kg m^{-3}]
σ_P	Power deficit estimation uncertainty	
σ_t	Wall-tangential Reynolds stress	[kg m^{-1} s^{-2}]

σ_{ij}	Reynolds stress tensor component	[kg m^{-1} s^{-2}]
τ_{ij}	Viscous stress tensor component	[kg m^{-1} s^{-2}]
ε	Turbulent Kinetic Energy Dissipation	[m^2 s^{-3}]
ε_P	Wind turbine power estimation relative error	
ε_{U_∞}	Free-stream velocity estimation relative error	
ξ_1, ξ_2, ξ_3	Orthogonal computational space coordinates	
$\zeta_i, \zeta_j, \zeta_k$	Tri-linear extrap. factors to CV face centroids in Cartesian coords.	

Operators

$()'$	Perturbation	
$\delta()$	Discrete fraction	
Δ	Absolute/relative difference	
$\frac{\partial}{\partial}$	Partial derivative	
d	Derivative	
$\overline{()}$	Spatial filtering; temporal average	
$\widetilde{()}$	Quantity in density form (divided by volume)	[m^{-3}]
MAPD	Mean absolute percentual deviation	

Symbols - Latin

n, **t**, **r**	Polar coordinate versor	
ΔP_p	Pressure potential energy	[kg m^2 s^{-3}]
$\dot{m}$	Mass flux	[kg s^{-1}]
κ	von Kármán constant	
x	Cartesion position vector	[m]
$\mathcal{P}_k$	Viscous energy dissipation	[kg m^2 s^{-3}]
c_x,c_y,c_z	Peak resolution per Cartesian direction	[m]
D_x,D_y	High resolution area dimensions	[m]
N_i,N_j,N_k	Domain node count per Cartesian direction	

σ_k	$k-\varepsilon$ turbulence model constant	
A	Actuator surface area	[m^2]
a	Axial induction factor	
A_∞	Stream tube cross-section in free-stream conditions	[m^2]
A_w	Stream tube cross-section in fully expanded wake	[m^2]
A_d	Actuator Disk area	[m^2]
A_{nac}	WT nacelle frontal area	[m^2]
A_{rt}	WT rotor span area	[m^2]
c	Wing profile cord	[m]
C_1	$k-\varepsilon$ turbulence model constant	
C_2	$k-\varepsilon$ turbulence model constant	
C_D	Drag coefficient of a wing profile	
C_L	Lift coefficient of a wing profile	
C_T	Thrust Coefficient	
C_μ	$k-\varepsilon$ turbulence model constant	
D	Drag force exerted on a wing profile	[N]
e_{energy}	Energy budget error	[kg m^2 s^{-3}]
e_{mom}	Momentum budget error	[kg m s^{-2}]
f_n	Actuator surface normal load factor	
F_p	Pressure force	[kg m s^{-2}]
F_t	Torque exerted on a WT rotor blade section	[N]
f_t	Actuator surface tangential load factor	
F_{B_i}	Buoyancy model momentum sink per Cartesian direction	[N]
F_{C_i}	Canopy model momentum sink per Cartesian direction	[N]
$F_{p_{in}}$	Inlet boundary pressure force	[kg m s^{-2}]
$F_{p_{out}}$	Outlet boundary pressure force	[kg m s^{-2}]

F_{t_i}	Torque at a rotor blade section per Cartesian direction	[kg m s^{-2}]
F_{wall}	Domain wall drag	[kg m s^{-2}]
G_k	Buoyancy model T.K.E. source term	[kg m^2 s^{-3}]
i, j, k	Domain cell index per Cartesian direction	
L	Lift force exerted on a wing profile	[N]
M	Momentum flux	[kg m s^{-2}]
M	Momentum flux	[kg m s^{-2}]
M_{in}	Inlet boundary momentum flux	[kg m s^{-2}]
M_{in}	Inlet boundary momentum flux	[kg m s^{-2}]
M_{out}	Outlet boundary momentum flux	[kg m s^{-2}]
P	Kinetic energy flux	[kg m^2 s^{-3}]
p	Pressure	[Pa]
P_∞	Free stream kinetic energy flux through AD section	[W]
p_∞	Free-stream pressure	[Pa]
p_w	Pressure at the fully expanded wake side of the stream tube	[Pa]
P_{AD}	Power extracted by the AD from the flow	[W]
$P_{c_{in}}$	Inlet boundary mean kinetic energy flux	[kg m^2 s^{-3}]
P_c	Mean kinetic energy flux	[kg m^2 s^{-3}]
p_{d^+}	Maximum pressure on the upstream side of the AD	[Pa]
p_{d^+}	Minimum pressure on the downstream side of the AD	[Pa]
P_{def}	Power deficit relative to reference WT power output	
P_{rated}	Wind turbine peak rated power, as per manufacturer	[kW]
P_{ref}	Reference WT power output	[kW]
P_{WF}	Overall wind farm power output	[kW]
r	Radial coordinate	[m]
r_{nac}	WT nacelle radius	[m]

r_{rt}	WT rotor radius	[m]
Res_{energy}	Energy budget residual	[kg m^2 s^{-3}]
Res_{mom}	Momentum budget residual	[kg m s^{-2}]
s_d	Local actuator disk area	[m^2]
s_t	Local actuator disc tangential area	[m^2]
S_{C_ε}	Canopy model ε source term	[kg m^2 s^{-3}]
S_{C_k}	Canopy model T.K.E. source term	[kg m^2 s^{-3}]
T	Thrust exerted on a WT rotor blade section	[N]
T_∞	Free-stream momentum flux through AD section	[kg m s^{-2}]
T_i	Thrust at a rotor blade section per Cartesian direction	[kg m s^{-2}]
T_{AD}	Thrust exerted by the AD on the flow	[N]
t_{CPU}	Computation time to convergence	[h]
U	Streamwise velocity magnitude	[m s^{-1}]
u,v,w,u_i	Cartesian velocity vector components	[m s^{-1}]
u', v', w', u_i'	Cartesian velocity fluctuation components	[m s^{-1}]
u_*	Friction velocity	[m s^{-1}]
U_∞	Free-stream velocity	[m s^{-1}]
U_∞^*	Estimated Free-stream velocity	[m s^{-1}]
U_d	Velocity at the Actuator Disk	[m s^{-1}]
u_t	Log-law wall-tangential velocity	[m s^{-1}]
U_w	Velocity at the fully expanded wake side of the stream tube	[m s^{-1}]
U_{rel}	Relative flow velocity perceived by the rotor blade section	[m s^{-1}]
x,y,z,x_i	Cartesian coordinates	
z_0	Characteristic surface roughness	[m]
$\mathbf{n_i}$, $\mathbf{n_j}$, $\mathbf{n_k}$	Cartesian coordinate versor	
$\mathbf{n_{AD}}$,$\mathbf{r_{AD}}$,$\mathbf{t_{AD}}$	Actuator disk normal, radial and tangential unitary vectors	

$\mathbf{n}$	Surface-normal unitary vector	
$\mathbf{u}$	Velocity vector	[m s^{-1}]
${C_D}^{hub}$	Hub equivalent drag coefficient	
${F_C}^x$, ${F_C}^y$, ${F_C}^z$	Domain cell momentum equation convective flux term	[kg m s^{-2}]
${F_D}^x$, ${F_D}^y$, ${F_D}^z$	Domain cell momentum equation diffusive flux term	[kg m s^{-2}]
${P_G}^x$, ${P_G}^y$, ${P_G}^z$	Domain cell momentum equation pressure gradient term	[kg m s^{-2}]
k	Turbulent Kinetic Energy	[m^2 s^{-2}]
L_{total}	Precursor and main domain combined length	[m]

This page intentionally left blank

Chapter 1

Introduction

The global future of the energy sector relies primarily on renewable sources, with a major part played by wind energy. It has grown continuously in the past three decades (WindEurope), to the point where wind turbines are ubiquitous in modern landscapes.

With the growth of the sector and the increased difficulty in finding locations adequate for wind energy harvest, there is a strong push towards maximization of extracted energy and exploration of more challenging sites for the installation of wind farms, including high complexity and off-shore locations. As wind turbine density increases, the atmospheric flow inside wind farms becomes increasingly complex and non-linear, and the energy extraction becomes enough that the wind farm has a noticeable impact on the wind regime even at large distances.

1.1 Wind turbine wakes

Wind Turbines (WT) convert the wind's convective kinetic energy into rotational kinetic energy at the rotor, and finally into electrical energy. Consequently the flow's kinetic energy content will be lower on the downstream end of the WT, i.e. an operating WT affects the surrounding flow and therefore the production of any WTs placed in its wake.

Horizontal axis WTs, our focus, have a rotor typically with 3 wing-shaped blades. These blades are oriented to convert flow momentum into aerodynamic lift and drag, the torque of which is converted into power at the hub. The boundary layer (BL) formed on the surface of the blades and their aerodynamic drag mean that part of the energy transfers into turbulence as the BLs form and detach from the blades and, most importantly, into vortices shed by the blade tips. This turbulence is of high frequency and decays relatively quickly.

The shape of the blades, their angle relative to the rotor plane, the rotor's angular velocity and the incoming flow conditions all contribute to the resulting lift and drag forces, and to the conversion efficiency. Determining the process efficiency is not simple, leading to efforts by the WT manufacturers to, firstly, optimize rotor shape and operation and, secondly, measure and reliably predict the WT's production on a wide range of

inflow conditions (IEC, 2005).

The changes made to the flow by the rotor are convected downstream. The reduced wind speed inside the wake of the rotor leads to an annular shear layer at the interface between the WT's wake and the surrounding free-stream flow. This shear layer becomes a strong turbulent mixing area where momentum is transferred into the wake region, progressively expanding until it reaches the center of the wake and wind speed returns to near free-stream conditions. As the shear layer expands, it produces larger scale turbulence, particularly at its top edge unrestricted by the ground effect, which take longer to dissipate. The small scale turbulence (produced at the blade scale) rapidly breaks down leaving the large scale shear layer turbulence to dominate (Chamorro and Porté-Agel, 2009), marking the transition between the near-wake (where rotor dynamics dominate) and far-wake (where atmospheric flow dynamics dominate) zones.

The WT wake is characterized by lower wind speeds and increased turbulence, decaying back to free-stream conditions with distance to the WT. In a Wind Farm (WF), where multiple WTs operate in close proximity, it is largely inevitable to have wakes affect WT operation. When operating in waked inflow a WT will see its maximum harvesting potential reduced - there being less kinetic energy available in the flow - while also being subject to added strain - the increased turbulence leads to greater material fatigue - due to unstable aerodynamic loads and structural vibrations. In this case, where WT wakes combine with a possibly already complex flow, one needs to be able to estimate the amount of energy left in the flow for other downstream WTs, and how those WT's operation (in both production and fatigue loads) are affected by the changes made to the flow.

The ability to predict the wake effects inside a WF is first useful at the planning phase. A wake model facilitates the task of optimizing the WF layout by tuning individual WT placement (or even by reducing installed power) to materialize a better overall economical result, either through reduced electrical production losses or through maintenance cost savings. Recently, the access to installation sites is only becoming more restricted (even in off-shore), so one current trend is to increase WF power density - by reducing WT spacing or having larger WTs - further enhancing the importance of good wake effect predictions.

In a long-term cost/benefit analysis, an accurate wake model will improve the quality of the estimates of Annual Energy Production (AEP) and planned maintenance costs. A better wake model also reduces the uncertainty associated to both. The wake effect prediction has a direct effect on the competitiveness of a wind power project, by improving its economical benefits and reducing the investment risk.

During the operational phase, estimating the WF's internal wake effects reliably can improve energy production forecasting, allowing for the operator to bid in the energy market with increased confidence and reducing the chances of bidding low/high. Another advantage is to be able to change the WF operation with greater precision: there is frequently the need to stop one or more WTs or curtail their power, be it due to maintenance needs, WF output regulation or even to reduce strain in extreme events. Since the wakes affect the operation of neighbouring downstream WTs, testing these strategic changes and having them reflect on the forecast allows for a finer control of the WF

operation. Naturally, the accuracy and uncertainty of the forecasts should improve with the quality of the wake model.

1.2 Wind turbine rotor modelling

Wind flow close to the rotor is complex, with phenomena of very different scales: from blade's chord length to the rotor diameter itself. Depending on the level of fidelity required, modelling the flow near the WT's rotor will require more or less detail and effort. If the simpler models are meant to represent the aggregate effect a WT has on the flow, they will not be able to reproduce small particularities of the flow, such as individual blade wakes and the associated turbulent structures. Sanderse et al. (2011) covers the spectrum of modelling techniques that have been developed for the purpose of representing the rotor.

Arguably the oldest and most accessible form of representing the rotor is the Actuator Disk (AD) concept, introduced by Froude (1889) and based on Rankine's one-dimensional momentum theory. It approximates a multi-bladed rotor to a permeable infinitely thin flow-facing disk, where in its fundamental form the blade's loads are assumed to be distributed uniformly, acting exclusively in the AD-normal direction. Glauert (1935) proposed an extension to Froude's theory with Blade-element momentum theory (BEM), by splitting the disk into successive annular sections, sections where momentum theory is individually applied taking into consideration the blade's lift and drag characteristics. This allows for a more complex non-uniform load distribution, where the rotor exerts both normal and tangential force components, each varying along the radial direction. The work of Van Kuik (1991) and Hansen (2000) (specifically oriented to horizontal axis WTs) are a good revision and critique of the AD and the associated load distribution methods.

An early Computation Fluid Dynamics (CFD) application of the uniformly loaded AD is that by Madsen (1997), replicating momentum theory's setup and conclusions regarding the AD. Later works by Jimenez (Jimenez et al., 2007, 2008) prove that despite the model's simplicity, the AD concept is able to adequately represent wake flow characteristics of a full-scale WT. Recent works, such as Calaf et al. (2010) and Castellani and Vignaroli (2013), actually use the AD/momentum theory combo to model the complex interactions between Atmospheric Boundary Layer (ABL) flow and multiple WT wakes. The overall thrust exerted by the AD is typically prescribed by the user, either explicitly or through the effective thrust coefficient C_T, inferring the total force via the axial induction factor, as per Calaf et al. (2010) and Prospathopoulos et al. (2010).

Modelling the AD loads with BEM, the assumption of uniform and AD-normal load are dropped. The velocity vector at any point of the AD, typically combined with lookup-tables describing the blade lift and drag curves, results in dynamic load distribution more representative of the forces acting on the flow in a WT. This approach potentially yields far more realistic near-wake flow conditions, which has historically made it the preferred approach whenever high-cost CFD simulations were involved. An example of early CFD work with BEM is that of Sørensen and Myken (1992), simulated in asymmetric form. Among many recent contributions those of Wu and Porté-Agel (2011, 2012)

stand out, with one or more WTs simulated in full 3-D form to investigate the impact of the wake rotation induced by the AD-tangential forces.

Inspired by the AD concept and BEM, actuator line models (ALM) are attempt to represent the rotor's individual blades. This allows for completely inhomogeneous load distributions, where blade wakes and tip vortices are created, requiring simulation in time-dependent formulation to model the rotor movement. The first to apply ALM to WT flows was Sørensen and Shen (2002), work later continued in Mikkelsen (2003); Mikkelsen et al. (2007). The technique may however be best suited the study of the transient effects involved, as Porté-Agel et al. (2011) concludes that the time-averaged results are comparable to those of an AD/BEM model. An edge-case extension to the ALM approach is explored by Shen et al. (2009), where each blade is modelled as 2-D surface, where the pressure distribution is solved.

On a final tier of fidelity are full rotor simulations, where a body-fitted mesh is used to obtain flow over the exact shape of the rotor. This approach requires precise measurements of the blade geometry. The best known documented cases are those involving the NREL phase VI rotor (Duque et al., 1999; Johansen et al., 2002; Mo et al., 2013) and the MEXICO rotor (Bechmann et al., 2011), both associated to scaled wind tunnel experiments providing validation flow data. In addition to the computational cost there are considerable technical difficulties involved, such as matching between rotor (rotating referential) and boundary layer (static referential) meshes or the modelling of the turbulent/laminar transition (Laursen et al., 2007).

1.3 Wake flow modelling

The wake flow is composed of features at multiple scales, which behave and evolve differently. The smaller scale wake features, result of the rotor geometry, are the quickest to dissipate and be homogenized through turbulent mixing. After that has occurred - typically between 1D (distance of one WT rotor diameter) and 3D downstream of the WT - they should be mostly indistinguishable from the larger scale wake flow characteristics, and the wake can be considered to approximately axisymmetric, self similar and Gaussian-shaped, as gathered by Sanderse (2009). This way, the wake flow can be broken down into two phases, with vastly different characteristics: in the first (near wake) the small scale structures released by the rotor are still relevant and have not yet broken down, and in the second (far wake) the expanding annular shear layer that results of the momentum extraction is dominant.

It is commonplace and convenient to exploit the characteristics of the later, which being near Gaussian-shaped and self similar can be approximated using simple models, including analytical solutions. This way, if estimating the effect of the WT on the flow is the priority, the WT's wake model can ultimately be completely dissociated from the rotor representation. Otherwise, to model the complex turbulent flows involved in simulating the rotor and all phases of wake development, in addition to a detailed rotor model, high-order turbulence modelling techniques are required. These techniques - Reynolds averaged Navier-Stokes (RaNS) and Large Eddy Simulation (LES) - and their particularities in wake modelling are discussed in Sanderse et al. (2011).

Most engineering models used for wind energy purposes are based on simple mathematical expressions of velocity deficit and turbulence increase downstream of the WT. Even though they often compare well with measurements, they are not so versatile as to cover the more complex cases that the wind energy industry frequently faces. These typically assume uniform inflow, and produce a wind-speed reduction pattern that is superimposed into other CFD results of flow at the Area of Interest (AOI). The simplest treat the wake analytically, assuming the wind speed and turbulence effect to be self-similar, with auxiliary functions for combining wakes, such as Jensen (1983) or Frandsen et al. (2006). The former is at the root of the popular Park model, used in the wind energy evaluation code WAsP. Others are based on parabolic versions of the RaNS equations, applied in either axisymmetric form (Ainslie, 1988; Quarton and Ainslie, 1990) or in 3-D form, most importantly in UPMWAKE/UPMPARK code with the continued line of work of Crespo et al. (1988), Crespo and Hernández (1996) and Gómez-Elvira et al. (2005). These models are now the industry standard, so still quite relevant due to the quick turnaround and thorough validation they've been subjected to over the years.

An early application of RaNS equations in full elliptic formulation for wake modelling was by Crespo et al. (1990). Far more expensive and with little comparative advantage, these models were at the time dropped in favour of other simpler models of analytical or parabolic RaNS origin. Recently this type of models has been revitalized, with works such as Réthoré (2009), Troldborg et al. (2011) and Bechmann et al. (2011), all using different rotor modelling approaches.

A common criticism on the ability of typical RaNS turbulence closure schemes (turbulent viscosity, associated to k-ε or k-ω equations), particularly when using an actuator disk rotor model, is that excessive diffusion is promoted in the wake, resulting in underestimated near-wake wind speeds. The publications Réthoré (2009), Prospathopoulos et al. (2010) and Cabezón et al. (2011) explore potential alternatives in turbulence modelling to resolve the issues identified. These generally approach the problem assuming that in the vicinity of the WT either: some form of turbulence suppression or increased dissipation regime occurs as per Kasmi and Masson (2008); or that the Boussinesq approximation is severely invalidated in Réthoré (2009), meaning the Reynolds stresses and diffusive transport prediction is problematic. Results have proven largely unsatisfactory, struggling to consistently predict near wake flow conditions or requiring calibration on a case-by-case basis.

Large Eddy Simulations are suited to represent the transient and anisotropic nature of turbulent flows, by fully solving the majority of range of temporal and spatial scales involved in Navier-Stokes equations. This also make them a natural candidate for solving wake flows, although at a higher computational cost. For that reason, only in recent years have LES simulations of WT wake flows become more common, with the examples of Wubow et al. (2007) and Jimenez et al. (2007, 2008). One group has produced a body of work (Wu and Porté-Agel, 2011; Porté-Agel et al., 2011; Wu and Porté-Agel, 2012) where multiple rotor modelling solutions have been compared in an LES environment, representing both wind tunnel and real world WF cases. LES was used with fine spacial and temporal resolution to determine the value added by increasingly detailed rotor descriptions. Finally, the SOWFA project (Churchfield et al., 2012) assembles a set of tools –including an actuator line WT model– around the freely distributed OpenFOAM

LES solver, enabling it to model WT and WF operation.

With large WFs, and particularly when spatial resolution is low, it can be preferable to represent the aggregate impact of multiple WTs as an area effect. In a large enough WT array the boundary layer will developed into an asymptotic regime where «changes in the stream-wise direction can be neglected and the relevant exchanges occur in the vertical direction» (Calaf et al., 2010). Often this flow regime is characterized by a change in effective surface roughness, effectively modifying the boundary layer conditions to have a correct profile above the WTs, as in Frandsen (1992) and Crespo et al. (1999). These models are compared in recent works from Calaf et al. (2010) and Wu and Porté-Agel (2012) to the aggregate effect of individually modelled WTs on the boundary layer. Markfort et al. (2012) on the other hand attempts to model the aggregate WT array drag using a canopy model approach. These area effect models are particularly suited to the modelling of the overall effect of a WF on large scale meteorological effects.

Wake flows can now be modelled with acceptable quality, but not much is known about how wake flow interacts with other complex atmospheric flow phenomena. Migoya et al. (2007) identifies the difficulties in correctly modelling the interaction between multiple non-linear effects, such as topography and WT wakes, extensively modelled in isolation but unknown how they combine. Politis et al. (2012) and Makridis and Chick (2013) attempt to study how the effects of topography and wake combine in the boundary layer; another example is Yang et al. (2014), which interprets the impact of varying sea wave parametrizations (effectively changing the surface roughness) on the BL and on wake flow of an off-shore WF. The impact of other atmospheric characteristics, such as stability and ambient turbulence, have been identified through measurements and their reproduction attempted in works such as Abkar and Porté-Agel (2015).

1.4 Experimental data

When modelling WT wakes, many assumptions and simplifications are made, from the inflow conditions and rotor approximation to the BL and wake flow modelling, where each can be a considerable source of error. Validation via comparison to measured data is necessary prior to their proper application, either in prediction or in providing insight where traditional measurement techniques are not available/not cost-effective.

Wind tunnel experiments can be constrained issues regarding scaling and reproducing real-world atmospheric turbulent conditions, but allow for maximum control over flow conditions, making it an invaluable tool for flow model validation. Vermeer et al. (2003) lists a considerable number of wind tunnel studies conducted in the past, to which some more recent ones should be added. The work in Medici and Alfredsson (2006) and Medici et al. (2011) stands out in the detail presented, using particle image velocimetry (PIV) measurements of a model rotor all the way upwind of the rotor to the far-wake. The NREL Phase-VI rotor experiment placed a large scale model rotor –possibly the closest yet to real WT rotor dimensions– in the NASA-Ames wind-tunnel (Simms et al., 2001), and tested it under a wide variety of test conditions. Likewise, the MEXICO project had an associated wind tunnel experiment with a scaled rotor (Schepers and Snel, 2007), with blade pressure and PIV data from from the upwind and near-wake

flows. The wind tunnel experiments of Porte-Agel et al. (Chamorro and Porté-Agel, 2009, 2010; Zhang et al., 2012; Markfort et al., 2012) cover a multitude of setups and flow conditions, and are sufficiently detailed (both temporally and spatially) for use in comparison to LES simulations. Finally, Aubrun et al. (2013) experimented with both model rotors and porous discs, mimicking the different approaches to rotor modelling used in CFD.

Full-scale measurement campaigns necessarily imply greater cost and time investments. The classic cases of Sexbierum and Nibe (Cleijne, 1993 and Taylor, 1990, respectively) have been extensively documented and utilized for wake model validation. However, these datasets are limited by the reduced number of measurement points and by the quality of the inflow characterization. The recent development of remote sensing techniques, particularly Light Detection and Ranging (LIDAR) technology, allow for flexible measurement setups where a line or an area is covered nearly instantaneously. Notable applications of the technology for wake measuring are those of Bingol et al. (2010), Trujillo et al. (2011) and Machefaux et al. (2012). Under the WindScanner project a measurement campaign around a single WT was conducted in Portugal in 2015 with a triple LIDAR setup, documented in (Vasiljević et al., 2017), allowing for full velocity vector measurements covering both inflow and wake of an operating WT. This experiment also paved the way for further studies in the area, for instance Witze (2017) and Fernando et al. (2018), using an ambitious combination of multiple remote sensing and measurement masts on the same site.

Wind farm operation data can be a form of obtaining large volumes of wake data, particularly in high density WFs. However, being indirectly measured (only in the form of relative power losses) and frequently lacking adequate calibration and reference measurements do provide considerable challenges. The ECN test wind farm Machielse et al. (2007) has long provided comprehensive data and control over the WF wake measurements. The ENDOW (Barthelmie et al., 2004) and UpWind (Barthelmie et al., 2009) projects were largely responsible for making publicly available a series of off-shore WF datasets, most notably the Horns-Rev WF dataset. Barthelmie and Pryor (2013) list some of the publicly available off-shore WF datasets and comments on the particularities of processing that data, with Gaumond et al. (2013) further expanding on the difficulties of handling wind direction uncertainty in these datasets, and how it affects processed relative power loss values. Much of the WF operational data described above was aggregated in the WAKEBENCH project (Moriarty et al., 2014), with the intent of establishing a protocol and platform for wake model testing, including research on best practices for WF operational data validation and processing.

1.5 The VENTOS®/2 CFD code

At the root of the present work is VENTOS®/2 , a dedicated parallel CFD computer code build for solving neutral ABL flows over complex terrain. Based on the work of Castro et al. (2003), it solves the RaNS equations in their elliptical form, with a k-ε turbulent viscosity model for closure. It has long been in use for wind resource assessment and micro-siting as in Palma et al. (2008), and has since been developed to account for forest

canopy drag and non-neutral atmospheric stability regimes.

The approach used (RaNS coupled with the turbulent viscosity k-ε model) strikes a convenient compromise between accuracy, convenience and computational cost that is suited to an engineering level site-assessment tool. The temporal and spatial resolution required to adequately resolve ABL flows in complex topography with approaches such as LES or DNS (Direct Numerical Simulation) are much more fine those of a typical RaNS simulation. Similarly, higher-order turbulence closure models for RaNS introduce many additional equations to the system. In any of those alternative approaches, the configuration of turbulent boundary conditions is also more complex and cumbersome.

Core equations

For a statistically steady turbulent flow, the solved core equations for mass and momentum conservation are, in the tensor form and in a Cartesian coordinate system:

$$\frac{\partial \left(\rho \overline{u_i}\right)}{\partial x_i} = 0, \tag{1.1}$$

$$\rho \frac{\partial \left(\overline{u_j}\ \overline{u_i}\right)}{\partial x_j} = -\frac{\partial \overline{p}}{\partial x_i} + \frac{\partial \overline{\tau}_{ij}}{\partial x_j} + \frac{\partial \overline{\sigma}_{ij}}{\partial x_j} + \underbrace{\widetilde{F_{C_i}}}_{\texttt{(1)Canopy}} + \underbrace{\widetilde{F_{B_i}}}_{\texttt{(2)Buoyancy}} + \underbrace{\widetilde{T_i}}_{\texttt{(3)Wind Turbine}}, \tag{1.2}$$

where the viscous stress tensor $\overline{\tau}_{ij}$ is defined by,

$$\overline{\tau}_{ij} = \mu \left(\frac{\partial \overline{u}_i}{\partial x_j} + \frac{\partial \overline{u}_j}{\partial x_i} \right), \tag{1.3}$$

and the Reynolds stress tensor σ_{ij} is defined according to the Boussinesq approximation:

$$\sigma_{ij} = -\rho \overline{u_i' u_j'} = -\frac{2}{3}\rho k \delta_{ij} + \mu_T \left(\frac{\partial \overline{u_i}}{\partial x_j} + \frac{\partial \overline{u_j}}{\partial x_i} \right) \tag{1.4}$$

Terms `(1)`, `(2)` and `(3)` in equation 1.2 represent the local momentum sink/sources. The first two respectively associated to the canopy model (documented in Lopes et al. (2013)) and to the atmospheric stratification model (based on the surface-layer empirical relations of Högström, 1988). The third term pertains to the thrust force exerted by the wind turbines on the flow, and is the focus of the work documented in this thesis.

The turbulent viscosity μ_T is the key to determining the Reynolds stresses $\overline{u_i' u_j'}$, and is defined by,

$$\mu_T = \rho C_\mu \frac{k^2}{\varepsilon}, \tag{1.5}$$

where k and ε are the turbulent kinetic energy and its dissipation rate, respectively. The turbulence model used is that of Launder and Spalding (1974), where each is determined

C_1	C_2	C_μ	σ_k	σ_ε
1.44	1.92	0.033	1.0	1.84

Table 1.1: $k-\varepsilon$ constants for atmospheric flows.

by solving its own transport equation,

$$\rho\frac{\partial\left(\overline{u_j}k\right)}{\partial x_j}=\frac{\partial}{\partial x_j}\left[\left(\mu+\frac{\mu_t}{\sigma_k}\right)\frac{\partial k}{\partial x_j}\right]+\mathcal{P}_k-\rho\varepsilon+\underbrace{S_{C_k}}_{\texttt{(1)Canopy}}+\underbrace{G_k}_{\texttt{(2)Buoyancy}}, \tag{1.6}$$

$$\rho\frac{\partial\left(\overline{u_j}\varepsilon\right)}{\partial x_j}=\frac{\partial}{\partial x_j}\left[\left(\mu+\frac{\mu_t}{\sigma_\varepsilon}\right)\frac{\partial \varepsilon}{\partial x_j}\right]+\frac{C_1\varepsilon}{k}P_k-\frac{C_2\rho\varepsilon_2}{k}+\underbrace{S_{C_\varepsilon}}_{\texttt{(1)Canopy}}+\underbrace{\frac{C_1\varepsilon}{k}G_k}_{\texttt{(2)Buoyancy}}, \tag{1.7}$$

with a production term given by,

$$P_k=\sigma_{ij}\frac{\partial\overline{u}_i}{\partial x_j}. \tag{1.8}$$

The canopy and atmospheric stratification models also extend to the turbulence equations 1.6 and 1.7: the associated sink/sources are highlighted respectively as terms `(2)` and `(1)`. The turbulence model constants adopted here were tuned for atmospheric flows and are presented in Table 1.1.

Boundary conditions

Wall functions (e.g. Ferziger and Peric, 2002, pp.297) are required to model the flow near the ground surface, since vertical mesh resolution is insufficient to resolve it adequately. The bottom boundary is modelled as a rough surface, using the wall laws of Launder and Sharma (1974), setting a wall-adjacent region of constant tangential Reynolds stress $\sigma_t=\rho\,u_*^2$ and a log-law tangential velocity u_t,

$$u_t=\frac{u_*}{\kappa}\ln\left(1+\frac{z}{z_0}\right), \tag{1.9}$$

where $\kappa=0.4$ is the von Kármán constant, u_* is the friction velocity, z is the distance above the ground with surface roughness z_0. As part of the wall *wall function*, the kinetic energy of turbulence and its dissipation in the wall adjacent control volumes is given by

$$k_{wall}=\frac{u_*^2}{C_\mu^{1/2}}\qquad\text{and}\qquad\varepsilon_{wall}=\frac{u_*^3}{\kappa\left(z+z_0\right)}, \tag{1.10}$$

and the tangential Reynolds stress and the mean production and dissipation of k are as follows:

$$\sigma_t=\frac{\rho\,C_\mu^{1/4}\,k_{wall}^{1/2}\,u_t\,\kappa}{\ln\left(1+z/z_0\right)}, \tag{1.11}$$

$$\overline{\mathcal{P}_k}=\|\sigma_t\|\,\frac{C_\mu^{1/4}\,k_{wall}^{1/2}}{\kappa\,\left(z+z_0\right)}, \tag{1.12}$$

$$\bar{\varepsilon}=\frac{C_\mu^{3/4}k_{wall}^{3/2}}{\kappa\,\left(z+z_0\right)}. \tag{1.13}$$

A zero-shear boundary condition is used at the top of the domain, modelling an idealized atmosphere with no Coriolis forces:

$$\mu_T \frac{\partial U}{\partial z} = 0\,, \tag{1.14}$$

Under these conditions, to ensure an equilibrium shear stress profile (linearly decreasing with height) and limited boundary layer size growth, the k profile is approximated so that it decreases with the square of height a.g.l.. The inlet profiles (and initial solution) are as follows:

$$u(\mathbf{x}) = \frac{u_*}{\kappa} \ln\left(1 + \frac{z(\mathbf{x})}{z_0}\right)\,, \tag{1.15}$$

$$k(\mathbf{x}) = C_\mu^{-1/2} u_*^2 \left(1 - z(\mathbf{x})/\delta_m\right)^2\,, \tag{1.16}$$

$$\varepsilon(\mathbf{x}) = \frac{C_\mu^{3/4} k^{3/2}}{\kappa\ (z(\mathbf{x}) + z_0)}\,, \tag{1.17}$$

where δ_m is the boundary layer height. The boundary conditions applied to the simulation must be coherent between them and either be or quickly settle into equilibrium, so as to avoid stream-wise gradients. Outside the boundary layer (above δ_m), velocity and turbulent quantity gradients are reduced to zero, matching the top boundary condition. At the lateral boundaries symmetry boundary conditions are enforced: zero normal velocity and solved quantity gradients, meaning there is no flux across the boundary and it behaves as a zero-shear slip wall. A zero-gradient condition in the normal direction is applied at the outlet, coupled with a mass flux correction to match the domain inlet.

Meshing & coordinate transformation

The discretization occurs over a terrain-following quadrilateral element structured mesh, projected vertically to form a box-type domain enclosing the AOI and the ABL surrounding it. Since terrain shape is not elegantly or efficiently described in a Cartesian coordinate system, the core equations are transformed to a generic non-orthogonal curvilinear coordinate system.

To obtain this generic coordinate system, the physical space is mapped in a computational orthogonal space by the transformation,

$$x_i = F_i\left(\xi_1, \xi_2, \xi_3\right)\,, \tag{1.18}$$

where the axes ξ_1 and ξ_2 follow the topography, and ξ_3 coincides the physical space vertical axis z. The transformed equations retain their original structure and conservative form, differing only in the presence of the domain transformation terms.

The surface geometry is obtained from the input topography using bi-linear interpolation, with greater node concentration within a rectangle (in a horizontal projection) surrounding the AOI. Similarly, the volumetric mesh is most concentrated at the surface. From the area of maximum mesh concentration, it expands geometrically in both horizontal and vertical directions towards the domain boundaries: the ratio between consecutive grid nodes is kept constant.

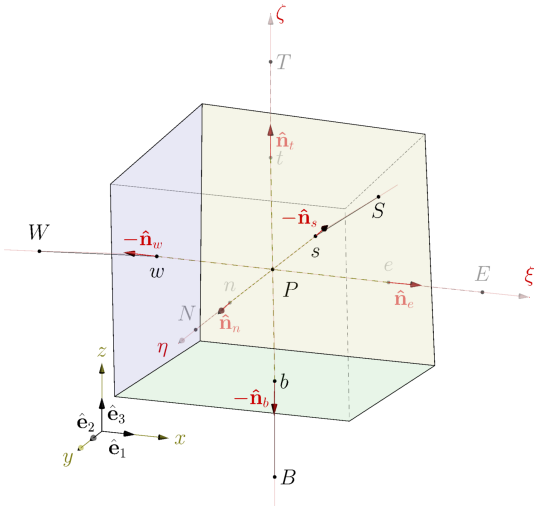

Figure 1.1: Control volume.

Numerical methods

The flow equations are solved using the segregated finite volume implicit method. The variables are stored in a collocated arrangement, and the SIMPLE algorithm (Caretto et al., 1973) for non-collocated grids is used, combined with the Rhie and Chow (1983) method for velocity-pressure coupling.

Each equation is integrated in control volumes (Figure 1.1) to produce an algebraic system of equations, solved by a TDMA (Tri-Diagonal Matrix Algorithm) solver. The algebraic equations produced are of the form:

$$A_P\Phi_P = A_N\Phi_N + A_S\Phi_S + A_E\Phi_E + A_W\Phi_W + A_U\Phi_U + A_D\Phi_D + S_\Phi, \tag{1.19}$$

The A_P, A_N, A_S, A_E, A_W, A_U and A_D are the coefficients for the generic variable Φ at the corresponding nodal positions, presented in Figure 1.1. S_Φ represents a source/sink term and is also the place where the explicit contributions from the fundamental equations are summed up.

The discretization of the convective terms for the momentum equations is done through the QUICK scheme (Leonard, 1979), achieved through deferred correction. On the k and ε equation convective terms, the hybrid scheme (Spalding, 1972) is used. Diffusive terms are discretized using the second-order finite difference methods.

Code parallelisation is achieved via domain decomposition: division into multiple sub-problems, each associated to a separate sub-domain and differential equation system, solved by one VENTOS®/2 thread. Adjacent sub-domains share boundary condition data, guaranteeing no loss of discretization accuracy for the methods previously described.

The criteria for convergence is based on the highest dimensionless global residual among the solved equations. Adimensionalization is done using inlet boundary flux integrals for the momentum and mass equations. In the case of the turbulence model equations, due to scale of the production term P_k in complex flow cases, the norm sum of the system matrix main diagonal terms $|A_P\Phi_P|$.

1.6 About this Thesis

1.6.1 Motivation

The industry standard for wake modelling is based on semi-empirical formulas, unable to cope with more complex flow cases such as high turbulence and separated on-shore flows, or irregular and high density WF arrays. They are computationally very affordable and allow for very quick turnaround, ideal for time constrained tasks such as forecasting. There is however a place for higher-level approaches to flow and wake modelling, making use of more of the computational resources available in modern high-performance computers. Additionally, as the wind power industry and individual projects (and their costs) grow, the use of more accurate and flexible tools for WT wake estimation becomes more and more justified. The intent behind this PhD was to develop a WT wake model that could improve upon the current techniques, particularly in complex cases where strong non-linear flow effects are present, while maintaining some accessibility and reasonable computational cost.

1.6.2 Author's contributions to the VENTOS®/2 code

The wake model was borne from the need to expand the capabilities of the in-house CFD code VENTOS®/2 to account for WT wakes. The main features developed and implemented form a rotor model, which couples with the CFD solver to model the wake flow.

Two core features were implemented in the code, the first of which was the AD discretization method. It had to provide the flexibility necessary to freely position a WT within the non-Cartesian structured mesh, as well as non-homogeneously distribute virtual rotor characteristics.

The second of the two core features is the capability to dynamically predict WT operating conditions as the CFD solution converged. The solution established internally iterates to find the WT's operating point within the manufacturer curve. Since WT/flow interaction is strongly non-linear, relaxation between solver iterations is required to avoid over-excitation of the flow solution.

There were other contributions to the code, auxiliary to the development and convenient applied use of the wake model. These include global momentum and energy budget assessment modules, used to numerically validate the model implementation, and one-directional simulation coupling interface, fundamental for the model's application in a WF cluster context.

1.6.3 Thesis structure

The development of this model is covered in this thesis, divided into three chapters: the second discussing the implementation and its numerical validation (Chapter 2), the third covering its application to real world WFs and comparison to measured wakes

(Chapter 3) and finally, the fourth exploring paths for improvement and evolution of the base model (Chapter 4). The fifth and final Chapter 5 is reserved for concluding remarks on the merits and performance of the proposed model, plus suggestion of future avenues of development.

Model development was initiated on a simpler 2-D version of the RaNS CFD code, allowing for faster model iteration before porting to the final 3-D code. The basic model results and the CFD solver's numerical consistency were validated for both codes. This initial implementation steps are discussed in Chapter 2, along with the subsequent developments that would form the core of the proposed WT wake model. These include the two-step rotor discretization method and the dynamic WT performance estimation algorithm, the latter previously presented in poster (Gomes and Palma, 2014) and publication (Gomes et al., 2014) form.

The wake model was then applied to real-world WF cases, more specifically two Danish off-shore wind power projects. Associated to either project were datasets with WF operational data, processed and shared with members of the EERA-DTOC project (Hasager and Giebel, 2015). Chapter 3 results of the collaboration in that project, and of the participation in multiple wake model benchmarks, documented in public project reports Réthoré et al. (2013a), Hansen and Hasager (2014), Schepers et al. (2015) and Beck et al. (2015) as well as public communications Réthoré et al. (2013b), Beck et al. (2015) and Hansen et al. (2015). Two significant sets of comparison cases are presented: the first focusing on internal wake effects within the Horns Rev WF and another focusing on the aggregate WF wake effect felt in an offshore cluster, between two neighbouring WFs Rødsand II and Nysted.

During the course of the model's development and application it was possible to identify some limitations. In Chapter 4 their causes are discussed and modifications to the base model implementation are proposed and tested. Some of the modifications are of an operational nature and respond to identified numerical issues, such as force singularities created by the AD discretization method or the need to lower computational costs of large WF cluster simulations. Others are related to the model formulation and the simplifications involved, such as the AD load distribution and the approximation to the disk-equivalent velocity. Elements of this work have been presented in peer-reviewed articles Gomes et al. (2014) and Gomes and Palma (2016).

This page intentionally left blank

Chapter 2

Wind turbine modelled as an Actuator Disk in RaNS

In this chapter, a model for simulating the presence of a Wind Turbine in ABL flows is formulated, based on one-dimensional momentum theory and Froude's Actuator Disk concept. This includes the form in which its equivalent thrust is calculated and distributed in the domain, as well how it is integrated into the flow solver to dynamically interact with the solution. The resulting model is able to simulate the operation of any number of WTs, with minimal intervention by the user.
After a brief introduction, the first two sections elaborate on the fundamental mathematics of rotor blade flow and of the Actuator Disc and one-dimensional momentum theory. On the fourth section the theory is translated into a functional wake model, tested in 2-D and 3-D flow solvers for consistent results – in comparison to theoretical and simplified model solutions – and robustness in handling the added force terms.
With a simplified version of the model in place, its implementation is elaborated. One part of that work – described on the fifth section – is on the actuator disc's discretization, in order for it to optimally adapt to variable mesh sizes and orientations. The sixth section concerns to the model's functionality, specifically on how it is enabled to dynamically estimate the WT's performance as the flow solution iterates.

2.1 Introduction

The VENTOS®/2 CFD code is oriented to use in wind resource assessment and micro-siting (Palma et al., 2008) purposes. The development – of this and other products of the VENTOS® software family – results of the continued effort to expand the features and ability to simulate complex real-world atmospheric flows. Adding the capability to model the aerodynamic forces of WTs on the flow is another step in that same direction.

In order to fully exploit the elliptical nature of the RaNS code, the WT's aerodynamic forces are modelled as terms in the momentum equations, meaning they will also affect the pressure field and diffusive transport. Unlike in simpler analytical and parabolized-

RaNS equation wake models, the influence of the WT also propagates upstream. Ideally, adding the WT modelling terms should not require dramatic changes to either simulation method or computational requirements, keeping it accessible and cost-effective as an engineering-level model. The WT thrust terms are thus modelled through the principles established with the AD and the one-dimensional momentum theory, allowing for the simplest description and lowest demands as far as spatial resolution goes.

2.2 Wind turbine rotor flow

A rotating WT rotor extracts momentum from the flow via aerodynamic forces. Its wing profile shaped blades produce lift and drag forces, the torque of which is harvested and transformed into electrical power at the hub. The flow as well as the lift and drag forces can be geometrically characterized at any given section of the blade, as illustrated in Figure 2.1.

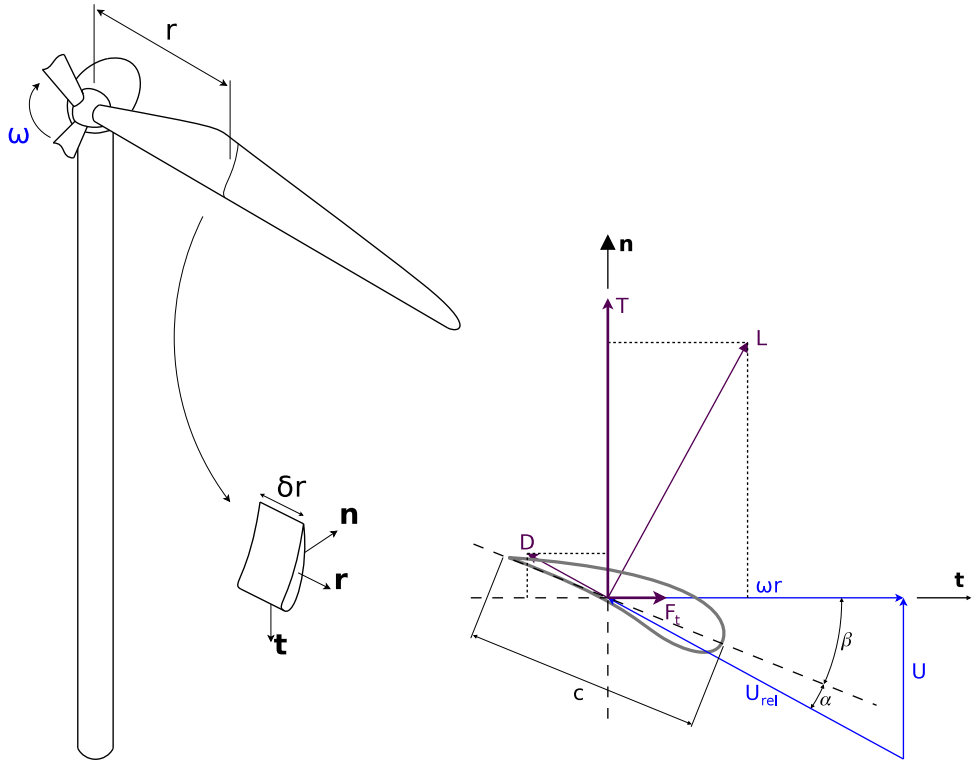

Figure 2.1: Flow over section of blade: determining lift and drag forces at a blade element.

The rotor has an angular velocity ω, leading to a local blade section velocity ωr which, combined with the axial inflow wind speed U results in an apparent flow velocity U_{rel}, as perceived by the blade section:

$$U_{rel} = \sqrt{U^2 + (\omega r)^2}\,. \tag{2.1}$$

The apparent flow velocity hits the blade section at an angle α, the angle-of-attack

(AOA), which is the angle formed between the local blade orientation and local U_{rel} vector. The blade geometry, typically based on the shape of standardized wing profiles, has well known lift and drag coefficients C_L and C_D curves, function of α. A blade section of length δr and chord c will produce lift and drag forces of δL (2.3) and δD (2.2).

$$\delta L = \frac{1}{2} c\, C_L \rho {U_{rel}}^2\, \delta r \tag{2.2}$$

$$\delta D = \frac{1}{2} c\, C_D \rho {U_{rel}}^2\, \delta r \tag{2.3}$$

These forces will change dramatically along the length of the blade. The velocity of the blade section increases with the radial position r, reflecting also on the orientation and magnitude of U_{rel}. The section will vary in shape and chord, combined with twisting incorporated into the blade shape to change β and optimize the AOA throughout it's length.

These radially varying forces can be geometrically decomposed into statically oriented components in a polar coordinate system, resulting in thrust T (2.4) and rotational F_t (2.5) forces, respectively in the directions normal and tangential to the rotor plane. The blade section is subject to these aerodynamic forces and naturally exerts equal and opposite forces on the flow. These latter forces acting on the flow are the main focus of a WT rotor model, when attempting to simulate it's presence and wake effect in the flow solution of a CFD code.

$$\delta T = -\delta L\, cos(\beta + \alpha) - \delta D\, sin(\beta + \alpha) \tag{2.4}$$

$$\delta F_t = -\delta L\, sin(\beta + \alpha) + \delta D\, cos(\beta + \alpha) \tag{2.5}$$

2.3 The Actuator Disk

The actuator surface technique allows for a virtual substitute of a rotating wind turbine, as an approximation to the real rotor with a static, discrete surface covering the same area as the rotor span. This virtual surface (the Actuator Disk) is permeable to incoming flow, and the forces known to be exerted by the real rotor (thrust and rotational forces T and F_t from individual blades, described in Section 2.2) are redistributed over it. An area element δA on that surface exerts forces on its normal (δT) and tangential (δF_t) directions (see Figure 2.2), and no forces on the radial direction.

Real world WT rotors usually have a certain amount of conicity engineered into their geometry. This angle γ is typically quite low (5-10°), enough to allow the area covered by the blade span A_{rt}, combined with the nacelle frontal area A_{nac}, to approximate the

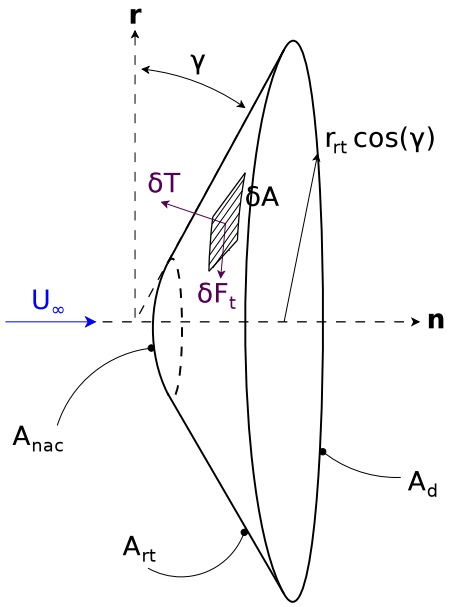

Figure 2.2: Actuator disk concept, representing a WT rotor's span. Rotor conicity angle γ exaggerated for clarity.

rotor's frontal area and the AD's surface area A_d (2.6).

$$\begin{aligned} A_d &= A_{rt} + A_{nac} \\ A_d &= A_{rt}\pi \left(r_{rt}^2 - r_{nac}^2\right) \underbrace{\cos\gamma}_{\approx 1} + A_{nac} \\ A_d &\approx \pi\, r_{rt}^2 \end{aligned} \tag{2.6}$$

The resulting actuator disk is a two-dimensional permeable surface, placed frontally to an incoming three-dimensional flow and acting upon it with forces normal and tangential to itself. The description of these forces can be of varied complexity, from the simple uniform load distribution of one-dimensional momentum theory to a dynamical load model such as Glauert's blade element method.

2.3.1 Betz's one-dimensional momentum theory

Consider an AD, placed within a stream tube in zero-shear incompressible inflow at free-stream velocity U_∞. Consider also that the AD exerts a force on the flow exclusively in the normal direction, uniformly distributed and opposite the flow.

By exerting a thrust force and extracting momentum from the incoming flow, mass conservation ensures velocity is reduced and the wake expands downstream of the AD. Figure 2.3 demonstrates the expected flow velocity and pressure along the streamlines inside the stream-tube. Equations for mass (2.7), momentum (2.8) and energy (2.9) conservation can be applied to the control volume bounded by it.

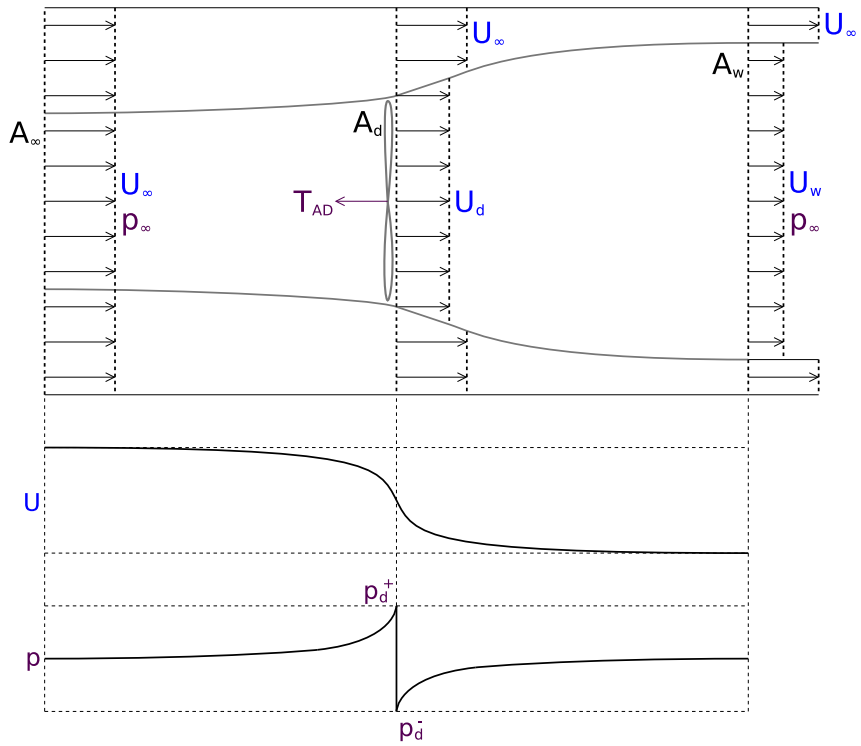

Figure 2.3: Momentum theory's stream tube, where flow through an actuator disk is simplified to a one-dimensional solution.

$$\dot{m} = \rho A_\infty U_\infty = \rho A_d U_d = \rho A_w U_w \tag{2.7}$$

$$\begin{aligned} T_{AD} - \Delta M &= 0 \\ T_{AD} &= \dot{m}\left(U_\infty - U_w\right) \end{aligned} \tag{2.8}$$

$$P_{AD} = \frac{1}{2}\dot{m}\left({U_\infty}^2 - {U_w}^2\right) . \tag{2.9}$$

The thrust exerted by the AD can also be expressed using the pressure jump that occurs on it:

$$T_{AD} = A_d\left({p_d}^+ - {p_d}^-\right) . \tag{2.10}$$

Bernoulli's equation for incompressible flows can be applied independently to the two branches of the system either side of the AD:

$$p_\infty + \frac{1}{2}\rho {U_\infty}^2 = {p_d}^+ + \frac{1}{2}\rho {U_d}^2 , \tag{2.11}$$

$$p_\infty + \frac{1}{2}\rho {U_w}^2 = {p_d}^- + \frac{1}{2}\rho {U_d}^2 . \tag{2.12}$$

The difference between (2.12) and (2.11), combined with the AD thrust definition (2.10) yields a form of expressing the AD thrust (2.13) that is dependent only on boundary

conditions.

$$\begin{aligned}
&\frac{1}{2}\rho\left({U_\infty}^2 - {U_w}^2\right) = {p_d}^+ - {p_d}^- \\
&\frac{1}{2}\rho A_d\left({U_\infty}^2 - {U_w}^2\right) = T_{AD}\,.
\end{aligned} \tag{2.13}$$

Finally, equating (2.8) and (2.13),

$$\frac{1}{2}\rho A_d\left({U_\infty}^2 - {U_w}^2\right) = \dot{m}\left(U_\infty - U_w\right)$$

and using the mass flux at section d (2.7),

$$\frac{1}{2}\rho A_d\left({U_\infty}^2 - {U_w}^2\right) = \rho A_d U_d\left(U_\infty - U_w\right)$$

the velocity at the AD can be determined:

$$U_d = \frac{U_\infty + U_w}{2}\,. \tag{2.14}$$

2.3.2 Thrust and power coefficients

Being able to determine flow velocity at the actuator disk (and consequently mass flow in the stream tube), we can express the efficiency of the AD at extracting momentum and energy from the inflow. The thrust coefficient (C_T, equation 2.15) relates the AD thrust to the free-stream flow's momentum flux T_∞ through an equivalently sized section:

$$\begin{aligned}
C_T &= \frac{T_{AD}}{M_\infty} \\
C_T &= \frac{\rho A_d U_d\left(U_\infty - U_w\right)}{\frac{1}{2}\rho A_d {U_\infty}^2} \\
C_T &= 2\frac{U_\infty - U_w}{U_\infty}\frac{U_d}{U_\infty} \\
C_T &= 4\left(1 - \frac{U_d}{U_\infty}\right)\frac{U_d}{U_\infty}
\end{aligned} \tag{2.15}$$

Similarly, the power coefficient (C_P, equation 2.16) relates the power extracted by the AD to the free-stream flow's kinetic energy flux P_∞ through an equivalently sized section.

$$\begin{aligned}
C_P &= \frac{P_{AD}}{P_\infty} \\
C_P &= \frac{\frac{1}{2}\rho A_d U_d\left({U_\infty}^2 - {U_w}^2\right)}{\frac{1}{2}\rho A_d U_\infty {U_\infty}^2} \\
C_P &= 2\frac{U_\infty - U_w}{U_\infty}\left(\frac{U_d}{U_\infty}\right)^2 \\
C_P &= 4\left(1 - \frac{U_d}{U_\infty}\right)\left(\frac{U_d}{U_\infty}\right)^2
\end{aligned} \tag{2.16}$$

We can use the axial induction factor a (2.17) – a measure of the velocity reduction relative to free-stream – to parametrize the equations for both C_T and C_P. This way, (2.15) and (2.16) result in their simplified forms (2.18) and (2.19).

$$a = 1 - \frac{U_d}{U_\infty} \tag{2.17}$$

$$C_T = 4a\,(1-a) \tag{2.18}$$

$$C_P = 4a\,(1-a)^2 \tag{2.19}$$

When plotted against a (Figure 2.4), it can be observed that C_P reaches a maximum of $\frac{16}{27} \approx 0.59$ at $a = \frac{1}{3}$. It occurs as flow in the wake side of the stream tube approaches velocities close to zero ($U_\infty = 0$ at $a = 0.5$), after which Betz's theory breaks down due to mass conservation. This theoretical maximum of energy extraction by an actuator disk is known as the *Betz limit*, and it serves as a guide for power efficiency of any horizontal axis WT.

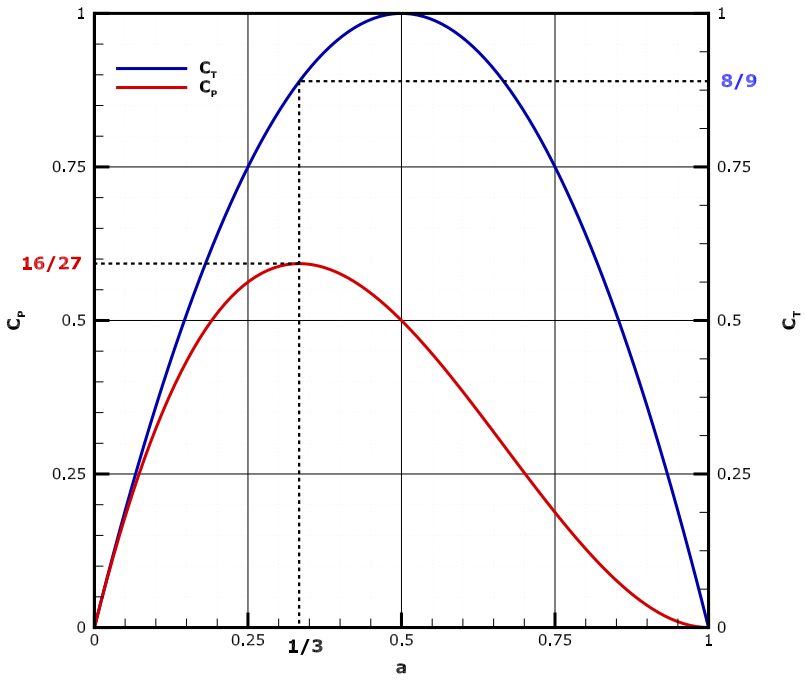

Figure 2.4: Thrust and power coefficients as function of the axial induction factor a. The *Betz limit* (a=1/3) marks peak mechanical efficiency of the theoretical AD.

2.4 Prototype CFD implementation

A significant part of the simplified flow conditions assumed under Betz's one--dimensional momentum theory – axisymmetric inviscid flow – severely clash with real world ABL flows, simulated by CFD solvers. However, the concepts established by the Betz model allow for parametrization of the forces exerted by a WT on the flow, while the CFD code is able to solve the WT wake and its interaction with the underlying ABL flow.

For any testing purposes the AD model prototype is placed in a flat plane domain, tall and wide enough that the constriction caused by the AD is not significant. Typical synthetic ABL inflow conditions were set at the inlet boundary, with a log-law velocity profile and equilibrium turbulence conditions. Mesh nodes are concentrated near the wall and near the WT, where gradients and flow complexity are greatest. The AD model was configured in order to represent a real WT model, with a 68 m high hub and 70 m diameter rotor, operating at a prescribed 7 m/s free-stream velocity (equal to inflow velocity at hub height) and at a corresponding thrust coefficient of $C_T = 0.78$.

As a measure of the model's implementation, wake flow will be compared to an equivalent solution from the Ainslie (1988) wake model, extended with the Quarton and Ainslie (1990) model for additional turbulence generation, covering the wake's recovery from 2D downstream and onwards.

2.4.1 Determining total rotor thrust

With information on the inflow hitting the WT position, the forces exerted on the flow via the AD are easily quantifiable using the thrust coefficient concept. Since one-dimensional momentum theory that assumes thrust acts exclusively in the AD-normal direction, the aggregate normal component of those forces T_{AD} can be uniformly distributed over the AD surface and the tangential component F_t is zero:

$$T_{AD} = \frac{1}{2} C_T \rho {U_\infty}^2 A_d \,, \qquad F_t = 0 \tag{2.20}$$

The formulation in equation (2.20) requires the following parameters:

- WT's rotor radius r_{rt} – to determine actuator disk area A_d;
- Free-stream velocity U_∞ – wind speed at the WT position in its absence, i.e. in undisturbed flow; and
- WT's operating thrust coefficient C_T – obtainable via the WT's thrust curve (supplied by the WT manufacturer), which relates thrust coefficient to local free-stream velocity.

2.4.2 Distributing the rotor thrust as body-forces

Surface forces such as the AD thrust can be modelled in a finite-volume RaNS solver as discrete forces if described as a pressure term. However, since their placement may not

coincide with any CV boundaries conversion to body force formulation is preferable. This allows for untethered placement over the domain mesh, at the cost of attributing a discrete thickness to the AD.

Equation 2.20, in integral form, defines the WT force per unit of frontal AD area. If s_d is the actuator disk area contained within a given control volume (and $\widetilde{s_n}$ the respective area density), it follows that the force density of the wind turbine thrust $\widetilde{T}$, acting only on the normal direction $\mathbf{n_{AD}}$, in finite-volume form is defined by

$$\widetilde{T} = \frac{1}{2} C_T {U_\infty}^2 \widetilde{s_n} \,. \tag{2.21}$$

The momentum sinks resulting of the discretized rotor will, as body forces independent of local or neighbour cell velocities, appear on the right-hand side of the momentum transport equation: (2.22).

$$\rho \frac{\partial \left(\overline{u_i}\ \overline{u_j} \right)}{\partial x_i} = -\frac{\partial \overline{p}}{\partial x_i} + \frac{\partial \overline{\tau}_{ij}}{\partial x_j} - \rho \overline{u_i' u_j'} + \rho \widetilde{T} \mathbf{n_{AD}} \cdot \delta_{ij} \quad . \tag{2.22}$$

The sum of every contribution on all three momentum equations will approximate the overall AD thrust T_{AD}. Additionally, with the local velocity vector $\mathbf{u}$ at the AD, it is possible, via volume integral, to determine the mechanical power P_{AD} extracted by the WT (2.23). An alternative to the power indicated by the manufacturer's power curve, it takes into consideration the actual inflow hitting the AD surface (including its inhomogeneities). Depending on the rotor's aerodynamic efficiency, which can change with wind speed and with the WT control regime, the gap between P_{AD} and the effective WT electrical power will change.

$$P_{AD} = \int \rho \widetilde{T} \mathbf{n_{AD}} \cdot \mathbf{u} \mathrm{d}\Omega \tag{2.23}$$

2.4.3 Actuator disk discretization

The domain shape and boundary conditions ensure that flow will be predominantly lengthwise, aligned with the structured Cartesian mesh used on the CFD solver. Under normal conditions, the WTs will operate facing the inflow, meaning the AD will be contained within a single row of control volumes. In its simplest form, the discretized AD will include all control volumes the central node of which is enclosed within the AD circle shape, defined by the WT's hub position and rotor radius and oriented towards the inlet boundary, as exemplified in Figure 2.5.

$$\widetilde{s_n} = \frac{\int \mathbf{n} \cdot \mathbf{i} \mathrm{d}S}{\int \mathrm{d}\Omega} \frac{A_d}{A_{app}} \tag{2.24}$$

In the resulting AD discretization each CV will contain an AD area s_d equal to its own x-direction frontal cross-section, and $\widetilde{s_n}$ will be approximately the ratio between the

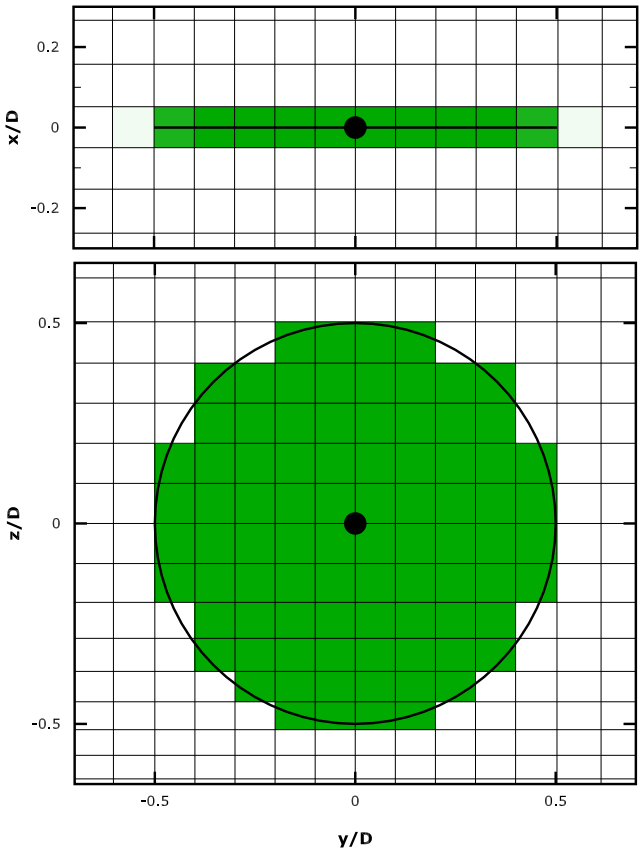

Figure 2.5: Actuator disc area density $\widetilde{s_n}$ distribution for the prototype AD discretization, in top (above) and frontal (below) views.

CV's frontal area and volume. The total frontal area A_{app} only approximates the correct rotor's span A_d, so this has to be compensated for when calculating $\widetilde{s_n}$ (2.24) to obtain the correct thrust T_{AD}. The AD will also have a discrete thickness, equal to the CV's x dimension.

2.4.4 Domain-wide budget validation

The external forces and boundary fluxes relevant to the domain flow (summarized in Figure 2.6) are well identified and easily quantifiable. In a correctly solved flow solution they should cancel out. To confirm the preservation of the code's conservative properties after introducing the wake model's WT thrust terms, the global momentum and energy budgets are verified. Small and mesh-converged budget residuals should confirm the wake model's correct implementation and an appraisal of the associated uncertainty.

The CFD code attempts to ensure momentum conservation at every domain cell, the overall sum of the respective balances being minimized with solver convergence. In this manner, the code assumes overall conservation comes as a consequence of conservation at each cell. The global budget on the other hand analyses the domain as a whole, including potential momentum losses at cell boundaries. Although not directly enforced, energy conservation should come as a consequence of mass and momentum

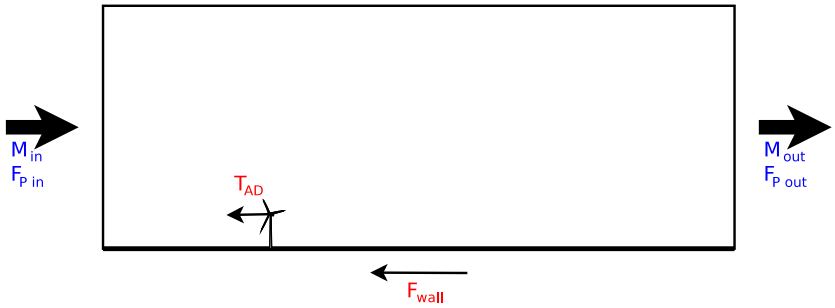

Figure 2.6: 2-D schematic of forces (in red) and boundary fluxes (blue) acting on the domain.

conservation in simple equilibrium ABL flows.

2.4.4.1 Momentum

The momentum transport equations are applied to the whole domain as a single control surface. The AD applies force terms exclusively in the x-direction, meaning the remaining y and z momentum equations are not directly affected by the WT's presence and can be ignored in this exercise. The classic boundary conditions – inlet with log-law velocity profile and equilibrium turbulence conditions, symmetry condition on the top and a no-slip rough wall bottom boundary – ensure flow is exclusively in the x-direction. This way the integral form of the x-momentum equation (2.22), applied to the whole domain, can be simplified once its terms reflect the boundary conditions.

$$\begin{aligned}\int \rho u \left(\mathbf{u}\cdot\mathbf{n}\right)\, \mathrm{d}S = &-\int \left[p\mathbf{n_i} - \left(\mu+\mu_T\right)\left(2\frac{\partial u}{\partial x}\mathbf{n_i} + \left(\frac{\partial u}{\partial y}+\frac{\partial v}{\partial x}\right)\mathbf{n_j} + \left(\frac{\partial u}{\partial z}+\frac{\partial w}{\partial x}\right)\mathbf{n_k}\right)\right]\cdot\mathbf{n}\,\mathrm{d}S \\ &+\int \rho\widetilde{T}\mathbf{n_{AD}}\cdot\delta_{1j}\,\mathrm{d}\Omega \end{aligned} \tag{2.25}$$

$$\begin{aligned}\Leftrightarrow \int_{out}^{in}\rho u u\,\mathrm{d}S = &-\int_{out}^{in}\left[p-2\left(\mu+\mu_T\right)\frac{\partial u}{\partial x}\right]\,\mathrm{d}S + \int_{north}^{south}\left(\mu+\mu_T\right)\left(\frac{\partial u}{\partial y}+\frac{\partial v}{\partial x}\right)\,\mathrm{d}S \\ &+\int_{top}^{wall}\left(\mu+\mu_T\right)\left(\frac{\partial u}{\partial z}+\frac{\partial w}{\partial x}\right)\,\mathrm{d}S + \int\rho\widetilde{T}\,\mathrm{d}\Omega \\ \Leftrightarrow \int_{out}^{in}\rho u u\,\mathrm{d}S = &-\int_{out}^{in}\left[p-2\left(\mu+\mu_T\right)\frac{\partial u}{\partial x}\right]\,\mathrm{d}S + \int\rho\widetilde{T}\,\mathrm{d}\Omega \\ &+\int^{wall}\left(\mu+\mu_T\right)\left(\frac{\partial u}{\partial z}+\frac{\partial w}{\partial x}\right)\,\mathrm{d}S \\ \Leftrightarrow \Delta M = &-\Delta F_p + F_{wall} + T_{AD} \\ \Leftrightarrow e_{mom} = &\Delta M + \Delta F_p - F_{wall} - T_{AD}\end{aligned} \tag{2.26}$$

The explicit x-momentum equation (2.25) is reduced down to the momentum budget equation (2.26), which has the terms: momentum (2.27)) and pressure (2.28)) (including the normal component of the viscous stress tensor, acting on the x-oriented boundaries) differentials between inlet and outlet sections ΔM and ΔF_p, shear stress at the ground

surface boundary F_{wall} (2.29) plus the WT thrust T_{AD} (2.30) as an additional external force applied to the AD.

$$\Delta M = \int_{out}^{in} \rho u^2 \mathrm{d}S \tag{2.27}$$

$$\Delta F_p = \int_{out}^{in} \left(p - (\mu + \mu_T) \frac{\partial u}{\partial x} \right) \mathrm{d}S \tag{2.28}$$

$$F_{wall} = \int^{wall} (\mu + \mu_T) \frac{\partial u}{\partial z} \, \mathrm{d}S \tag{2.29}$$

$$T_{AD} = \int \rho \widetilde{T} \, \mathrm{d}\Omega \tag{2.30}$$

$$Res_{mom} = \frac{e_{mom}}{M_{in}} \tag{2.31}$$

In the solved x-momentum equation, the code ensures that for every cell (i, j, k) the sum of all convective (F_C) fluxes, diffusive (F_D) fluxes and pressure gradient (P_G) terms cancel out (2.32), ensuring conservation.

$$F_C{}^x + F_D{}^x + P_G{}^x = 0 \tag{2.32}$$

If (2.32) is verified at the cell level, and should the code maintain conservation across cell boundaries the aggregate sum over all domain cells $(\mathrm{N}_i, \mathrm{N}_j, \mathrm{N}_k)$ (2.33) will too.

$$\sum_{i,j,k=1}^{\mathrm{N}_i,\mathrm{N}_j,\mathrm{N}_k} (F_C{}^x + F_D{}^x + P_G{}^x) = 0 \tag{2.33}$$

The sum of the terms on the local budgets have a logical match to terms in the global budget (2.34, 2.35, 2.36, and their values should be comparable.

$$\sum_{i,j,k=1}^{\mathrm{N}_i,\mathrm{N}_j,\mathrm{N}_k} F_C{}^x \Longleftrightarrow \Delta M \, , \tag{2.34}$$

$$\sum_{i,j,k=1}^{\mathrm{N}_i,\mathrm{N}_j,\mathrm{N}_k} P_G{}^x \Longleftrightarrow \Delta F_p \, , \tag{2.35}$$

$$\sum_{i,j,k=1}^{\mathrm{N}_i,\mathrm{N}_j,\mathrm{N}_k} F_D{}^x \Longleftrightarrow F_{wall} \tag{2.36}$$

Table 2.1 confirms that there is a good match between global and sum of local budget terms. Because the code fails to conserve momentum between control volumes, there is a difference between the two momentum balance terms ΔM and $\sum F_C{}^x$ (2.34). That difference has a very close correspondence to the increase in budget error e_{mom}.

2.4.4.2 Energy

Under the prescribed stationary boundary conditions the ABL should be close to turbulent equilibrium, where turbulence production and dissipation cancel out. Combined with momentum conservation (ensured by the solver), this should result in mean flow

Sum of local momentum budgets			
$\sum {F_C}^x$	$\sum {P_G}^x$	$\sum {F_D}^x$	e_{mom}
-30.0	411.0	380.0	1.1
Global momentum budget			
ΔM	ΔF_p	F_{wall}	e_{mom}
-37.2	410.2	380.3	-7.3

Table 2.1: Cell-wise sum of local momentum budgets and global momentum budget in the 2-D flow model. All quantities in [kg m s^{-2}].

kinetic energy conservation, despite not being directly enforced via a solved equation. The introduction of the WT thrust forces, in addition to the extracted mechanical energy, will disrupt the turbulence production/dissipation balance, with the energy budget equilibrium degrading as a consequence.

The mean flow kinetic energy equation (2.37) is obtained from the sum of all momentum component equations –such as (2.25) for x-momentum– each integrated with respect to their velocity components.

$$\begin{aligned}
\int \frac{1}{2}\rho u^2 \mathbf{u}\cdot\mathbf{n}\,\mathrm{d}S &= -\int \left\{ pu - (\mu+\mu_T)\left[2\,u\frac{\partial u}{\partial x} + v\left(\frac{\partial u}{\partial y}+\frac{\partial v}{\partial x}\right) + w\left(\frac{\partial u}{\partial z}+\frac{\partial w}{\partial x}\right)\right]\right\}\mathbf{n_i}\cdot\mathbf{n}\,\mathrm{d}S \\
+\int \frac{1}{2}\rho v^2 \mathbf{u}\cdot\mathbf{n}\,\mathrm{d}S &\quad -\int \left\{ pv - (\mu+\mu_T)\left[2\,v\frac{\partial v}{\partial y} + u\left(\frac{\partial v}{\partial x}+\frac{\partial u}{\partial y}\right) + w\left(\frac{\partial v}{\partial z}+\frac{\partial w}{\partial y}\right)\right]\right\}\mathbf{n_j}\cdot\mathbf{n}\,\mathrm{d}S \\
+\int \frac{1}{2}\rho w^2 \mathbf{u}\cdot\mathbf{n}\,\mathrm{d}S &\quad -\int \left\{ pw - (\mu+\mu_T)\left[2\,w\frac{\partial w}{\partial z} + u\left(\frac{\partial w}{\partial x}+\frac{\partial u}{\partial z}\right) + v\left(\frac{\partial w}{\partial y}+\frac{\partial v}{\partial z}\right)\right]\right\}\mathbf{n_k}\cdot\mathbf{n}\,\mathrm{d}S \\
&\quad +\int \rho\widetilde{T}\mathbf{n_{AD}}\cdot\mathbf{u}\,\mathrm{d}\Omega
\end{aligned} \tag{2.37}$$

$$\begin{aligned}
\Leftrightarrow \int_{out}^{in} \frac{\rho}{2}u^2 u\,\mathrm{d}S &= -\int_{out}^{in} pu\mathrm{d}S + \int \rho\widetilde{T}u\,\mathrm{d}\Omega \\
&\quad +\int (\mu+\mu_T)\left\{2\left[\left(\frac{\partial u}{\partial x}\right)^2+\left(\frac{\partial v}{\partial y}\right)^2+\left(\frac{\partial w}{\partial z}\right)^2\right]+\left(\frac{\partial u}{\partial y}+\frac{\partial v}{\partial x}\right)^2\right. \\
&\qquad \left.+\left(\frac{\partial u}{\partial z}+\frac{\partial w}{\partial x}\right)^2+\left(\frac{\partial v}{\partial z}+\frac{\partial w}{\partial y}\right)^2\right\}\mathrm{d}\Omega \\
\Leftrightarrow \Delta P_c &= -\Delta P_p + \mathcal{P}_k + P_{AD} \\
\Leftrightarrow e_{power} &= \Delta P_c + \Delta P_p - \mathcal{P}_k - P_{AD}
\end{aligned} \tag{2.38}$$

We arrive at the mean flow energy budget equation (2.38), with the terms: mean kinetic energy (2.39) and pressure potential energy (2.40) (including the isotropic stress component) differential between inlet and outlet sections ΔP_c and ΔP_p, viscous energy dissipation (from the mean flow field to turbulent form i.e. turbulent kinetic energy production) $\mathcal{P}_k$ (2.41) and, finally, an external energy sink P_{AD} from the WT (2.42).

$$\Delta P_C = \int_{out}^{in} \frac{\rho}{2} u^2 u \, \mathrm{d}S \tag{2.39}$$

$$\Delta P_P = \int_{out}^{in} pu \, \mathrm{d}S \tag{2.40}$$

$$\mathcal{P}_k = \int (\mu + \mu_T) \left\{ 2 \left[\left(\frac{\partial u}{\partial x} \right)^2 + \left(\frac{\partial V}{\partial y} \right)^2 + \left(\frac{\partial w}{\partial z} \right)^2 \right] + \left(\frac{\partial u}{\partial y} + \frac{\partial v}{\partial x} \right)^2 + \left(\frac{\partial u}{\partial z} + \frac{\partial w}{\partial x} \right)^2 + \left(\frac{\partial v}{\partial z} + \frac{\partial w}{\partial y} \right)^2 \right\} \mathrm{d}\Omega \tag{2.41}$$

$$P_{AD} = \int \rho \widetilde{T} u \, \mathrm{d}\Omega \tag{2.42}$$

$$Res_{energy} = \frac{e_{energy}}{P_{Conv_{in}}} \tag{2.43}$$

The mean kinetic energy budget at the local level can be obtained through the product of the momentum budget terms with the corresponding velocity, and should the code maintain conservation across cell boundaries, the aggregate sum over all domain cells (N_i,N_j,N_k) will too:

$$\sum_{i,j,k=1}^{\mathrm{N}_i,\mathrm{N}_j,\mathrm{N}_k} u_i \left({F_C}^{x_i} + {F_D}^{x_i} + {P_G}^{x_i} \right) \approx 0 \tag{2.44}$$

The sum of local energy budgets terms should, in a simple equilibrium BL, be comparable those coming from the global budget (2.45, 2.46, 2.47).

$$\sum_{i,j,k=1}^{\mathrm{N}_i,\mathrm{N}_j,\mathrm{N}_k} u_i {F_C}^{x_i} \Longleftrightarrow \Delta P_c \ , \tag{2.45}$$

$$\sum_{i,j,k=1}^{\mathrm{N}_i,\mathrm{N}_j,\mathrm{N}_k} u_i {P_G}^{x_i} \Longleftrightarrow \Delta P_p \ , \tag{2.46}$$

$$\sum_{i,j,k=1}^{\mathrm{N}_i,\mathrm{N}_j,\mathrm{N}_k} u_i {F_D}^{x_i} \Longleftrightarrow \mathcal{P}_k \tag{2.47}$$

The residual given by the sum of local budgets in Table 2.2 in the absence of a WT is acceptable. Two of its terms have a good match to the global budget's equivalents, but there is a large discrepancy in the viscous dissipation term ($\mathcal{P}_k$ is nearly half of $\sum u_i {F_D}^{x_i}$). That difference has a very close correspondence to the increase in budget error e_{energy}.

A major part of the turbulent kinetic energy production (Figure 2.7) is concentrated near the wall, peaking at the first and smallest cell in the vertical direction. Since $\mathcal{P}_k$ is the only term in the global balance equation (2.38) obtained via volume integral, it is based on cell centre and not cell boundary quantities. As a consequence it is sensitive to near-wall resolution, requiring a very fine mesh to adequately capture.

Table 2.3 shows the growth of the viscous dissipation term $\mathcal{P}_k$ captured via volume integral as the near-wall resolution is refined. Although there is a noticeable increase, the gap to the equivalent local budget sum term (which remains virtually unchanged)

Sum of local energy budgets			
$\sum u_i F_C{}^{x_i}$	$\sum u_i P_G{}^{x_i}$	$\sum u_i F_D{}^{x_i}$	e_{energy}
-347.2	3190.6	2941.7	-98.3
Global energy budget			
ΔP_c	ΔP_p	$\mathcal{P}_k$	e_{energy}
-403.8	3183.8	1493.9	1286.1

Table 2.2: Cell-wise sum of local energy budgets and global energy budget in the 2-D flow model. All quantities in [kW].

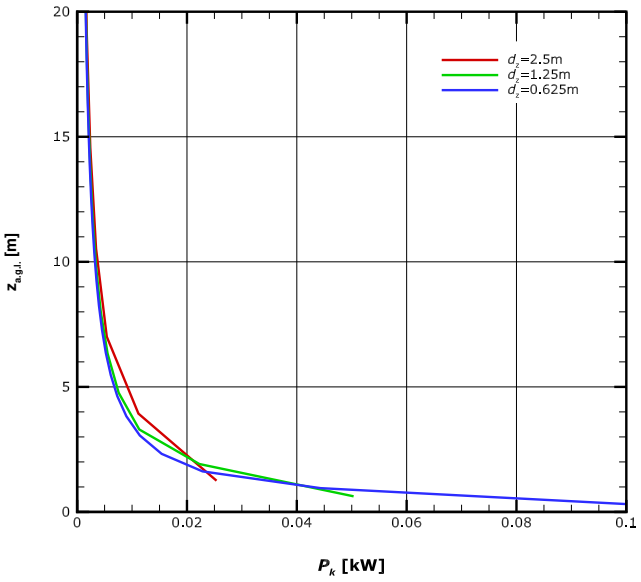

Figure 2.7: Turbulent kinetic energy production $\mathcal{P}_k$ near the wall for various vertical mesh resolutions.

remains close to 1000 kW. For any conclusive energy budget analysis the viscous dissipation term $\mathcal{P}_k$ must be replaced with its local budget counterpart $\sum u_i F_D{}^{x_i}$ (2.47).

d_z [m]	$\mathcal{P}_k$ [kW]	$\sum u_i F_D{}^{x_i}$ [kW]
2.5	1181.9	2225.6
1.25	1280.7	2221.6
0.625	1381.9	2218.8

Table 2.3: Viscous dissipation term and equivalent cell-wise sum of local budget diffusive fluxes at various near-wall vertical resolutions.

2.4.4.3 Results

The momentum and budget terms were calculated for 2-D and 3-D implementations of the AD model. The budget residual was analysed in light of the flow solver convergence criteria, which required the equation residual to be less than 5×10^{-5} of the respective flux at the inlet. The exercise was repeated for three equally sized domains M0, M1 and M2, each with double the mesh resolution per direction of previous.

2-D model budget

Successively refining the mesh does not significantly change the global momentum budget terms (2.26) in the 2-D flow model, as demonstrated by Table 2.4. Equilibrium is maintained within acceptable residuals (same order of magnitude as the residual convergence criteria) irrespective of mesh or WT presence. Introducing the WT thrust to the budget leads to an increase in the momentum differential ΔM between inlet and outlet boundaries, both of which compensated by a growth in the pressure force differential ΔF_{press}. The budget error level, although low, responds favourably to the successive mesh refinements, dropping by an order of magnitude between M0 and M2 as the CV boundary losses become largely insignificant.

Flat plate domain

Mesh	ΔM	ΔF_p	F_{wall}	T_{AD}	Res_{mom}	e_{mom}	M_{in}
M0	-39.6	403.6	380.6	-	-0.007%	-16.5	225995.5
M1	-37.2	410.2	380.3	-	-0.003%	-7.3	225993.4
M2	-36.2	414.7	380.1	-	-0.001%	-1.6	225993.4

Wind turbine present

Mesh	ΔM	ΔF_p	F_{wall}	T_{AD}	Res_{mom}	e_{mom}	M_{in}
M0	-719.0	2698.7	366.3	1622.6	-0.004%	-9.3	225995.5
M1	-728.8	2696.1	368.7	1602.6	-0.002%	-4.0	225993.4
M2	-709.8	2681.3	372.1	1600.1	-0.000%	-0.7	225986.7

Table 2.4: Momentum budget for the domain in the 2-D flow solver, with and without the WT and for varying mesh resolutions. All quantities in [kg m^2 s^{-2}].

The same global budget exercise, repeated for the mean kinetic energy (2.38) in Table 2.5, sees some degradation in budget closure compared to momentum, reflecting the non-conservative nature of the quantity. Activating the wake model introduces strong shear layers at the WT and in its wake, changing turbulence levels away from an otherwise equilibrium state. This change reflects in an increase in the viscous dissipation term – not accountable for without enforcing energy conservation – and worse energy budget closure, with an increase in residuals by nearly one order of magnitude. There is however a clear improvement in residuals as the mesh is refined (both with and without the presence of a WT), the healthy expected behaviour for a mesh converging budget.

Flat plate domain

Mesh	ΔP_c	ΔP_p	$\sum u_i F_D{}^{x_i}$	P_{AD}	Res_{energy}	e_{energy}	P_{in}
M0	-428.9	3135.1	2964.7	-	-0.029%	-258.5	889940.6
M1	-403.8	3183.8	2941.7	-	-0.018%	-161.7	889929.1
M2	-392.5	3217.2	2934.7	-	-0.012%	-110.0	889891.6

Wind turbine present

Mesh	ΔP_c	ΔP_p	$\sum u_i F_D{}^{x_i}$	P_{AD}	Res_{energy}	e_{energy}	P_{in}
M0	-7719.7	20965.5	4477.9	7437.6	0.149%	1330.3	889940.6
M1	-7816.8	20951.7	4762.7	7403.9	0.109%	968.4	884285.3
M2	-7630.3	20841.3	4772.1	7896.6	0.061%	542.3	889891.6

Table 2.5: Global energy budget for the 2-D flow solver, with and without the WT and for varying mesh resolutions. All quantities in [kW].

3-D model budget

The 3-D model's flow solver results in a well resolved global momentum budget, with residuals of the same order of magnitude as the convergence criteria. As can be seen in Table 2.6, this is the case regardless of the mesh refinement and presence of an active WT. Introducing the WT forces to the budget leads to an increase in the ΔM momentum differential. Both WT thrust and momentum differential increases are compensated by a growth in the pressure forces ΔF_p.There is no clear pattern relating mesh refinement and budget residual, suggesting that the budget is already mesh converged at the coarsest mesh, and that the solver convergence criteria is the limiting factor.

Flat plate domain

Mesh	ΔM	ΔF_p	F_{wall}	T_{AD}	Res_{mom}	e_{mom}	M_{in}
M0	-31344.0	313987.2	286510.9	-	-0.002%	-3867.7	173546850.0
M1	-30464.0	308333.5	286315.7	-	-0.005%	-8446.2	173542640.0
M2	-30128.0	320780.1	286254.1	-	-0.003%	-4398.0	173538180.0

Wind turbine present

Mesh	ΔM	ΔF_p	F_{wall}	T_{AD}	Res_{mom}	e_{mom}	M_{in}
M0	-80896.0	464419.5	284148.8	107167.9	-0.004%	-7793.2	173546850.0
M1	-80160.0	462628.1	284227.7	107167.9	-0.005%	-8927.5	173542640.0
M2	-77536.0	466846.6	285615.7	107167.9	-0.002%	-3473.0	173538180.0

Table 2.6: Momentum budget for the domain in the 3-D flow solver, with and without the WT and for varying mesh resolutions. All quantities in [kg m s^{-2}].

The global energy budget (Table 2.7) has a behaviour similar to that of the momentum budget, despite conservation not being guaranteed. As with the momentum budget, the activation of the WT wake model results in the growth of the pressure term ΔP_p, overcoming the power extracted by the WT and the additional kinetic energy lost between in inlet and outlet. The shear introduced by the WT wake disrupts the turbulent equilibrium state, leading to a moderate increase in the viscous dissipation term. Although

residual levels suffer slightly, they again they appear to be mesh converged and limited only by the CDF solver's convergence criteria.

Flat plate domain

Mesh	ΔP_c	ΔP_p	$\sum u_i F_D{}^{x_i}$	P_{WT}	Res_{energy}	e_{energy}	P_{in}
M0	-351.0	2544.7	2225.6	-	-0.004%	-31.9	715793.2
M1	-337.1	2499.2	2228.1	-	-0.009%	-66.0	715773.2
M2	-336.8	2600.2	2228.4	-	0.005%	35.0	715745.9

Wind turbine present

Mesh	ΔP_c	ΔP_p	$\sum u_i F_D{}^{x_i}$	P_{WT}	Res_{energy}	e_{energy}	P_{in}
M0	-902.6	3767.5	2435.1	429.2	0.000%	0.7	715793.2
M1	-895.9	3754.2	2460.4	432.0	-0.005%	-34.0	715773.2
M2	-873.4	3789.1	2468.0	462.3	-0.002%	-14.6	715745.9

Table 2.7: Global energy budget for the 3-D flow solver, with and without the WT and for varying mesh resolutions. All quantities in [kW].

2.4.5 2-D wake flow

Initial implementation of the AD wake model occurred on a two-dimensional RaNS code. Less complex than a full 3-D solver, it facilitated the iteration of the prototype implementation. The discretization detailed in Section 2.4.3 is adapted to a bi-dimensional domain, reducing the actuator disk to a line ranging the vertical span of the rotor. Domain height is more than 40 times as tall and the rotor span, to ensure blockage effects are negligible.

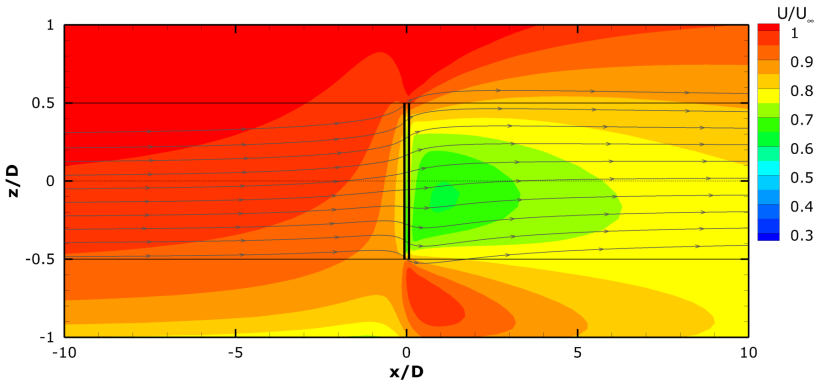

Figure 2.8: Wind speed contours and stream-tube deformation for flow passing through the 2-D AD model.

The CFD solution in Figure 2.8 shows the stream-lines that pass through the actuator disk, defining the equivalent to Betz's stream tube. Starting approximately at 80% the size of a rotor diameter, the stream tube is already noticeably expanding 5D upstream of the AD. Growth is fastest within 0.5D either side of the AD reaching a peak of circa 1.1D, but contraction starts early in the wake at 1D–2D downstream, as turbulent mixing

transfers momentum in from the outside free-flow. After 10D distance, the stream tube has not yet recovered to free-stream dimensions.

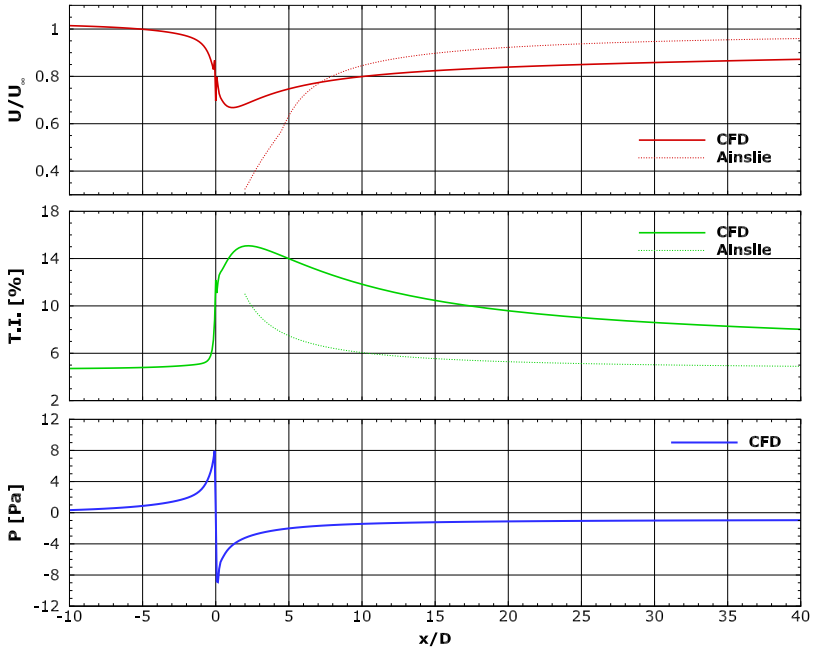

Figure 2.9: Wind speed, T.I. and pressure along the WT axis line using the 2-D flow model. Linear model predictions of velocity and T.I. included as a baseline.

The CFD solution wake centreline quantities – velocity, T.I. and pressure – in Figure 2.9 match the trends predicted by one-dimensional momentum theory up to the near wake, where the shear-enhanced momentum mixing (absent from Betz's theory) causes rapid wake recovery, despite a full recovery to free-stream values not being complete even after 40D of wake. The minor pressure gap remaining in the far wake is associated to the boundary conditions and the driving force required to overcome the surface and AD drag.

Considerable differences are observable under comparison to the Ainslie model estimation in both near and far wake. Velocity is severely over-estimated up to 5D, as is the recovery rate to free-stream values. This in turn leads to under-estimated wind speeds in the far wake, reaching little more than $0.85U_\infty$ by 40D downstream.

The model's T.I. predictions also differ significantly, in overall values and trend. The Ainslie model seems to suggest turbulence peaks in the very near wake and rapidly drops, whereas the AD model predicts T.I. peaking at 2D and recovering to down to atmospheric values at a much slower rate.

The contours of wind speed, pressure, and T.I. in the CFD solution for the vicinity and far wake of the AD are shown in Figure 2.10. The blockage effect of the AD forces a jet between the AD and the ground, retaining near free-stream wind speeds for some WT diameter's length. Beyond that point, the wake signature begins to blend with the surface layer, remaining visible after 40D.

Turbulence is mainly being created near the AD edges, where shear is strongest. A

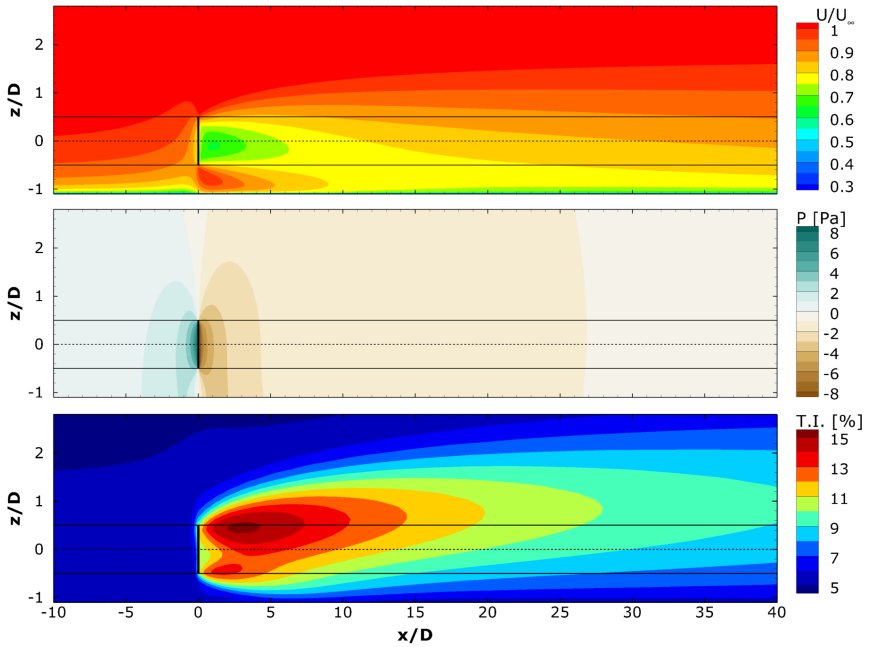

Figure 2.10: Wind speed, pressure and T.I. contours on vertical streamwise planes passing through the WT axis, with the 2-D flow model.

single wake signature is formed, centred at the top of the rotor span that, similarly to wind speed, has yet to dissipate 40D downstream. The AD pressure jump on the other hand is concentrated in the close vicinity of the WT, within 5D either side of the AD.

2.4.6 3-D wake flow

Moving to a 3-dimensional RaNS formulation, the actuator surface now approximates the circular shape of the rotor. The AD is laterally centred in a domain with a cross-section over 150 times larger than the rotor area, meaning blockage effects will be negligible. This way the wake will still be symmetric around the wake central plane, but diffusion will occur on all three directions, including the transverse.

The expansion of the stream tube (Figure 2.11) is more subtle in the 3-D flow model. From a free-stream height of circa 90% of the AD diameter, expansion only clearly starts within half a diameter upstream of the AD. Peak stream-tube size is little more than 1 WT diameter, occurring before the first 0.5D of the wake. After 10D of wake the stream-tube has contracted close to the original free-stream dimension.

The wake centreline quantities – velocity, T.I. and pressure, plotted in Figure 2.12 – generally follow the same behaviour as seen in the 2-D formulation, but with more abrupt transitions between free-stream, near-wake and recovery. Pressure behaves as predicted by one-dimensional theory, while velocity does so up to the very early wake, where diffusion begins to dominate the flow and recovery initiates.

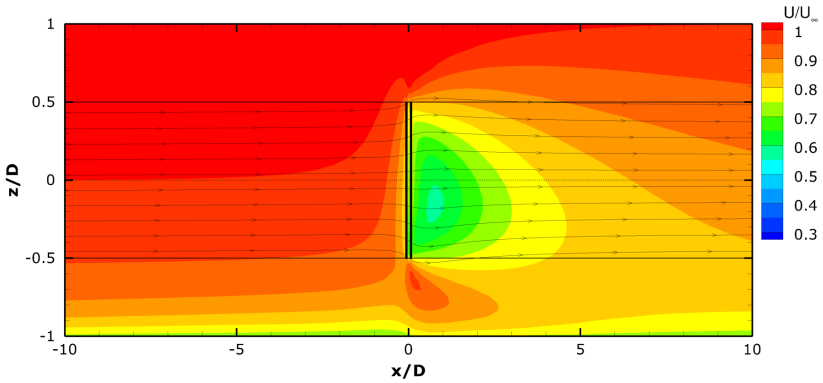

Figure 2.11: Wind speed contours and stream-tube deformation for flow passing through the 3-D AD model.

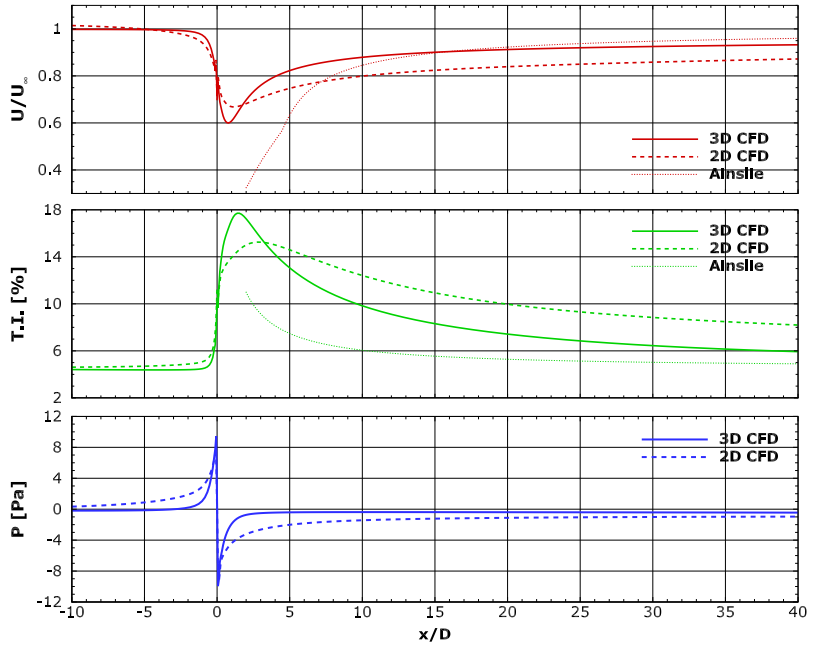

Figure 2.12: Wind speed, T.I. and pressure along the WT axis line with 3-D flow model. Linear model predictions of velocity and T.I. included for comparison.

Between 2-D and 3-D models there is enough improvement to achieve a much better match to the Ainslie model predictions. Minimum velocity in the wake, while still not as low as the Ainslie values, is lower in the 3-D CFD results and maximum recovery rate is much closer to that seen in the engineering model. On aggregate the result is still an over-estimation of velocities in the near-wake, but large improvements are seen in the far-wake, where the two profiles nearly match.

The 3-D CFD results in Figure 2.12 show higher (compared to the 2-D model) peak T.I. values in the near-wake, but the recovery to atmospheric values starts sooner and at a stronger rate. Although still higher than the Ainslie model's, the CFD model predictions are a much better match overall, with the gap between them reduced to 1% after 40D.

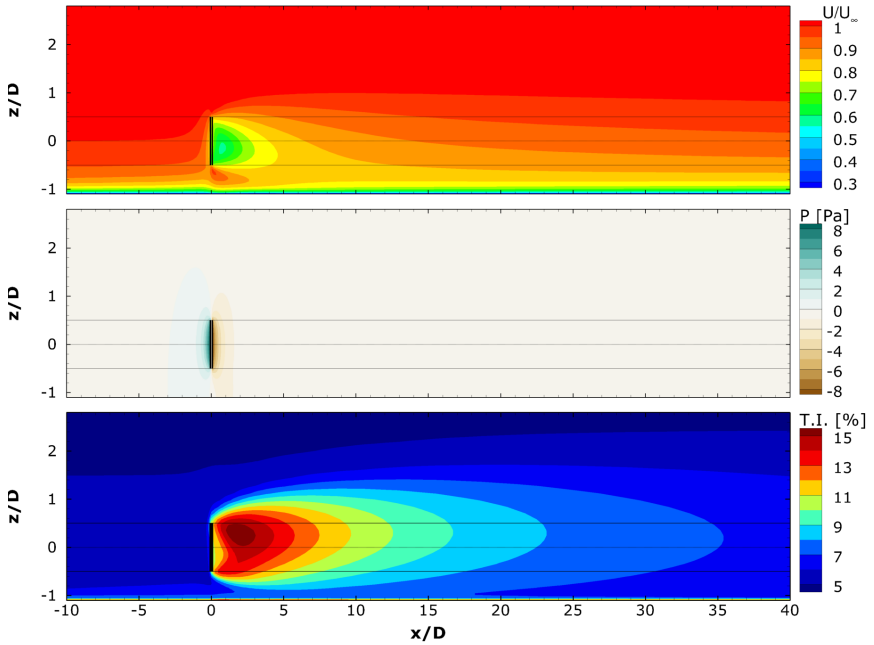

Figure 2.13: Wind speed, pressure and T.I. contours on vertical streamwise planes passing through the WT axis, with the 3-D flow model.

The contours of wind speed, pressure, and T.I. in the vertical plane in the centre of the rotor (Figure 2.13), when compared to the corresponding 2-D contour maps (Figure 2.10), show a much faster wake recovery. The length of the wake signatures is significantly reduced on either of the three mapped quantities, with the ABL having largely recovered by 40D downstream of the AD.

The jet present under the AD in the 2-D results has here largely disappeared, consequence of the added degree of freedom in the 3-D AD discretization. As a consequence, the reduced shear in the lower AD edge also leads to reduced turbulence production in that area, resulting in a wake with less pronounced rotor edge turbulence signatures and a more homogeneous near-wake T.I. map.

2.4.7 Conclusion

The simple model implemented produces a wake flow solution that partly matches the theoretical prediction of one-dimensional theory (Section 2.3): the pressure field behaviour is very similar and, up to an early point in the wake development, so is the velocity field. Beyond that point (approximately 1D downstream of the WT) the mechanisms behind turbulent ABL flows take over and, through diffusive transfer into the wake area, velocity begins to recover to free-stream values. The stream-tube's shape no longer continuously expands downstream, being interrupted in the near wake and initiating a contraction back to free-stream dimensions (Sections 2.4.5 and 2.4.6).

The wake recovery pattern is predicted in both 2-D and 3-D implementations of the model, although in 3 dimensional representation trends on analysed flow variables are accentuated: the pressure jump at the AD is sharper and the initial velocity reduction

(upstream of the AD) begins later and more abruptly, reaching a lower minimum value in the wake (Section 2.4.6). This comes as a result of the added degree of liberty of the third dimension, effectively decreasing the blockage effect introduced by the AD and increasing the ratio of shear layer to wake section, augmenting the impact of diffusive transport. Comparison to linear wake model predictions suggest that although near-wake velocities are under-estimated, recovery rate and far-wake velocity are well predicted. Turbulence on the other hand tends to be over-estimated, with agreement with linear model results occurring only in the very far-wake.

The global domain budget exercise proves that the terms introduced by the WT do not disturb the balance in the momentum nor energy domain balances, the latter despite not being directly enforced via a mean flow kinetic energy equation solved by the code (Section 2.4.4. Budget residuals are generally low, in the order of magnitude of the solver convergence criteria. The response to mesh refinements suggest that, at the resolutions utilized, the 3-D model was mesh converged even at the coarsest level tested, regardless of the WT presence.

2.5 Rotor discretization

The CFD solver has to be able to model the presence of one or more WTs, located and oriented freely inside the simulated domain. The ability to do so should not be compromised by the constraints of the orthogonally-structured terrain-following mesh.

The prototype AD model (Section 2.4.3) is only able to place inlet-oriented AD, and as such is upgraded into a more complex but flexible approach, with a two-stage discretization. The rotor span is first described in a separate local coordinate system, accurately defining the rotor shape and position. The second discretization comes in the form of a redistribution of the quantities described in the first rotor mesh to the domain mesh, to cumulatively form variable fields used to calculate the RaNS equation source terms, as described in Section 2.4.2.

These terms depend exclusively on the AD position and load distribution, so they are mostly static fields. This way the rotor discretization process is executed once at model initialization and only repeated as necessary, whenever a significant rotor misalignment is detected and WT re-orientation is necessary, justifying an update to the rotor discretization.

Irrespective of the rotor mesh description, the quality of the discretized AD is still ultimately limited by the mesh resolution. A mesh sensitivity study was conducted, evaluating the consequences on flow around the AD and in its wake, as well as the model's WT performance.

2.5.1 Virtual rotor mesh

Using the known WT data, the AD shape is positioned by defining the rotor's centre (WT hub position) and span (rotor radius and hub height). Initially it is assumed to be oriented towards the inlet boundary, facing the expected predominant flow direction. Like Réthoré (2009), the AD shape is discretized using a fine cylindrical coordinate mesh (Figure 2.14), ensuring that individual virtual rotor cells are much smaller than the finest of the domain mesh CVs.

Each cell of the virtual rotor mesh contains a fraction δA_d of the total AD area. To it is also attributed dimensionless WT rotor load factors f_n and f_t (for normal and tangential directions respectively), responsible for scaling the rotor load at that cell relative to a uniform load distribution. The fraction of the overall thrust δT and δF_t corresponding to each virtual rotor cell are defined via equations (2.48-2.49).

$$\delta T = \frac{1}{2} C_T \rho {U_\infty}^2 f_n \delta A_d \tag{2.48}$$

$$\delta F_t = \frac{1}{2} C_T \rho {U_\infty}^2 f_t \delta A_d \tag{2.49}$$

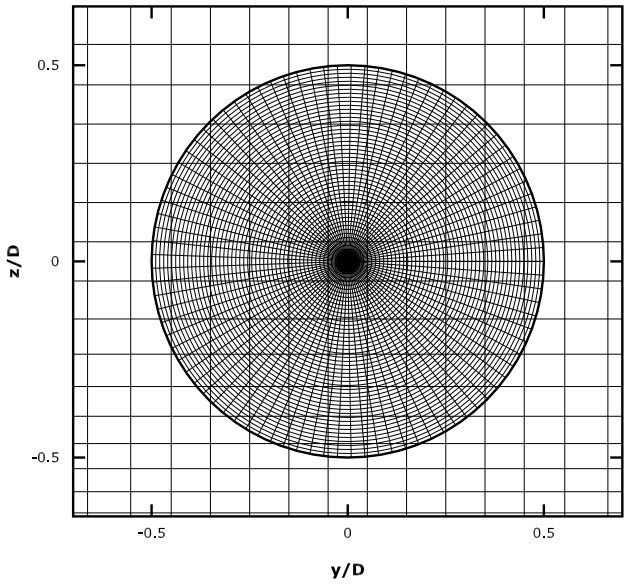

Figure 2.14: The virtual rotor mesh, the first step in the two-stage AD discretization.

2.5.2 Domain mesh discretization

For every virtual rotor mesh cell c, tri-linear interpolation coefficients $\eta_{i/j/k}$ are calculated from the cell centre to the domain mesh's CV centres. These coefficients enable the second stage of the discretization, with the product of each cell's AD area and load factor being cumulatively redistributed to the nearest domain mesh CV centres. Replicating the Betz's one-dimensional momentum theory, for now the rotor is assumed to be uniformly loaded and acting exclusively on the normal direction ($f_n = 1$, $f_t = 0$). The accumulation of distributed product of AD area and normal load factor (for every contributing cell c), divided by the domain mesh cell's volume, results in the AD area density $\widetilde{s_n}$ (2.50) distribution, smoothed over the domain mesh CVs near the AD (Figure 2.15).

$$\widetilde{s_n} = \frac{1}{\int \mathrm{d}\Omega} \sum_c \eta_i \eta_j \eta_k f_n \delta A_d \tag{2.50}$$

This method allows for the necessary flexibility in the orientation of the AD (not being restricted to orthogonally oriented rotors) and is less sensitive to the domain's mesh resolution, compared to the "binary" CV selection method used in the prototype AD. It also inherently ensures conservation of both total AD surface area A_d and total rotor thrust T_{AD} between virtual rotor mesh and domain mesh discretizations of the AD.

Every domain mesh CV with AD contributions will have an AD surface density $\widetilde{s_n}$, and the total force density of the wind turbine thust $\widetilde{T}$ will be defined as per equation 2.21. The global amount is decomposed into i-th components (equation 2.51) depending on rotor orientation to appear on the right-hand side of the respective momentum equations as source terms.

$$\widetilde{T_i} = \frac{1}{2} \rho C_T {U_\infty}^2 \widetilde{s_n}\, \mathbf{n_{AD}} \cdot \delta_{ij} \tag{2.51}$$

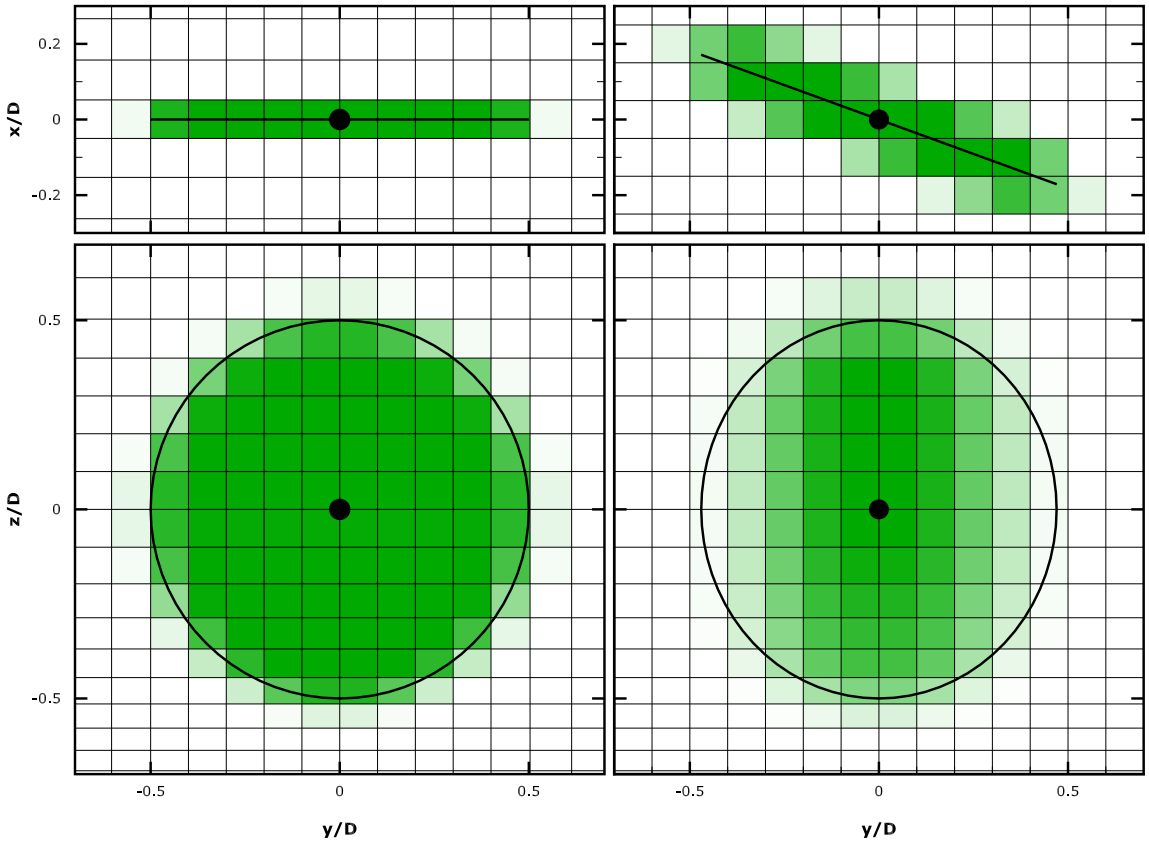

Figure 2.15: Actuator disc area density $\widetilde{s_n}$ distribution after the two-stage AD discretization, in top (above) and frontal (below) views. Inlet oriented (left) and 20°rotated (right) ADs represented.

2.5.3 Mesh resolution sensitivity

Regardless of the improvements brought by the two-step discretization in approximating the rotor shape, the AD model will still ultimately be limited by the domain mesh resolution. The simulated wake flow is expected to depend on the resolution with which the rotor and its vicinity are resolved. The strongest gradients will be in the streamwise direction (in the AD's vicinity) and in the wake's annular shear layer, and as such resolution in the AD plane and streamwise directions are relevant.

The flow around a single WT was solved in a range of mesh resolutions. A baseline was established, where the AD and its vicinity were resolved in CVs measuring D/10 (or less) on all three directions. Simulations with variations of that baseline mesh were run, where resolutions in each direction were halved to D/20, doubled to D/5 or increased up to the coarsest at D/2. The mesh sensitivity study is focused on the effect of changing:

- overall resolution – changing in all three direction simultaneously (Figure 2.16);

- AD-plane resolution – changing in vertical and transversal directions, keeping constant streamwise resolution (Figure 2.18);
- streamwise resolution – changing in the streamwise direction, keeping constant AD-plane resolution (Figure 2.17).

The WT is modelled under the same standardized flow conditions of the prototype AD (Section 2.4.3), which means it is laterally centred in a flat plane domain with a cross-section over 150 times larger than the rotor area. Typical synthetic ABL inflow conditions were set at the inlet boundary, with a log-law velocity profile and equilibrium turbulence conditions. Mesh nodes are concentrated near the wall and near the WT, to accurately describe flow where it is most complex. The AD model was set up to emulate an actual WT production model, with prescribed free-stream velocity (equal to inflow velocity at hub height) and a corresponding thrust coefficient of $C_T = 0.709$.

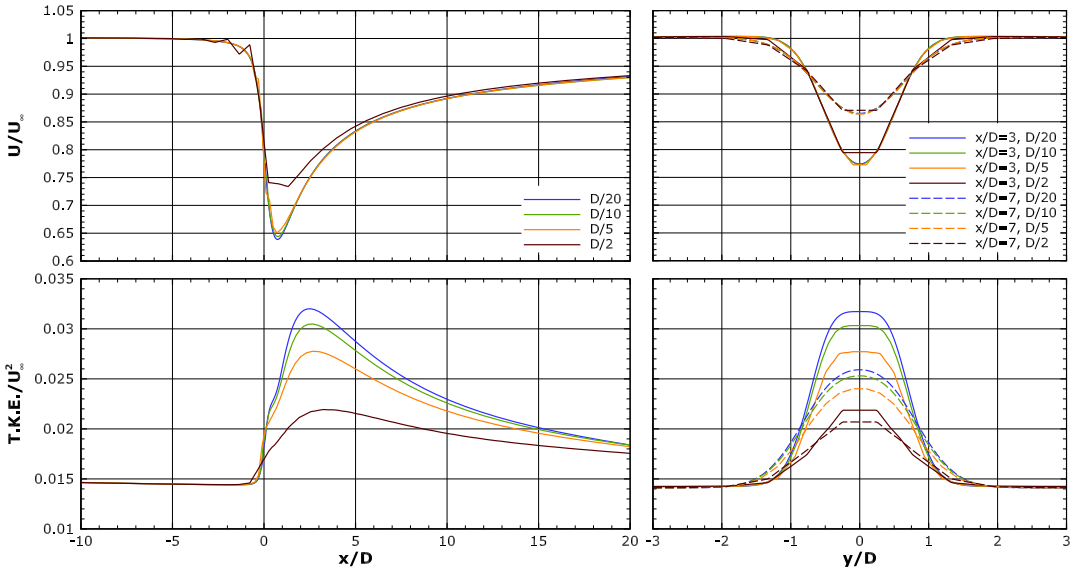

Figure 2.16: Velocity (above) and turbulent kinetic energy (below) along rotor axis line (left) and across the wake (right) at four different overall mesh resolutions.

The WT axis line and cross wake velocity profiles in Fig. 2.16 show that the velocity field is largely insensitive to overall resolutions finer than D/5. Downgrading to D/2 however introduces not only large differences in the near-wake, which take a long time to recover from, but also wiggles in the vicinity of the WT. The turbulence field on the other hand appears to have not yet reached mesh convergence even on the finest mesh. With the coarsest mesh, wake centreline T.I. is unable to match the finer mesh solutions, even after 20D. In spite of the considerable differences found here, they do not seem to reflect directly in the momentum side of the solution.

Looking separately at streamwise (Figure 2.17) and AD-plane (Figure 2.18) resolutions, the conclusions are not significantly different. The largest differences are again found in the turbulence field: although the T.I. gap between different meshes is smaller, both peak values and wake signature width increase with mesh refinement. The wiggles observed in the overall resolution comparison seem to appear exclusively with the introduction

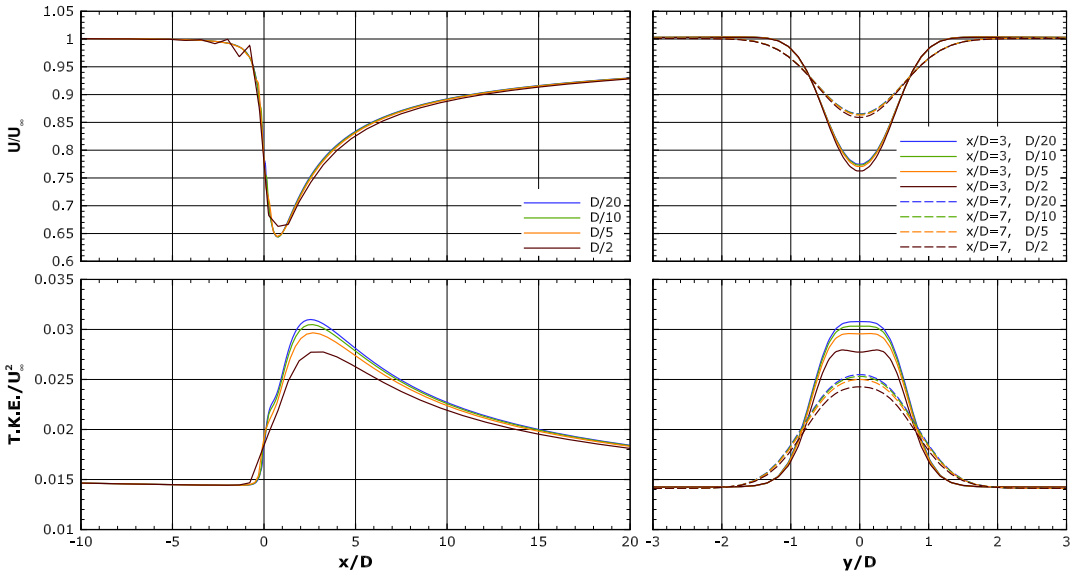

Figure 2.17: Velocity (above) and turbulent kinetic energy (below) along rotor axis line (left) and across the wake (right) at four different streamwise mesh resolutions.

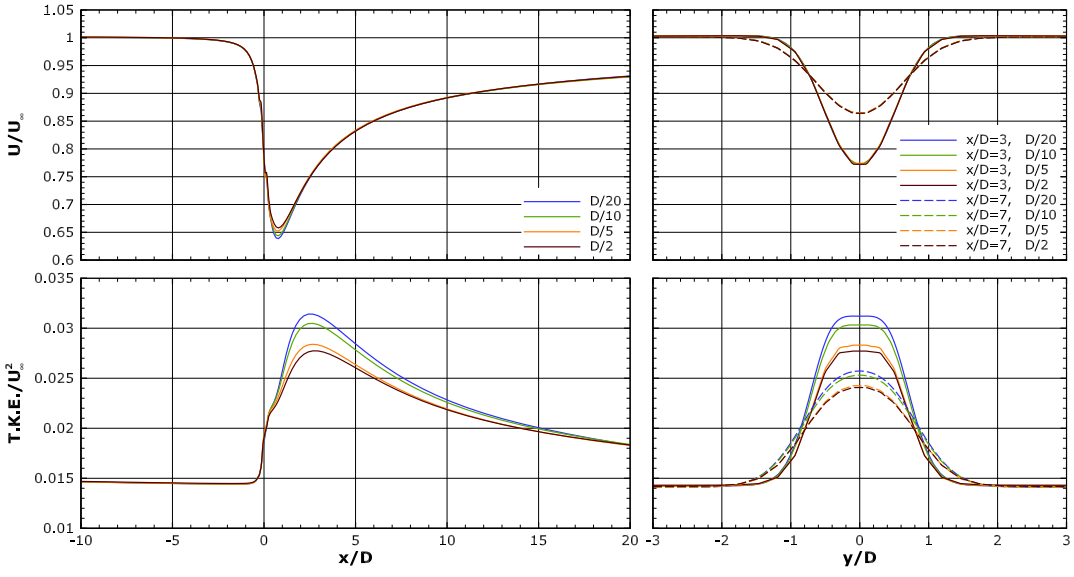

Figure 2.18: Velocity (above) and turbulent kinetic energy (below) along rotor axis line (left) and across the wake (right) at four different rotor-plane mesh resolutions.

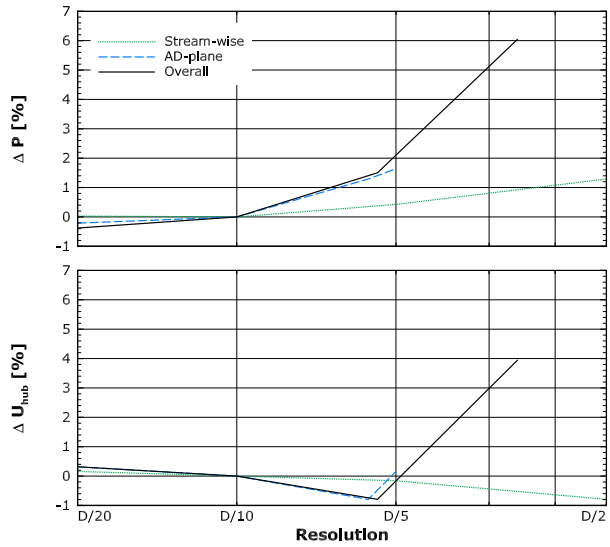

Figure 2.19: WT power estimation (above) and hub position velocity (below) at varying streamwise, rotor plane and overall mesh resolutions (referenced to D/10 resolution).

of course streamwise resolutions. The reason behind these is discussed in further detail in Section 4.1.

The AD velocity (at the hub position in particular) and the WT power (obtained via integration, see Section 2.4.2) in Fig.2.19 are also affected by the mesh resolution. Both appear to be largely insensitive to longitudinal resolution, with the AD plane resolution being dominant. While hub velocity is largely mesh converged at D/5, WT power still sees some change by reducing resolutions to D/10, suggesting that velocities at the AD edge are not yet stabilized at those resolutions.

2.5.4 Conclusion

The improved discretization through the rotor mesh allows for the necessary positioning flexibility and, most evidently with low resolution meshes, a smooth rotor shape (Section 2.5.2). With it the wake flow also proved resilient to mesh resolution changes, particularly in the velocity field. Both wake velocity and WT power estimations were found insensitive to resolutions finer than D/5 (Section 2.5.3), while wake turbulence required a finer mesh at D/10 to achieve mesh independence.

Additionally the two-stage discretization establishes a framework (Section 2.5.1) for expanding model functionality: just as the AD area, any quantity distributed over the rotor can transferred to a domain mesh discretization, ultimately allowing for non-uniform contributions to rotor forces or to the turbulence model equations.

2.6 Dynamical wind turbine thrust estimation

To determine the total amount of thrust applied by the WT on the flow and close equation (2.20), the free-stream velocity U_∞ and corresponding thrust coefficient C_T have to be determined. In previous sections of this chapter there were directly prescribed, which would not be acceptable in most model applications.

A precursor simulation would provide the correct U_∞ for a single WT, by measuring the undisturbed wind velocity at the WT position (in it's absence). The corresponding thrust coefficient comes via interpolation from a C_T curve, supplied by the WT manufacturer. In the case of multiple WTs, wake interaction could require multiple precursor simulations (in the correct order) to reach a complete solution, similarly to the work of Politis et al. (2012). Impractical in single WT cases, this method would be infeasible in most real-world complex cases.

Alternatively IEC standards 61400-12-1 (IEC, 2005) suggest that for WT calibration procedure, in low complexity sites, the wind velocity at 2D to 4D upwind of the rotor hub gives an acceptable estimate of the relevant free-stream velocity. In most real-world cases however, complex terrain or ground cover (including other WTs) mean distances of that magnitude are sufficient to affect that correlation between locations.

To determine both unknowns simultaneously, a function (in addition to the C_T curve) relating U_∞ and C_T is required. We resort again to one-dimensional theory, specifically the thrust coefficient definition (2.18) as done by Calaf et al. (2010) and Prospathopoulos et al. (2010). An additional unknown is introduced, velocity at the AD U_d, which will be approximated via interpolation from the solver's flow solution, meaning the problem is solvable and an unique solution to the U_∞/C_T dependency can be reached.

2.6.1 Approximating the actuator disk velocity

As the CFD solver iterates, the overall flow field and the flow in the vicinity of the WT in particular will converge towards the final solution. The latest update to the intermediate flow solution should, in principle, be closest to the final inflow hitting an AD and most adequately represent the final flow in the AD's vicinity. While polling the intermediate solution for an approximation to the disk velocity U_d at every iteration, the overall thrust T_{AD} and the flow field will converge simultaneously.

The IEC standards (IEC, 2005) suggest that velocity at a single point at hub height provides, in clear inflow, an adequate approximation to the free-stream velocity. Similarly, the velocity at the hub position will be where flow conditions best match those assumed at the disk in one-dimensional theory, being least affected by the rotor edge's shear layer. This way, AD-normal velocity at the hub position is assumed to be a good approximation to 1-D momentum theory's U_d.

2.6.2 Iterative momentum theory model

Armed with an approximation to the momentum theory's U_d, an initial guess of the relevant U_∞ will allow for iteration between the manufacturer's thrust coefficient curve and momentum theory's thrust coefficient definition, converging on a U_∞^*/U_d pair that obeys to one-dimensional momentum theory, as proposed by Prospathopoulos et al. (2010). This way, from a solution polled approximation to U_d the model repeats as follows:

1. Prescribe an initial estimate to the free-stream velocity ${U_\infty^*}^0$;
2. Interpolate ${C_T}^n$ from manufacturer's curve using the latest ${U_\infty^*}^n$ estimate;
3. Update ${U_\infty^*}^{n+1}$ estimation using the thrust coefficient equation ${C_T}^n = 4a\,(1-a)$, with $a = 1 - \frac{U_d}{{U_\infty^*}^{n+1}}$;
4. Repeat from step 2 until convergence, when ${U_\infty^*}^{n+1} - {U_\infty^*}^n$ reaches the intended tolerance.

This algorithm is iterated until convergence within each flow solver iteration, reaching an adequate U_∞^* value for the latest U_d value. The polled disk velocity U_d, guaranteed to be below the converged U_∞^* value but of comparable magnitude, is a good initial ${U_\infty}^0$ estimate.

2.6.3 Thrust estimation convergence

WT performance estimation is updated at every iteration, as the flow solution converges. This method avoids the need for precursor simulations or model calibration, and can also be applied to any number of WT in the domain, with the flow solver ensuring that neighbouring WTs influence each other.

A typical convergence pattern of U_∞^* is shown in Figure 2.20, along with the corresponding U_d value polled from the intermediate solution at a given solver iteration. Since the initial U_d approximation is naturally over-estimated, the convergence rate at which the free-stream velocity is updated has to be limited. Applying a under-relaxation factor α_{WT} slows down the initial WT thrust transfer to the solved flow field, but dampens the convergence pattern to avoid local instabilities. After 40 solver iterations both values have converged, long before solver convergence is achieved. With an under-relaxation factor of $\alpha_{WT} = 0.01$ the U_∞ over-estimation at model start-up is controlled, without significantly affecting U_d convergence.

Since U_∞ and C_T are rigidly connected via the manufacturer curve, the AD velocity U_d approximation becomes pivotal to the total thrust estimation. Section 2.5.3 showed that U_{hub} is insensitive to streamwise resolution and is largely mesh converged at resolutions finer that D/5. This way, an adequately resolved wake flow will also have a mesh converged U_d approximation, to the benefit of the U_∞ estimation algorithm.

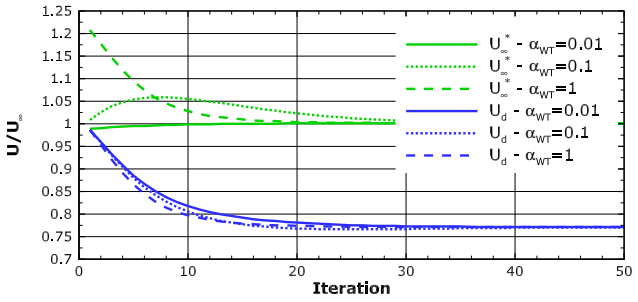

Figure 2.20: Free-stream velocity estimate U_∞^* and disk velocity approximation U_d convergence at various under-relaxation factors α_{WT}

2.6.4 Thrust coefficient curve sensitivity

The thrust exerted by a WT on the flow cannot be directly measured, usually being derived from structural stress data. The assumptions assumed when deriving it mean there is considerable uncertainty associated, in addition to the uncertainty inherent to the WT calibration procedures. With the free-stream velocity estimation depending directly on the thrust coefficient curve, the thrust estimation algorithm and the wake flow will inevitably be affected by the said uncertainties.

The free-stream velocity estimated by the proposed method, along with the U_∞^* estimate as suggested by IEC standards (wind speed 2D upstream of the hub position), are compared to the actual simulated undisturbed velocity (at the hub position, in the WT's absence). The comparison is presented in the form of a relative error $\varepsilon_{U_\infty} = (U_\infty^* - U_\infty)/U_\infty$ in Fig. 2.21, extending from cut-in to cut-off wind speeds of two common WT models, the ENERCON E66 and the Vestas V80.

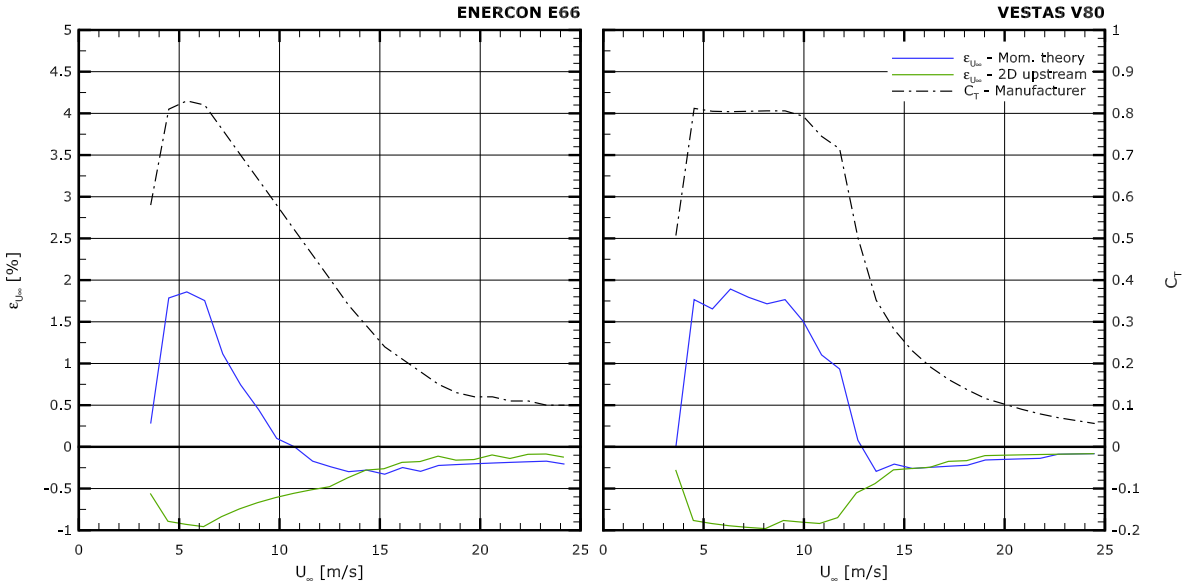

Figure 2.21: Relative error of U_∞^* estimate for different U_∞ estimation methods, over the operating ranges of ENERCON E66 (left) and VESTAS V80 (right) WTs.

The proposed iterative method over-estimates the free-stream velocity in the lower part of the WT operating range, peaking at nearly 2% for either method. Said peaks also coincide with the WT manufacturer curve's C_T peaks. Because it results in polling the solution at an area affected (even if marginally) by the AD's presence, the IEC upstream method naturally tends to under-estimate U_∞, with lower absolute errors levels. This is in agreement with the Medici et al. (2011) scaled wind tunnel study, where at 2D upstream the hub height velocity exhibits moderate under-estimation of the actual undisturbed hub position value.

Irrespective of WT model and U_∞ estimation method, C_T and estimation error behave synchronously: both peak simultaneously in the lower half of the wind speed range, and rapidly fall to near zero in the higher half of the wind speed range.

The synchronized behaviour of the C_T and error curves suggest that high mechanical efficiency in the WT operation affects the U_∞ estimation method. The high thrust coefficients the WT operates at under low wind speeds promote strong streamwise velocity gradient. The turbulent viscosity-based closure employed by the flow solver means that the strong streamwise shear is translated to strong diffusive transport, leading to increased velocities at the AD and over-estimated free-stream velocities.

2.6.5 Estimating a wind turbine power curve

The total power extracted by the WT model is a product of the model's total thrust estimation and the velocities at the AD. For this reason, errors from the model's free-stream velocity estimation will carry over and potentially influence power estimation, through both U_∞^* and the corresponding C_T values. In addition, the model has no information on the aerodynamic efficiency of the rotor, meaning the mean flow kinetic energy sink and actual mechanical power harvested by the rotor are not necessarily correlated.

The model's WT power estimation P_{AD} is compared to the expected WT electrical power – as per the manufacturer's power curve – in Figure 2.22, adimensionalized by the manufacturer rated power P_{rated} and in relative error format $\varepsilon_P = (P_{AD} - P_{rated})/P_{rated}$. The comparison extends from cut-in to cut-out wind speeds, for two known WT models (similarly to Section 2.6.4), and for WT power estimates resulting of U_∞^* values obtained via both the proposed iterative method and the IEC 2D upstream method.

The two examined WTs exhibit very distinct behaviours:

- The modelled ENERCON E-66 (on the left in Fig. 2.22) is inconsistent in its response, going from over-estimation at either end of the curve and under-estimation in the mid-range. The slope of the power curve in the ramp-up region is underestimated, culminating in underestimation as WT management transitions between ramp-up and rated power regimes. At the top end of the wind speed range, WT power estimates begin to climb at a steady rate as C_T stabilizes at circa 0.1 but wind speed increases.
- The modelled VESTAS V80 (on the right in Fig. 2.22) on the other hand consistently estimates above the manufacturer's power curve, by a stable margin (circa 20%)

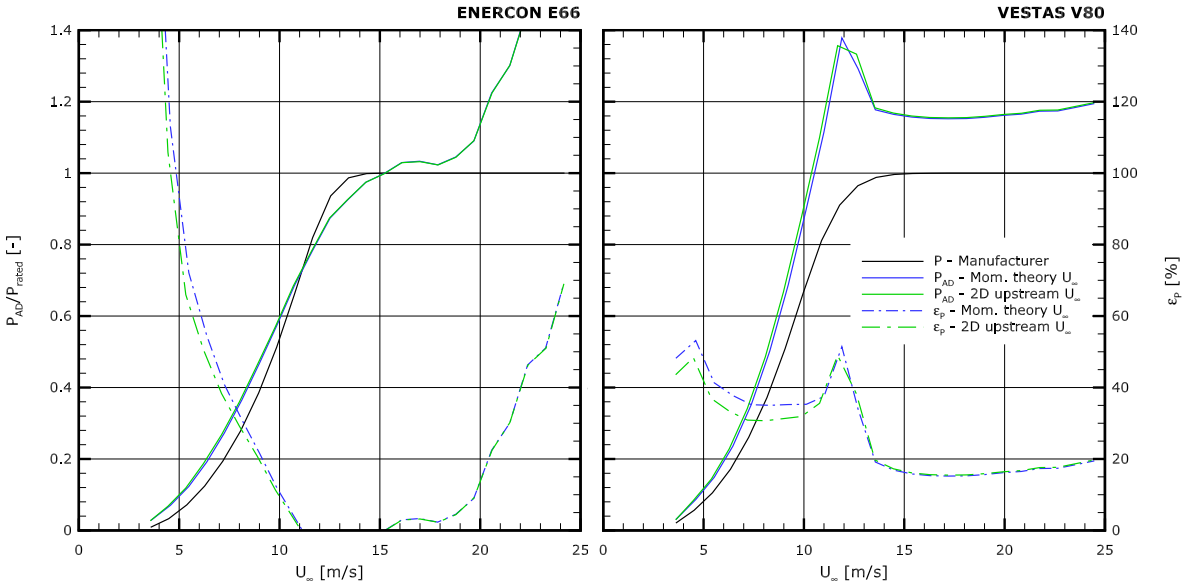

Figure 2.22: Power estimation P_{AD} (relative to P_{rated}) and estimation error ε_P for different U_∞ estimation methods, over the operating ranges of ENERCON E66 (left) and VESTAS V80 (right) WTs.

in the rated power part of the curve. In areas where the WT management is transitioning between regimes (cut-in, cut-out and transition between ramp-up and rated power), the power estimation error is higher.

The different U_∞^* estimates, with the peak errors of 2% as seen in Section 2.6.4, do not significantly change the WT power estimates, particularly in light of the overall power estimation errors. On the other hand, not accounting for aerodynamic and conversion (mechanical to electrical) efficiency will generally cause power over-estimation, like much of what is observed on the VESTAS V80.

Larger over-estimations are likely to be caused by WT management where the WT intentionally operates at a lower aerodynamic efficiency, such as in transitions between operating regimes. The case of the ENERCON E-66 however, where severe power over-estimations and curve slope under-estimations are found, is hard to comprehend if not due to a significant detachment between C_T and power curves as presented by the manufacturer.

2.6.6 Free-stream velocity estimation in waked conditions

Estimating U_∞ in strongly non-homogeneous inflow conditions, such as in complex terrain or in the wake of neighbouring WTs is challenging. The IEC method of polling velocity 2D upstream of the hub will be subject to considerable errors, as in strong spatial gradients that velocity might not be representative of wind speeds at the WT. With zero displacement between WT and solution polling positions, the proposed iterative U_∞ estimation method should be far less sensitive to spatial gradients in the vicinity of the AD.

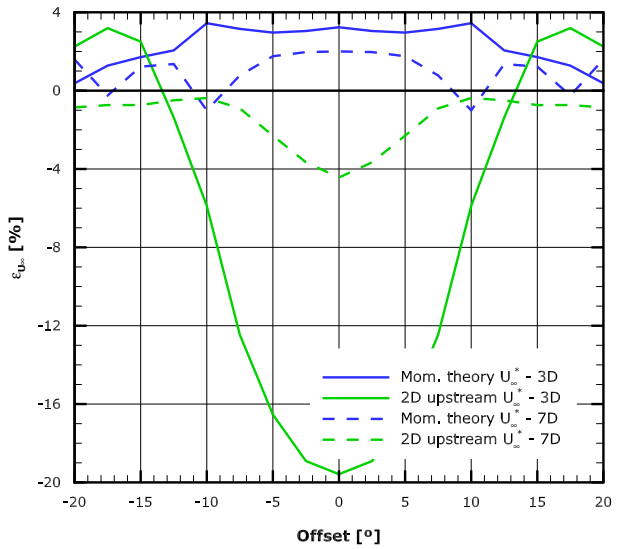

Figure 2.23: Relative error of U_∞^* estimate for a WT in waked inflow, for two different WT spacings and over a range of wind direction offset to the row alignment.

Figure 2.23 shows the estimation error ε_{U_∞} for a WT T2 operating in the wake of an upstream WT T1. Results are shown for both the iterative momentum theory method and IEC's 2D upstream method, and for WTs separated by distances of 3D and 7D. Estimation error is obtained by comparing the undisturbed velocity at the downstream WT's hub position (modelling only T1) and the estimated U_∞^* velocities for T2 (when modelling both WTs). By doing this over a range wind directions it is possible to see how the model handles U_∞ estimation from fully waked flow (0 °, when flow is aligned with the WT row) to partially waked flow and, finally, undisturbed flow (misalignment of $\pm$20 °or more, depending on row spacing). The ENERCON E-66 curves are used in this comparison, for an undisturbed inflow velocity at hub height of circa 8 m/s.

For very closely spaced WTs (close to T1's near wake at 3D), under row aligned flow the proposed method's estimation error is greater than that of a WT in clear inflow, at more than 3%. Steering away from row aligned flow, estimation error for the momentum theory method drops to nearly zero as T2 operates in clearer inflow. Using the 2D upstream method moves the position very close to T1, naturally resulting in a U_∞ under-estimation of nearly -20%.

As WT spacing widens to 7D the IEC method's estimation error is much improved, reducing to a peak under-estimation of 4%, but a non-negligible improvement is also observed for the proposed iterative method, yielding lower absolute errors.

2.6.7 Conclusion

The addition of the thrust estimation algorithm allows for the WT forces at the AD to dynamically adjust to local flow (Section 2.6.2). This occurs at every solver iteration, converging simultaneously with the flow solution and successfully calculating WT thrust

with no prior knowledge of the WT operating conditions (Section 2.6.3).

The proposed method was able to estimate a WT's free-stream velocity based on the premises established by one-dimensional momentum and on an approximation to the disk velocity U_d, interpolated at the hub position (Section 2.6.4). Tested for two different WT models, peak estimation error was below 2% and reducing to near zero values at high wind speeds. Peak estimation errors were associated to low wind speeds and high thrust coefficients: high streamwise velocity gradients promoting diffusive flux and greater velocities at the AD. This effect is minimized at higher wind speeds, as C_T values decrease and convection over-powers diffusion as a momentum transport mechanism.

Under waked inflow the model's U_∞ estimation degrades, since the turbulence added by the wake further enhances diffusive momentum transport in the vicinity of the AD and increases velocities at the AD(Section 2.6.6). Given sufficient space between WTs turbulence return to ambient levels and the wake effect on estimation errors is attenuated. Regardless, the proposed U_∞ estimation method is far less prone to errors than the IEC alternative of interpolating velocity 2D upstream of the WT.

Estimating WT power via volume integral of the force-velocity resulted in high errors, due to its reliance on the C_T curve supplied by the manufacturer (Section 2.6.5). Not only is the quality of the curve unknown, it does not consider the process of going from mean inflow kinetic to electrical energy: the efficiencies associated to the aerodynamic, mechanical and electrical conversions occurring at the rotor blade and hub are not known, and are highly dependent on WT management regimes.

2.7 Conclusion

The implemented wake model was able to represent the effect a WT has on the flow solution of a RaNS CFD code, matching the expected flow behaviour as predicted in the theory and by linear models (Section 2.4). It uses the actuator disk approach and takes full advantage of the principles established by Betz's theory (Section 2.3), combining two main components: the discretization method, allowing for a WT rotor to be described in the computational domain (Section 2.5), and the WT performance estimation algorithm, allowing the model to estimating its operating conditions dynamically as the flow solution iterates (Section 2.6).

The prototype implementation AD model was able to qualitatively match the theory's flow predictions in the near wake (Section 2.3.1). The CFD code's modelling of diffusive transport, absent from Betz's theory, meant that after the near wake the flow recovers to free-stream conditions, trend that agrees with predictions by linear wake models (Section 2.4.6). This implementation was validated numerically, by confirmation of the momentum and energy budgets in the domain, with the CFD code proving to globally conserve both quantities to low degree of error, irrespective of the presence of the model WT and the mesh resolution (Section 2.4.4).

To minimize the impact of mesh resolution on the discretized AD, the rotor shape is described in a "virtual rotor" mesh (Section 2.5.1) before being distributed to the actual domain mesh. This allows for unconstrained and precise positioning of the AD and a smooth final discretization (Section 2.5.2). With it, the flow solution was largely mesh converged at resolutions of D/5 or finer (Section 2.5.3).

Concurrently with the modelling of the thrust effect on the flow, the performance estimation algorithm predicted the WT's free-stream velocity to a low degree of error. This results from the combination of the manufacturer's C_T curve and definition (Section 2.3.2) with the velocity interpolated from the solution at the hub position. Estimation error was kept under 2% when in clear inflow conditions (Section 2.6.4), but doubled when in waked inflow (Section 2.6.6) as hub position velocities are affected. Since the C_T curve is not a definitive representation of the WT's conversion efficiency, estimating WT power via force integral proved unreliable (Section 2.6.5).

Strong streamwise velocity gradients caused excess streamwise diffusion in the vicinity of the AD, generally increasing velocities. One reflection of this behaviour can be seen in the U_∞ estimation errors: these occur at low wind speeds, where diffusion is not overpowered by convection, and coincide with peak C_T values, where momentum extraction is most efficient (Section 2.6.4). Another consequence is found in the near wake velocities, which comparison to linear model results suggests are over-estimated (Section 2.4.6).

This page intentionally left blank

Chapter 3

Applying the wake model at the wind farm scale

In this chapter the wake model is applied to complete wind farms, modelling the simultaneous operation of all the included WTs in a single simulation. Operational data from two off-shore wind farms are used to evaluate the model's performance, namely how WT operating conditions are predicted in inflow affected by wakes from one or multiple upstream WTs.
On the first introductory section, the particularities and fundamentally different natures of WF datasets and simulation results are discussed and how that influences the comparison between them.
In section two the model's prediction of a WT's wake effect is studied, by observing the sensitivity of individual or sets of WTs inside an array to wake effects under selected operating conditions and compared to binned measurements.
The last section focuses on the aggregate ABL effect where individual WT wakes combine, forming a WF scale wake that propagates far downstream. With two neighbouring WFs operating in each other's wake, the model attempts to predict the global and localized performance degradation due to the upstream WF.

3.1 Introduction

In Barthelmie et al. (2009) and Réthoré et al. (2013b) several wind farm datasets are thoroughly studied and processed. A wealth of knowledge was uncovered on the characteristics of these datasets and their use for wake model validation purposes, namely on how to deal with the stochastic nature of atmospheric flows and the uncertainty associated with the measured data. These are tackled on one hand with data quality control and on the other with adequate processing, typically is split into two phases: determining reference inflow conditions and processing WT power data.

The first phase focuses on determining the representative inflow conditions (mainly wind direction and speed, but also turbulence intensity, stability regime and others) at the site in any given instant, fundamental to understand WF operation during that pe-

riod. The result is the reference against which all other measurements are synchronized, assuming that the conditions set by the reference are representative of the inflow at all measurement points on the site.

The second comes after binning the data for a give type of inflow, where instantaneous WT power measurements are combined to produce representative absolute power levels (for individual or sets of WTs or the Wind Farm on aggregate) or relative power losses (compared to a reference power level), as a measure of the wake effect.

3.1.1 Data processing and quality control

These datasets usually involve data from one or more meteorological masts and a large number of WTs. Réthoré et al. (2009) describes the work necessary to go from raw wind farm data to a usable dataset, dealing with data corruption through three main vectors:

- choosing the data structure that aids in finding and recovering corrupted data, assessing quality as well as documenting the data processing;
- dealing with sensor miscalibration, mainly finding and correcting wind direction and time offsets; and
- flagging sensor failures in meteorological mast installed anemometers and wind vanes and, most importantly, in WT's blade pitch and power output sensors and distinguishing them from WT operation in non-standard regimes.

The key in the process is establishing a set of robust rules that associate each type of sensor with its neighbours. The correlation between neighbouring sensors is necessarily strong when they are in close proximity, and when this correlation degrades, action is taken to identify possible sensor miscalibration or failure, correcting or discarding data accordingly.

Since the data still has to undergo filtering (for normal WF operation status, low wind speeds, etc.) and binning (for wind direction, wind speed or even turbulence and stability regime), recovering corrupted data and maximizing the dataset's size is key for obtaining data points with representative samples. This is especially important with larger WT counts, as the probability of all WTs and sensors simultaneously operating optimally decreases, and with it overall data availability.

3.1.2 Data uncertainty

Individual records typically consist of the measured quantities averaged over a standard 10 minute period, often with an associated standard deviation. For this reason, the first source of uncertainty is that associated to the small scale turbulence (oscillations of period smaller than the time averaging scale), but other factors contribute to the data's uncertainty.

Meteorological masts are typically instrumented with high precision sensors that follow strict calibration procedures, and after data quality assessment they tend to provide low uncertainty data. WT instrumentation on the other hand is mostly used for internal con-

trol procedures, where data quality requirements can be less strict. This is aggravated by the fact that both the individual WT's and the global WF's blockage effect will impact the WT mounted sensor data.

Where no direct measurements are available derived data can be used, but Réthoré et al. (2009) emphasizes how the processing methods interfere with the final data uncertainty:

- With a validated power curve, wind speed can be reliably derived from electrical power output and vice versa. The power curves do however introduce a non-insignificant level of uncertainty over the raw measurement, and their calibration can differ significantly and independently from WT to WT. The quality of the correlation will also largely depend on the removal of outliers and on the occurrence of external WT control.
- Peak power losses between neighbouring WTs will occur for inflows along the WT alignment. The yaw offset is determined by plotting the ratio between WT powers relative to nacelle yaw data, allowing the correction of raw yaw position measurements (typically uncalibrated) for wind direction. This however will not eliminate yaw misalignment (between flow and nacelle yaw position), inherent to the hysteresis and inability of the WT control to respond to fast wind direction changes.

In addition to the implicit uncertainty of the established reference measurement, spatial variability under changing wind conditions are relevant since travel time at common wind speeds on off-shore wind farms can be considerable. This means that if assuming correlated flow conditions between two points of the wind farm, the amplitude of the associated uncertainty will increase with the distance between them.

The uncertainty associated to spatial variability will be imbued into the final data products, since the assumption of spatial correlation plays a part in so many steps of the dataset processing, from the quality assessment and data recovery to the data binning. Ultimately, spatial variability will also be aggravated by large scale turbulence (time scale larger than the measurement period) and, at each individual WT, by error sources such as yaw misalignment, wind direction sensor and wake deflection and meandering.

3.1.3 Establishing reference inflow conditions

Understanding WF operation requires first and foremost to know the characteristics of inflow. Records are split into bins (characterized by a target value and a tolerance) of inflow wind speed, wind direction or any other measured variables. To a selected bin is associated all data recorded simultaneously to the filtered reference measurements (including WTs as well other measurement stations), creating ensembles that match the WF and individual WTs operation to filtered inflow conditions.

Establishing accurate reference inflow conditions is thus key to transform the dataset into usable information: the uncertainty associated to the reference inflow data will have a direct impact on the reliability of the record binning process. High uncertainty data will increase the amount of incorrectly binned records and the filtered interval misrepresentation, reflecting on the ensemble data and its average.

Undisturbed wind speed and direction measurements are in some cases available from meteorological masts in close proximity to the wind farm. Such data is prioritized as a source for inflow reference conditions unless it is affected by the WF's wake. To cover the full 360° of inflow direction additional data is required, from meteorological masts or derived from WT mounted sensors operating in clear inflow.

When using meteorological mast data, often it is possible to derive data such as turbulence intensity and atmospheric stratification regime, in addition to the standard wind speed and direction data measurements. Both the T.I. level and the stratification regime can be critical factors in wind farm behaviour (Hansen et al., 2012) and are often required model inputs. However data collected in this form will suffer from much greater uncertainty, being indirectly obtained by mathematical manipulation of measured data.

The position of the reference measurement mast has to be taken into account, to ensure that the distance to the relevant WTs and measurement locations is not too large. The balance between the quality of the collected data and the effects of spatial variability has to be considered, as it may be preferable to use other sources for reference inflow data. WT operation derived data is often a necessity for this reason, when the displacement is large and correlation between locations is severely degraded.

For all the reasons above, the uncertainty associated to a given reference measurement changes with the inflow sector and with the location within the site. This means that the choice of reference measurement for inflow characterization should change depending on the wind direction considered, in order to create optimal filtering conditions for the binning process.

3.1.4 Wind turbine power and power loss

After filtering and correction (essentially for power and pitch sensor failures, see Réthoré et al., 2009), WT power measurements tend to be error free, with uncertainty mostly associated to the inherent temporal averaging of the data recorded. One source of error that can be difficult to contain is the possibility of external control on a WT, by the grid operator or WF owner to reduce power. When wind farm datasets are void of information regarding external control, it can go undetected during dataset pre-processing and artificially increase power losses in the case of frequent occurrence.

While not directly associated to the WT power measurements, the binning process can effectively impact the uncertainty of ensembled WT power data. Gaumond et al. (2013) discusses how incorrect record binning, particularly due to reference inflow wind direction uncertainty, can have considerable impact on SCADA ensembles, as even a small wind direction difference can mean a WT moves from fully waked to clear inflow. Using narrow wind direction bins will significantly amplify the issue, with noticeable impact on average ensemble WT power.

Using WT power data for wake model validation relies on calculation of relative power losses rather than absolute WT power. This means that there is the need to establish a reference power level, reflective of typical WT operation under the inflow conditions defined by the inflow bin. The choice of reference and the absolute power value set by it will impact the significance of the calculated power deficits (equation 3.1) at individual

WTs, as a poor choice of reference can result in efficiencies above 100% at individual or sets of WTs or, on the other hand, to globally over-estimated power losses.

$$P_{def} = 1 - \frac{P}{P_{ref}} \tag{3.1}$$

Barthelmie and Jensen (2010) discusses the pros and cons of a number of options for calculating a reference free-stream wind turbine power output:

- Power output of a single inflow facing WT – an ad-hoc choice of WT can produce a representative power level, but leaves the power deficit calculations susceptible to quality and availability issues at the reference WT's power data;
- Average power output of a group of inflow facing WTs – a direct measure of power output under the filtered wind conditions, and safeguarded from data issues at any individual WT, but can often be below the highest average power output, so efficiencies above 100% can still occur;
- Peak individual WT power output within the array – unambiguous criterion that ensures efficiency is equal or below 100% across the whole WF, but can lead to over-estimated free-stream power outputs if the result of non-uniform inflows or local flow acceleration effects, distorting all power deficits;
- Derive reference power output from nearby measurement mast wind speed observations – unaffected by wind turbine operation or its power output data quality, will introduce uncertainty associated to the WT's power curve (the calibration of which can differ significantly from WT to WT) and to spatial variability given the displacement between mast and wind farm.

The WT power measurement quality will apply to both the target WT's and the reference power levels, accumulating on the power deficit value when calculating the relative power losses. Finally, using a static reference to calculate power deficits across the WF means that the distance between the reference and the target WTs will vary, and power deficit uncertainty will increase with distance to the reference.

3.1.5 Comparing simulation and SCADA bins data

After averaging out short term oscillations within the measurement period and binning to a given interval, all the data measured on the WF for that bin is concentrated in a bin average value representing a spread of wind conditions. Simulation data on the other hand is only illustrative of wind flow and WF operation in very specific homogeneous flow conditions, both time and space-wise.

To compensate for the disparity between simulated and measured data, the binning intervals can be resolved with a discrete set of individual simulations. The average result of the simulation aggregate should reasonably approximate WF operation under the spread of wind conditions found inside the SCADA binned data. This approach assumes that all unfiltered variables have an impact that cancel out during bin averaging, limiting the number of inflow characterization variables that require representation

through simulation aggregate.

Since the number of runs is limited by computational resources, the approach is a balance between resource usage and the quality of the comparison. WF operation however will not be equally sensitive to every variable, and the number of individual runs necessary to achieve accurate bin representation will change:

- The wake width at typical WT spacing in a wind farm can be as low as 10°, meaning a change of 5° in wind direction between runs can cause a WT to change from operating in a fully waked state to free-stream flow. Considering the number of WTs and the layout of a WF, its operating conditions can be very sensitive –with a non-linear response– to wind direction changes.
- In the WT operating range where power loss from wakes is relevant – the lower half, up to 10-15 m/s on most modern WTs – power is highly sensitive to WT and inflow characteristics, particularly free-stream velocity as it scales with velocity cubed. Concentrating on relative performance losses reduces the wake effect to a dimensionless parameter, largely independent of WT model and inflow characteristics, even though free-stream velocity ratio and relative power deficit still have super-linear responses to inflow wind speed change, the latter more so. The WT's responses to changes in other inflow parameter like ambient T.I. and stratification regime will be comparatively mild.

However finely resolved any SCADA bin may be, reference inflow uncertainty inherent to the bin average cannot be directly accounted for in simulation aggregate result.This can be particularly relevant to inflow wind direction data uncertainty, which as discussed in Section 3.1.3 can have vast consequences in the operational data quality.

Acknowledging the difficulty to retroactively combat it at the SCADA data level, Gaumond et al. (2013) proposes to emulate the effect of directional uncertainty found in measured data in model results by replacing each simulation's contribution with a weighted average of results from simulations covering the direction and its expected error range. A normal distribution is used as averaging weight, matching the nature of the wind direction uncertainty, and only requiring an estimate of wind direction uncertainty. This technique however requires the modeller to use an increased number of simulations, to cover a span of wind directions that is greater than of the bin width.

A final factor to take into consideration is the occurrence of non-uniform inflow conditions, for example in coastal areas or near neighbouring offshore WFs, affecting WF operating conditions. The flow conditions assumed at the domain boundaries, as well as the boundary's placement, will limit the model's capability to adequately represent these conditions. Unless these inhomogeneities are considered in the simulations from the outset, the comparison will be fundamentally flawed.

3.2 Wind Turbine scale wakes inside a wind farm (Horns Rev)

A wake model benchmark (Réthoré et al., 2013b) was organized under the EERA-DTOC project to evaluate WT scale models under a series of standard cases, based on operational data from the Horns Rev wind farm. Here, we report on the results of those tests and assess performance when modelling individual wakes and combined wakes in a row, with focus on capturing sensitivity to wind direction.

3.2.1 The Wind Farm: Horns Rev

Horns Rev wind farm is located just off the west coast (14 km) of Denmark (Figure 3.1; source 4C Offshore, 2016), on shallow waters. The location was instrumented with multiple meteorological masts for wake study purposes, forming with the WT operation data a large dataset for off-shore wind farm studies and WT wake research (Hansen et al., 2012).

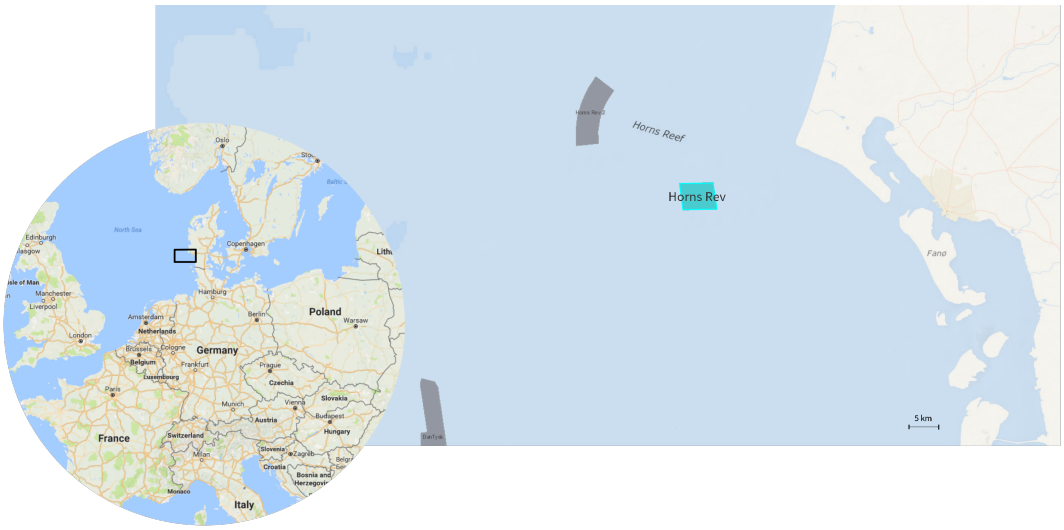

Figure 3.1: The Horns Rev Wind farm location and surroundings. Note that the neighbouring WF Horns Rev 2 to the NW was not yet installed at when the used dataset was recorded.

The resource assessment studies (documented in Hansen et al., 2012) suggest a dominance of flow along the East-West axis sectors, with the Westerly sector having the highest directional frequency and high average wind speeds (above 9 m/s). While Westerly sector inflows are characterized by a large clear fetch, Easterly inflows can be affected by the nearby Danish coast.

With a rated capacity of 160 MW, the wind farm is equipped with VESTAS V80 WTs (Figure 3.2), which are 2 MW rated power pitch-controlled machines with 80 m rotor diameter and 70 m of hub height. They are arranged in a parallelogram-shaped regular array (Figure 3.3) with 8 rows –numbered 1 through 8 and oriented East to West– and 10 columns –numbered 0 through 9 and at a 7° inclination from North-South axis. Inter-WT spacing is 7D in the two main directions and 9.4D and 10.4D in the two diagonal directions (221° and 312° respectively).

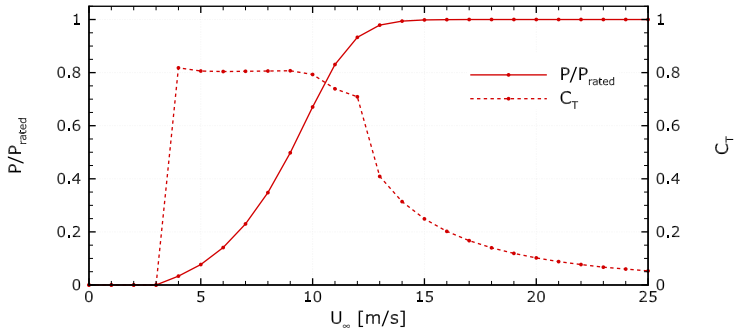

Figure 3.2: Manufacturer power and thrust coefficient curves for VESTAS V80 Wind Turbine, equipped on the Horns-Rev wind farm.

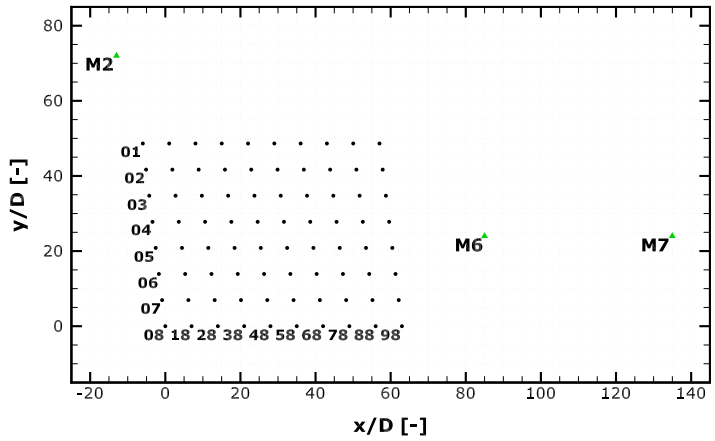

Figure 3.3: The Horns-Rev wind farm layout map. Black dots represent WTs and green triangles represent meteorological masts.

3.2.1.1 The dataset: SCADA and mast measurements

One meteorological mast (M2) was installed prior to WF deployment for the initial wind resource assessment measurement campaign, located to the NW of the array (Figure 3.3). Two additional masts (M6 & M7) were later erected to the East of the array, instrumented up to a maximum height of 70 m (matching the WT hub height), as part of a measurement program to register wake flow under western sector flow, taking advantage of the large inflow fetch and the dominant meteorological conditions.

The dataset made available for wake analysis was comprised of 3 years of consecutive SCADA data, from 2005-2007, along with concurrent measurements from towers M6 and M7. Data from the M2 was not included in the dataset, as concurrent measurements were affected by quality issue. Due to its size, the SCADA data was pre-filtered and processed (discussed in Chapter 4 of Réthoré et al., 2013a) by benchmark coordinators, while participants received instructions on how to adjust wake models to ensure consistent comparison between SCADA and model results.

Comparison data points were produced by averaging measurements binned for intervals

of inflow wind speed, direction and T.I., under Easterly and Westerly sector inflows. To cover the two opposing inflow sectors, the choice of reference measurement sources for each (Table 3.1) reflect the need to minimize ensemble average uncertainty. Furthermore, the first of each set of consecutive binned records, the initial part of which still belonging to the transition into the consecutive set, is filtered out from the bin in an effort to minimize uncertainty associated to spatial variability.

The M6 measurements provide reference undisturbed inflow data for the Eastern sector, being based on high quality measurements and in close proximity to the nearest WTs. In the case of the Westerly sector inflows, a reference had to be derived out of operational data from WTs on the West facing edge of the array wt0X (machines wt01-wt08), carrying with it a greater uncertainty that can reach, for wind direction data, values of 5° or more. data.

	W sector inflows	E sector inflows
Wind dir.	Col. 0 WTs (8-row avg., derived [1])	M6 @ 68 m
Wind speed	wt07 (derived [2])	M6 @ 70 m
T. I.	–	M6 @ 70 m

[1] Using offset-corrected nacelle yaw position data. Note that this does not eliminate WT yaw misalignment errors.
[2] Using electrical power measurements and the WT's calibrated power curve.

Table 3.1: Sector-wise inflow reference data sources for the Horns Rev WF dataset.

3.2.2 Simulating the wind farm

Assuming that WF operation is far more sensitive to changes in wind direction, there was a focus was on reproducing variability within the wind direction bins, in opposition to other filtering parameters. Table 3.2 shows the inflow conditions and mesh characteristics corresponding to every simulations run. Given the regular, anti-symmetric array layout and the homogeneous inflow conditions, every run is a representation of WF operation in the chosen inflow direction as well as its polar opposite (i.e. 270° and 90°), meaning both Westerly and Easterly sector inflows are represented with the simulations run.

The range of wind directions included in the test case bins was resolved with individual simulations at every 2.5°. This resolution results of a compromise between computational cost and the ability to reproduce the narrowest of wind direction bins utilized in the benchmark. With every simulation assumed to represent a 2.5°-wide wind direction sector, simulation aggregates are the result of averaging of the individual WT powers weighted by the relative fraction of the SCADA bin covered by simulation's 2.5° sector width.

WF operating conditions were assumed be constant or change linearly inside the bins of inflow characteristics other than wind direction. This way, a single simulation calibrated to match a value at the center of a wind speed or T.I. bin adequately represents the bin average operating conditions. Where no binning is applied, benchmark coordinators indicated a target value assumed to be representative of the ensemble average.

Sector	Run	Inflow [1] Dir. [°]	U_∞ [m/s]	T.I. [%]	Nodes $N_i \times N_j \times N_k$	WF area [m] D_x	D_y
221°	1	216.0	8.1	6.6	390×390×50	5920	6840
	2	218.5	8.1	6.6	"	5980	6820
	3	221.0	8.1	6.7	"	6020	6800
	4	223.5	8.1	6.7	"	6060	6780
	5	226.0	8.1	6.7	"	6080	6720
270°	6	247.5	8.1	6.4	370×320×50	5780	5780
	7	250.0	8.1	6.5	360×310×50	5600	5460
	8	252.5	8.1	6.5	360×310×50	5600	5460
	9	255.0	8.1	6.6	350×300×50	5500	5280
	10	257.5	8.1	6.6	350×290×50	5380	5080
	11	260.0	8.1	6.6	350×280×50	5260	4880
	12	262.5	8.1	6.7	340×270×50	5120	4660
	13	265.0	8.1	6.5	360×250×50	5240	4440
	14	267.5	8.1	6.6	"	5440	4220
	14b	"	8.0	3.8	"	"	"
	14c	"	8.2	9.8	"	"	"
	15	270.0	8.1	6.6	"	5600	4000
	15b	"	8.0	3.8	"	"	"
	15c	"	8.2	10.8	"	"	"
	16	272.5	8.1	6.6	"	5800	4200
	16b	"	8.0	3.8	"	"	"
	16c	"	8.1	10.2	"	"	"
	17	275.0	8.1	6.6	"	5920	4360
	18	277.5	8.1	6.6	380×260×50	5960	4400
	19	280.0	8.1	6.7	390×280×50	6200	4720
	20	282.5	8.1	6.7	390×280×50	6320	4880
	21	285.0	8.1	6.7	400×290×50	6420	5020
	22	287.5	8.1	6.7	400×290×50	6420	5020
	23	290.0	8.1	6.7	410×300×50	6600	5300
	24	292.5	8.1	6.8	410×310×50	6680	5420
312°	25	307.0	8.0	6.8	450×350×50	6840	5940
	26	309.5	8.1	6.7	"	6820	6000
	26b	"	8.0	3.8	"	"	"
	26c	"	8.1	10.1	"	"	"
	27	312.0	8.1	6.6	"	6800	6040
	27b	"	8.0	3.8	"	"	"
	27c	"	8.1	10.1	"	"	"
	28	314.5	8.0	6.6	"	6760	6060
	28b	"	8.1	3.8	"	"	"
	28c	"	8.1	10.0	"	"	"
	29	316.0	8.1	6.6	"	6700	6080

[1] Windspeed and T.I. measured 2D upstream of reference wind turbine WT07.

Table 3.2: Inflow and mesh characteristics of individual simulations run for the Horns Rev case, covering the 221°, 270° and 312° sectors.

3.2.2.1 VENTOS®/2 simulation setup

Boundary layer

The default VENTOS®/2 boundary conditions (Section 1.5) are applied. They are parametrized for a uniform surface roughness of $z_0 = 0.0001$ m and a friction velocity u_*, calibrated to meet the target inflow windspeed immediately upstream of the first WTs.

Neutrally stratified flow was imposed on all simulations, and the boundary layer height limited only by the top boundary and the zero-gradient condition. The turbulent equilibrium conditions imposed at the inlet boundary are in conflict with the top boundary condition at the top edge of the domain, meaning there is some stream-wise flow profile development while the flow adjustment near the top boundary propagates down towards the surface. The stream-wise development of the boundary layer is presented in (Figure 3.4, both length-wise at hub-height (top figure) and in vertical profiles at key domain positions (bottom figure).

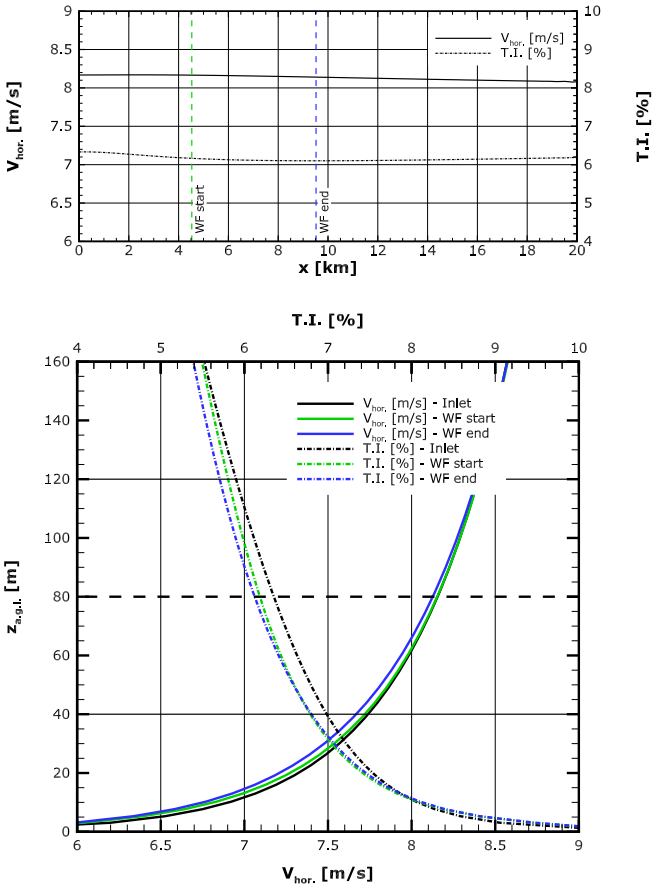

Figure 3.4: Flow conditions over the length of the domain in the absence of the WF: stream-wise development of velocity and T.I. at hub height (top) and vertical profiles at inlet and edges of the WF area (bottom).

The WF is contained in the $[-2.5; +2.5]$ km range (after the initial development length, up to the -2 km mark), where the hub height flow characteristics are stable or developing

at a slow rate: velocity is dropping at a constant rate of approximately 0.006 m/s per km, and T.I. is stabilizing at a value of 6.1%. The vertical gradients of either quantity suffer only marginal increases between WF start and WF end points. Given these observations, the potential free-stream inflow conditions for WTs within the WF area are considered homogeneous.

Where necessary (runs ##b and ##c, in Table 3.2), inflow T.I. was adjusted by scaling the turbulent kinetic energy profile at the inlet boundary. This interference on the default inlet boundary conditions results in a profile that is not in turbulent equilibrium, from which the flow solution will tend to recover over the length of the domain. Although the stream-wise flow profile development is not negligible in those conditions, the absolute change in ambient flow conditions between any two adjacent WTs should be small.

Domain and meshing

Different inflow directions mean that the WF's position relative to the inflow changes, requiring readjustment (in dimensions and node count) of the domain's mesh to resolve the WF area under the same conditions on all simulations. Other mesh characteristics, such as overall domain dimensions and peak vertical and horizontal resolution (in Table 3.3), were kept constant across all simulations belonging to the same inflow sector.

	Domain dimensions [m]					Max. res. [m]		
Sector	$x_{min.}$	$x_{max.}$	$y_{min.}$	$y_{max.}$	$z_{max.}$	c_x	c_y	c_z
221°	-7000	13000	-6000	6000	1000	20	20	4
270°	"	"	-4000	4000	"	"	"	"
312°	"	"	-6000	6000	"	"	"	"

Table 3.3: Domain mesh dimensions common to simulations of each sector for the Horns Rev site.

Maximum spatial resolution in the horizontal plane was fixed at D/4, covering a rectangular area encapsulating all WTs in the array (Figure 3.5). This resolution (20 m) was chosen as a compromise between adequate wake flow modelling, power estimation accuracy and computational cost. Associated mesh dependency tests are presented in Section 3.2.2.2. Horizontal mesh dimensions expand from the limits of that high resolution area towards the domain boundaries, with CV dimension growth following a geometric progression rate. A maximum vertical resolution of 4 m was used at surface level, expanding geometrically towards the maximum domain height of 1 km. The resulting vertical resolution inside WT rotor span heights was below half the peak horizontal resolution.

The domains were dimensioned to have a margin of at least 1 km between the lateral boundaries and the nearest WT, to avoid excessive blockage effect by the WF. In Figure 3.6 the velocity ratio at the core of the WF and far outside it is plotted over the length of the domain, for the worst case scenario in terms of WF blockage effect (run 6 in Table 3.2). The blockage ratio (WF frontal area relative to domain cross-section) was

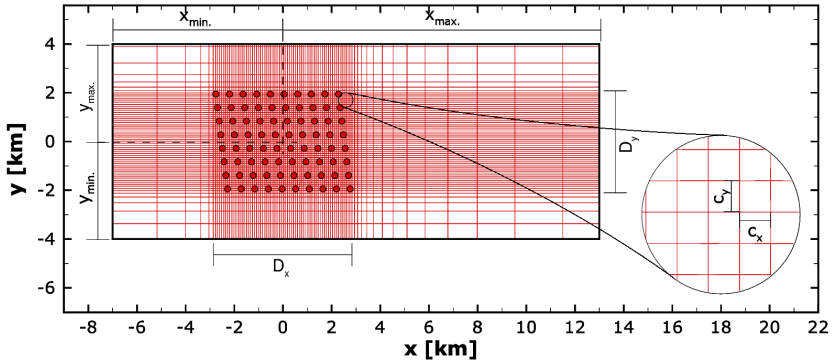

Figure 3.5: Horizontal projection of the mesh covering Horns Rev, in local array-centred coordinates. Mesh represented at half of the full resolution.

less than 6%, and the artificial flow acceleration that it produced lead to a maximum $U/U_\infty \approx 1.03$ at the WF end point.

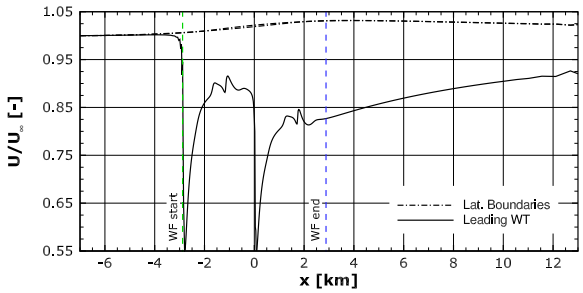

Figure 3.6: Length-wise hub height velocity profile outside the WF (at the lateral boundaries) and at the core of the WF (along the leading WT axis) at peak simulated blockage effect.

The inlet boundary was placed at least 3 km upstream of the first WT, and the outlet boundary approximately 10 km downstream of last WT. These values were considered sufficient to allow for any initial BL adjustment near the inlet and for unrestricted wake development towards the outlet. The simulations model the offshore BL as flow over a flat and smooth surface, with homogeneous inflow conditions and well adapted boundary conditions near the surface, so no severe stream-wise boundary layer adjustments occur near inlet or outlet boundaries in the presence of the WF (Figure 3.6).

Steady-state solutions were reached on all cases, with convergence accepted at a residual level of 5×10^{-4}. The WF power output predictions at that level of numerical tolerance were found to be within 0.1% of the final converged value. Further information on the numerical and mesh convergence behaviour of the simulations can be found in Section 3.2.2.2.

3.2.2.2 Power estimation convergence

From the simulations will result individual WT power estimates, which as seen in Chapter 2 are not independent of numerical aspects of the simulation: WT performance is sensitive to the mesh resolution (Section 2.5.3) and will have a delayed response to changes in the flow solution field (Section 2.6.3). These effects will naturally extend to the wind farm on aggregate, particularly when wake losses are considerable: flow solution and WT performance in neighbouring WTs are inter-dependent, and can take some time to stabilize. The impact of these effects should be minimized or assessed for consideration during further model result analysis.

One individual wind direction run (run 12 in Table 3.2, 263°sector inflow) was repeated at four resolution levels: low (LR), medium (MR), high (HR) and very high (vHR) (Table 3.4), with horizontal CV dimensions $c_{x/y}$ halving between vHR–HR–LR meshes. The average vertical resolution $\overline{c_z}$ within the rotor span is kept comfortably below the horizontal resolution on all meshes. Simulations were stopped after 20k iterations or when a residual tolerance of 5×10^{-5} surpassed. The residual convergence pattern is compared

	Mesh statistics			Simulation statistics			
Res.	$c_{x/y}$ [m]	$\overline{c_z}$[1] [m]	Node count	Iters.	Max. res.	t_{CPU} [h]	t_{CPU}/iter. [s]
LR	40	≈10.7	1.60 M	7500	5×10^{-5}	16.2	7.7
MR	30	≈9.42	2.78 M	10365	5×10^{-5}	41.8	14.5
HR	20	≈8.15	5.99 M	20000	7×10^{-5}	161.3	29.0
vHR	10	≈6.83	22.6 M	20000	1×10^{-4}	411.2[2]	74.0

[1] Average vertical resolution within the rotor span.
[2] Simulation run on twice the number of cores of other runs.

Table 3.4: Mesh resolution at the WF area for four meshes, with the respective mesh node count and computation time consumed.

between the four runs, focusing on the x-momentum and mass equation residuals as the greatest limiters to numerical convergence (Figure 3.7). While the mass equation residual continuously drops, the x-momentum residual begins to stabilize at values close to that threshold. The minimum possible residual at numerical convergence increases with the mesh refinement, meaning it stabilizes at numbers closer to 10^{-4} at the two finest resolution meshes (HR and vHR).

In the absence of the WF and with the HR mesh, the iterations required to reach a residual tolerance of 5×10^{-4} was 7494, lower than the corresponding WF simulation by ~1000. After 20k iterations, the highest residual had stabilized at 7×10^{-5} for the x-momentum equation. This suggests that convergence rate is slightly diminished by the addition of the WF, but that the solver is capable of reaching the same levels of numerical precision regardless.

Total wind farm power (Table 3.5) demonstrated sensitivity to mesh resolution: between 40 and 10 m horizontal resolution (D/2–D/8) it is dropping from 68.1 kW to 61.3 kW at a diminishing rate, suggesting that mesh convergence is approached at D/8. This matches the behaviour observed for a single WT (Figure 2.19), where power estimates stabilize at resolutions between D/5 and D/10. However, more importantly to the study

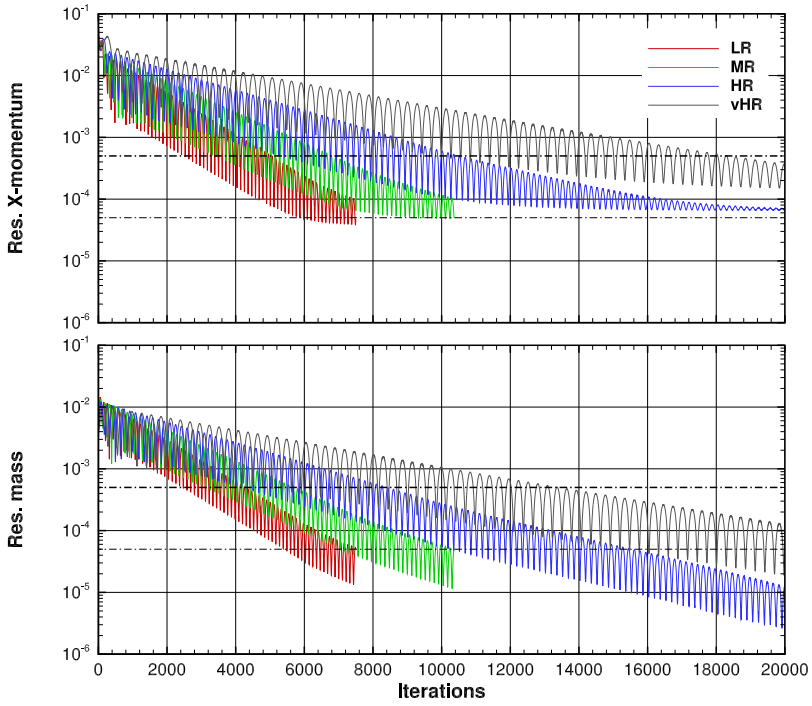

Figure 3.7: Mass and x-momentum residual evolution with CFD flow solver iteration.

Res.	P_{WF} [MW]	η_{WF} [%]	Row avg. P_{def} Row 0	Row 3	Row 6	Row 9
LR	68.1	81.7	-0.021	0.121	0.177	0.437
MR	65.4	79.6	0.013	0.137	0.203	0.437
HR	63.1	81.8	0.004	0.109	0.181	0.425
vHR	61.2	82.0	-0.017	0.136	0.174	0.405

Table 3.5: Sensitivity to mesh resolution of total wind farm power and efficiency, as well as by-row average power deficit.

of relative power losses, the wind farm efficiency (total wind farm power relative to the reference power level, the average of the 6 inner WTs of row 0) varies marginally in the 81.7–82.1% range between D/2, D/4 and D/8. No clear response pattern is discernible in the row average power deficits, suggesting that by-row variations cancel out overall.

At D/3 the WT rotor diameter is not a multiple of the horizontal resolution, which might explain the dip in WF efficiency to 79.6%. The per-row average power deficits also reflect that, systematically producing the highest power deficit values on all rows.

The total power output and WF efficiency were also observed over the length of the simulation's numerical convergence, to assess the model's WF performance convergence behaviour. In Figure 3.8 the WF's total power and efficiency level is plotted alongside the mass and x-momentum residuals, for the HR mesh (matching that used in the runs of Table 3.3). Overall WF power drops from maximum theoretical power (100% efficiency) to values close to converged ones within the first 500 iterations. This happens despite x-

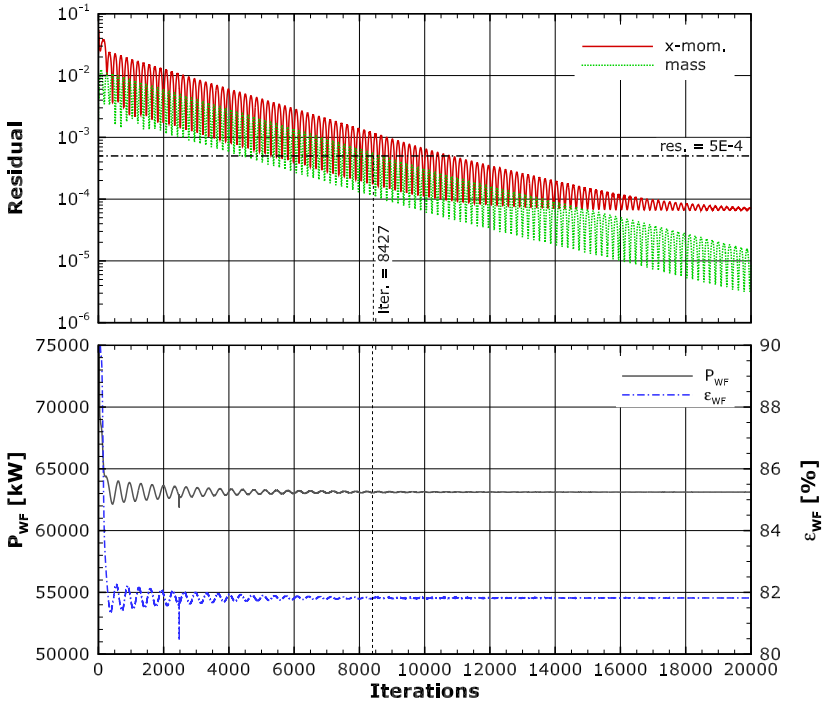

Figure 3.8: Wind farm overall power convergence with CFD flow solver iteration.

momentum and mass equation residuals still being close or above 1×10^{-2}, i.e. far from numerical convergence. The WF power fluctuations slowly diminish with the solver equation residuals, reaching amplitudes of circa 50kW (less than 0.1% of total WF power) shortly after 8000 iterations, where the residual tolerance of 5×10^{-4}, matching that applied to the runs in Table 3.3, is reached by all equations. The x-momentum equation is approaching numerical convergence after nearly 20000 iterations, at a residual of 7×10^{-5}. The further progress in solution precision between these two points has negligible impact on the WF power estimation.

3.2.2.3 Power estimation consistency

Upon conclusion of the projected runs, a preliminary analysis of of simulation output was conducted, assessing the pattern and consistency of WT power estimations. One behaviour stood out, most noticeable in the leading column WTs under Easterly sector inflows: operating under clear and homogeneous inflow, WTs in that column should have similarly homogeneous power output. However, considerable variation was observed both between simulations and between WTs in each simulation.

The relative standard deviation σ_P / P_{ref} of the leading column's average power output (Figure 3.9) tended to values between 4 and 6% within the 270°sector. Although greater than expected, there cases of 265° and the 285° wind direction stand out, with nearly zero and more than 8% σ_P / P_{ref} respectively.

The power estimates of each leading column WT in 265° and 285° directions are plot-

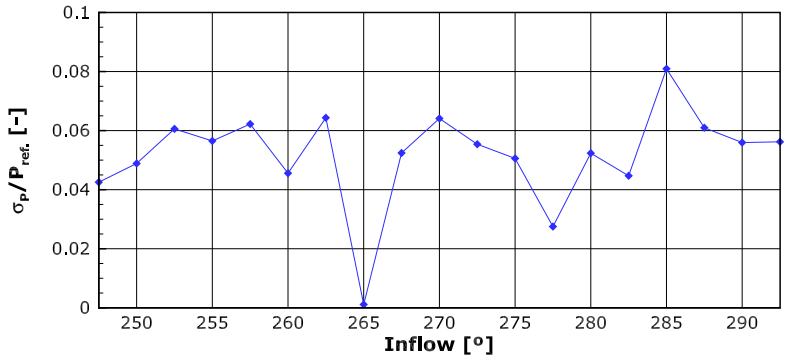

Figure 3.9: Relative standard deviation of the leading column of WTs of the Horns Rev WF under Eastern sector inflows.

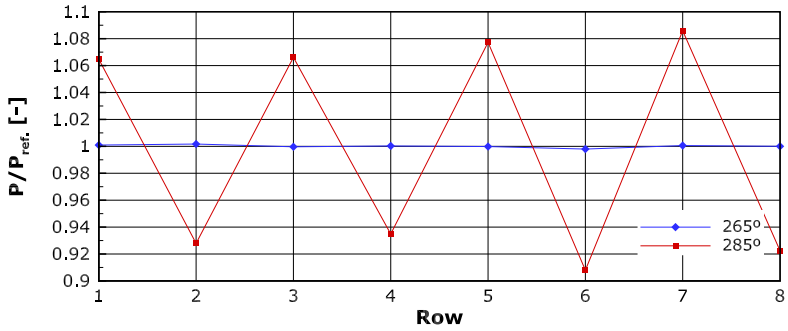

Figure 3.10: Power deficit distribution across the leading column of WTs of the Horns Rev WF for 265° and 285°sector inflows.

ted in Figure 3.10. Despite sharing similarly homogeneous inflow conditions, severe oscillations in power output (over 10% between neighbouring WTs) were found in the 285° case, which contrasted with the 265° case where power output exhibits the expected behaviour, with homogeneity across the whole column.

These inconsistencies are caused by spatial oscillations in the velocity flow solution. Depending on the position of the WT in the mesh (relative to CV centres), the oscillations can influence the WT thrust estimation algorithm and affect both free-stream velocity and power output estimates. They are discussed in further detail in Section 4.1, where a modification to AD discretization method is proposed as a solution. At the time of participation on the Horns Rev benchmark that modification had not yet been introduced in the wake model. The implication of this effect on results will vary with inflow characteristics and with the WT's position in the array. On a WT facing clear inflow its impact can be considerable, and particularly significant for WTs contributing to the reference power output value. The impact decreased on wake affected WTs, where differences in absolute power values decrease relative to the reference, and as increased diffusion promoted by the upstream WT wakes helped to smooth out the velocity field. Averaging across multiple WTs and simulations will also contribute to lessen its impact.

3.2.3 Results

The Horns-Rev benchmark included a large number of test cases, several of which were reproduced with VENTOS®/2 wake model simulations. These included the characterization of power deficit along rows of WTs (their sensitivity to inflow sector width and row spacing), on a single waked WT (and its sensitivity to inflow direction and ambient T.I.) and, finally, the WF's overall efficiency within the simulated sectors.

3.2.3.1 Wind direction sector width sensitivity

For inflows aligned with WT rows, as wind direction sector width increases the average power losses should decrease, as more occurrences where flow is not aligned with the rows are included in the ensemble. To quantify that behaviour and determine if the model can reproduce it, the power deficit along the East-West rows of WTs was determined for the 270° wind direction inflow with varying sector widths.

Sec. width	Inflow	SCADA	Reproduced	Runs
±2.5°	Dir. W.Speed	$270 \pm 2.5°$ 8 ± 0.5 m/s	$270 \pm 2.5°$ ~ 8 m/s	14-16
±7.5°	Dir. W.Speed	$270 \pm 7.5°$ 8 ± 0.5 m/s	$270 \pm 7.5°$ ~ 8 m/s	12-18
±15°	Dir. W.Speed	$270 \pm 15°$ 8 ± 0.5 m/s	$270 \pm 15°$ ~ 8 m/s	9-21

Table 3.6: Sector width sensitivity cases studied on the Horns Rev dataset, with SCADA filtering criteria and corresponding simulation ensembles.

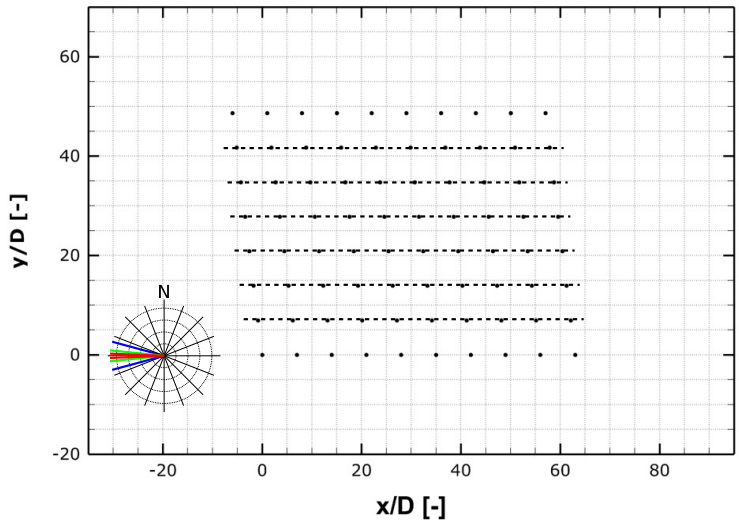

Figure 3.11: Inflow direction sector and WT rows considered in the sector width sensitivity case on the Horns Rev WF.

The key filtering criteria applied to SCADA data was wind direction, filtering for inflow sectors of $270 \pm 2.5°$, $\pm 7.5°$ and $\pm 15°$. The full binning criteria for each case and the corresponding simulation runs included for comparison are listed in Table 3.6. Refer to Table 3.2 for further information on the runs included.

The reference power level for a given inflow is determined by averaging the power from WTs on the leading column of array, exposed exclusively to clear inflow. Only the WT rows illustrated in Fig. 3.11 contribute to the average row analysis, with rows 1 and 8 are excluded as they operate in clear or partly clear inflow as wind direction approaches the extremes of the sector, exhibiting a different behaviour to the array's inner rows.

The power deficit along the average inner row for the three inflow sector widths is shown in Fig. 3.12. Agreement between model results and SCADA degrades as the width of the applied wind direction filter narrows: at a $\pm 15°$ sector width the model compares very well with SCADA data, but on the middle width sector of $\pm 7.5°$ a gap begins to appear between them (from x/D=14 to 35), while finally for the narrower sector model results diverge significantly from x/D=14 onwards.

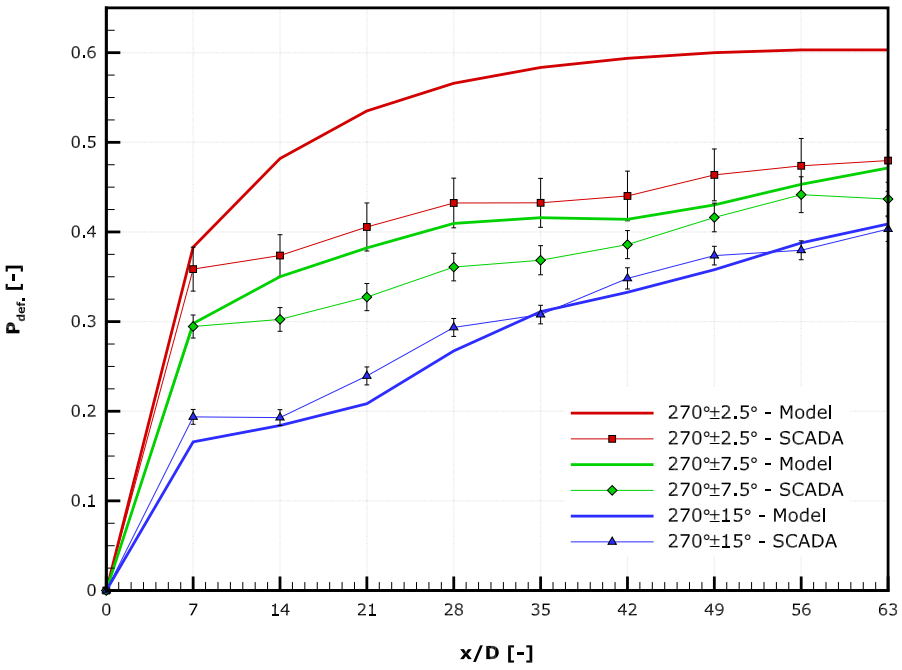

Figure 3.12: Average power deficit along Horns Rev WF rows per inflow direction sector width: filtered SCADA data *versus* VENTOS®/2 wake model result ensemble.

Uncertainty in the reference wind direction measurement (see Section 3.2.1.1) are thought to play a significant part in the narrow sector case comparison. A 5° wide sector is of the same order of magnitude as the reference inflow direction data uncertainty for the Easterly sector, meaning many records will be incorrectly binned and cases with more WTs in part-wake or free-stream are included, effectively decreasing the average power deficit. The impact of incorrect binning for inflow direction decreases as the sector widens, to the point where on the wider 30° sector SCADA data is tightly matched by the wake model results.

3.2.3.2 Wind turbine spacing sensitivity

Under row-aligned flow, wider WT spacing should allow for longer wake recovery between WTs, reducing power losses from individual and combined wake. Horns Rev's parallelogram-shaped array layout includes regularly-spaced WT rows in multiple directions, offering the possibility to verify that behaviour. Under Eastern sector inflows, the power deficit along those differently spaced rows is determined under flow aligned with the array's rows and diagonals.

Table 3.7 details the inflow conditions applied for each of the three cases. Refer to Table 3.2 for more on the runs included in each case. The rows of WTs illustrated in Fig. 3.13 contribute to the average row behaviour in each case. Power deficits calculated relative to average power output of the leading WTs of the included rows.

Spacing	Inflow	SCADA	Simulated	Runs
7D	Dir. W.Speed	$270 \pm 5°$ 8 ± 0.5 m/s	$270 \pm 5°$ ~ 8 m/s	13-17
9.4D	Dir. W.Speed	$221 \pm 5°$ 8 ± 0.5 m/s	$221 \pm 5°$ ~ 8 m/s	1-5
10.4D	Dir. W.Speed	$312 \pm 5°$ 8 ± 0.5 m/s	$312 \pm 5°$ ~ 8 m/s	25-29

Table 3.7: WT spacing sensitivity cases studied on the Horns Rev dataset, with SCADA filtering criteria and corresponding simulation ensembles.

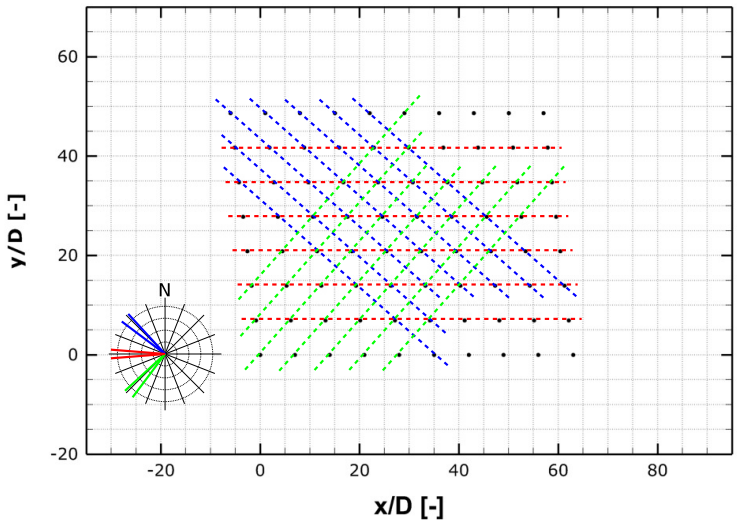

Figure 3.13: Inflow direction sector and WT rows considered in the WT spacing sensitivity case on the Horns Rev WF.

The key filtering criteria applied to SCADA data was wind direction, filtering for inflow sectors of $221 \pm 5.0°$, $270 \pm 5.0°$ and $312 \pm 5.0°$. This allows for the capture of flow along the E-W rows, SW-NE and NW-SE diagonals of the array and 7D, 9.4D and 10.4D

spacing between WTs respectively. The full binning criteria for each case and the corresponding simulation runs included for comparison are listed in Table 3.7. Refer to Table 3.2 for further information on the runs included.

The row selection in Fig. 3.13 avoids the outer rows operating in clear or partly clear inflow at the extremes of the wind direction sectors, and ensures that all cases share the same number of rows and a similar overall row length. The reference power level for a given inflow is determined by averaging power of the leading WTs on the contributing rows, exposed exclusively to clear inflow.

The average power deficit along the three differently spaced rows is shown in Fig. 3.14. The expected trend is demonstrated by both SCADA and model data, lowering deficits as WT spacing increases. However, unlike with model results, SCADA profiles shows no noticeable improvement with row spacings above 9.4D. The model data has a good match on the first waked WT for all three row spacings, but downstream of that agreement changes significantly. Model results over-estimate SCADA profiles at 7D, quickly deteriorating after the first waked WT. At 9.4D spacing there is over-estimation to a lesser degree, with agreement beginning to improve after 20D of row length. At 10.4D spacing there is slight but stable under-estimation throughout the row's length.

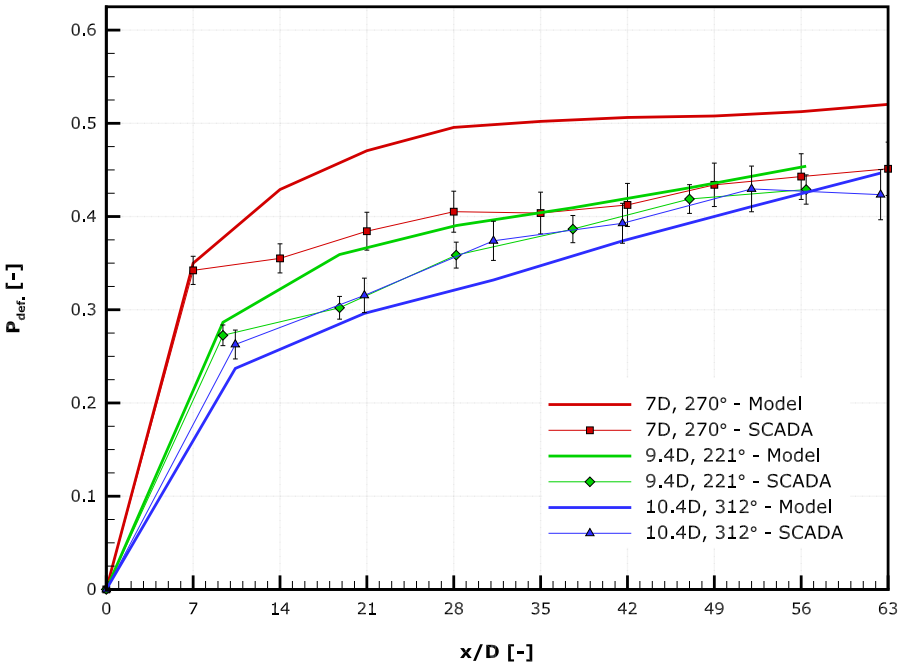

Figure 3.14: Average power deficit along differently spaced Horns Rev WF rows: filtered SCADA data versus VENTOS®/2 wake model result ensemble.

The SCADA profiles suggest that ultimately the length covered along the row is the dominant factor, as power deficit vale and profile gradient is very close on all three rows spacings after 35D travelled in the WF. This should be a consequence an equilibrium being reached between momentum extraction by the WTs and the flow's momentum recovery between WTs, ultimately limiting maximum power deficits. The model is close to reproducing this trend only on the two most widely spaced rows.

The overall behaviour seems to suggest that the transition into the momentum extraction/recovery equilibrium in the model is slower than SCADA data indicates. While that balance is not reached, the momentum-deprived flow results in over-estimated power deficits. This could be explained by exaggerated decay of turbulent mixing in the wake, requiring a greater number of combined wakes in a row to reach the level of downwards momentum transfer from the upper boundary layer through diffusive transport.

3.2.3.3 Wind turbine wake profile

The relative powers outputs between two neighbouring WTs will reflect the alignment between row and inflow direction, hitting maximum power deficit when flow is along the alignment between WTs. A wake profile will capture this row alignment effect, along with the transition zero power deficit under clear inflow. For this purpose, two WTs on consecutive leading rows of the Easterly facing edge WF were selected, with power deficit on the waked WT calculated over range of wind direction centred around the 90° sector.

Offset	Inflow	SCADA[1]	Simulated[2]	Runs
-20°	Dir.	$70 \pm 2.5°$	$70 \pm 2.5°$	6-8
	W.Speed	8 ± 1.0 m/s	~ 8 m/s	
⋮		⋮	⋮	⋮
20°	Dir.	$110 \pm 2.5°$	$110 \pm 2.5°$	22-24
	W.Speed	8 ± 1.0 m/s	~ 8 m/s	

[1] -20° to 20°offset range resolved in 1° increments.
[2] -20° to 20°offset range resolved in 2.5° increments.

Table 3.8: Inflow sector cases that form the WT wake profile case studied on the Horns Rev dataset, with SCADA filtering criteria and corresponding simulation ensembles.

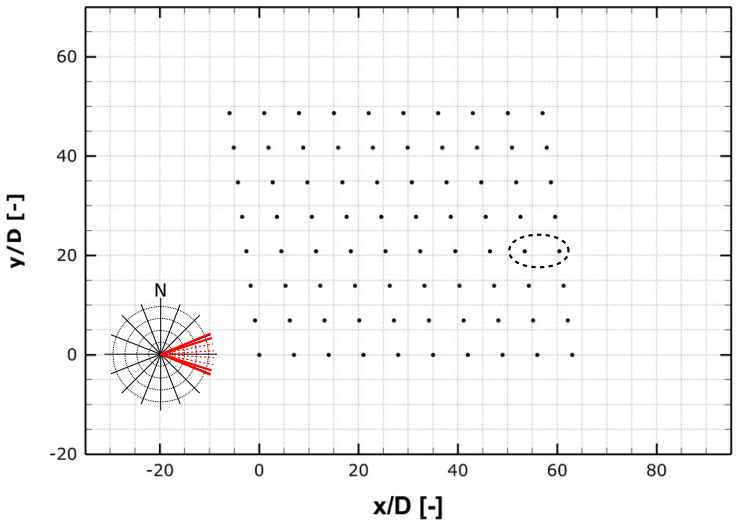

Figure 3.15: Inflow direction sector and WTs considered in the WT wake profile case on the Horns Rev dataset.

To produce the WT wake profile, a sequence of 5.0°-wide SCADA data bins covered the inflow direction range in increments of 1°, from $70 \pm 2.5°$ to $110 \pm 2.5°$. The wake model data lacked sufficient simulations to reproduce the inflow range with the same resolution, being limited to increments of 2.5° for the same range. The full binning criteria and corresponding simulation runs included for comparison in some exemplary cases are listed in Table 3.8. Refer to Table 3.2 for further information on the runs included.

The WTs used to produce both SCADA and model profile data were wt95 and wt85 (illustrated in Figure 3.15). The reference power level was calculated by averaging power at wt95 (leading row, in clear inflow) over the whole range of inflow conditions in the test case.

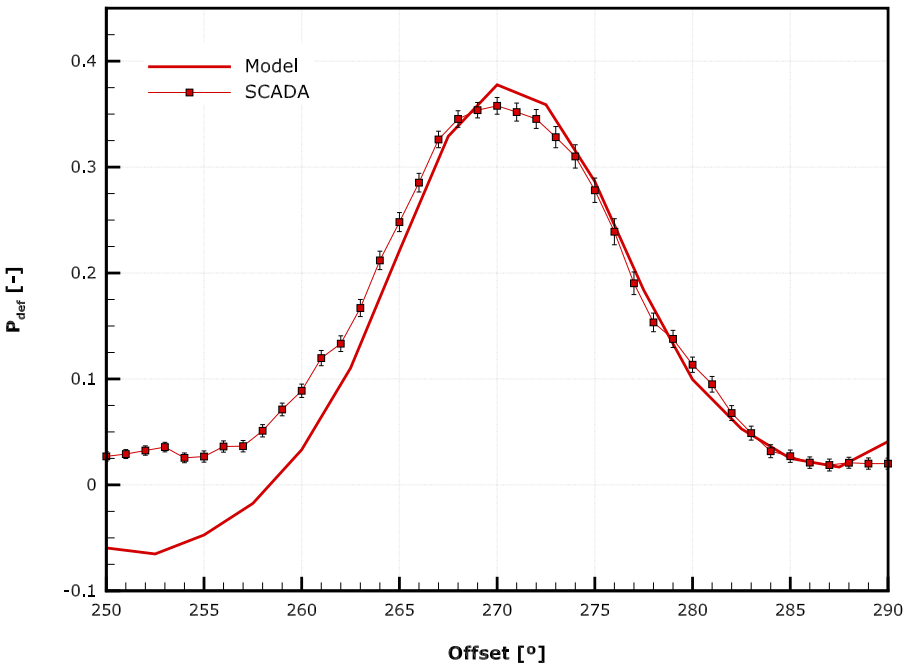

Figure 3.16: Power deficit profile of a waked Horns Rev WT: filtered SCADA data versus to VENTOS®/2 wake model ensemble data.

The SCADA and Model data single wake profiles are shown in Fig. 3.16 and the comparison between them shows that, despite an asymmetry not seen in the SCADA data, the overall shape is well predicted by the model and the match in most of the covered range (between -5° and 20°) is good. The agreement in left and right hand slopes suggest that wake width 7D downstream of the leading WT is well predicted. It has to be noted that the use of Easterly inflow sector in this case is relevant, as access to the much higher quality reference inflow measurements provided by M6 allows for much reduced uncertainties in the SCADA data profile, which uses narrow sector bins (2.5°) at very small increments (1°).

Given the asymmetry, the left-hand side sees the model under-estimating the measured data, particularly outside the wake (>10-15°). This means that in that region, power at the downstream WT is greater than the reference power level. Although the reasons for

this are not clear, the model's unstable power estimation (Section 3.2.2.3) is thought to be one of the main causes: affecting both WTs independently, the power deficit between them will be susceptible to significant over or under-estimations. This happens despite the fact that the reference power level is an average over the whole inflow condition range, thus reducing its sensitivity to such oscillations.

3.2.3.4 Ambient T.I. sensitivity

Increased ambient turbulence intensity will promote turbulent mixing, which should result in faster wake expansion and recovery and reflecting on WT power under waked inflow with reduced power deficits. To understand how power deficits are affected by inflow turbulence along the wake's length, the peak power deficit between two neighbouring WTs was observed under increasing ambient T.I. inflows and WTs separated by 7D and 10.4D.

Spacing	Inflow	SCADA[1]	Simulated	Runs
7D	Dir.	$90 \pm 2.5°$	$90 \pm 2.5°$	
	W.Speed	8 ± 1.0 m/s	≈ 8 m/s	
	T.I.	$2 \pm 0.5\%$	$\sim 4\%$	14b-16b
		$3 \pm 0.5\%$		
		⋮	$\sim 7\%$	14-16
		$12 \pm 0.5\%$	$\sim 10\%$	14c-16c
		$13 \pm 0.5\%$		
10.4D	Dir.	$132 \pm 2.5°$	$132 \pm 2.5°$	
	W.Speed	8 ± 1.0 m/s	≈ 8 m/s	
	T.I.	$2 \pm 0.5\%$	$\sim 4\%$	26b-28b
		$3 \pm 0.5\%$		
		⋮	$\sim 7\%$	26-28
		$12 \pm 0.5\%$	$\sim 10\%$	26c-28c
		$13 \pm 0.5\%$		

[1] 3% to 13% inflow ambient T.I. range resolved in 1% increments.

Table 3.9: Inflow cases that form the ambient T.I. sensitivity profile case studied on the Horns Rev dataset, with SCADA filtering criteria and corresponding simulation ensembles.

The key filtering criteria applied to SCADA data was inflow T.I., filtering for inflows with turbulence levels between 2±0.5 % and 12±0.5 %, at 1 % increments. This was combined with binning for inflow sectors 90±2.5° and 132±2.5°, to capture the same effect at 7D and 10.4D spacing between WTs. The choice of Easterly sector inflows was a necessity, to access the inflow T.I. measurements available from the M6 meteorological mast. The wake model data lacked sufficient simulations to reproduce the inflow T.I. covered by SCADA data, and was limited to simulations at approximately 4%, 7% and 10%. The full binning criteria for each case and the corresponding simulation runs included for comparison are listed in Table 3.9. Refer to Table 3.2 for further information on the runs included.

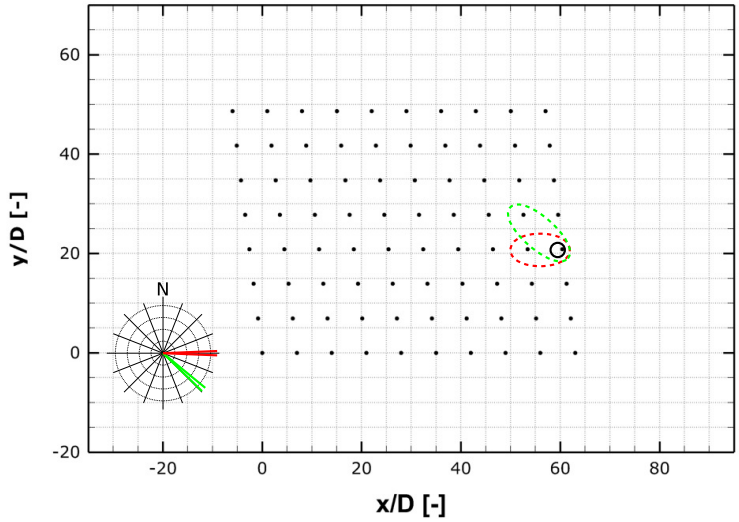

Figure 3.17: Inflow direction sectors and WT pairs considered in the inflow T.I sensitivity case on the Horns Rev dataset.

The WTs used to produce both SCADA and model profile data were wt95 and wt85 for 7D spacing and wt95 and wt84 for 10.4D spacing (illustrated in Figure 3.17). The reference power level was calculated by averaging power at wt95 (leading row, in clear inflow) over the whole range of inflow T.I. covered in each case.

The peak power deficit response to the increasing ambient T.I. levels is plotted in Fig. 3.18, for the 7D and 10.4D spaced WT pairs. The SCADA data profiles indicate a mostly linear decrease in power deficit with ambient T.I. irrespective of WT spacing. Although this type of behaviour is reproduced by model results, the steeper profiles imply greater sensitivity to inflow T.I.. Additionally, the gap between 7D and 10.4D is smaller than that seen in SCADA profiles, and for this reason the best agreement occurs at different points of the T.I. range: at 7D spacing this is somewhere between 4% and 7% T.I., whereas at 10.4D spacing the optimum agreement is found closer to 10%.

The comparison indicates that wake recovery prediction suffers as a consequence of the turbulence model: ambient T.I. appears to promote excessive turbulent mixing, but also excessive dissipation of wake induced turbulent diffusion. This would mean that even though wake recovery is generally over-estimated, at distances above 7D it has reduced to an excessively low rate, bellow that indicated by measurements.

3.2.3.5 Wind farm efficiency

Wind farm efficiency provides a global performance evaluation parameter, glossing over local heterogeneities - like those found in the previous cases - to find the aggregate result for a given inflow. To understand the model's ability to capture the combined effect of all WT wakes, WF efficiency is studied for a range of both Easterly and Westerly inflow direction sectors.

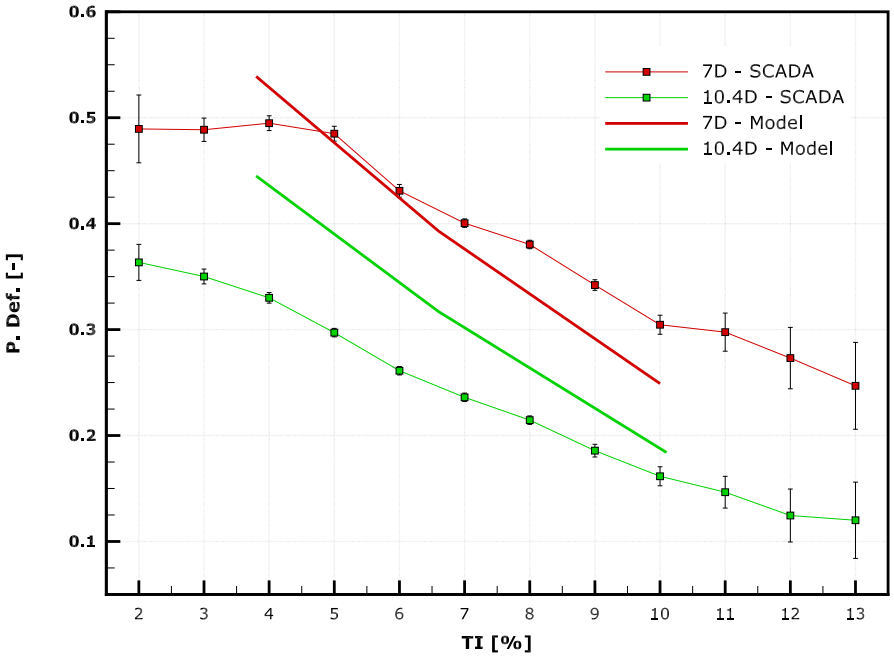

Figure 3.18: Power deficit sensitivity to inflow T.I. profiles for two differently spaced pairs of Horns Rev WTs: filtered SCADA data versus VENTOS®/2 wake model ensemble data.

Offset	Inflow	SCADA–E[1]	SCADA–W[1]	Simulated[2]	Runs
-20°	Dir.	$70 \pm 2.5°$	$250 \pm 2.5°$	$250 \pm 2.5°/70 \pm 2.5°$	6-8
	W.Speed	8 ± 0.5 m/s	8 ± 0.5 m/s	~ 8 m/s	
⋮		⋮	⋮	⋮	
20°	Dir.	$110 \pm 2.5°$	$290 \pm 2.5°$	$290 \pm 2.5°/110 \pm 2.5°$	22-24
	W.Speed	8 ± 0.5 m/s	8 ± 0.5 m/s	~ 8 m/s	

[1] -20° to 20°offset range resolved in 1° increments.
[2] -20° to 20°offset range resolved in 2.5° increments.

Table 3.10: Inflow sector cases that form the WF efficiency case studied on the Horns Rev dataset, with SCADA filtering criteria and corresponding simulation ensembles.

The key filtering criteria applied to SCADA data was inflow direction, through a sequence of 5.0°-wide data bins covering the inflow direction range in increments of 1°, from $70 \pm 2.5°$ to $110 \pm 2.5°$ (Easterly sector) and $250 \pm 2.5°$ to $290 \pm 2.5°$ (Easterly sector). Both inflow ranges are represented by the same set of simulations, taking advantage of the anti-symmetry of the array layout. The full binning criteria for each case and the corresponding simulation runs included for comparison are detailed in Table 3.10. Refer to Table 3.2 for more information on the runs included in each simulated case.

The SCADA data presented in this comparison is part of a full WF efficiency wind-rose. To capture undisturbed inflow, reference inflow data source had to adjust to inflow direction so, for consistency throughout the inflow range, reference inflow data and power levels were produced from undisclosed sector-wise undisturbed WT measurements (derived from nacelle position and electrical power signals) and not from the inflow data

sources discussed in Section 3.2.1.1. Wake model WF efficiency values are the result of the ratio between average WT power in the array and reference power level. The latter was calculated by averaging power at wt07 (always in clear inflow) over the inflow direction range covered.

The WF efficiency relative to offset (yaw relative to the 90° and 270° directions) is plotted in Fig. 3.19, for both Easterly and Westerly inflow SCADA data and wake model ensemble results. The measured WF efficiency sees a big drop between 250° and 290°, as flow aligns with the E-W rows. While that behaviour is generally picked up by the wake model, minimum efficiency and the transitions between flow unaligned and aligned with the East-West direction do not compare well between SCADA and wake model. The latter shows a narrower 'U' shaped curve, contained approximately in the $\pm 10°$ range compared to $\pm 15°$ for the SCADA profiles.

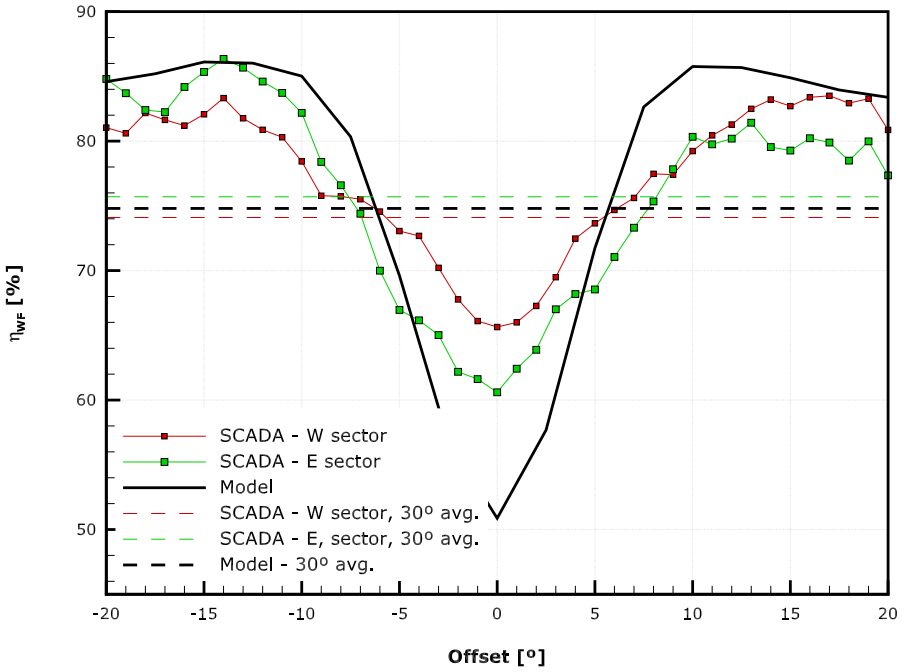

Figure 3.19: Horns Rev WF efficiency distribution around E-W row aligned inflows: filtered SCADA data versus VENTOS®/2 wake model ensemble data.

SCADA profiles for the opposite inflow sector (East sector inflows, between 70° to 110°) falls between the other two profiles, with a narrower and deeper drop in efficiency under row-aligned flow than seen for Westerly sector inflow SCADA data, but not as pronounced as the model prediction. This could be explained by the more complex inflow conditions (due to the proximity to the Danish shore) that characterize Eastern sector inflows, as well as the presence of the nearby M6 measurement mast, possibly contributing to improved WT sensor calibration and reduced reference data uncertainty.

Contrasting with the narrow sector values, the 30°-wide inflow sector averages from Model and SCADA data are very close, between 74% and 76% on all cases. The differences found close to row-aligned flow and in the transition regions of $[5, 15]°$ and $[-15, -5]°$ cancel out, resulting in a very good wide-sector model estimation.

3.2.4 Conclusions

In general the model was able to match the power deficit patterns resulting of the SCADA data collected, aided by ensemble averaging of multiple simulations to reproduce inflow conditions contained within SCADA bins (Section 3.2.2). However, because of the mismatch between the wind direction spread included in binned measurements and resolved via simulation ensembles (Section 3.1.5), agreement between model and SCADA tended to degrade with the reduction of the sector width.

The wake width and power deficit of a single WT were well predicted (Section 3.2.3.3), but combining multiple wakes over a row of WTs resulted in mixed agreement between model and measurements. Using wide sector widths (Section 3.2.3.1) and WT spacings (Section 3.2.3.2) provided the best agreement, with model predictions matching the SCADA power deficit profiles over the length of the WT rows.

When using narrow sector widths power deficits were over-estimated by a considerable margin, due to the different sensitivities of simulation ensembles and SCADA bins to the peak velocity deficit found at the center of the wake, further enhanced by proximity between WTs. The simulation capturing flow along the row's alignment weights heavily on the ensemble average since the number of simulations included is low, meaning average power deficits are too high. On the other hand, wind direction uncertainty (Section 3.1.2) in the inflow reference data leads to an increase in incorrectly binned records, effectively lowering bin averages and resulting in power deficits that are too low (Section 3.1.5). This effect was evident in the WF efficiency comparison (Section 3.2.3.5), where model predictions agreed best with Eastern sector inflow measurements, which benefited from higher quality inflow data.

The model predicted a near-linear impact of ambient turbulence on power deficit between two WTs, in agreement with the trend observed in SCADA measurements (Section 3.2.3.5). However, both the mixing promoted by the ambient turbulence and the turbulence dissipation are over-estimated by the flow solver, resulting in over-estimation of the sensitivity to inflow T.I. and an under-estimation in the power deficit recovery with the growth in WT spacing.

Finally, it became apparent that the model's power estimates can be sensitive to the AD's position in the domain mesh, due to oscillations in the velocity solution. The leading column of WTs, operating in homogeneous inflow, demonstrated an uneven power distribution (Section 3.2.2.3). However this had minimal impact on model results, due to averaging over multiple WTs and simulations (Section 3.1.4) and to the increased diffusion downstream in the WF, smoothing out the velocity field.

3.3 Wind farm scale wakes (Rødsand II cluster)

To understand WF operation when inserted in a cluster and assess wake model performance in that context, a benchmark based on operational data from the Rødsand II and Nysted cluster was organized under the EERA-DTOC project ((Hansen et al., 2015)). Participation involved prediction not only of wakes inside either wind farms at the WT scale, but also how these aggregate to form a larger wake effect and, how over long distances, it impacts WF within the cluster.

3.3.1 The wind farm cluster: Rødsand II and Nysted

The test site is composed of two wind farms in close proximity (3 km), forming a small WF cluster immediately south (5-10 km) of the Danish coast. Due to their relative positions (shown in Fig. 3.20; source 4C Offshore, 2016), the wind farms' operating conditions will not be disconnected when under Easterly or Westerly inflows, affecting each other and effectively forming a combined array that spans more than 20 kms in length and more than 150 WTs. The cluster will however benefit from a large fetch of undisturbed inflow from either of those inflow sectors.

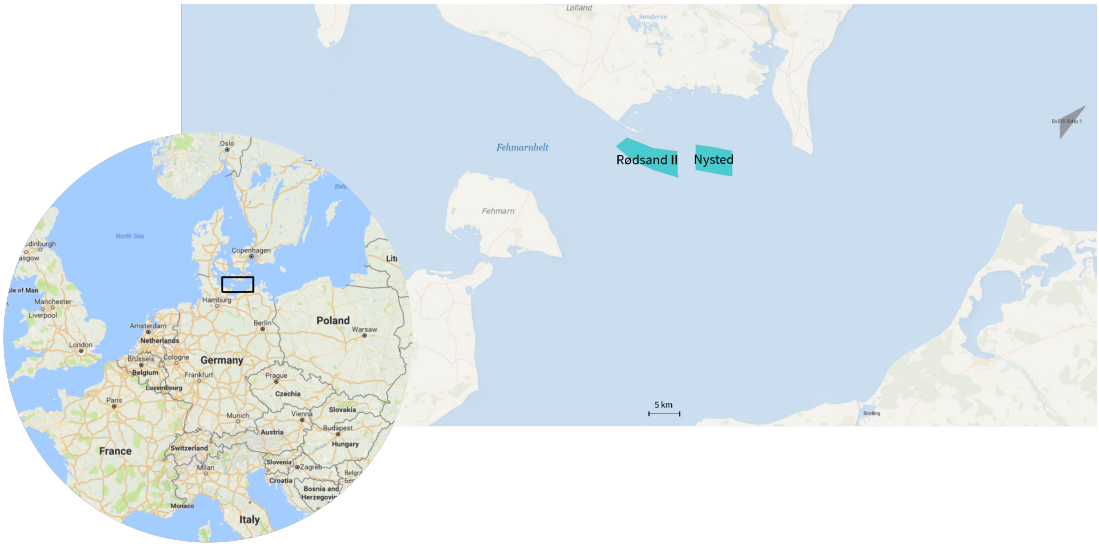

Figure 3.20: The Rødsand II and Nysted wind farms location and their surroundings.

The two wind farms that form the cluster are:

- Nysted, in operation since 2004, composed of 72 Bonus 2.3 MW WTs (see power and thrust coefficient curves in Fig. 3.21), with a hub height of 68.8 m and 82.4 m rotor diameter. Arranged in a parallelogram-shaped 9×8 regular array (Figure 3.22), the WTs are spaced along the E-W orientation at 10.3D gaps and along N-S orientation at 5.7D. The wind farm is also equipped with four meteorological mast measuring at up to 70 m high at the East and West ends of the array, installed post WF construction.
- Rødsand II, in operation since 2010, composed of 90 SWP 2.3 MW WTs (see power

and thrust coefficient curves in Fig. 3.21), with a hub height of 68.5 m and 92.6 m rotor diameter. The WT array is composed of 5 arced rows (named I, J, K, L and M), each 18 WT long with irregular WT spacing and orientation (Figure 3.22). The rows follow consistent trends (Figure 3.23) and are generally oriented in the West-East direction. A single meteorological mast was installed on-site, between WTs M1 and K1, measuring at up to 68.8 m high.

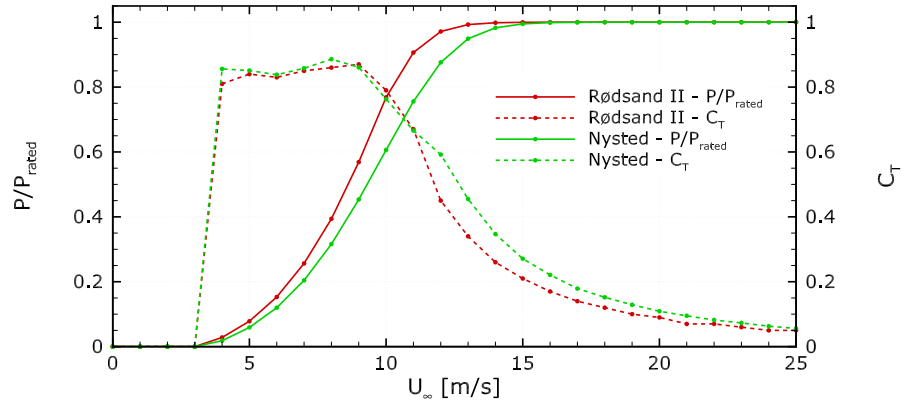

Figure 3.21: Manufacturer power and thrust coefficient curves for SWP and Bonus 2.3 MW WTs, equipping Rødsand II and Nysted WFs respectively.

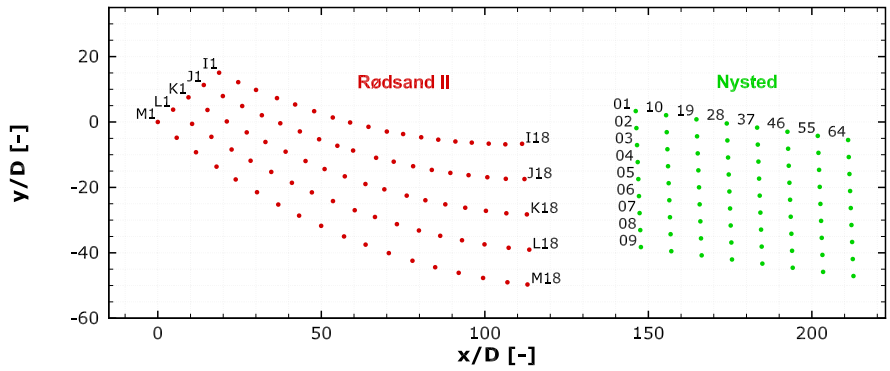

Figure 3.22: Rødsand II and Nysted WF layouts, forming a small cluster due to their close proximity. X/Y axis origin at Rødsand II's M01 WT and scaled by the Rødsand II WT diameter.

Prior to Rødsand II's construction, it was possible to study operation and performance of the Nysted WF (see (Barthelmie and Jensen, 2010)) without the cluster effect, using the four erected measurement masts to characterize the local wind regime. There is a clear dominance of Easterly and South-easterly inflows, but Westerly sector inflows were also a frequent occurrence. This was later corroborated by measurements taken at the Rødsand II measurement mast, during the WF's commissioning to assess turbulence conditions due to the proximity of the Nysted WF.

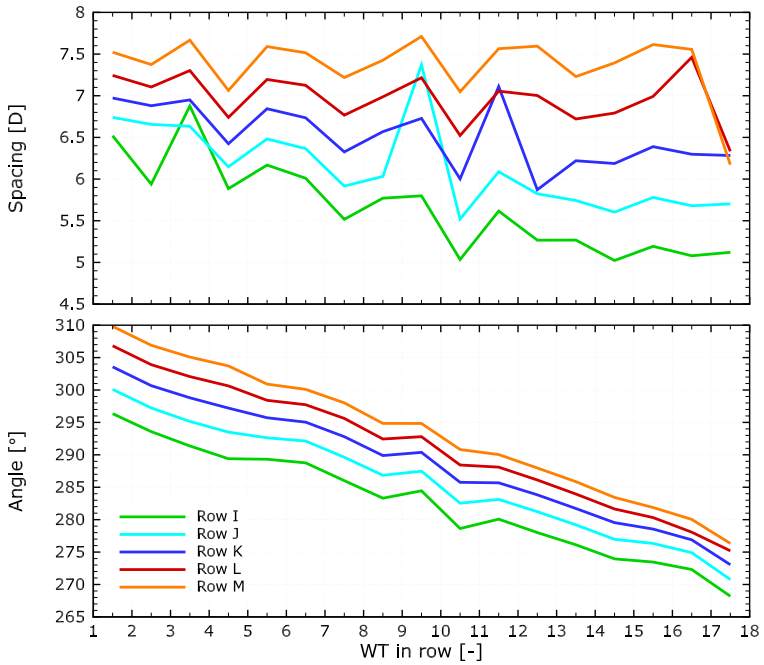

Figure 3.23: WT spacing (above) and alignment (below) along each Rødsand II row.

3.3.1.1 The SCADA dataset

The dataset consisted of 6 weeks in total of Rødsand II operational data. Because no synchronized Nysted SCADA data was made available, the comparison will focus exclusively on the larger of the two wind farms, and that when under Easterly inflows Rødsand II will be in the wake of a fully operational Nysted WF. East and West sector inflows are represented in equal parts in the dataset, i.e. 3 weeks of Rødsand II operation in clear inflow and another 3 of operation in Nysted's wake.

The SCADA data was organized and quality controlled according to guidelines set in Barthelmie et al. (2011) and Réthoré et al. (2009). However the records are supplied without time stamps and with no guarantees of concurrence. Additionally, because no WT status or blade pitch signals were available, the records affected by stopped WTs or power curtailment are hard to detect and are an unknown factor.

No synchronized inflow measurement data is associated with this production data, despite the existence of measurement masts on both Nysted and Rødsand II. Only the general wind speed, direction and turbulence regimes in the region are known. Inflow reference conditions had to be derived from nacelle position and electrical power signals at one or more undisturbed WTs. Due to its dimensions, spatial variability across the WF was large, with nacelle position signals differing by as much as 10° between opposing ends of the array.

The WTs contributing to either sector's reference inflow conditions are presented in Table 3.11. For West sector inflows there are several WTs in undisturbed inflow for a wide range of wind direction, most notably the row's leading WTs I01, J01, K01, L01 and M01. In the case of Easterly inflows, no WT on the Eastern edge of the array goes totally

	W sector inflows		E sector inflows	
Wind dir.	Col. 0 WTs	(5-row avg., derived [1])	M18	(derived [1])
Wind speed	Col. 0 WTs	(5-row avg., derived [2])	M18	(derived [2])
T. I.	–		–	

[1] Using offset-corrected nacelle yaw position data. Note that this does not eliminate WT yaw misalignment errors.
[2] Using electrical power measurements and the WT's calibrated power curve.

Table 3.11: Sector-wise inflow reference data sources for the Rødsand II and Nysted WF cluster dataset.

unaffected by Nysted's wake throughout the sector's wind direction range. The WT M18 does however operate in clear inflow at wind directions above 90°, and is arguably the least affected of all below that value.

3.3.2 Simulating the wind farms

Simulating Easterly sector inflows will require any simulation covering Rødsand II to include the flow perturbation introduced by Nysted. With no information on flow conditions in the space between WFs, modeling the presence of Nysted upwind becomes necessary . This causes the problem to grow from 90 WTs in an area of circa 15 × 10 km (Rødsand II, including immediate surroundings) to model an additional 72 WTs and the 10x10 km area occupied by Nysted.

The resulting cluster flow case is solved by splitting the problem in two and solving them sequentially, exploiting the computational advantages of smaller meshes to achieve faster and more stable solutions. The division is made in the area between WFs, creating two simulations: first a precursor simulation is run where only the Nysted wind farm is modelled, with the results of that simulation used to provide inflow conditions for simulation of the flow over the Rødsand II.

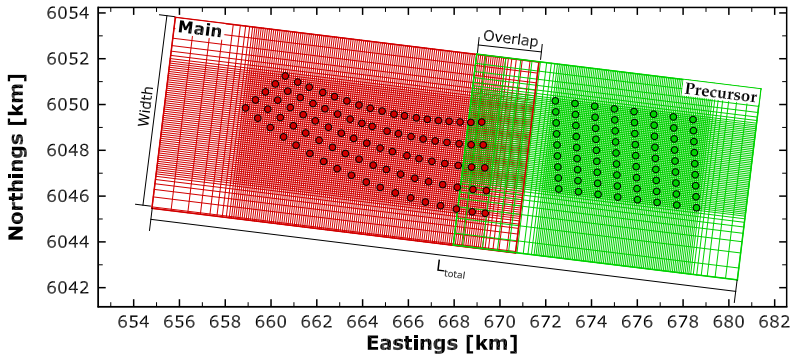

Figure 3.24: Superimposed horizontal projections of the domain meshes covering Rødsand II and Nysted WFs, used in coupled simulations. Meshes represented at half the full resolution.

ABL flows, and offshore flows in particular, tend to be parabolic in behaviour, with convection dominated transport and no occurrence of reversed flow. Between WFs flow will

		Domain [km]					Nodes	Res. [m]			WF area [km]	
	Dir.	$x_{min.}$	$x_{max.}$	$y_{min.}$	$y_{max.}$	$z_{max.}$	$N_i \times N_j \times N_k$	c_x	c_y	c_z	D_x	D_y
Rødsand II	077°	-6.50	9.00	-6.50	7.80	0.70	497×412×50	23	23	2	10.0	7.90
	087°	"	"	-5.00	5.10	"	512×339×50	"	"	"	10.4	6.56
	097°	-7.00	"	-4.40	4.00	"	541×270×50	"	"	"	11.1	4.99
	107°	-6.50	"	-7.00	4.00	"	550×250×50	"	"	"	11.4	4.19
	117°	-6.00	"	-8.45	4.50	"	544×280×50	"	"	"	11.5	4.78
	270°	-8.00	"	-4.50	4.50	"	540×316×50	"	"	"	10.7	6.16
	275°	"	"	-4.20	4.20	"	558×282×50	"	"	"	10.9	5.31
	280°	"	"	-5.50	5.50	"	522×382×50	"	"	"	10.2	7.59
	285°	"	"	-6.00	6.00	"	506×422×50	"	"	"	9.87	8.46
	290°	"	"	-6.00	6.00	"	500×434×50	"	"	"	9.66	8.79
Nysted	077°	-5.50	7.00	-9.30	5.00	0.70	393×375×51	20	20	2	6.50	6.02
	087°	"	"	-6.00	4.10	"	375×318×51	"	"	"	6.10	5.08
	097°	"	"	-3.55	4.85	"	407×260×51	"	"	"	6.78	3.98
	107°	-6.00	"	-4.50	6.50	"	436×305×51	"	"	"	7.36	4.70
	117°	-6.50	7.50	"	8.45	"	452×345×51	"	"	"	7.70	5.46

Table 3.12: Mesh dimensions and characteristics of every domain used on Rødsand II and Nysted simulations for the cluster runs, covering East and West sectors.

be characterized by the recovering wakes, with low streamwise gradients and no pressure perturbations, meaning flow features have little effect on upstream conditions and the parabolic assumption holds validity. This makes the area between WFs ideal for the coupling of precursor and main simulations, as the parabolic assumption introduces the least error. Figure 3.24 exemplifies the superposition of precursor and target simulation meshes, with the coupling section and the associated downstream overlap area. Section 4.4 further details on the process involved: precursor and target simulation adjustments, coupling method and associated computational gains.

Table 3.12 lists the domains used when simulating cluster wake case for both Rødsand II (RsII) and Nysted (Ny) WF, with their respective orientation, dimensions and mesh characteristics. The different inflow directions mean the WF's positions relative to the inflow changes, requiring readjustments (in dimensions and node count) to either mesh to resolve the WF areas under the same conditions on all simulations. Additionally, with simulations for coupled runs, the need for matching lateral boundaries led to additional adjustments to the domain's transversal dimensions.

Although WF operation is highly sensitive to changes in wind direction, the SCADA binned data was compared to the results of individual simulations instead of simulation ensemble averages. This way each simulation is assumed to be representative of inflow sectors 5° and 10° wide, for Westerly and Easterly inflows respectively. WF operating conditions should otherwise be constant or change linearly inside the bins of inflow characteristics other than wind direction, meaning that wind speed and T.I. bins are assumed to be adequately represented by a single simulation calibrated to the central value.

The resulting runs are as presented in Table 3.13, with the inflow conditions and domains applied. Note the Easterly sector runs are the result of two coupled simulations, and the aggregate domain dimensions an node count can be as much as twice those of

Inflow			Domains		Agg. Domain [km]			
Dir. [°]	U_∞ [m/s]	T.I. [%]	Precursor	Main	L_{total}	Width	Overlap	Nodes
077	7.9	7.0	Ny-077°	RsII-077°	25.3	14.3	2.72	∼17.8M
087	7.9	7.0	Ny-087°	RsII-087°	25.8	10.1	2.17	∼14.8M
"	5.9	7.1	"	"	"	"	"	"
097	7.9	7.0	Ny-097°	RsII-097°	26.2	8.4	3.23	∼12.7M
"	5.9	7.1	"	"	"	"	"	"
107	7.9	7.0	Ny-107°	RsII-107°	25.8	11.0	2.70	∼13.6M
"	5.9	7.1	"	"	"	"	"	"
117	7.9	7.0	Ny-117°	RsII-117°	25.5	13.0	2.48	∼15.6M
"	5.9	7.1	"	"	"	"	"	"
270	6.9	6.1	-	RsII-270°	17.0	9.00	-	∼8.53M
"	4.9	6.1	-	"	"	"	-	"
275	6.9	6.1	-	RsII-275°	17.0	8.40	-	∼7.87M
"	4.9	6.1	-	"	"	"	-	"
280	6.9	6.1	-	RsII-280°	17.0	11.0	-	∼9.97M
"	4.9	6.1	-	"	"	"	-	"
285	6.9	6.1	-	RsII-285°	17.0	12.0	-	∼10.7M
"	4.9	6.1	-	"	"	"	-	"
290	6.9	6.1	-	RsII-290°	17.0	12.0	-	∼10.8M
"	4.9	6.1	-	"	"	"	-	"

Table 3.13: Flow cases run for the Rødsand II and Nysted WF cluster, with corresponding inflow conditions, aggregate domain characteristics and domain coupling information, covering Easterly and Westerly inflow sectors.

the Westerly sector runs. Overlap between precursor and main domains did not drop below 2 km, ensuring proper detachment between precursor outlet boundary and the section from which are extracted the main simulation's inflow conditions.

3.3.2.1 VENTOS®/2 model setup

The VENTOS®/2 model setup used in the simulation was equal to that described in Section 3.2.2.1, apart from the inlet boundary conditions where domain coupling was applied, and parameters pertaining to domain dimensions and mesh resolution, as listed in Table 3.12. The conclusions pertaining to numerical convergence and mesh dependency were assumed to apply here as they did in Section 3.2.2.2.

The domains were dimensioned to allow a margin of approximately 1.5 km between the lateral boundaries and the nearest WT on either WF. The resulting combined blockage ratio (total WF cluster frontal area relative to domain cross-section) varied in the 8–9.5% range. This suggests a stronger blockage effect than that found in the Horns-Rev case (Figure 3.4). Inlet boundaries with synthetic inflow conditions were placed at least 3.5 km upstream of the first Rødsand II WT, and the outlet boundary 3.5 km downstream of the last WT. Maximum spatial resolution in the horizontal plane was 1/4D (23 m), covering the WF area in a constant resolution area (Figure 3.25), with a maximum vertical resolution of 2 m at surface level, expanding up to top of the 700m-high domain.

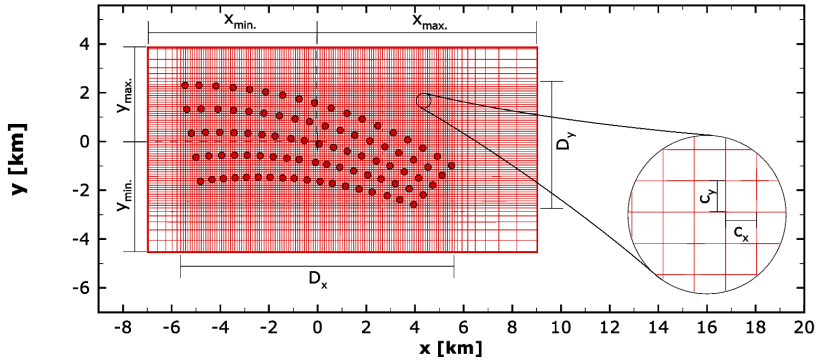

Figure 3.25: Horizontal projection the domain mesh covering Rødsand II, in local array-centred coordinates. Mesh not represented at full resolution.

3.3.3 Results

From the three inflow wind speeds indicated in the benchmark proposal, it was decided to reproduce the lower two using VENTOS®/2 runs. Simulation convergence and adequate SCADA binning was not possible on all inflow wind speed and sector combinations attempted. The overall listing of completed model runs and filtered SCADA cases is presented in Table 3.14.

E sectors	6 m/s		8 m/s		10 m/s	
	SCADA	Model	SCADA	Model	SCADA	Model
077° ±5°	✓		✓	✓	✓	
087° ±5°	✓	✓	✓	✓	✓	
097° ±5°		✓	✓	✓	✓	
107° ±5°		✓	✓	✓	✓	
117° ±5°		✓		✓		
W sectors	**5 m/s**		**7 m/s**		**9 m/s**	
	SCADA	Model	SCADA	Model	SCADA	Model
270° ±2.5°		✓	✓	✓	✓	
275° ±2.5°		✓	✓	✓	✓	
280° ±2.5°		✓	✓	✓	✓	
285° ±2.5°		✓	✓	✓	✓	
290° ±2.5°		✓	✓	✓	✓	

Table 3.14: Match-up between flow cases (wind speed and direction combinations) filtered from the SCADA dataset and simulated with the VENTOS®/2 wake model.

The mismatch between simulated and measured flows meant that not all cases planned could be explored. Still, there was a nearly complete match at one wind speed level for East (8 m/s) and West (7 m/s) sector inflows, meaning the WF wake effect (East versus West sector inflows) and the changes in Rødsand II operation with inflow direction (within each sector) could be studied on both SCADA and model under the same inflow conditions. This section is focused on the comparison between the two and the their agreement.

Wake model data at different inflow wind speeds was also compared by sector, but not

included here. Estimated free-stream velocity and WT power ratios – relative to those of the reference WT(s) – were found to be largely unchanged between simulated wind-speeds, apart from a small number of WTs operating near cut-in wind-speeds. This behaviour is as expected, given that the WT model presents a flat C_T curve (Figure 3.21) throughout the 4–9 m/s range, meaning extracted momentum is proportional to free-stream velocity.

3.3.3.1 Capturing the cluster wake effect in the model

Mappings of model estimations of WT operating conditions, in terms of equivalent free-stream velocity, are shown in Figure 3.26 for both Nysted and Rødsand II under all inflows in the Easterly sector. Comparing equivalent free-stream velocities (referred to inflow's wind speed) allows, in comparison to WT power or power deficit, a measure of individual WT efficiency over irrespective of differences in WT model power curves in the cluster.

The wake of Nysted wind farm is visible on all 5 cluster cases, with the Rødsand II WTs frontal to the inflow (column 18 and parts of rows I and M, depending on inflow sector) seeing reduced inflow wind speeds. This reduction was as high as 20%, as in the 87° inflow (Figure 3.26b). Inversely, at 107° and 117° inflow sectors (Figures 3.26d and 3.26e), the alignment is such that most of Rødsand II leading WTs operate in clear inflow and only a small wind speed reduction (circa 5%) in noticeable on the leading WTs of the I and J rows.

Flow alignment with Nysted rows seems to have a largely negligible effect on the free-stream velocity seen at Rødsand II's leading edge. On the 97° inflow case (Figure 3.26c), where free-stream velocities at Nysted drop by as much as 30%, the operating conditions at Rødsand II leading WTs are not noticeably different than other sectors where internal wakes at the upstream WF are less severe.

Being in partially waked inflow does however have an impact on the leading edge of Rødsand II: on the 77° inflow case (Figure 3.26a), free-stream velocities decrease between rows I and M, as the number of WTs directly upstream increases.

Downstream of Rødsand II's leading WTs, the Nysted wake effect rapidly fades under the impact of Rødsand II's inner WT scale wakes. In the cases where only part of the WF operates in waked inflow (most notably under 107°, in Figure 3.26d), after the first 5-7 columns of WTs the operating conditions seems mostly indistinguishable between waked and clear inflow conditions.

The power estimation consistency problems discussed in Section 3.2.2.3, although present do not appear to be significant in the Rødsand II WF, presumably masked by wake effects in the irregular layout. On the Nysted WF however they are more apparent, exhibiting oscillations in the 77° and 87° inflow cases (Figures 3.26a and 3.26b) between WTs of the same column.

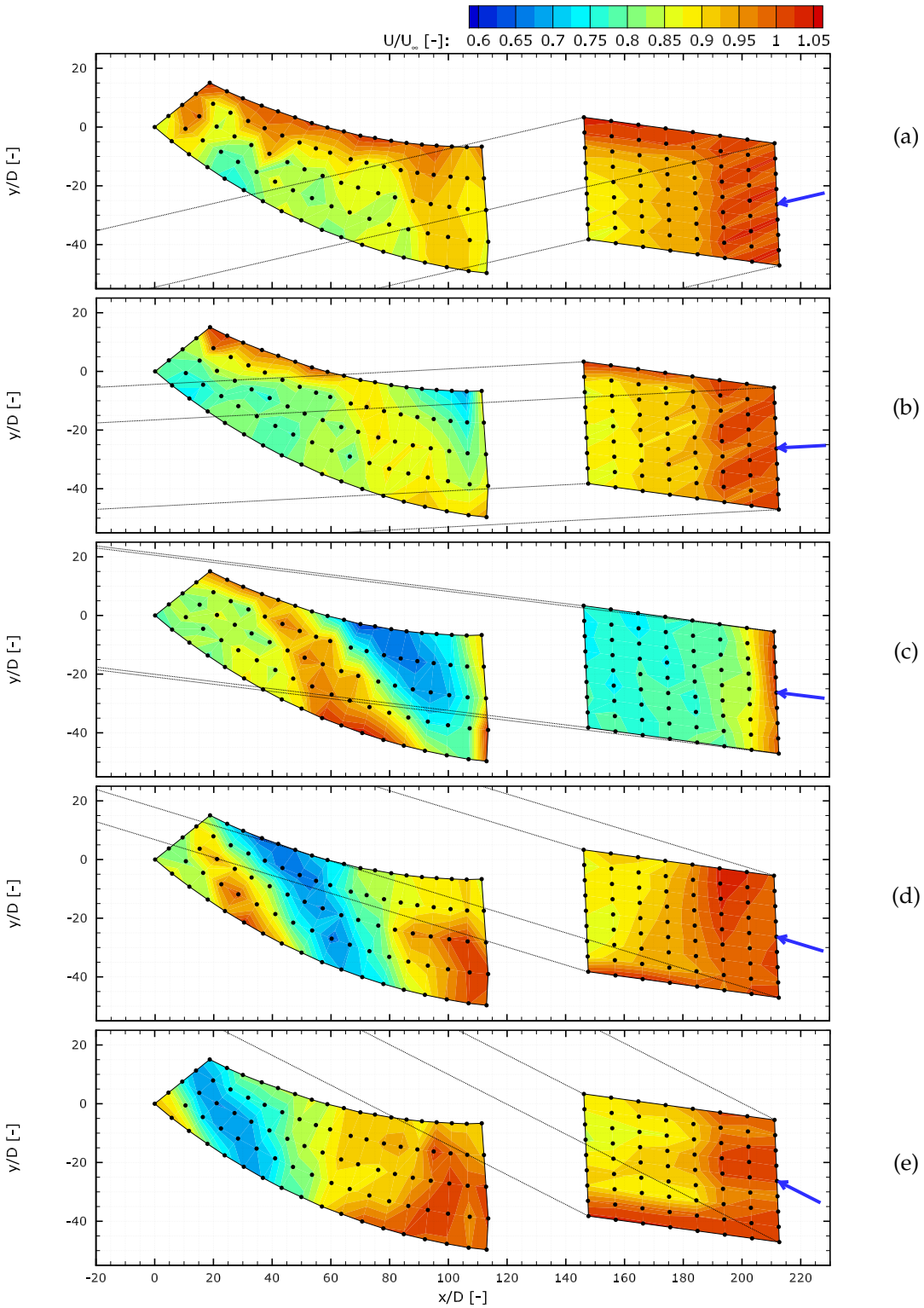

Figure 3.26: Dimensionless free-stream velocity over the Rødsand II and Nysted WF cluster for Easterly sector inflows: (**a**) 077°, (**b**) 087°, (**c**) 097°, (**d**) 107° and (**e**) 117°.

3.3.3.2 Power deficit mapping – clear inflow

The power deficit distribution over Rødsand II when operating under Westerly inflows (outside the Nysted wake's influence) is shown in Fig. 3.27, as measured in the SCADA data on the left hand side and as estimated via the wake model on the right.

The spatial distribution mapping is complemented by Fig. 3.28, where the measured and modelled power deficits for each row and inflow direction are plotted individually. Alongside is also plotted the alignment between inflow direction and local row orientation: internal wakes should be more significant (and power deficits greater) when flow direction matches row orientation.

Both SCADA and model power deficit distributions exhibit concentrated areas of degraded WT operating conditions, moving West along the WF as inflow direction increases (Figure 3.27a) through 3.27e). With no other relevant flow effects, individual WT wakes dominate WF operation, with peak power deficits occurring near flow is aligned with WT rows.

Analysing on a row-by-row basis, peak power deficit is consistently predicted by the model to occur earlier in in the WF than suggested by SCADA data. This is particularly evident in Figure 3.28 plots for 285°and 290°inflows, with peak deficit consistently occurring in the model profile first, nearly matching 0°alignment on all rows, and 3 to 4 WTs further downstream in the SCADA profile.

The individual row's power deficit profiles also indicate that until flow to row alignment reaches 0°, model predictions of power deficit agree well with the plotted SCADA profiles. This is evident in Figure 3.28 plots for all rows in inflows 270° and 275°, as well as the in the Southern-most rows K, L and M of the array under 280° inflow.

With the model predictions of peak power deficit being strongly correlated to row-aligned flow, there is even WT power recovery beyond the point of 0°alignment, as seen in model results on the Eastern end of the WF (Figures 3.27d and 3.27e). This effect is only slightly apparent on the SCADA data results, and largely limited to rows I and J and rows I, J and K under 285° and 290° inflows respectively (see Figure 3.28).

The over-estimated sensitivity to row-aligned flow is likely to be associated to the lack of representation of wind direction spread found in the SCADA bins. While simulations only capture the wake effect under one particular direction, the SCADA bins include a wide span of inflow conditions that smooth localized wake effects. The use of WT-sensor derived inflow reference data in a narrow sector width (5°) in the dataset further enhances this effect, with probable occurrence of incorrect record binning.

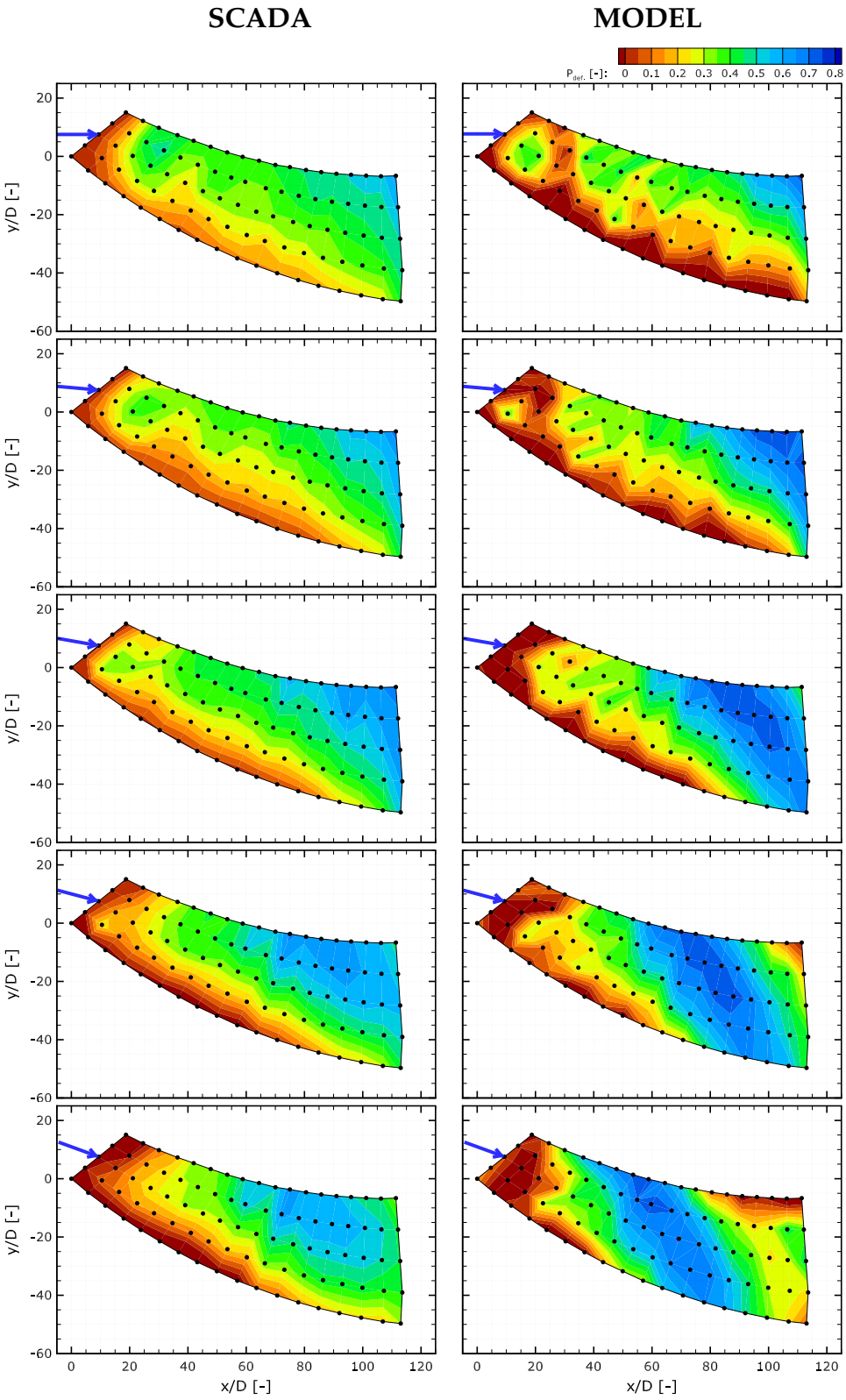

Figure 3.27: Power deficit distribution over the Rødsand II WF from SCADA data (left) and model results (right), for 7 m/s wind speed and Westerly sector inflows: (**a**) 270°, (**b**) 275°, (**c**) 280°, (**d**) 285° and (**e**) 290°.

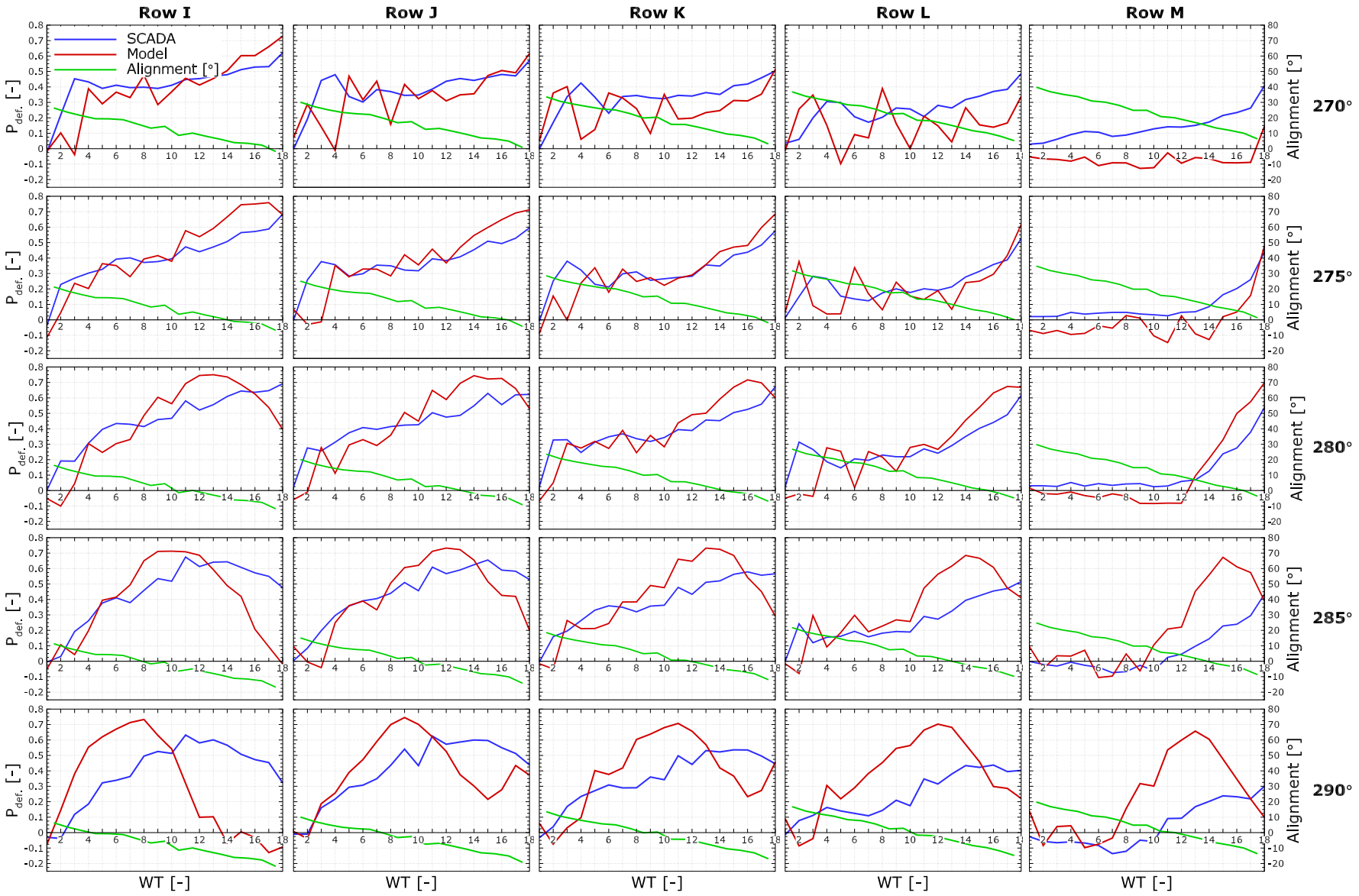

Figure 3.28: Power deficit profiles for SCADA and wake model results, combined with alignment between flow and row, for Western inflow sectors. Plots arranged vertically per sector (downwards from 270°to 290°) and horizontally per row (left to right from row I to M).

3.3.3.3 Power deficit mapping – waked inflow

Under Easterly inflows –and in the wake of Nysted– Rødsand II WF operating conditions are degraded. The power deficit distribution over the WF is shown in Fig. 3.29, as measured in the SCADA data on the left hand side and as estimated via the wake model on the right.

The spatial distribution mapping is complemented by Fig. 3.30, where the measured and modelled power deficits for each row and inflow direction are plotted individually. Alongside is plotted the alignment between inflow direction and local row orientation: internal wakes should be more significant (and power deficits greater) when flow direction matches row orientation.

On a preliminary analysis the SCADA results for the 77° inflow case (left hand side of Figure 3.29a) stand out, with a large portion of the array operating at zero or negative power deficits, contrasting with those of other inflow directions. To a lesser degree, a similar pattern can be seen in model results, with similar contour shapes.

However, the reference power level appears to be representative of other Easterly sector inflows, which suggest a biased reference. This could be associated to significantly different inflow conditions on the 77° case compared to other inflow sectors, to which upwind presence of the Danish shore could be relevant.

Focusing on the Rødsand II's leading edge WTs, the model predict well their performance under the influence of the Nysted wake effect. As the WF wake effect moves across them over the studied inflow range, agreement is best on the 87° and 97° inflow cases (WT18 of all rows for those sectors, in Figure 3.30), where the Nysted wake effect is largest on Rødsand II.

This WF wake impact is noticeable only on the very first part of the Rødsand II array, after which internal wakes fully dominate WF operation. This is evident in Figures 3.29a and 3.29d, where power deficit in parts of the array that are in clear, partially or fully waked inflow are similar after 3-4 columns.

The regions with strongest power deficits are well predicted by the model, in both peak value and in position within the array (Figures 3.29a through 3.29d). Unlike what occurred under clear inflows, peak power deficit on both SCADA and Model result plots is strongly correlated with row-aligned flow (Figure 3.30).

There is a wide gap between rows at the Eastern edge of the Rødsand II layout, between which inflow is able to pass mostly undisturbed and hit inner parts of the array, making some WTs in the central part of the WF operate in partly clear inflow. This effect is noticeable in parts of the Southernmost rows L and M, for the 87°, 97°and, to a lesser extent, 107°(left hand side of Figures 3.29b, 3.29c and 3.29d respectively). The same pattern is also found in the model results, although when that occurs power deficits are considerably lower and extend over a larger part of the array. The span of inflow direction included in each 10°-wide bin is considerable, smoothing out localized extreme wake effects and possibly explaining this difference between SCADA and model results.

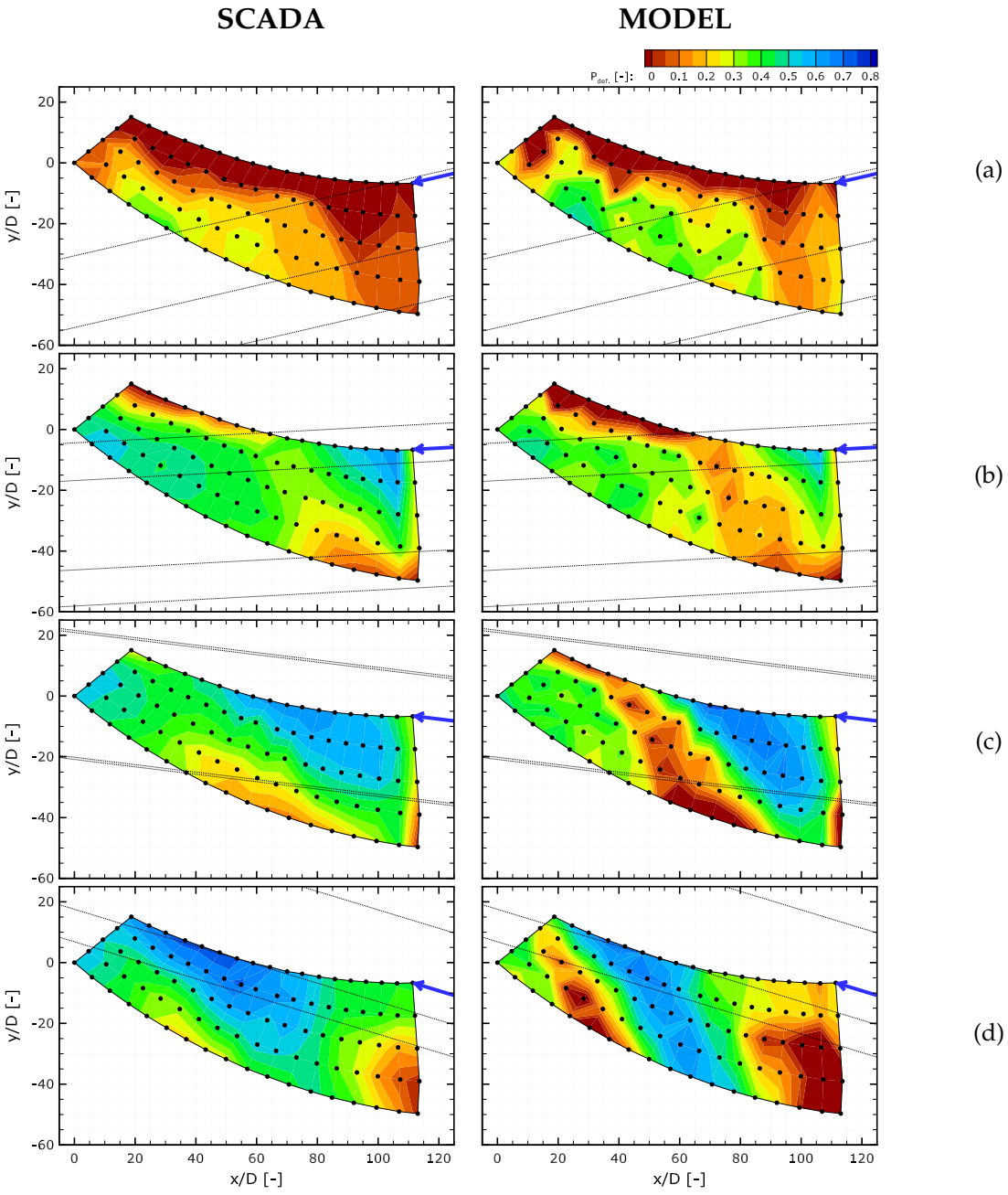

Figure 3.29: Power deficit distribution over the Rødsand II WF from SCADA data (left) and model results (right), for 8 m/s wind speed and Easterly sector inflows: (**a**) 77°, (**b**) 87°, (**c**) 97° and (**d**) 107°.

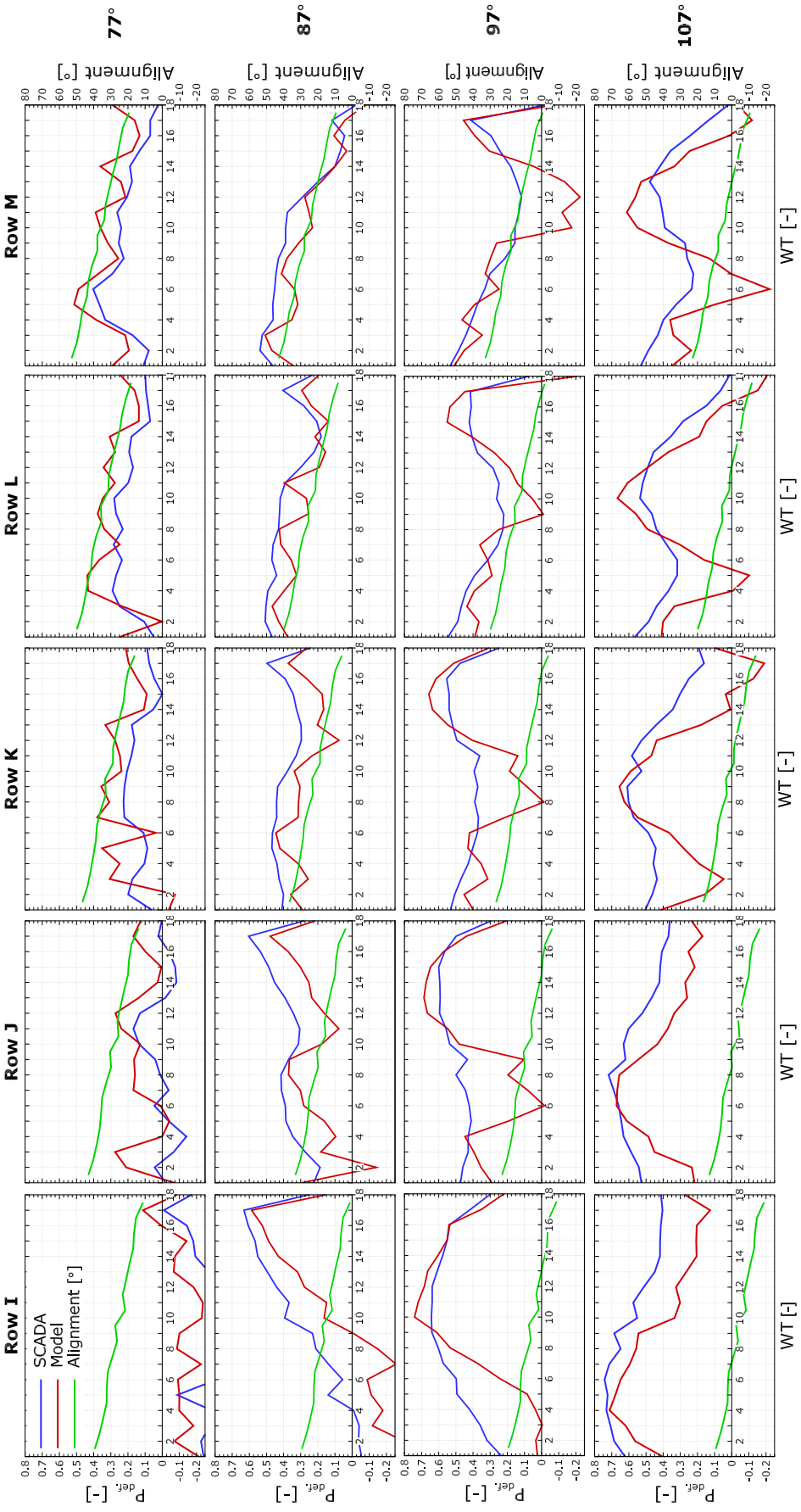

Figure 3.30: Power deficit profiles for SCADA and wake model results, combined with alignment between flow and row, for Eastern inflow sectors. Plots arranged vertically per sector (downwards from 77° to 107°) and horizontally per row (left to right from row I to M).

3.3.3.4 Wind farm efficiency

Due to nearby presence of the Nysted WF, Rødsand II's overall performance will differ significantly under Easterly and Westerly, difference which reflects on the wake model estimations of WF power. The comparison between model predictions and SCADA aggregate values of Rødsand II's overall efficiency comparison is presented in Fig.3.31 for each inflow, grouped into Eastern (clear inflow) and Western (in Nysted's wake) sectors.

The WF's efficiency is calculated by comparing the array's average WT power to the reference power level (see Table 3.11 for East and West sector references), assumed to be representative of maximum WT power under the reigning inflow conditions.

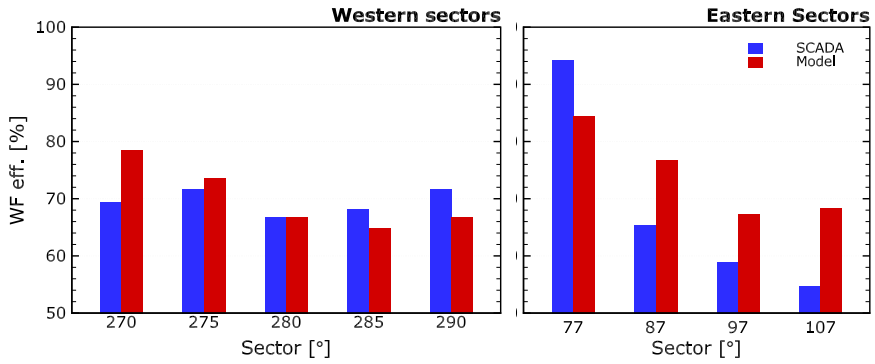

Figure 3.31: Rødsand II overall WF efficiency, as calculated from SCADA data and model results, per Western (left) and Eastern (right) inflow sector.

Under Westerly sector inflows, the model predictions are close (mostly within $\pm 5\%$) to the SCADA ensemble results. The localized under and over estimations seen in Section 3.3.3.2 cancel out, resulting in a reasonable overall agreement. However, the trend and dispersion found throughout the inflow range in the SCADA data in not matched by model results: measurements indicate efficiency oscillating in the 65% to 70% range, whereas model predicts a continuous decrease (from nearly 80% to 65%) with inflow angle.

Power deficits for the 77° inflow case were seen in Section 3.3.3.3 to be low, particularly in SCADA measurements, suspected to be due to a biased reference power level. The SCADA array efficiency values reiterate this, being nearly 20-30% greater than in any other sector. For this reason the 77° SCADA case was ignored in this comparison.

There is a clear impact (in the Eastern sector cases) of the Nysted wake on Rødsand II WF efficiency, with SCADA data exhibiting a decrease of as much as 15% (for 107° inflow) compared to the average efficiency under the clear inflow of Westerly flows. Model predictions however over-estimate their respective measured values by a margin of 10% or more, even predicting WF efficiency comparable or greater than that seen in clear inflow.

3.3.4 Conclusions

In general, the WF wake effect is well captured by the model predictions, with Rødsand II's leading WTs noticeably affected by lower energy inflow in Easterly sector flows (Section 3.3.3.1). Model and SCADA data agree that the impact of the Nysted on Rødsand II is concentrated on the first 4 columns of the array (Section3.3.3.3), and that beyond that point the WF wake effect has largely diluted into the WF's internal wakes.

The curved row layout (Section 3.3.1) means that maximum power deficits tend to occur in areas where row alignment matches flow direction. This is the case for both clear and, after the Nysted wake effect of the leading columns has faded, waked inflow sectors. The model consistently predicts peak power deficits coinciding with row-aligned flow, which is not always in agreement with SCADA data averages: there is a good match for the waked inflow sectors in both peak value and its location in the array (Section 3.3.3.3), but the same does not occur under clear inflows, with predicted maximum deficits being too high and occurring too early in length of the WF (Section 3.3.3.2).

A better prediction of peak internal wake effects on Easterly inflows occurs in spite of a growth in SCADA bin sector width relative to the opposite sector (Table 3.14, in Section 3.3.3), which should tend to smooth out such localized effects. The reasons for this are not clear, and could be associated to the inflow resulting of the upstream Nysted WF, as the added ambient turbulence could contribute to a mixing boundary layer that better matches the simulated conditions.

The measured Rødsand II efficiency under the clear Westerly inflows dwells at circa 70%, matched by model results within a margin of $\pm 5\%$ (Section 3.3.3.4). However, under the waked inflows of the Eastern sector WF efficiency is consistently over-estimated (10% gap) by the model, even failing to predict the loss in WF efficiency due to the WF wake effect that SCADA data evidences. This is caused by the Rødsand II layout asymmetry: Westerly sector inflows find a dense leading array edge, whereas for Easterly cases it takes the form of 5 widely spaced rows between which inflow can pass undisturbed. This characteristic layout results in low power deficits on WTs deep into the WF under Easterly inflow, effect that is much stronger in the model results than in SCADA data (Section 3.3.3.3), possibly due to smoothing over the wind direction bin.

3.4 Conclusion

The prediction of large off-shore WT array performance was acceptable, generally being able to capture how wakes combine and what effect that has on operating conditions of individual WTs. This was the case over short distances, i.e. the wake effects internal to the WF (Section 3.2), as well as over the long distances that separate WFs in a cluster (Section 3.3), particularly at the leading WTs of the waked WF.

Because wake effects are maximized when flow direction matches WT alignment (Section 3.2.3.1), agreement between model results and SCADA data averages proved sensitive to the representation of wind direction in the comparison (Section 3.1.5). Although the general behaviour of power loss in waked WTs is captured (Section 3.2.3.3), peak power deficits (Sections 3.2.3.1 or 3.2.3.2) and where they occur in the array (Section 3.3.3.2) are harder to predict.

By ensembling multiple simulations (Section 3.2.2), the model was able to reproduce the range of inflow direction included in each SCADA bin and better match the SCADA power deficits over rows of WTs. This was most effective for wide sector widths (Section 3.2.3.1), as the ensemble sample size is increased (reducing sensitivity to extreme wake effects) and the impact of inflow reference data uncertainty (Section 3.1.4) is lessened.

The WF efficiency value aggregates the impact of all wake losses in WF, and thus many power estimation errors tend to cancel out. This was not the case for inflows capturing specific extreme array effects, particularly for narrow wind sectors and for lower quality inflow reference data. For example, clear inflow capturing flow along a row of WTs lead to the model under-estimating WF efficiency by 10% or more, depending on the reference wind direction data uncertainty (Section 3.2.3.5). By comparison, in another array less prone to such extreme wake effects and under similar inflow, model prediction was more in line with measurements (Sections 3.3.3.2 and 3.3.3.4).

The long distance wake effect of an upstream WF was concentrated on the first four columns of WTs on the leading edge of the WF, and the respective power losses well predicted by the model (Section 3.3.3.2). From thereon, the WF's internal wake effects are dominant and WF operation becomes equally prone to specific array effects as when in clear inflow, to the point where these can overpower the cluster effect and fail to predict any degradation of WT performance (Section 3.3.3.4).

Chapter 4

Improving the wind turbine wake model

Limitations on the base model were identified under comparison with linear model results and with WF operational data. Among these were errors in the estimation of free-stream velocity U_∞ and WT power P_{AS}, as well as prediction of flow velocity in the near-wake and wake recovery rate.
In this chapter, changes to the wake model formulation are tested, addressing some of the flaws identified. The first modification tested concerns the rotor discretization, made ensure a smooth AD area distribution and velocity field in the WT's vicinity. Secondly, the way the solution is polled for a disk velocity approximation the AD velocity U_d is changed to make the AD adequately sensitive to non homogeneous inflow. On a third section, the load distribution over the AD area is modified to better approximate the rotor description to its real life counterpart. Finally a simulation coupling technique is presented, allowing the long range wake effects of WFs to be modelled in complex cluster cases at a reduced computational cost.

4.1 WT performance consistency

The WT thrust force discretization method (described in Section 2.5) is robust, but was found to introduce oscillations in individual WT power estimations. One case where these were evident was in the conditions described in Section 3.2.2.3, where power estimation along Horns Rev's leading row of WTs was uneven and responded inconsistently to changes in inflow direction, despite being in homogeneous inflow. The use of row-average and direction bin-average in many Horns Rev test cases (Section 3.2.1) means the impact on power deficit results is minimal. Conversely, in cases where ensemble size is small, due to having no row (Sections 3.2.3.3 and 3.2.3.4) nor wind direction bin averaging (Section 3.3), the nefarious effects of inconsistent power estimation either on the target or reference WT is not negligible.

This results of the inability of the collocated grid strategy to handle discrete body forces, as demonstrated by Réthoré (2009). The sinks introduced by the WT model in the

momentum equation lead to a sudden jump in the pressure-correction solution, as a consequence of mass conservation. Depending on the AD's position within the domain mesh, a sudden change in pressure gradient in the vicinity of the AD can mean that artificial negative pressure gradient terms contribute to the momentum equation, and wiggles in velocity solution can appear.

To overcome this, the two-step discretization method was adapted to first distribute body force terms to the CV faces, and only then split those between adjacent CV centers. The body force distribution is smoothed, avoiding edge cases where discrete counter-stream WT forces appear and largely eliminating the conditions for wiggles to appear in the pressure-correction solution. This reflects positively in the WT performance estimates, as the velocity field at the AD becomes less dependent on the AD's position within the domain mesh.

4.1.1 Sensitivity to mesh placement

Section 3.2.2.3 highlighted how the Horns Rev front column demonstrated strong variation in WT performance both between simulations and between WTs in each simulation. On one particular inflow direction the front column power distribution produced a saw-like profile (where neighbouring WTs have power estimations that differ by 15% or more). The relative power throughout the column for that inflow direction –285°– is plotted in Figure 3.10, where it contrasts with another –265°– where power was near-constant.

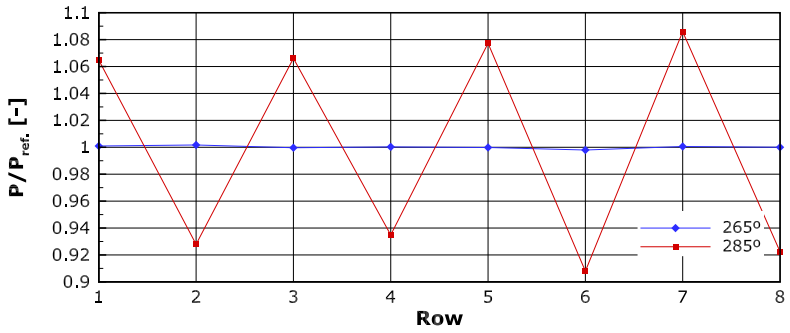

Figure 4.1: Power deficit distribution across the leading column of WTs of the Horns Rev WF for 265° and 285°sector inflows.

Figure 4.2 shows both the AD positions of four Horns Rev WTs (belonging to the leading column) and the domain mesh grid-lines (connecting CV centers along each mesh direction) for the two same inflow directions, 285 °on the left and 265 °on the right. While for 265°inflow all four WTs are placed at CV faces (midway between CV centers), for the 285°direction their placement alternates between CV face and CV center. The velocity field oscillations are noticeable on the two WTs placed at CV centers in the 285°inflow contour map. This alternating pattern is repeated throughout the column, resulting in the power estimation distribution shown in Figure 4.1 and making the dependency of power estimation on AD placement evident.

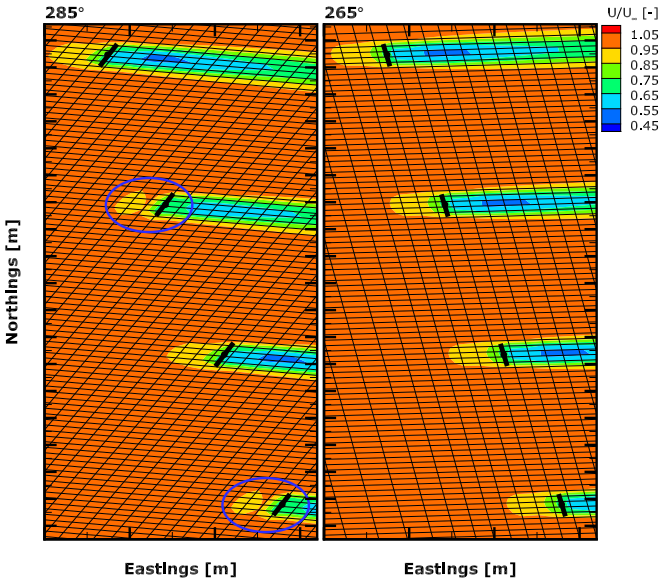

Figure 4.2: Leading column WT positions (dark dashes) relative to the domain mesh on the on the Horn Rev WF array, for the inflow directions 285°(left) and 265°(right). Velocity oscillations highlighted by the blue line under the 285°sector.

4.1.2 Velocity oscillations at the actuator disk

When placing the AD and distributing its force terms over the computational mesh, the tri-linear interpolation-based distribution will accumulate fractions of the overall WT thrust on the nearest neighbouring CVs to the virtual rotor cell's center. Depending on the position of the AD, one or more of the coefficients responsible for distributing from virtual rotor to domain mesh will reduce to 1 or 0. Since the WTs will tend to be oriented towards the domain inlet, the AD will frequently be aligned with the mesh and, on the worst case scenario, concentrate its body force terms on a single i-plane of CVs, creating a discrete jump in body force in the x-momentum equation.

Two differently positioned ADs were modeled in otherwise matching simulation setups: one was placed on a plane coinciding with CV centers, and another on a plane coinciding with CV faces (midway between CV centers). The resulting force density and pressure solutions are plotted in the top half of Figure 4.3, and the corresponding velocity field in the bottom half of the figure. These two cases represent the two extremes of the body force distribution span, with a discrete body force jump concentrated on a single cell or split evenly between consecutive cells, as was captured in the 285° inflow case shown in Figure 4.2.

When the AD coincides with the CV centers a discrete force density jump is produced, and through momentum conservation a sharp pressure jump is materialized around cell P. With the collocated grid approach and the Rhie-Chow correction (Rhie and Chow, 1983), the pressure gradient is constant between cells E and W and the driving force $(p_E - p_W)\,A$ captures the correct pressure gradient. However, at the neighbouring cell E (and similarly at cell W), the effective pressure pressure forces $(p_{EE} - p_P)\,A$ are not representative of the pressure gradient on either side of the CV, ignoring the pressure

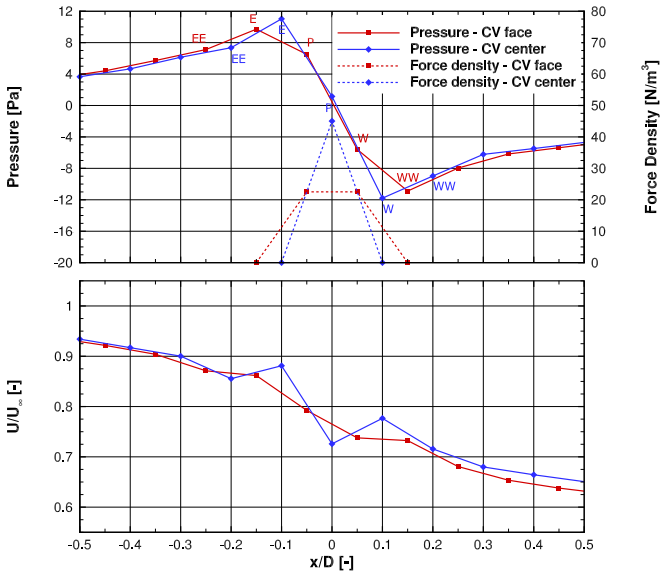

Figure 4.3: Streamwise velocity (below) and the driving forces behind it, pressure and WT force density (above), in the vicinity of a mesh aligned AD. Two rotor positions plotted, one coincident with a CV centre plane (turquoise) and another with CV faces (red).

peak at E. This way the oscillating pressure field is a valid solution, despite the Rhie-Chow correction, introduced to avoid issues of this very nature. This inability to handle discrete body forces is explained in extensive detail in Chapter 2 of Réthoré (2009). More importantly than the pressure solution, the net effect of the oscillations is pressure induced flow acceleration immediately fore and aft of the AD, and an unphysical oscillating velocity field.

The AD coinciding with the CV faces (midway between cell centers) distributes the force density over two consecutive CVs, and the consequent pressure jump gradually occurs between cell E and WW. Unlike previously, the pressure forces $(p_E - p_W)\,A$ acting on cell P suggest a pressure gradient that under-estimates the actual pressure gradient at the AD ($X/D = 0$), leaving a pressure hike (in cell P) that does not contribute to the momentum equation. A similar error occurs in the momentum equation terms of cell W. However, on the cells immediately fore and aft of the ones with non-zero force density, the oscillation in the pressure solution – cells EE, E and P – are much milder than before, and result in a negligible effect on the velocity field, with no numerically induced accelerations near the AD and a near-constant velocity gradient.

The velocities two or more cells up/downstream of the AD are not affected by its positions within the domain mesh. However, within that close proximity the solution that yields the more consistent velocity gradient is preferable: the oscillating solution results in lower velocities at the AD, which naturally is reflected in the disk velocity U_d approximation and on the thrust estimation algorithm.

4.1.3 Discretizing forces at control volume faces

To ensuring that the solution in the vicinity of the AD is free of velocity oscillations the emergence of discrete body forces has to be avoided. This was achieved by distributing force density in the stream-wise direction, in such a way that the wake model is not impeded from freely positioning WTs inside the domain, nor individual WTs from rotating towards the inflow during wind direction changes.

The approach used in Réthoré (2009) (and later improved in Troldborg et al., 2015) aims to achieve similar goals, and does so by modeling the effect of the WT on the flow not as a body force (distributed action over the whole CV) by as a surface force, acting on CV faces and added to the momentum equation via Rhie-Chow correction. The method used here is similar in that the key is to distribute the WT forces to the CV faces, but does so while conserving the body-force approach. Only the second step of the discretization method covered in Section 2.5 – where the contributions of each virtual rotor cell c are distributed over the domain – is changed: rotor cell force terms are distributed to the CV faces (their centroid position) instead of CV centers, using trilinear interpolation factors $\zeta_{i,j,k}$. The final accumulated forces (in each direction) are split evenly between the CVs they divide. For CV faces $f = (e, w, n, s, t, b)$, the AD area density $\widetilde{s_n}$ at each domain cell becomes the sum of half of each face's accumulated virtual rotor area:

$$\widetilde{s_n} = \frac{1}{2\int \mathrm{d}\Omega} \sum_c \sum_f \zeta_i \zeta_j \zeta_k f_n \delta A_d \tag{4.1}$$

The contributions of every virtual rotor cell are distributed over a minimum of two CVs in each direction, similarly to the Gaussian smoothing approach used by Mikkelsen (2003). The modified force distribution method defaults to the previous method when the AD coincides with the CV face plane, but otherwise smooths out the WT thrust terms, namely in the WT-normal direction. With this smoothing comes the drawback of less precisely defined AD shape, particularly in the case of coarser meshes.

4.1.4 Results

The impact this modification has on pressure and velocity in the vicinity of the AD (in Figure 4.4) is considerable, regardless of the WT's position relative to the CV's central plane.

As the pressure jump (top half of Figure 4.4) is increasingly distributed in the stream-wise direction, by action of the modified discretization method, the maximum pressure difference between consecutive cells decreases and with it the potential errors associated to the pressure gradient. The velocity oscillations (in the bottom half) are practically eliminated, leading to a nearly constant velocity gradient in the upstream and downstream vicinity of the AD regardless of the WT's position relative to the mesh.

The WT thrust estimation algorithm benefits from the modifications to the force term distribution, through the improved consistency in velocity values at the AD ($x/D = 0$ in Figure 4.4). By stabilizing the velocity field at AD and at the hub position in particular, the uncertainty of the U_d approximation decreases, reflecting on the U_∞ and

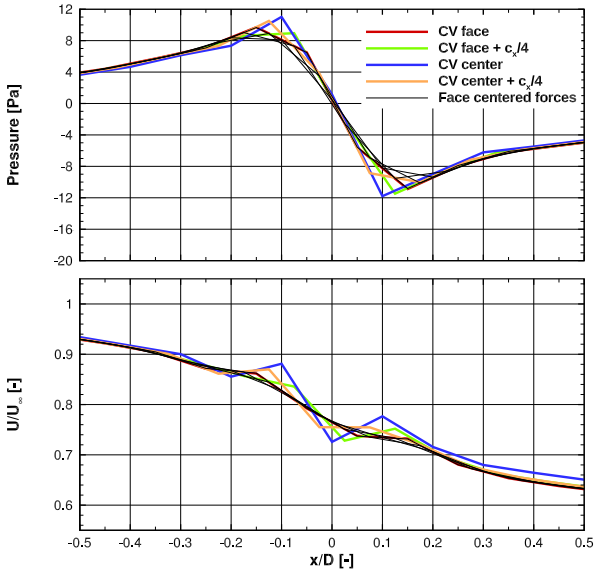

Figure 4.4: Pressure and streamwise velocity in the vicinity of a mesh aligned AD, using the standard force distribution (coloured lines) and face-centred forces (black lines). WT rotor longitudinal position includes the CV faces plane, CV centre plane and midway planes between them.

AD placement	Standard method		Face-centred forces	
	U_∞ [m/s]	P_{AS} [kW]	U_∞ [m/s]	P_{AS} [kW]
CV face	8.13	616.9	8.13	624.3
CV face + $c_x/4$	8.05	601.8	8.13	629.5
CV center	7.83	560.4	8.13	630.8
CV center + $c_x/4$	8.05	601.8	8.15	630.4

Table 4.1: WT performance estimation (free-stream velocity U_∞ and Power P_{AS}) for a mesh aligned AD using the standard force distribution and face-centered forces. WT rotor longitudinal position includes the CV faces plane, CV centre plane and midway planes between them.

C_T estimates. Whereas the U_∞ values estimated using the standard force distribution oscillated between 7.83 and 8.13 m/s (Table 4.1) depending on the WT's position within the CV, those resulting of the face-centred forces were consistently at the later value. The impact on the velocity field extends to the whole AD span, so the WT power estimate sees improvements via both U_∞ estimate and local velocities, also stabilizing at values close to $\sim$ 630 kW.

The changes to the force distribution are focused on eliminating velocity wiggles in the AD vicinity, but their impact also extends to the near wake. This is evident in the stream-wise velocity and turbulent kinetic energy profiles (Figure 4.5). When the AD is placed at CV center plane, peak velocity deficit was reduced, even if that difference has disappeared after 5D downstream in the wake. This contrasts with all other cases, neither of which produce discrete body force distributions.

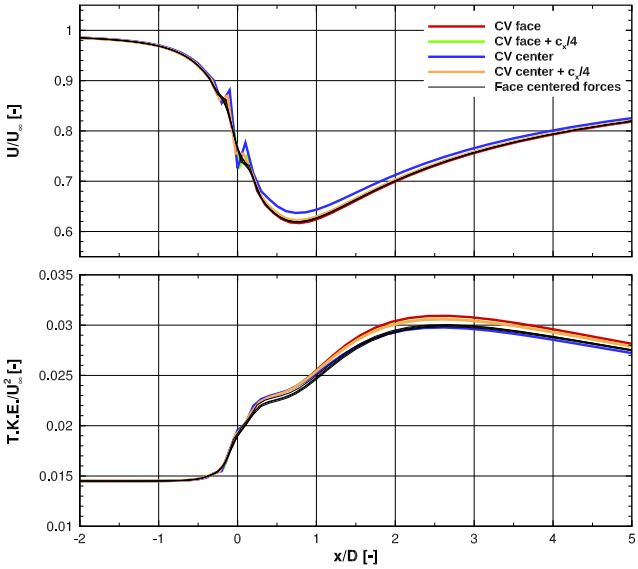

Figure 4.5: Streamwise velocity and turbulent kinetic energy along the axis line a mesh aligned AD, using the standard force distribution (coloured lines) and face-centred forces (black lines). WT rotor longitudinal position includes the CV faces plane, CV centre plane and midway planes between them.

Turbulent kinetic energy profile (in the bottom half of Figure 4.5) was also affected by the discretization method, to a lighter degree. Although sensitivity to the WT placement was small with the standard method, it was nearly eliminated by the modification to the force distribution.

4.1.5 Conclusion

The standard WT force distribution method could create, depending on the WT's position relative to the mesh CVs, a body force distribution where all terms are concentrated in a single plane of CVs. Despite the use of the Rhie-Chow correction for the collocated grid, the existence of discrete body forces means oscillations in the pressure field are ignored by the momentum equation and wiggles in the velocity field can appear.

The oscillations in the velocity solution meant that any interpolation in that region is prone to errors. Because the WT thrust estimation algorithm relies on an approximation to U_d, polled from the solution at the hub position, it too is affected by the existence of discrete body forces. This has an impact not only on WT thrust and power estimations, but also on the velocity and turbulence wake fields.

The proposed modifications largely isolates the flow solution from WT placement, by changing the target of the AD discretization process: virtual rotor cell contributions are extrapolated to CV faces instead of CV centers, and only the consolidated result is split to CV centers to create the corresponding body forces. This ensures that no AD force term is ever concentrated exclusively in one CV, being split into at least two CV's in each direction.

The velocity oscillations are suppressed with the modification to the force distribution, leaving a smoothed pressure jump and a velocity field near the AD that is independent of the relative WT position. Interpolations to approximate U_d benefit from the change, improving WT performance estimation and the consistency of wake flow predictions.

The main driving cause behind the modification was the model's predictions for Horns Rev WF front row behaviour: WT performance in homogeneous inflow was prone to high errors in a specific wind direction (Section 3.2.2.3). The same case was repeated using the modified AD discretization method, with the WT power estimation results compared in Figure 4.6. In the worst-case scenario, where WTs alternated between CV-face and CV-center alignment, maximum deviation from the average power level reduced from over 8% to than 2%.

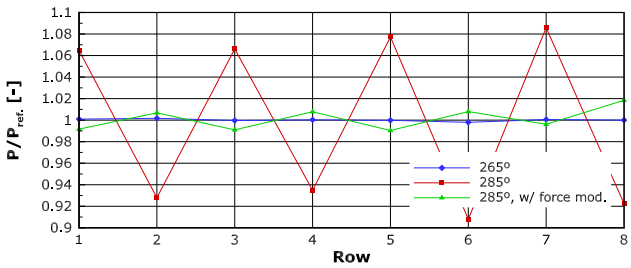

Figure 4.6: Power deficit distribution across the leading column of WTs of the Horns Rev WF for 285°sector inflow, using the standard force distribution and face-centred forces.

4.2 Disk velocity approximation

According to IEC standards on WT performance measurement (IEC, 2005), the undisturbed inflow velocity at hub height is sufficient for characterization of inflow conditions. This is based on the assumption that inflow is laterally homogeneous, and that vertical profile gradient is nearly constant, which means that the velocity at that height is representative of average wind speed hitting the rotor.

The WT thrust estimation algorithm (Section 2.6) also reflects this, assuming that the velocity interpolated at the WT hub position is a good approximation to the AD velocity U_d, despite the momentum deficit the AD imposes on the flow when compared to free-stream conditions.

However the inflow conditions are often not ideal, in cases such as in complex terrain or in the wake of upstream WTs. Because the operating rotor load depends on the overall momentum flux crossing the rotor span, the velocity at any single position may be a bad approximation to the average velocity over the AD.

To reduce U_d approximation error under non homogeneous inflow, it is calculated by averaging rotor-normal velocity at the AD. The impact of the different U_d approximation on the thrust estimation algorithm should be reduced in both clear inflow, but considerable in the wake of an upstream WT.

4.2.1 Inflow non-homogeneity

The assumption that velocity at hub height is representative of momentum distribution over the rotor span area will introduce error, as even in clear inflow the proximity to the ground implies a non-constant vertical gradient. Wagner et al. (2011) sees improved power coefficient C_P estimations by taking into consideration the vertical wind speed distribution, particularly in non power-law inflow profiles.

It is evident that errors will occur when polling the solution for U_d. Whenever complex flow conditions are prevalent, particularly in the case of WTs operating in waked inflow (such as those in Chapter 3), velocities at the hub position are susceptible to U_d misrepresentation. Since peak velocity deficits are found at the center of the wake, using individual or narrow sector simulation ensembles for flows aligned with WT rows amplify the issue, resulting in over-estimated power deficits.

4.2.2 Velocity profile at the actuator disk

The method to approximate U_d should be inflow independent, performing equally in simple and complex inflow conditions. However, the hub position will provide be a worse approximation the U_d the further inflow is to homogeneity, moving way from the conditions idealized by one-dimensional momentum theory. Additionally, the WT thrust effect will have a strong impact on velocities at the AD, possibly interfering with the U_d approximation and the performance of the thrust estimation algorithm.

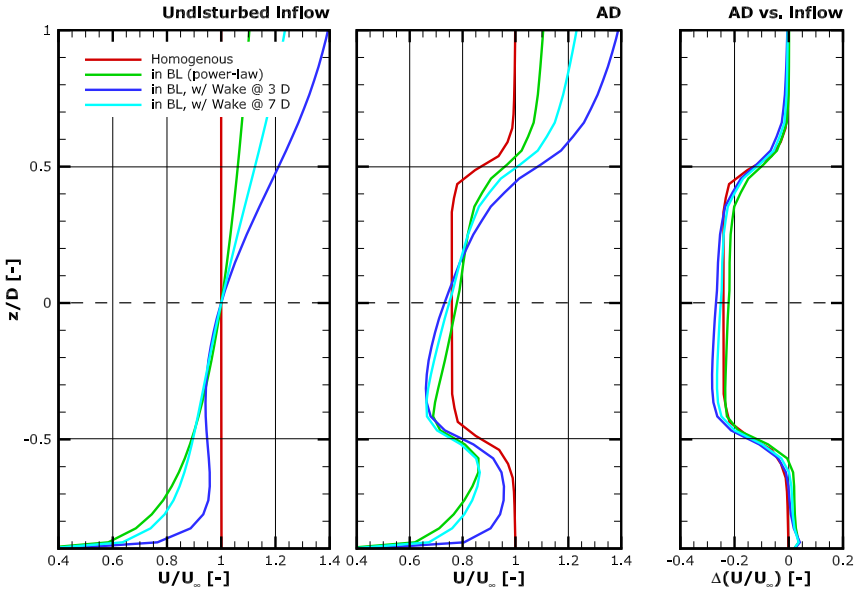

Figure 4.7: Dimensionless velocity profile undisturbed (left) and in the presence (middle) of the AD, under inflow conditions of varying complexity. To the right is the corresponding velocity deficit brought by the addition of the AD.

In Figure 4.7 the dimensionless velocity profile at an AD is plotted for various inflow conditions, along with the corresponding undisturbed inflow velocity profile and the resulting velocity deficit. Flow conditions and the WT model's C_T were kept the same for all cases.

The velocity deficit profiles are very similar in shape, with a 0.2-0.3U_∞ deficit in the inner 80% of the AD span, transitioning to free-stream flow at the AD edge shear layer. The velocity deficit profile is not significantly affected by inflow conditions, all being with a 0.05U_∞ range throughout the AD span. less.

The undisturbed velocity profile's shape changes considerably within the rotor span: from no shear (homogeneous flow) to near-constant shear (power-law) to shear increasing with height (at 3D downstream of another WT). Since the velocity deficit imposed by the AD is independent from the inflow conditions, the complexity of the undisturbed inflow conditions is not altered by the presence of the AD. The shear layer that AD introduces causes an increase in velocity near the AD's edges, which will reflect on the average velocity within the AD.

4.2.3 Weighted average disk velocity approximation

To calculate the average AD-normal velocity, the AD area density $\widetilde{s_n}$ distribution is used as a weighting factor in to average the velocity field over the discretized AD (equation 4.2). Because it results from the virtual rotor mesh extrapolation (see Section 2.5.1), doing so is equivalent to calculating the average velocity field on the virtual rotor mesh. The static AD area density distribution makes this process cost-effective when multiple

WTs are involved.

$$U_d = \frac{\sum \widetilde{s_n} \mathbf{u} \cdot \mathbf{n_{AD}}}{A_d} \tag{4.2}$$

The weighting factor incorporates the rotor load distribution f_n, meaning that when non-uniform load distributions are in place, the high-load areas of the rotor will provide larger contributions to the averaged U_d.

4.2.4 Impact on clear inflow

In clear inflow conditions, with near constant shear at the rotor span (Section 4.2.2), the velocity at the hub position should be a good approximation to the average velocity inside the rotor span, and the U_∞ estimation should not be significantly affected by the U_d approximation.

The U_∞ estimation resulting of hub position and AD averaged U_d values are compared for two WT models in Figure 4.8, similarly to what was done in Section 2.6.4. The comparison is presented in the form of the U_∞ estimation error ε_{U_∞}, assessed by application of the same method (interpolation at hub position or AD averaging) to the velocity field in undisturbed flow and at the AD.

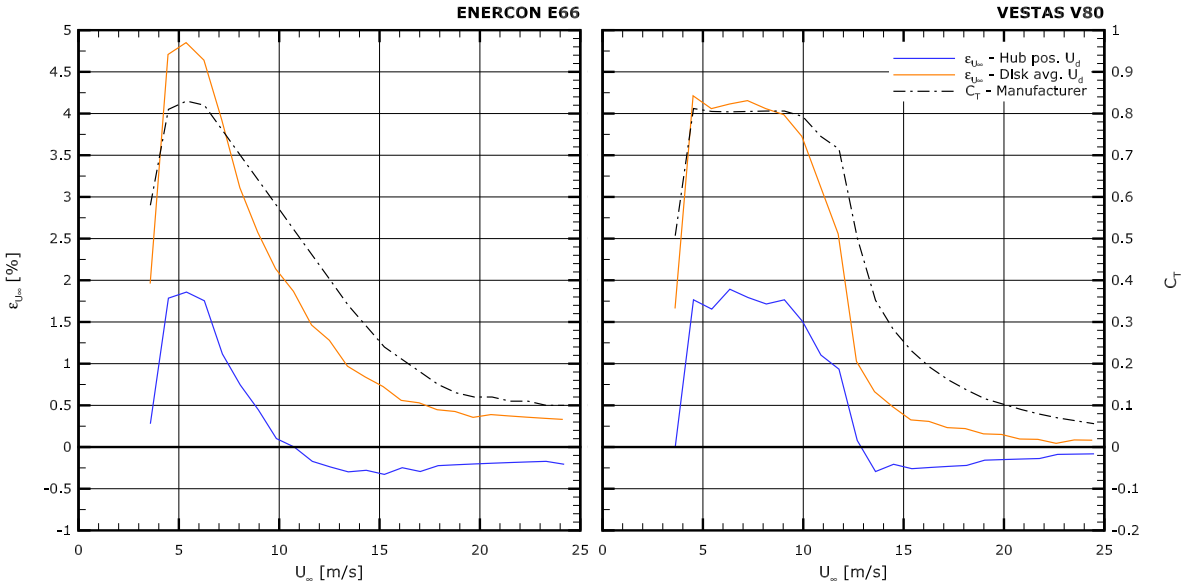

Figure 4.8: Relative error of U^*_∞ estimate using hub and disk average U_d approximation methods, over the operating ranges of ENERCON E66 (left) and VESTAS V80 (right) WTs.

The change to an AD averaged U_d approximation increases estimation error levels. Peak errors are more than doubled for either WT model, reaching levels of 4-5%. The estimation error pattern however does not change, remaining correlated to C_T curves and decreasing to near zero levels as wind speeds increase.

By averaging over the AD, the high velocities at rotor span edges (see Figure 4.7) promote an increase in U_d values compared to the that interpolated at the hub position. This reflects in the thrust estimation algorithm with higher U_∞^* values regardless of the WT model in question. As inflow wind speed increases, the relative impact of the AD on the local velocity decreases and the rotor edge effect is lessened, so either U_d approximation method results in similar error levels.

4.2.5 Impact on waked inflow

The velocity field at an AD will be increasingly distorted by proximity to the upwind WT (Section 4.2.4) and by the alignment between flow direction and WT row: the maximum velocity deficit is found at the wake's centreline, from where it transitions into free-stream at the limit of the wake's width.

The velocity at the hub position is sensitive to both WT spacing and flow alignment, with U_d approximation error increasing the with the inhomogeneity of the velocity distribution in the AD. Approximating the disk velocity to the AD area averaged velocity should mean that U_d value is less responsive to localized changes in velocity, and that errors induced by complex inflow conditions are lower.

A pair of neighbouring WTs aligned with the inflow sector were modelled, and the free-stream velocity estimates for the downstream WT studied. Both WTs were VESTAS V80 models (see Figure 4.8), and wind speeds at both were within the 5-10 m/s region of the operating range, where C_T is constant.

In Figure 4.9 the U_∞ estimation error (using either U_d approximations) is compared for WTs separated by 3D and 7D, with the downstream WT transitioning between clear and fully waked inflow conditions. The estimation error ε_{U_∞} is assessed application of the same polling method (interpolation at hub position or AD averaging) to the undisturbed velocity fields at the waked WT's position (see Figure 4.7).

The oscillations visible in all U_∞ estimation error curves of Figure 4.9 are not realistic, and are clearly connected to the mesh position dependency issues covered in Section 4.1: as the inflow direction changes, so does the downstream WT's position within the mesh, with the discussed consequences to U_∞ estimation. Despite these issues, the AD-averaged U_d lead to higher overall U_∞ estimation errors, matching what was seen under clear inflow conditions (Section 4.2.4). It is also possible to observe that error is more consistent throughout the sector with the AD average U_d, whereas interpolating at the hub position resulted in errors worsening as operating conditions degraded, as in the case tighter WT spacings and proximity to the wake's centreline.

Using U_∞ estimates to calculate a ratio between the two WTs yields a dimensionless wake loss estimate. The expected free-stream velocity ratio can also be calculated, by polling with the same method (interpolation at hub position or AD averaging) the undisturbed velocity fields at either WT, i.e the clear inflow to the upstream WT and the waked inflow to the downstream WT. The resulting free-stream velocity ratios $U_{\infty T2}/U_{\infty T1}$ are plotted in Figure 4.10.

Within $\pm 10^\circ$ of the wake centreline, both the expected and the modelled free-stream

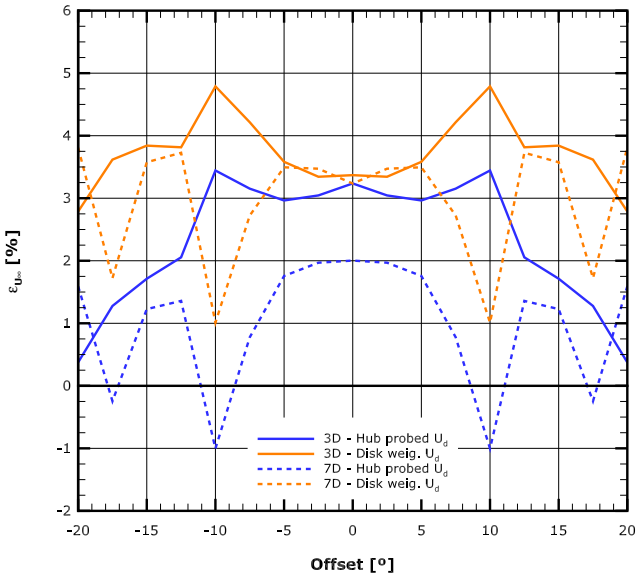

Figure 4.9: Relative error of U_∞^* estimate for a WT in waked inflow using hub and disk average U_d approximation methods, for two different WT spacings and over a range of wind direction offset to the row alignment.

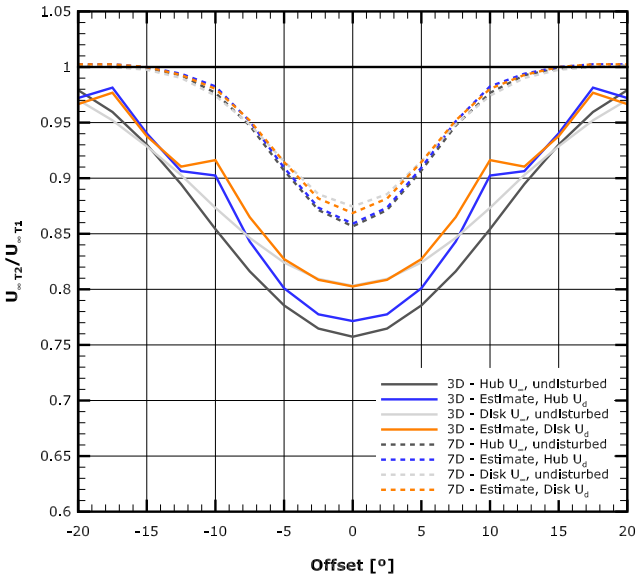

Figure 4.10: Free-stream velocity ratio between upstream (T1) and waked (T2) WTs using hub and disk average U_d approximation methods, for two different WT spacings and over a range of wind direction offset to the row alignment. The undisturbed equivalent to each profile highlights the ideal U_∞ estimation.

velocity ratios resulting of the AD averaged U_d are greater than those obtained by interpolating at the hub position. This is consequence of the AD averaged polling method's reduced sensitivity to the peak velocity deficit in the wake's center. Beyond the quantitative changes, at the narrow 3D spacing the match between expected and fully modelled U_∞ ratios is improved by the change to the AD averaged polling method, specially in near the wake centreline. At 7D spacing both hub positions and AD averaged methods are able to match their expected counterparts throughout the whole sector.

4.2.6 Conclusion

Approximating the momentum theory's disk velocity U_d by averaging over the AD area has had positive and negative effects on the WT thrust estimation algorithm. On one hand it resulted in an generally increased U_∞ estimation errors compared to using interpolation at the hub position. However, estimation errors were less sensitive to inflow conditions, suggesting that the influence of inflow complexity on free-stream velocity estimates is reduced.

The addition of the AD's thrust force imposes over the undisturbed inflow a velocity deficit that is homogeneous in the core of the AD area, but it also introduces an annular shear layer at the edge of the AD, where velocities are close to free-stream values. The hub position is set deep into the inner region of the AD area, and so velocities remain unaffected by that shear layer. The AD averaged velocity on the other hand considers that higher velocity area of the AD, causing disk velocity approximations as well as U_∞ estimation errors to increase.

The main advantage to the AD averaged U_d approximation is that its error is independent of inflow conditions. The over-estimation of U_∞ observed in clear inflow conditions was close to that seen in the wake of an upstream WT, regardless of the proximity to the wake's centreline. Furthermore, the modelled U_∞ ratio between upstream and waked WTs was a good match to the value expected from analysis of the flow undisturbed by the AD's presence, meaning that the $U\infty$ estimation suffered from exactly the same error margin on both WTs.

A correction to decrease the importance of the rotor span edge on AD area velocity averaging could help to have the best of both worlds, reducing U_∞ over-estimations while still being able to approximate the disk velocity correctly under non-uniform inflow conditions. Tip loss models account for the aerodynamic inefficiency of the rotor blade tips, and could provide clues towards the necessary solution.

4.3 Rotor force distribution

One of the premises of one dimensional momentum theory is that the AD exerts uniformly distributed force, and only in the AD-normal direction. However, the rotor blade's varying profile and angle of attack ensure that it also exerts tangential force (driving rotor rotation) and that both force components are radially varying. Blade element analysis models and full rotor simulations are able to dynamically estimate rotor load distribution depending on local flow, but do so using detailed blade geometry data and by modeling each individual rotor blade. However this level of detail is not feasible in a resource assessment context of wind engineering.

The works of Wu and Porté-Agel (2011, 2012) demonstrate how the wake rotation and load distribution – by comparing 1-D momentum theory and BEM based AD models – is not irrelevant to the wake flow. However Réthoré (2009) and Porté-Agel et al. (2011) also proved, through different approaches, that after time-averaging the effect of BEM calculated local loads or even the individual blades forces is not critical, and that capturing the radial inhomogeneity of the load distribution over the rotor span and the rotational effects are more important.

Studies on complete rotors (through either technique, see Sørensen and Shen, 2002 or Laursen et al., 2007) seem to indicate that blade load distributions follow a pattern. Assuming clear, homogeneous inflow, normal load tends to steadily increase along the blade length and drop near the blade tip, while tangential loads are a fraction of the normal, with a more shallow distribution (Figure 4.11).

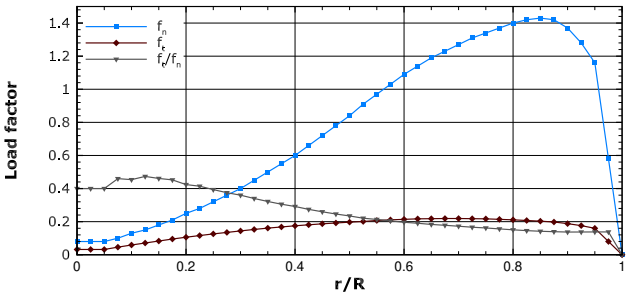

Figure 4.11: Distribution of normal (f_n) and tangential (f_t plus its size relative to the normal component) force ratios along a WT rotor radius, based on BEM model data of a 500 kW WT at an inflow velocity of 10 m/s, in Sørensen and Shen (2002).

Using the model's two-stage discretization (Section 2.5), more complex rotor load distributions can be applied, including radially variable load factors for normal (f_n) and tangential (f_t) components. Under the assumption that, after temporal averaging, the forces exerted over the rotor span can be considered steady and axisymmetric, static load distributions with or without tangential component and radial variability are applied via the AD, attempting to capture the complexity of the flow behaviour in the vicinity of the rotor.

4.3.1 Realistic rotor loading

The complexity of actual rotor flow means that loads along the rotor blades are not uniform. Section 2.2 shows how the blade profile produces lift and drag forces, and how these can vary considerably throughout the blade's span. Although decomposition into polar coordinate components results in a dominant AD-normal component (which the 1-D momentum theory approximates), it also leads to a non-zero tangential component which will induce wake rotation.

Due to the WT's rotation, the relative flow velocity at a blade section will increase radially. Blade geometry (shape, orientation and chord) will change accordingly along its length, and since lift and drag forces are proportional to the relative velocity squared, blade loads will tend to increase with the radial position. Inflow velocities will be much smaller than the average rotational component, so load behaviour should be the same regardless of inflow conditions.

On either extremity of the rotor blades, the two-dimensional blade section flow (as in Section 2.2) is increasingly more complex and less efficient. Close to end of the blade, instead of flowing along the blade chord, the path of least resistance will include flow towards the wing tip. This aerodynamic short-circuit will lead to the formation of tip vortices and aerodynamic efficiency loss, particularly where relative flow velocity and loads would be otherwise highest.

A rotor blade's load distribution results from the combination of all these factors and, although no two WT models share the exact same rotor dimensions and blade geometry, they will yield similarly shaped load distributions, regardless of the inflow wind speed. The normalized load distribution in Figure 4.11, based on blade geometry data of a real world WT, is representative of typical thrust (f_n) and torque (f_t) loads along an operating WT blade.

4.3.2 Modeling the tangential force component

The rotor's tangential force terms are discretized in parallel with the AD-normal thrust terms, also using the method detailed in Section 2.5. The product of the AD area and the tangential load factor f_t is distributed over the virtual rotor mesh and extrapolated to the domain mesh, resulting in the AD-tangential area density distribution $\widetilde{s_t}$ (4.3) and a tangential force density $\widetilde{F_t}$ (4.4).

$$\widetilde{s_t} = \frac{\sum f_t \delta A_d}{\int \mathrm{d}\Omega} \tag{4.3}$$

$$\widetilde{F_{t_i}} = \frac{1}{2} C_T {U_\infty}^2 \widetilde{s_n}\, \mathbf{t_{AD}} \cdot \delta_{ij} \tag{4.4}$$

Both normal and tangential force terms have to be decomposed into i-th components which, depending on the rotor orientation and position relative to the hub, will be have terms on all three Cartesian directions. They will appear on the right-hand side of the respective momentum equations, as source terms for each CV with AD contributions.

4.3.3 Low load hub area wind speeds

With a radially variable force distribution such as that in Figure 4.11, the majority of the AD thrust is exerted in the outer part of the rotor span. The exerted forces are particularly low near the root of the blade, combining to form an unrealistic high velocity jet in the center of the rotor (Figure 4.12). This occurs close to the sensitive hub region, where wind speeds should be low due to the presence of the WT hub.

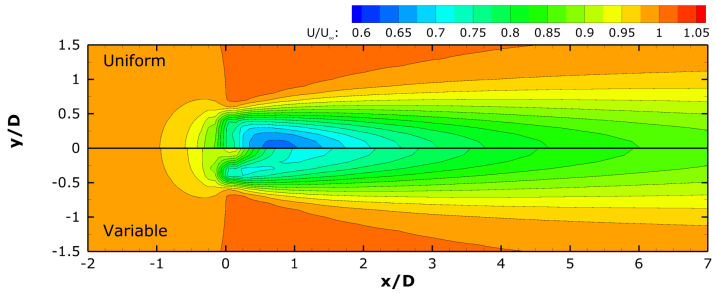

Figure 4.12: High velocity jet formed at hub position, due to low blade root loads.

The jet formed at the center of the AD means that the velocity at the hub position is greater than that of a uniformly loaded AD, and close to free-stream values. Changing to a weighted average U_d approximation (like that explored in Section 4.2) is necessary to avoid over-estimation of free-stream velocity and WT thrust. Irrespective of the method used to approximate U_d, the high speed jet formed at the center of the AD suggests that the hub drag should be modelled, as a form of moderating the velocities in that region.

4.3.3.1 Improving the disk velocity approximation

As a consequence of the jet formed at the center of the AD, the hub position velocity is no longer representative of the relevant U_d for the modelled WT. The discrepancy between velocity profiles at the AD for uniformly and non-uniformly loaded ADs (Figure 4.13) is evident, particularly at hub height ($z/D = 0$) where the velocities at the variably loaded AD are very close to undisturbed values. The added heterogeneity inside the rotor span must be taken into consideration by the U_d approximation.

The thrust estimation algorithm is dependent on the quality of the U_d approximation via polling from the flow solution, with an increased disk velocity directly translating to an increase in U_∞. Table 4.2 aggregates the U_d and U_∞ pairs obtained for various methods of polling the solution U_d. The methods included are: interpolation ate the hub position, weighted averaging as per (4.2) and a simple average over the rotor span area (ignoring the load-factor f_n in Equation 4.2). The undisturbed hub and AD area average values of the velocity included as a reference for the correct free-stream velocity.

Using Interpolation at the hub position, the U_d approximation increases by more than 1 m/s when changing AD load distribution from uniform to variable, with an increase in U_∞ of the same magnitude. Either averaging method lowers U_d values, with the weighted averaging method in particular matching both U_d and U_∞ estimates to of the

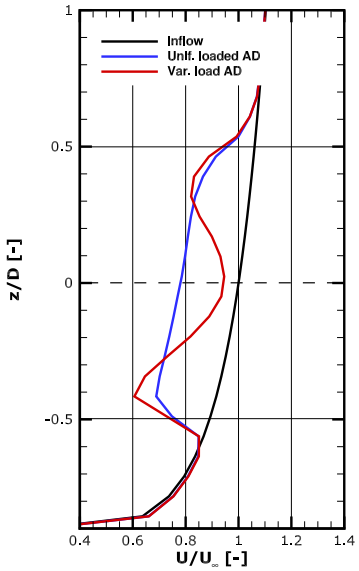

Figure 4.13: Dimensionless stream-wise velocity profile in undisturbed inflow and in the presence of uniformly and non-uniformly loaded ADs.

AD load	Polling method	U_d (m/s)	U_∞ (m/s)
no WT	hub pos.	–	8.07
no WT	Area avg.	–	8.04
Uniform	hub pos.	6.30	8.12
Variable	hub pos.	7.51	9.26
Variable	Area avg.	6.42	8.24
Variable	Weighted avg.	6.29	8.12

Table 4.2: WT performance estimation for a variable load distribution AD, using hub or disk averaged U_d approximation methods.

uniformly loaded AD. Using the weighted averaging polling method (Section 4.3.2), the thrust estimation algorithm suffers no error penalty from modeling non-uniform rotor loads.

4.3.3.2 Hub drag

The rotor load depicted in Figure 4.11 does not fully represent the obstruction to the flow posed by the rotor, as the presence of the hub increases drag on the flow and influences the flow near the blade root, decreasing aerodynamic efficiency. The hub can be simplified to a bluff body and the equivalent drag exerted by it, to avoid the unrealistic velocities in the hub region and compensate for the low loads near the blade root.

By estimating the frontal hub area A_{hub} and its drag coefficient ${C_D}^{hub}$, the corresponding

momentum loss can be calculated:

$$D_{hub} = \frac{1}{2}\rho {C_D}^{hub} A_{hub} U_\infty \tag{4.5}$$

The hub is assumed to have a circular section that scales with the rotor size, its radius being 7.5% of the rotor radius. With the variety of shapes WT nacelles assume and the non-linear interaction between rotor and hub, the effective drag coefficient of the nacelle is hard to guess. The impact of the drag coefficient on velocities along the axial direction is presented in Figure 4.14, passing through the hub and $y/D = 0.3$ positions at hub height. The velocity on the same axis with the simpler uniformly loaded AD is plotted alongside for comparison.

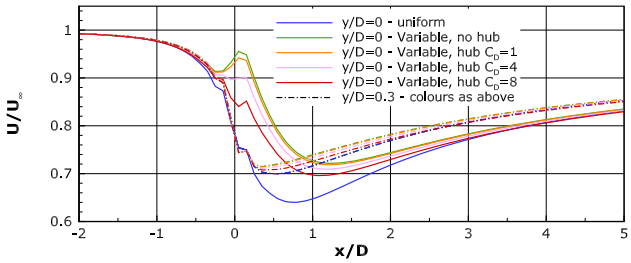

Figure 4.14: Streamwise velocity along the axial direction of a non-uniformly loaded AD, through the hub position and mid rotor span, with hub modelled as a drag-inducing bluff body. A range of hub drag coefficients are compared, along with a uniformly loaded AD of equivalent overall thrust.

Without hub modelling, the velocity at the center of the variably loaded AD increases to near free-stream values, matching the behaviour found in Figure 4.12 and contrasting with the $0.25U_\infty$ drop at the same position in the uniformly loaded AD. A minimum C_D of 4 is required to avoid an increase in velocity as the flow passes through the AD. Regardless, the velocities are increased in the near wake, with lower peak velocity deficits. After the initial 3D of wake the impact of the AD load and hub modeling is not relevant. At the y/D=0.3 rotor position, away from the hub area but still within the rotor span, the effect of the hub drag modelling is very small, with peak velocity deficits differing by $0.02U_\infty$ or less.

4.3.4 Uniform tangential load

In keeping with momentum theory and Froude's AD model and assuming a uniformly loaded AD, a homogeneous tangential component to the force term is added to the rotor. It will induce rotation into the wake flow and lead to source terms in all of the RaNS momentum equations, depending on the orientation of the AD relative to the mesh.

The tangential load factor is set to a ratio of 1:5 (equation 4.6) relative to the normal component, which remains unchanged and constant. This ratio is an approximation to the relative strength of the two components determined by Sørensen and Shen (2002) (Figure 4.11), particularly in the outer half of the blade.

$$f_n = 1, \qquad f_t = 0.2 \tag{4.6}$$

To evaluate the impact of adding a tangential force component to the AD load on the wake, the velocity field at various vertical cross-sections along the wake length is mapped in Figure 4.15, where the wake flow for a uniformly loaded AD with and without the tangential force component can be compared.

The tangential force component induces rotation into the wake flow, the magnitude of which remains considerable (up to $\tilde{0}.05U_\infty$) at 0.5D and 1.0D downstream of the WT. However it has mostly dissipated at the 3.0D section, leaving only mild effects on the streamwise velocity field. The overall wake signature shape or peak velocity deficit are not significantly affected in any part of the wake, with the exception of a lateral shift in the wake axis (+0.1D after 7.0D of wake length), presumably caused by interaction between surface friction and wake rotation.

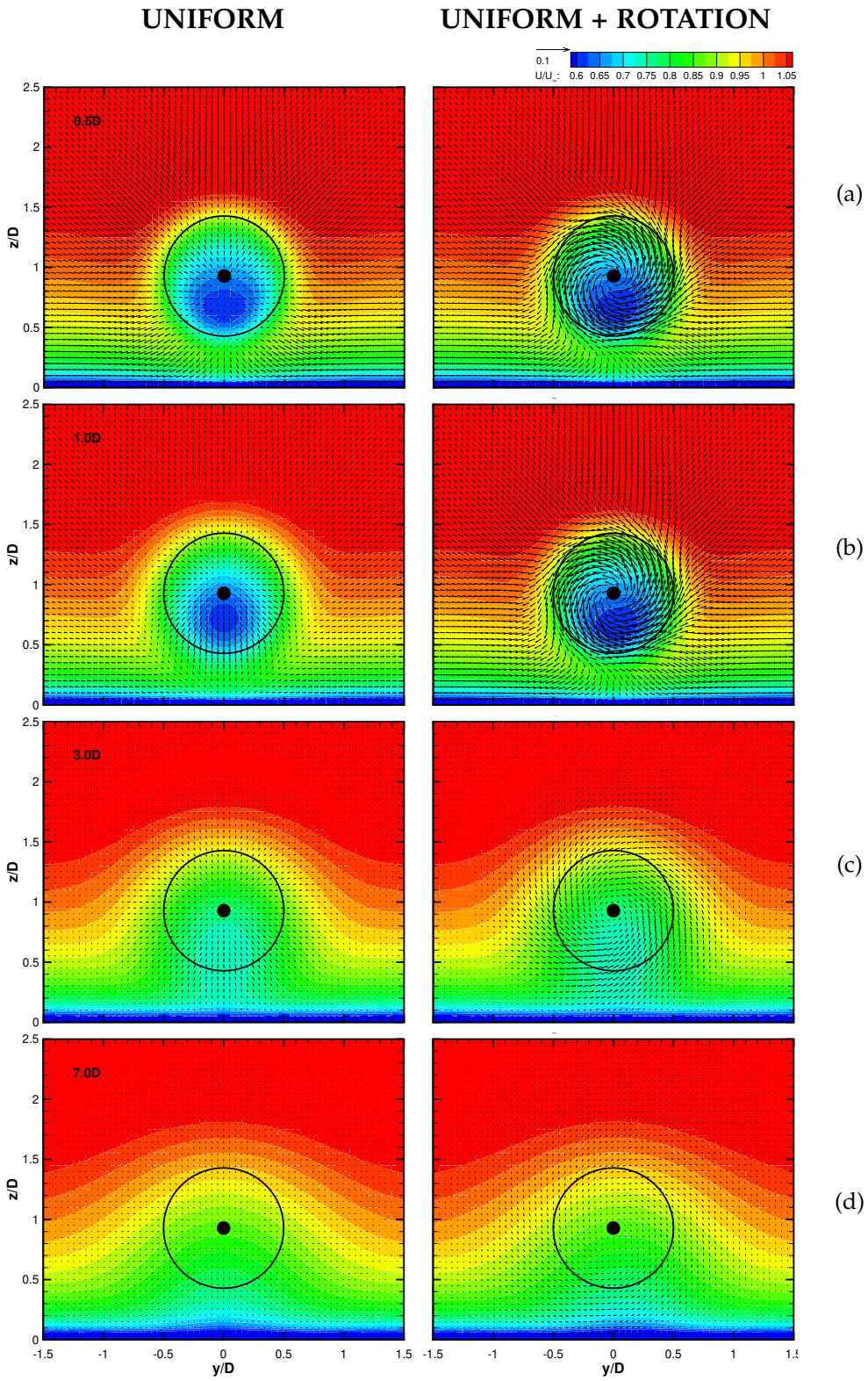

Figure 4.15: Wake flow downstream of a uniformly loaded AD, with normal loads only (left) or with with normal and tangential loads (right). The colour contours map dimensionless streamwise velocity and vectors map the cross-stream velocity direction and intensity ($0.1U_\infty$ scale vector represented alongside the colour map scale). Cross-stream sections at wake positions (**a**) 0.5D, (**b**) 1.0D, (**c**) 3.0D and (**d**) 7.0D.

4.3.5 Non-uniform load distribution

To have a more complex rotor load distribution, without discarding the AD as described in Froude's one-dimensional momentum theory, requires adopting an axisymmetric load distribution. Normalized load factor profiles (Figure 4.11) that describe the variation of normal (f_n) and tangential (f_t) loads along the blade length are used. These allow the AD to mimic the operating rotor blade loads, aggregated and distributed over the AD area.

To compensate for the high velocity jet that appears at the center of the AD with non-uniformly loaded ADs, both the adjustments to the model covered in Section 4.3.3 are applied: the U_d is approximated using weighted averaging over the AD to avoid gross WT performance over-estimations, and the hub's presence is modelled via a bluff body drag with a drag coefficient $C_{D_{hub}}$ of 8.

4.3.5.1 Variable normal load

The radially variable normal load (f_n) distribution of Figure 4.11 is applied exclusively, ignoring the tangential component that induces rotation to the wake. With a radically different load distribution at the AD, the flow's response to the presence of the AD and downstream wake development changes. The velocity field at various vertical cross-sections along the wake length is mapped in Figure 4.16, where the wake flow for ADs with uniform and variable load distributions can be compared.

The non-uniformly loaded AD shifts a significant portion of the exerted force from the center of the rotor area to its edges, which reflects immediately on the wake at the cross-section closest to the WT (0.5D downstream, Figure 4.16a): the peak velocity deficit area is concentrated at the bottom of the wake, acquiring an annular shape that follows the most heavily load regions of the AD. The cross-stream velocity intensity also increases within the inner wake area. However, these differences in wake patterns quickly homogenize downstream, with the wake flow fields of uniformly and non-uniformly loaded ADs being indistinguishable after 3.0D.

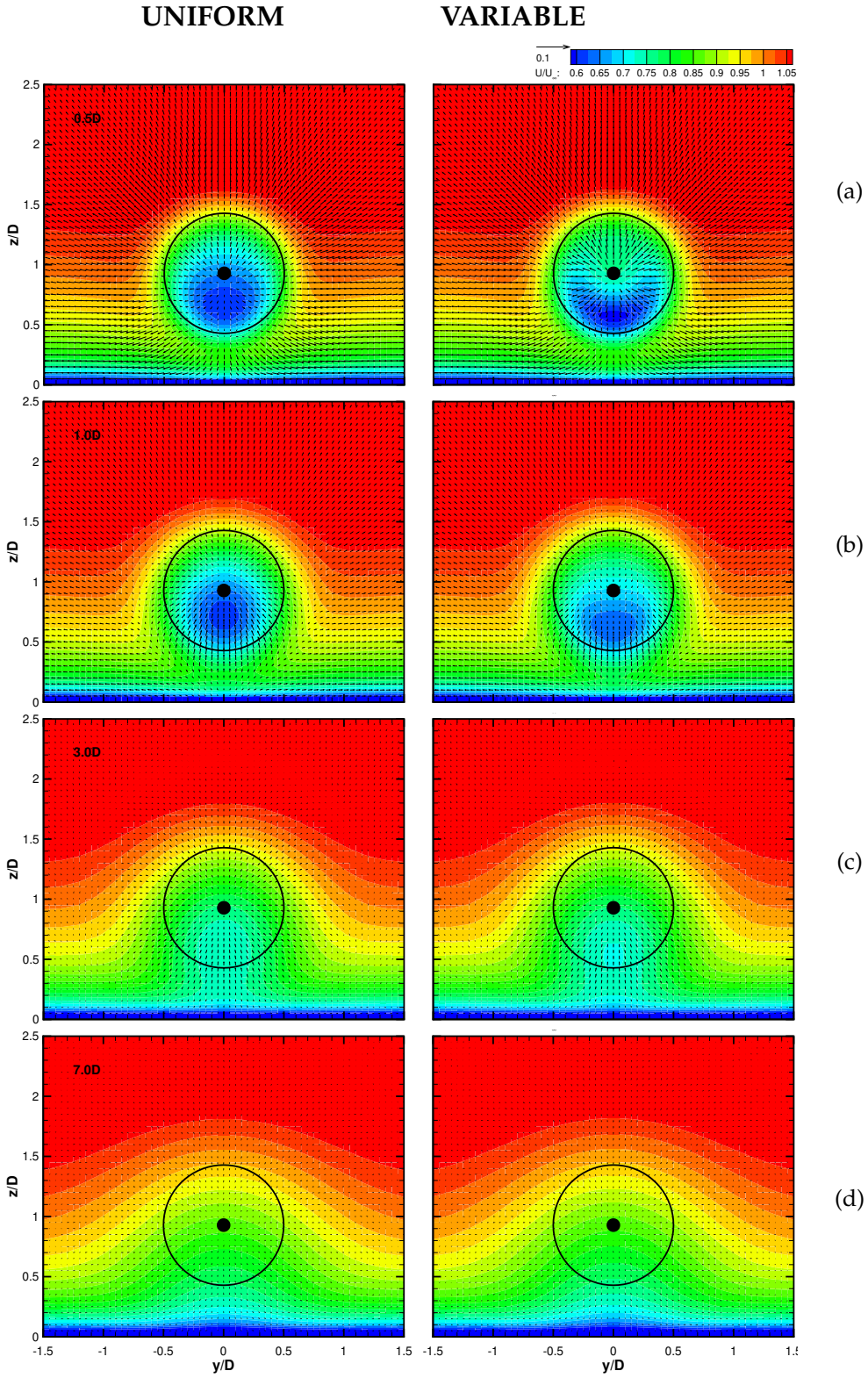

Figure 4.16: Wake flow downstream of an AD with uniform (left) or radially variable (right) load distributions. The colour contours map dimensionless streamwise velocity and vectors map the cross-stream velocity direction and intensity ($0.1U_\infty$ scale vector represented alongside the colour map scale). Cross-stream sections at wake positions (**a**) 0.5D, (**b**) 1.0D, (**c**) 3.0D and (**d**) 7.0D.

4.3.5.2 Variable normal and tangential loads

The combined normal (f_n) and tangential (f_t) load distributions of Figure 4.11 are applied to the AD, meaning that rotor load is both non-uniform and rotation inducing. In addition to the effect of variable AD loads, analysed in Section 4.3.5.1, the flow rotation will increase the complexity the flow in the vicinity of the AD. The velocity field at various vertical cross-sections along the wake length is mapped in Figure 4.17, where the wake flow for a non-uniformly loaded ADs with and without the tangential force component can be compared.

Adding the tangential component to the non-uniformly loaded AD induces rotation into the wake flow, which while considerable at close proximity to the WT ($\tilde{0}.05U_\infty$ at 0.5D downstream, in Figure 4.17a) quickly begins to dissipate. At the 1.0D section (Figure 4.17b) the cross-stream flow has decayed noticeably, and at 3.0D (Figure 4.17c) it has reduced to $\tilde{0}.01U_\infty$. The wake rotation effect causes a permanent lateral shift in the wake axis, visible even in the near wake (at the 0.5D section, in Figure 4.17a), that after 7.0D (Figure 4.17d) is approximately 0.1D to the right hand side, presumably promoted by the interaction between surface friction and wake rotation.

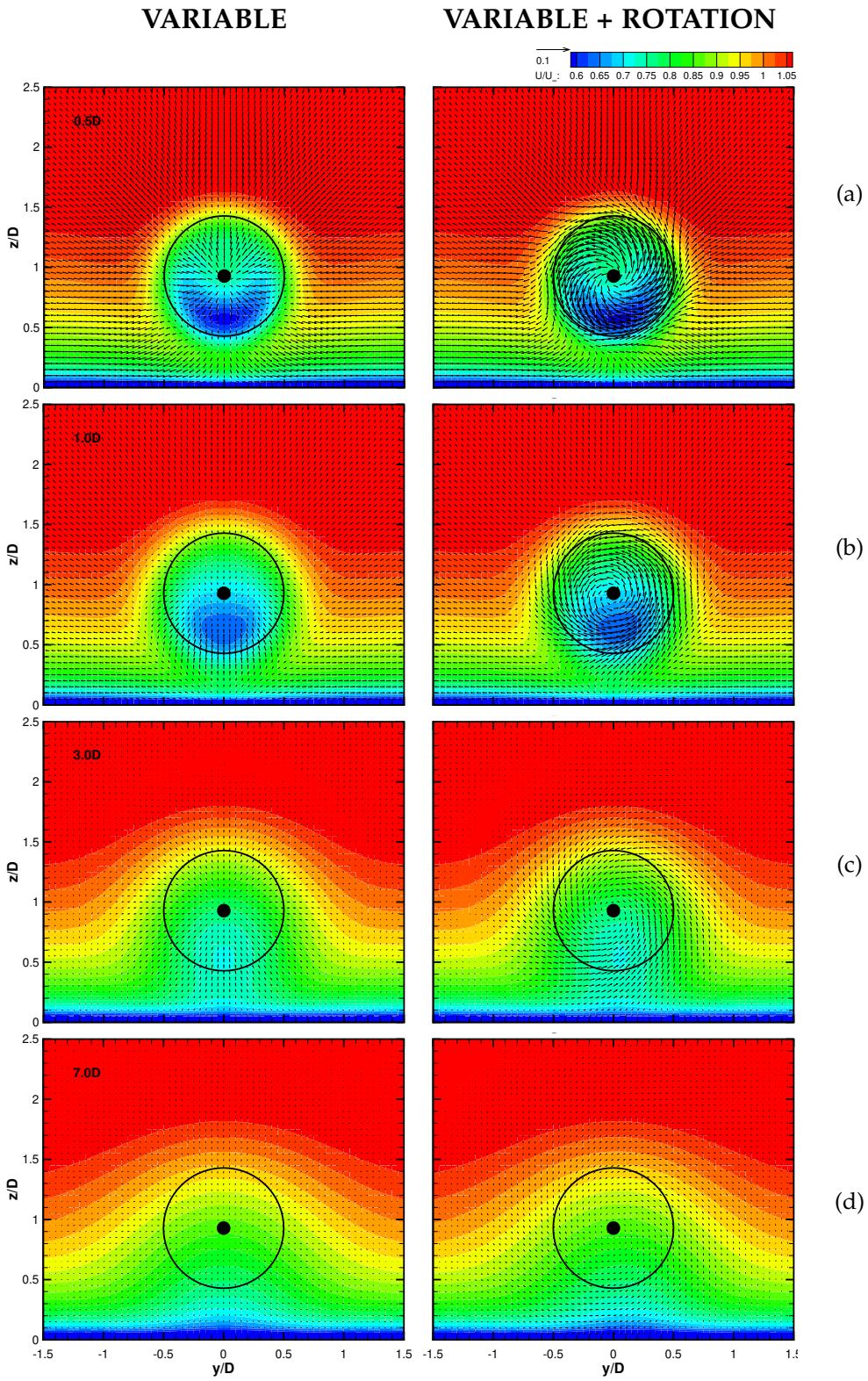

Figure 4.17: Wake flow downstream of a non-uniformly loaded AD, with normal loads only (left) or with with normal and tangential loads (right). The colour contours map dimensionless streamwise velocity and vectors map the cross-stream velocity direction and intensity ($0.1U_\infty$ scale vector represented alongside the colour map scale). Cross-stream sections at wake positions (**a**) 0.5D, (**b**) 1.0D, (**c**) 3.0D and (**d**) 7.0D.

4.3.6 Conclusion

The re-shaped wake pattern and rotation induced respectively by the varying load distribution and tangential force components are present in the near-wake, but have largely dissipated by 3.0D downstream of the WT. In the far wake, the remaining trace of the different AD load distributions is a lateral shift (0.1D) in the wake centreline, cause by the interaction between the ground and the rotating flow. This shift is visible in the streamwise velocity across the wake at 1D, 3D and 7D downstream of the WT (Figure 4.18).

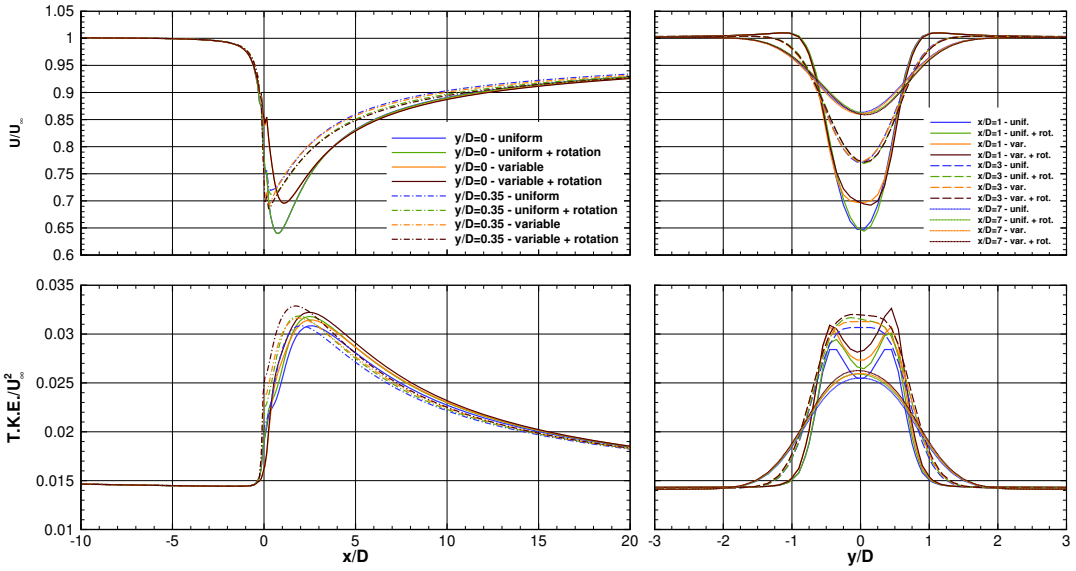

Figure 4.18: Streamwise velocity (above) and turbulent kinetic energy (below), for different rotor load distributions. Profiles along the hub axis and at $y/D = 3$ (left) and across the wake (right), at three downstream positions.

The effects of adding tangential forces and non-uniform AD loads appear to be independent from each other, with rotation superimposing over the wake pattern set by uniform or variable AD-normal loads. This is confirmed by the streamwise velocity along the rotor axis (Figure 4.18), where profiles are grouped according to the use of uniform or variable AD load. Closer to the outside edge of the rotor, that effect looses its relevance and only small differences remain due to the tangential forces: the rotating wake has a lower (by ~$0.01U_\infty$) stream-wise velocity in the first 10-15D of wake length. All load distribution complexity added over the basic uniform normal load causes increases in peak T.K.E. in the near-wake, but the differences quickly dissipate further downstream.

The variable load AD causes an increase in velocity at the center of the near wake, due to the reduced thrust near the hub area of the AD. Through the use of a weighed averaging approximation to U_d, the weighting attributed to this localized acceleration was reduced, to the point that the WT performance estimation was largely insensitive to the AD loads applied.

4.4 One-directional coupling

Using synthetic boundary conditions in complex flow cases can lead to unrealistic results, particularly where inflow conditions are misrepresented in the flow model. This can be the case wherever severe flow perturbations occur in close upstream proximity. One such case can be that of WF clusters, where distances separating neighbouring wind farms small enough that the influence on each other's performance is not negligible. In these conditions, to capture the far wake effect within a cluster the domain would have to be extended to include both WFs, leading to very large domains in both length and node count.

Alternatively to the extension of the domain to include all relevant upstream flow perturbations, the inlet boundary flow description can be improved to adequately capture the relevant inflow conditions, and using other CFD models as a source for boundary conditions is a common and valid approach. Applications of the concept within the VENTOS® software family are found in the model-chain approach of Rodrigues et al. (2015), where a RaNS micro-scale CFD model is one-directionally with meso-scale model results to improve flow description on all boundaries, or the use of precursor simulations in LES modelling (Silva Lopes et al., 2007) to generate and feed realistic turbulent ABL conditions to the inlet boundary, something synthetic boundary conditions are unable to.

To simulate the Rødsand II/Nysted cluster flow and capture the far wake effects (Section 3.3), modeling flow along the WF alignment required capturing the upstream WFs wake. To avoid the numerical disadvantages of the enlarged domain that includes both WFs, each is simulated separately and in sequence, with their solutions coupled via the downstream WF's inlet. The aggregate solution allows much faster simulation times, while achieving comparable quality in the downstream WF results.

4.4.1 Improving on traditional inlet boundary conditions

The inflow description is a dominant factor in flow solution at the AOI, more so than any other boundary condition. Synthetic ABL inlet boundary conditions (Richards and Hoxey, 1993; Hargreaves and Wright, 2007) assume lateral uniformity, turbulence equilibrium and flow exclusively in the boundary-normal direction, conditions which are only adequate when inflow is known to be free from the effects of obstructions (terrain, canopy or wind turbines). In a WF cluster it is simple to determine which sectors are affect by these effects, and thus where improving the inlet conditions is key to increasing accuracy of the AOI results.

Forced to comply to boundary conditions in a "channel" (with prescribed inlet and outlet, bounded by wall and symmetry boundaries), ABL flows tend to be parabolic in behaviour. This way, in simple flow cases it can be acceptable to consider the streamwise coordinate to have a one-way character and flow to be dependent on upstream conditions alone. If these assumptions hold true in the area between two WFs they can be solved separately without loss of relevant flow information at either end using a simple one-directional data transfer.

4.4.2 Coupling the two domains

Coupling those two simulations through the downstream domain's inlet boundary should allow the results of the coupled simulations to closely match those of the equivalent larger domain. Most importantly, solving the case with the two sequentially run small simulations should take far less time than doing so with a single, (much larger and numerically cumbersome) simulation covering both the AOI and the upstream flow, even if the total node count is comparable or greater in the coupled case.

Coupling is achieved through a transfer of solution data (velocity gradients and all solved variables bar pressure) from the concluded precursor simulation, covering the upstream WF, and using it to produce a static inlet boundary condition for the main simulation, covering the AOI and the downstream WF. To ensure the validity of the approximations and best results, some domain setup limitations apply:

- The lateral and top boundary positions of precursor and target simulation domains should coincide, to avoid mismatching flow conditions at the edges of the solutions. The section of wind flow solution transferred between domains is only relevant within the constraints of the imposed lateral and top boundary conditions, and ignoring those can lead to incorrect solutions or numerical instability.
- The two domains should sufficiently intersect, so that the target simulation's inlet is using solution data unaffected by the precursor simulation's outlet boundary condition. The precursor domain's outlet boundary placement should consider that fact, by incorporating sufficient downstream run.
- The coupling section should the validity of the assumptions behind parabolic flow: areas where non-negligible cross-flow effects or flow reversal occur should be avoided, so the final main domain's inlet boundary placement should be adjusted accordingly.

4.4.3 Rødsand II/Nysted wind farm cluster

Rødsand II and Nysted are separated by merely 3 kms of sea (Figure 4.19), forming a cluster problem where for the prevailing wind directions one WF operates in the wake of the other Hansen et al. (2015). Further information on this case can be consulted in Section 3.3.1.

Rødsand II operates in undisturbed flow for Western sectors flow, but under Eastern sector flows it will be affected by the wake from Nysted's WTs. Simulating those conditions would require considering both operating WFs, combining into a cluster of 162 WTs that spans more than 20 kms in length, i.e. a problem nearly twice the size of Rødsand II by itself (12 kms in length and 90 WTs).

Using the proposed coupling technique, a precursor simulation covers the upstream flow (Nysted WF only), using synthetic boundary conditions. This precursor provides the inlet conditions to adequately model the flow at the AOI, using a second simulation covering Rødsand II only. The two combined provide an equivalent solution to the cluster flow problem, using two smaller mathematical problems with potential compu-

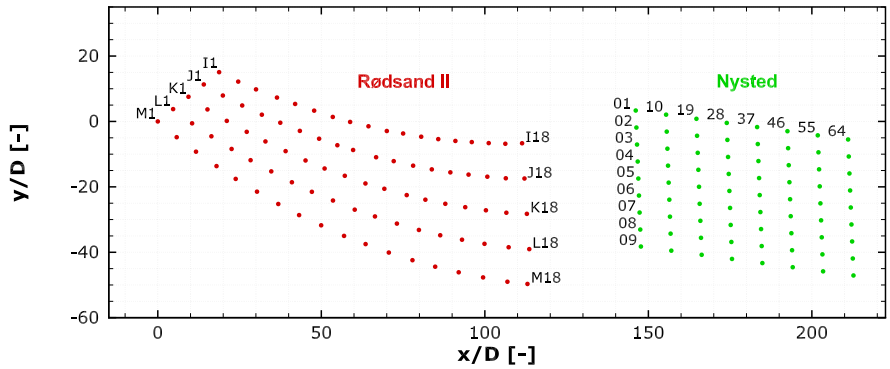

Figure 4.19: Modelled offshore WF cluster, formed by Rødsand II (left) and Nysted (right).

tational resource savings. Between wind farms flow will be characterized by the slowly recovering wakes, with very small streamwise gradients and no source of pressure perturbations, meaning the parabolic assumption holds validity and making it an ideal location for the domain coupling to occur.

4.4.4 Coupling and domain configuration

A single inflow sector (97°, as in Section 3.3.2) is represented here, for flow aligned with the Nysted WF rows. This direction guarantees a totally clear inflow to Nysted and partially waked inflow to Rødsand II. Four different domains (Table 4.3) covering part or all of the WF cluster were created, serving to simulate the same case in four configurations:

- Cluster (CLU domain): both WFs are included in a single 25.7 km long domain, using synthetic inlet boundary conditions.
- Coupled (RSII + NY domains): two simulations individually solve the flow at the two WFs, with the precursor simulation first solving the NY (Nysted) domain and providing inlet boundary conditions to the main simulation, solving flow over the RSII (Rødsand II) domain.
- Coupled Low.Res. (RSII + NY_{LR}): same as the Coupled configuration, but using downgraded quality data for the inlet boundary condition by coupling the main simulation (RSII domain) to a low resolution precursor(NY_{LR} domain).
- Regular (RSII domain): classical approach to modelling the Rødsand II flow with no precursor simulation, using synthetic inlet boundary conditions and a domain covering only the Rødsand II (RSII domain), disregarding the effect Nysted has on inflow.

Flow and mesh characteristics outside those covered in Table 4.3 were kept across domains. Peak horizontal resolution was set to 1/4D of the largest included WT diameter, and CLU and RSII domain meshes tuned to match in the Rødsand II area. The NY_{LR} domain differs from others by having halved peak resolution on all directions relative

Domain	Domain size [km]			Max. res. [m]						Nodes
	Length	*Width*	$z_{max.}$	c_x	c_y	c_z	$N_i \times N_j \times N_k$			
CLU	25.7	8.4	0.7	23	23	2	958	294	50	∼14.1M
RSII	16.0	"	"	"	"	"	542	270	"	∼7.3M
NY	12.5	"	"	20	20	"	407	260	51	∼5.4M
NY_{LR}	"	"	"	40	40	4	222	146	40	∼1.3M

Table 4.3: Main mesh characteristics of the domains used in the runs to simulate the cluster flow.

to those of the NY domain.

The RSII/NY and RSII/NY_{LR} domain coupling section (the RSII inlet section) is located between WFs, just downstream of the last Nysted WTs and outside the constant resolution area of either domain mesh: this area is one where reduction in node count is possible between Cluster and Coupled runs (observable also by the individual domain node counts in Table 4.3), maintaining high-resolution domain coverage on the high priority areas (the WFs). The overlap between precursor and main domain meshes was 3.23 kms.

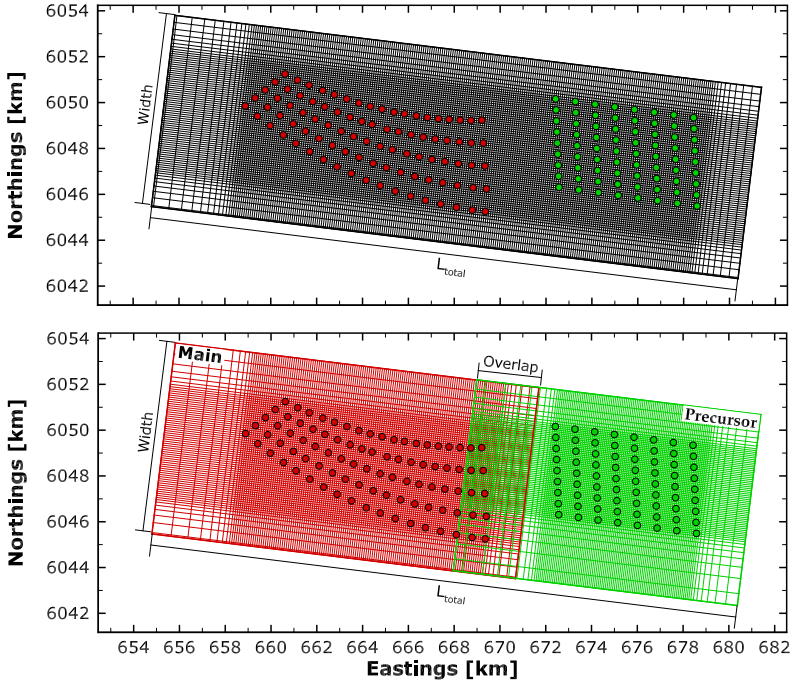

Figure 4.20: Horizontal projection of the domain meshes covering the combined cluster (above), and those covering Rødsand II and Nysted overlapping (below, in red and green respectively). Meshes represented at half of the full resolution.

4.4.5 Results

If the parabolic flow assumption holds validity, the change to a coupled domain configuration will have negligible impact on inflow conditions at the coupling section. As

a consequence the flow at the AOI and operating conditions for Rødsand II's WT be similar. The gains from modeling the upstream inhomogeneity are also quantified, by comparison to the classical approach of simulating the AOI with synthetic boundary conditions. Finally, the computational gains from the use of the coupling technique will be quantified.

4.4.5.1 Flow solution

The wind flow description for both wind speed and turbulence intensity across the main domain's inlet (Figure 4.21) changes dramatically between synthetic boundary conditions and the Cluster configuration solution, with the latter closely matched by both Coupled configurations. The distinct wake signatures of Nysted's 9 WT rows are clear, due to the perfect alignment between inflow and WT rows and the short gap between Nysted WF the coupling section. The vertical flow profiles corroborate that observation, with the synthetic boundary conditions being (inside the rotor span height) a very close match to clear inflow parts of Cluster and Coupled configurations.

Some flow acceleration is observable outside the Nysted's wake, when comparing to the synthetic boundary condition's uniform inflow distribution. This effect is observable either side of the WF wake signature and on the clear inflow vertical profiles in Figure 4.21, and is essentially caused by boundary layer development over the length of the Nysted domain and, to a minor extent, by the Nysted WF's blockage effect. Effects from reducing the resolution of the precursor simulation are noticeable only on turbulence intensity profiles, with slightly lower peaks in the WT row wakes.

As a consequence the similarity between solutions at RSII's inlet section, the downstream flow is also very similar between Coupled and Cluster configuration. In Figure 4.22 the two mapped solution contours (in colour and contour lines, respectively) agree in shape, differing only slightly in length. Very similar results came from the Coupled Low.Res. configuration.

4.4.5.2 Wind farm power estimation

Rødsand II WF's power estimation is largely unaffected by the division of the cluster case into two separate simulations: total WF power increases by only 0.2 % in the Coupled configuration compared to the Cluster setup (Table 4.4). This is in contrasts with the Regular configuration's result which, unlike Coupled and Cluster runs, is unable to reproduce the power loss from operating in partly waked inflow and over-estimates WF power by a margin of more than 10%.

Reducing the quality of the precursor simulation did have an impact (+6.9%) on the Nysted's overall power output, but the Rødsand II solution was not responsive to that change, with WF power estimation error of the same magnitude as with the full resolution precursor. This is in agreement with the unchanged inlet profiles and main domain solutions between using NY or NY_{LR} domains as source for inlet conditions.

The power estimations at Rødsand II from Cluster and the two Coupled configurations

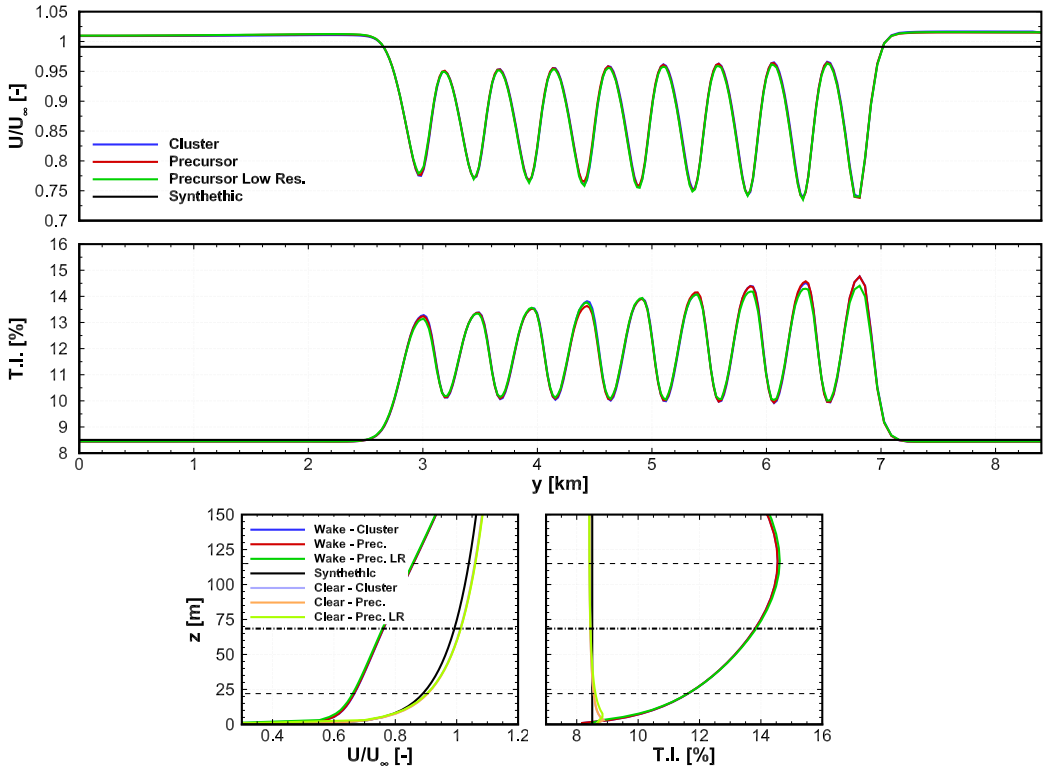

Figure 4.21: Wind speed and turbulence intensity profiles across the main domain's inlet (above) and vertical profiles at free-stream and in the wake of the middle Nysted WT row (below), when sourced from the precursor solutions, full cluster solution or synthetic boundary conditions.

were close at both the individual WT and overall WF level. The average change in individual WT power estimate (mean absolute percentual deviation, MAPD) relative to the Cluster configuration is low in both Coupled configurations, with 0.9% and 0.8% respectively for Cluster and Cluster Low Res. (Table 4.4).

Simulations on the Nysted WF had worse results at the individual WT level, with MAPD values close to 10% (due to a mismatch between meshes at the Nysted area) that cancel out on aggregate. These errors are in the same order of magnitude as found at Rødsand II in the Regular configuration, where the upstream presence of Nysted is ignored.

4.4.5.3 Computational time usage

Total computational resource requirements grew super-linearly with node count (Table 4.5). Concluding the simulation in the Cluster configuration took the longest at 178.7 h of computation time, while simulations on the RSII domain (with about half the nodes of the CLU domain) took less then a fifth of that time. Reducing the quality of the precursor simulation lowered the NY domain's node count from 5.4 to 1.2 million nodes, but required only a small fraction of the time (15 h to 1.2h) to complete.

Time-per-iteration t_{CPU}/iter. scaled proportionally with node count, meaning that the

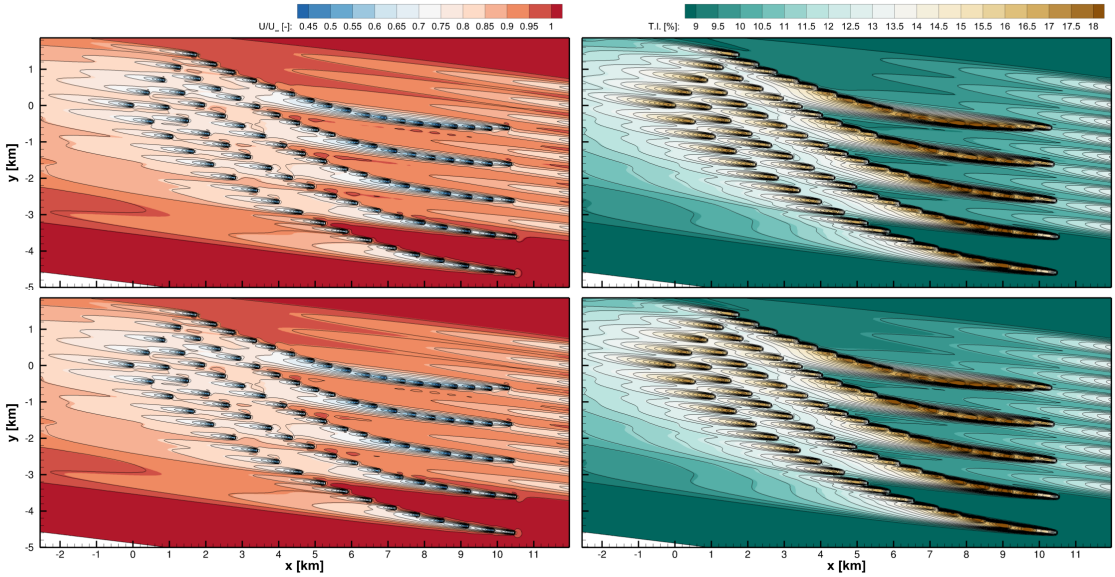

Figure 4.22: Wind speed (left) and turbulence intensity (right) at hub height over the Rødsand II WF, for the Coupled (top, in colour contours) and Coupled Low.Res. (bottom, in colour contours), compared with those of the Cluster solution (outlined contours).

Run	Rødsand II		Nysted	
(vs. Cluster)	ΔP_{WF} [%]	$\text{MAPD}_{P_{WT}}$ [%]	ΔP_{WF} [%]	$\text{MAPD}_{P_{WT}}$ [%]
Coupled	0.2	0.9	-0.8	5.9
Coupled Low Res.	-0.2	0.8	6.9	9.3
Regular	10.7	12.4	-	-

Table 4.4: Variation in WF overall power estimations and individual WT power dispersion (through the Mean Absolute Percentage Deviation) in from Coupled solutions, relative to Cluster solution.

bottlenecking factor – at the hardware level – is unchanged and that efficiency is unaffected. However the convergence rate was negatively affected by the problem size growth, with the number of iteration required to reach the same level of solution also increasing: examples are the growth between simulations for the NY_{LR} and NY domains, doubling the number of iterations for 4.5 times the nodes, and that between the RSII and CLU domains, with 2.5 times the iterations for twice the nodes.

As a result, the aggregate computational cost of the Coupled configuration is greatly reduced compared to that of the Cluster, representing a saving of over 70% CPU time despite the overall node count dropping by only 10%. The use of NY_{LR} as a precursor represented a further saving of approximately 30% in both aggregate node count and computation time in the Coupled Low. Res. relative to the Coupled run.

4.4.6 Conclusion

The tested approach showed that it is possible to model the long range effect of WTs on neighbouring WFs, covering larger domains at a sensible computational cost. Using

Run	Domain	Nodes	Iter.	t_{CPU} [h]	t_{CPU}/iter. [s]	$\sum$ Nodes	$\sum t_{CPU}$ [h]
Cluster	CLU	14.1M	19997	178.7	32.2	14.1M	178.7
Coupled	NY	5.4M	4586	15.0	11.8	12.7M	48.5
	RSII	7.3M	7461	33.5	16.2		
Coupled Low.Res.	NY_{LR}	1.2M	2186	1.2	2.0	8.5M	34.6
	RSII	7.3M	7472	33.4	16.1		
Regular	RSII	7.3M	7518	33.7	16.1	7.3M	33.7

Table 4.5: Computational cost of every simulation and of each run on aggregate.

the precursor-sourced inlet boundary conditions as form of coupling, results showed that splitting the WF cluster case into two simulations had a limited effect on the flow field and as a consequence on the overall WF power estimation, particularly on the downstream (Rødsand II) WF and AOI.

There were differences found in individual WT's power estimations, but these are mostly concentrated on the upstream WF where cluster and coupled run meshes were non-matching. By focusing resources on the domain covering the AOI (Rødsand II), further computational time savings were possible by reducing the quality (and thus cost) of the upstream solution, with negligible impact on the AOI results.

4.5 Conclusion

The WT model confirmed the expectations regarding the flow in the far wake, in that how the AD is discretized and forces distributed over is not relevant and that the dominant mechanisms are those from atmospheric turbulent flows. The impact of more complex AD load distributions, even those with forces inducing wake rotation, leave little evidence outside the near wake (Section 4.3). Similarly, correcting the oscillations introduced in the vicinity of the AD by the occurrence of discrete body forces had negligible impact outside the peak velocity deficit region (Section 4.1).

On the other hand, near the AD rotor flow dynamics dominate and using radially variable AD loads will result in greater in velocity inhomogeneity, at the AD and downstream in the near wake. The hub and centreline area of the near wake proved particularly sensitive, being prone to near free-stream velocities due to low loads near the root of the rotor blades (Section 4.3). For that reason, moving away from the hub position interpolation for the U_d value proved mandatory, to avoid gross approximation errors, with the weighted averaging method (Section 4.2) allowing the free-stream velocity estimations to be unaffected by the change in AD load.

Regardless of the load distribution, velocity homogeneity at the AD was already a concern for the model, as approximating the disk velocity by interpolation at the hub position made the thrust estimation algorithm susceptible of increased errors under complex inflow, such as in the wake of other WTs. This was successfully corrected by approximating U_d via AD area average velocity, but at the cost of a generally increased U_∞ estimation error (Section 4.2).

The modification made to the AD discretization method (Section 4.1) was mainly to the benefit of the WT performance estimation elements of the model: by eliminating the velocity oscillations in the vicinity of the AD, the U_∞ and WT power estimates became insensitive to the AD's position in the mesh.

Finally, the domain coupling technique proved to be adequate solve the WF cluster problem (Section 4.4). The coupled solution was able to capture the Nysted wake effect from the precursor simulation and apply it at the main domain to simulate Rødsand II's operation under waked inflow. The estimated power error, on aggregate in WF and at individual WT level, was quite low when compared to single larger simulation covering the whole cluster, while requiring a fraction of the computational resources.

This page intentionally left blank

Chapter 5

Conclusion

The wake model can be deconstructed into three main components: describing and positioning the AD, estimating the WT performance and modeling the downstream wake flow. The proposed wake model tackles the first two, combining with the RaNS flow solver which is responsible for modeling the wake flow development and inflow conditions in the ABL. The implementation was verified by evaluation of the overall momentum and energy budgets in the domain, proving to be mesh converged and limited only by the numerical solver's convergence criteria (Section 2.4.4).

It proved adequate to represent any number of WTs, from a single isolated unit up to a large array in a WF. Its performance was ultimately limited by the RaNS flow solver's ability to accurately model flow in the vicinity of the WT, and by the representation made of an inflow sector and the spread of inflow conditions included.

5.1 Conclusions

Dynamic estimation of WT performance

Based on the concepts established by one-dimensional momentum theory (Section 2.3), the AD combined with the proposed iterative method was able to estimate the free-stream velocity U_∞ and thrust exerted by it depending on the relevant inflow conditions (Section 2.6). This is possible by using the manufacturer's C_T curve and the RaNS flow solver's latest velocity solution iteration. As the velocity field solution iterates, the free-stream velocity U_∞ for each WT is updated and, upon convergence, a combined solution to the flow field and WT operation is reached.

The CFD solution is polled to approximate the AD's disk velocity U_d, and through iteration of momentum theory's C_T definition and the WT's C_T curve a value for the relevant U_∞ is obtained (Section 2.6.2). Polling the solution at a single point, the hub position, provided the lower U_∞ estimation error, particularly in clear inflow conditions (Section 2.6.4). However, under disturbed inflow conditions approximating U_d to the AD area averaged wind-speed proved less sensitive to spatial velocity gradients, yielding more consistent U_∞ estimates (Section 4.2).

WT power estimation via force-velocity integral over the AD surface was prone to errors, by under or over-estimation of the power as rated in the manufacturer's curve (Section 2.6.5). This estimate is largely dependent on the manufacturer's C_T curve, a dimensionless representation of the WT's as a momentum sink, but carrying no information regarding the efficiency of the momentum harvesting process. This is mainly tied to the aerodynamic efficiency of the rotor flow, highly dependent on the WT management regimes (and transitions between them), but also to the electrical conversion and transmission efficiencies of the hub machinery.

Wake flow and interaction between wakes

Momentum sinks are placed at the discretized AD to model the WT's aerodynamic thrust force, with the RaNS $k-\varepsilon$ equation solver responsible for modeling the flow's reaction the forces and the subsequent wake expansion and recovery. The model's solution matches Betz's theoretical predictions up to the very near wake (Section 2.3.1), before momentum diffusion into the wake causes velocity to depart from the theory, initiating a recovery to free-stream conditions.

The wake recovery trend is (in light of results from a linear wake model) well predicted, although a tendency to over-estimate wind-speeds in the near wake is evident (Section 2.4.6). Because of the low peak velocity deficit, the match between the two models within the first 5D distance to the WT is poor, but improves further downstream reaching very good agreement beyond 10D, close to the typical range of WT spacing in high density WT arrays.

Despite the difficulties in modeling near wake velocity, predictions of wake losses in offshore WT arrays matched those calculated via analysis of WF operational data. Model results for the wake shape of a single WT (Section 3.2.3.3) and the accumulation of power losses over rows regularly spaced WTs (Sections 3.2.3.1 and 3.2.3.2) agreed well with WF SCADA data. In an irregular WF array, with varying WT spacing and row orientation, the localized power losses that are consequence of complex wake interactions were generally well predicted (Section 3.3.3.2).

The wake effect of WTs over the large distances that separate neighbouring WFs in a cluster, in the order of several kms, was successfully reproduced, matching the power losses registered at the leading WTs of the affected WF (Section 3.3.3.3). On aggregate however, the WF's power loss as a consequence of the cluster wake effect was not reproduced (Section 3.3.3.4), arguably due to differences in SCADA data and model representations of sector specific array effects. This cluster case, spanning large distances and a WT count, was solved using a domain coupling technique, where upstream and downstream WFs are solved separately and sequentially (Section 4.4). As a result of this technique there were computational resource savings, with low impact on power estimations of the downstream WF.

Streamwise diffusion near the wind turbine

The RaNS flow model (using k-ε closure) assumes that turbulent diffusivity is proportional to the velocity gradients. This means that diffusive momentum transport is strong in the radial direction, due to the wake's annular shear layer, but also in the streamwise direction, because of the velocity drop in the AD's vicinity. The latter in particular is leading to excessive turbulent mixing, with momentum being transferred from the upwind free-stream region to the wake and effectively smoothing out the velocity field.

The most obvious effect of excess streamwise diffusion is on the wake of an isolated WT, with near wake wind speeds being over-estimated according to the comparison to linear model results (Section 2.4.6). However, the more important effect is in the WF's performance estimation, with high velocities at the AD increasing the disk velocity approximation error and causing the U_∞ estimation algorithm to over-estimate (Section 2.6.4). This effect is strongest when the WT operates at low wind speeds and at high thrust coefficients: streamwise velocity gradients are at their maximum, so the over-estimated diffusive transport results in increased estimation errors. As wind speeds increase, the WT tends to operate at lower C_Ts and convection begins to dominate the flow as a transport mechanism, with the over-estimated streamwise diffusion having a lesser effect and the U_∞ estimation error reducing to nearly zero.

The over-estimated diffusion has a diminished impact in a WF context, with the strong turbulent mixing regime that is characteristic of large WT arrays being well captured. Despite the large amount of WTs and combined wakes, they tend to operate downstream of each other's near-wake and outside the area most affected, where model performance is best. At 7D spacing the model predictions match power losses from SCADA data (Section 3.2.3.3), further confirmed by the agreement as WT spacing increases (Section 3.2.3.2).

Reproducing inflow sector width

Comparison between simulations and WF operational data depends heavily on the treatment made to inflow wind direction as binning criteria, as matching the spread of wind directions included in binned sector is essential (Section 3.1.5). To reproduce wind direction bins via simulations multiple CFD runs are required, modeling flow in specific wind directions within the sector (Section 3.2.2). The simulation ensemble becomes richer as the sector widens, with the CFD run count increasing and the ensemble average becoming less sensitive to cases where extreme array effects are captured, such as flow along row alignment, to the benefit of the agreement with SCADA data (Section 3.2.3.1).

The quality of the inflow reference data interferes with the SCADA binning, as high uncertainty wind direction data effectively increases the intended sector width, diluting sector specific array wake effects and altering bin averages (Section 3.1.4). This effect will have a greater impact as sector widths reduce, also contributing to a degradation of the match between model results and SCADA data (Section 3.2.3.1). On similar sectors with reference inflow data of different qualities, agreement was best where wind direction uncertainty was lowest (Section 3.2.3.5).

Discretization of the rotor and aerodynamic loads

The proposed two-stage AD discretization method allowed for unrestrained and precise placement of the WT on the domain mesh (Section 2.5), producing a static distribution of AD load density that only needs updating should the rotor orientation change. After modification to avoid creation of force singularities (Section 4.1), the resulting distribution is smooth and leads to smooth velocity fields.

Rotor load in momentum theory is assumed to be uniform and AD-normal, a crude simplification of real world rotor flow dynamics (Section 2.2). The force distribution was altered to mimic realistic rotor load loads, to vary over the length of blade and induce wake rotation (Section 4.3). However, wake flow changes were limited to the near wake, having largely dissipated 3D downstream of the WT (Section 4.3.5). This confirms the assumption that WT rotor flow dynamics are not relevant outside that region, with ABL flow dynamics being most relevant to wake expansion and recovery.

5.2 Future work

Over the course of the wake model performance assessment it became evident that streamwise diffusion over-estimation in the vicinity of the WT is one of the major limitations in the present formulation, particularly to the prediction of near-wake velocities and WT performance. Improvements on this subject should come via the addition of terms to the k and ε equations (Lopes et al., 2013) or, on a more fundamental level, directly interfering with directional diffusion and locally voiding turbulent viscosity's gradient-diffusion hypothesis. Given the potential impact of those changes, improvements to the rotor load distribution and solution polling options can and should be reassessed.

The behaviour in the wake of the WT is as expected given the predictions of momentum theory, and partly agree with calibrated engineering wake models. Wake dynamics should none the less be validated by comparison to real world wake flow measurements. Prime candidates for high resolution wake data are LIDAR (Vasiljević et al., 2017) measurements and scaled wind-tunnel experiments.

Real-world applications of the model were limited to off-shore WF flows, where inflow is uniform and local sources of flow complexity are (apart from WTs themselves) limited to the sea surface's roughness and, on some sectors, the effect of the shore or neighbouring WFs. Extending its application to on-shore cases will submit the model to additional sources of complexity, most importantly the topography, but also strong inflow inhomogeneity and surface cover, dramatically influencing WT operation and wake development. In such flow conditions the advantages of the techniques developed should be most evident, capturing non-linear flow effects that less complex engineering models cannot reproduce.

Bibliography

M. Abkar and F. Porté-Agel. Influence of atmospheric stability on wind-turbine wakes: a large-eddy simulation study. *Physics of Fluids*, 27(3):035104, 2015. doi: 10.1063/1.4913695. URL https://aip.scitation.org/doi/10.1063/1.4913695.

J. F. Ainslie. Calculating the flowfield in the wake of wind turbines. *Journal of Wind Engineering and Industrial Aerodynamics*, 27(1-3):213–224, 1988. ISSN 0167-6105. doi: 10.1016/0167-6105(88)90037-2. URL http://www.sciencedirect.com/science/article/pii/0167610588900372.

S. Aubrun, S. Loyer, P.E. Hancock, and P. Hayden. Wind turbine wake properties: Comparison between a non-rotating simplified wind turbine model and a rotating model. *Journal of Wind Engineering and Industrial Aerodynamics*, 120(0):1–8, 2013. ISSN 0167-6105. doi: 10.1016/j.jweia.2013.06.007. URL http://www.sciencedirect.com/science/article/pii/S0167610513001220.

R. J. Barthelmie and L. E. Jensen. Evaluation of wind farm efficiency and wind turbine wakes at the Nysted offshore wind farm. *Wind Energy*, 13(6):573–586, 2010. ISSN 1099-1824. doi: 10.1002/we.408. URL https://onlinelibrary.wiley.com/doi/full/10.1002/we.408.

R. J. Barthelmie and S. C. Pryor. An overview of data for wake model evaluation in the virtual wakes laboratory. *Applied Energy*, 104(0):834–844, 2013. ISSN 0306-2619. doi: 10.1016/j.apenergy.2012.12.013. URL http://www.sciencedirect.com/science/article/pii/S0306261912008951.

R. J. Barthelmie, Gunner Larsen, Sara Pryor, Hans Jørgensen, Hans Bergström, Wolfgang Schlez, Kostas Rados, Bernhard Lange, Per Vølund, Søren Neckelmann, Søren Mogensen, Gerard Schepers, Terry Hegberg, Luuk Folkerts, and Mikael Magnusson. ENDOW (efficient development of offshore wind farms): modelling wake and boundary layer interactions. *Wind Energy*, 7(3):225–245, 2004. ISSN 1099-1824. doi: 10.1002/we.121. URL https://onlinelibrary.wiley.com/doi/abs/10.1002/we.121.

R. J. Barthelmie, K. Hansen, S. T. Frandsen, O. Rathmann, J. G. Schepers, W. Schlez, J. Phillips, K. Rados, A. Zervos, E. S. Politis, and P. K. Chaviaropoulos. Modelling and measuring flow and wind turbine wakes in large wind farms offshore. *Wind Energy*, 12(5):431–444, 2009. ISSN 1099-1824. doi: 10.1002/we.348. URL https://onlinelibrary.wiley.com/doi/abs/10.1002/we.348.

R. J. Barthelmie, S. T. Frandsen, O. Rathmann, K. S. Hansen, E. Politis, J. Prospathopoulos, J.G. Schepers, K. Rados, D. Cabezon, W. Schlez, A. Neubert, and M. Heath. *Flow*

and wakes in large wind farms: Final report for UpWind WP8. Danmarks Tekniske Universitet, Risø Nationallaboratoriet for Bæredygtig Energi, 2011.

A. Bechmann, N. N. Sørensen, and F. Zahle. CFD simulations of the MEXICO rotor. *Wind Energy*, 14(5):677–689, 2011. ISSN 1099-1824. doi: 10.1002/we.450. URL https://onlinelibrary.wiley.com/doi/full/10.1002/we.450.

H. Beck, J. J. Trujillo, G. Wolken-Möhlmann, A. P. Diaz, V. C. Gomes, and J. Schmidt. Mesoscale effects on wind farm energy yield reported. Technical Report D5.10, EERA-DTOC, February 2015. URL http://www.eera-dtoc.eu/publications-results/technical-reports/.

F. Bingol, J. Mann, and G. C. Larsen. Light detection and ranging measurements of wake dynamics. Part I: one-dimensional scanning. *Wind Energy*, 13(1):51–61, 2010. doi: 10.1002/we.352. URL https://onlinelibrary.wiley.com/doi/abs/10.1002/we.352.

D. Cabezón, E. Migoya, and A. Crespo. Comparison of turbulence models for the computational fluid dynamics simulation of wind turbine wakes in the atmospheric boundary layer. *Wind Energy*, 14(ETSU-WN–5020):909–921, 2011. ISSN 1099-1824. doi: 10.1002/we.516. URL https://onlinelibrary.wiley.com/doi/full/10.1002/we.516.

M. Calaf, C. Meneveau, and J. Meyers. Large eddy simulation study of fully developed wind-turbine array boundary layers. *Physics of Fluids*, 22(1):015110, 2010. doi: 10.1063/1.3291077. URL https://aip.scitation.org/doi/10.1063/1.3291077.

L. S. Caretto, A. D. Gosman, S. V. Patankar, and D. B. Spalding. Two calculation procedures for steady, three-dimensional flows with recirculation. In Henri Cabannes and Roger Temam, editors, *Proceedings of the Third International Conference on Numerical Methods in Fluid Mechanics*, page 60–68, Berlin, Heidelberg, 1973. Springer Berlin Heidelberg. ISBN 978-3-540-38392-5.

F. Castellani and A. Vignaroli. An application of the actuator disc model for wind turbine wakes calculations. *Applied Energy*, 101(0):432–440, 2013. ISSN 0306-2619. doi: 10.1016/j.apenergy.2012.04.039. URL http://www.sciencedirect.com/science/article/pii/S0306261912003364.

F. A. Castro, J. M. L. M. Palma, and A. S. Lopes. Simulation of the Askervein flow. Part 1: Reynolds averaged Navier–Stokes equations (k-epsilon turbulence model). *Boundary-Layer Meteorology*, 107(3):501–530, 2003. ISSN 0006-8314. doi: 10.1023/A:1022818327584. URL https://link.springer.com/article/10.1023%2FA%3A1022818327584.

L. Chamorro and F. Porté-Agel. A wind-tunnel investigation of wind-turbine wakes: Boundary-layer turbulence effects. *Boundary-Layer Meteorology*, 132(1):129–149, July 2009. doi: 10.1007/s10546-009-9380-8. URL https://link.springer.com/article/10.1007%2Fs10546-009-9380-8.

L. P. Chamorro and F. Porté-Agel. Effects of thermal stability and incoming boundary-layer flow characteristics on wind-turbine wakes: a wind-tunnel study. *Boundary-Layer Meteorology*, 136(3):515–533, 2010. doi: 10.1007/s10546-010-9512-1. URL http://www.springerlink.com/index/10.1007/s10546-010-9512-1.

Matthew J. Churchfield, Sang Lee, John Michalakes, and Patrick J. Moriarty. A numerical study of the effects of atmospheric and wake turbulence on wind turbine dynamics. *Journal of Turbulence*, 13:N14, 2012. doi: 10.1080/14685248.2012.668191. URL https://www.tandfonline.com/doi/full/10.1080/14685248.2012.668191.

J. W. Cleijne. Results of the Sexbierum wind farm; single wake measurements. Technical report, TNO Institute of Environmental and Energy Technology, The Netherlands, 1993. URL http://repository.tudelft.nl/view/tno/uuid:7bb5570d-e223-4c4b-9448-bec95453f061/.

A. Crespo and J. Hernández. Turbulence characteristics in wind-turbine wakes. *Journal of Wind Engineering and Industrial Aerodynamics*, 61(1):71–85, June 1996. doi: 10.1016/0167-6105(95)00033-X. URL https://www.sciencedirect.com/science/article/pii/016761059500033X?via%3Dihub.

A. Crespo, J. Hernández, E. Fraga, and C. Andreu. Experimental validation of the upm computer code to calculate wind turbine wakes and comparison with other models. *Journal of Wind Engineering and Industrial Aerodynamics*, 27(1-3):77–88, 1988. doi: 10.1016/0167-6105(88)90025-6. URL https://www.sciencedirect.com/science/article/pii/0167610588900256?via%3Dihub.

A. Crespo, F. Manuel, and J. Hernandez. Numerical modelling of wind turbine wake. In *Proc. 1990 European Community Wind Energy Conf.*, page 166–170, Madrid, 1990.

A. Crespo, S. T. Frandsen, R. Gómez-Elvira, and S. E. Larsen. *Modelization of a large wind farm, considering the modification of the atmospheric boundary layer*, page 1109–1112. James and James Science Publishers, 1999. ISBN 1-902916-00-X.

E.P.N. Duque, C.P. van Dam, and S.C. Hughes. Navier-Stokes simulations of the NREL combined experiment phase II rotor. *AIAA*, 99(0037):143–153, 1999. doi: 10.2514/6.1999-37. URL https://arc.aiaa.org/doi/abs/10.2514/6.1999-37.

H. J. Fernando, J. Mann, J. M. L. M. Palma, J. K. Lundquist, R. J. Barthelmie, M. S. B. S. Pereira, W. O. J. Brown, F. K. Chow, T. Gerz, C. M. Hocut, P. M. Klein, L. S. Leo, J. C. Matos, S. P. Oncley, S. C Pryor, L. Bariteau, T. M. Bell, N. Bodini, M. B. Carney, M. Courtney, E. Creegan, R. Dimitrova, S. Gomes, M. Hagen, O. Hyde, S. Kigle, R. Krishnamurthy, J. C. Lopes, L. Mazzaro, J. M.T. Neher, R. Menke, P. Murphy, L. Oswald, S. Otarola-Bustos, A. K. Pattantyus, C. Rodrigues, A. Schady, N. Sirin, S. Spuler, E. Svensson, J. Tomaszewski, D. D. Turner, L. van Veen, N. Vasiljević, D. Vassalo, S. Voss, N. Wildmann, and Y. Wang. The Perdigão experiment: Peering into microscale details of mountain winds. *Bulletin of the American Meteorological Society*, 2018. doi: 10.1175/BAMS-D-17-0227.1. URL https://journals.ametsoc.org/doi/abs/10.1175/BAMS-D-17-0227.1.

Joel H. Ferziger and Milovan Peric. *Computational Methods for Fluid Dynamic*. Springer, Berlin, Heidelberg, 2002. doi: 10.1007/978-3-642-56026-2. URL https://link.springer.com/book/10.1007%2F978-3-642-56026-2.

S. Frandsen. On the wind speed reduction in the center of large clusters of wind turbines. *Journal of Wind Engineering and Industrial Aerodynamics*, 39(1-3):251–265,

1992. ISSN 01676105. doi: 10.1016/0167-6105(92)90551-K. URL https://www.sciencedirect.com/science/article/pii/016761059290551K?via%3Dihub.

S. Frandsen, R. Barthelmie, S. Pryor, O. Rathmann, S. Larsen, J. Hojstrup, and M. Thorgersen. Analytical modelling of wind speed deficit in large offshore wind farms. *Wind Energy*, 9(1-2):39–53, 2006. doi: 10.1002/we.189. URL http://onlinelibrary.wiley.com/doi/10.1002/we.189/abstract.

R. E. Froude. On the part played in propulsion by differences of fluid pressure. *Transactions of the Institute of Naval Architects*, 30:390–405, 1889.

M. Gaumond, P.-E. Réthoré, S. Ott, A. Peña, A. Bechmann, and K.S. Hansen. Evaluation of the wind direction uncertainty and its impact on wake modeling at the Horns Rev offshore wind farm. *Wind Energy*, 2013. ISSN 10954244. doi: 10.1002/we.1625. URL https://onlinelibrary.wiley.com/doi/full/10.1002/we.1625.

H. Glauert. Airplane propellers. In William Frederick Durand, editor, *Aerodynamic Theory*, volume IV, chapter 3, page 169–360. Division L. Springer, 1935.

V. M. M. G. C. Gomes and J. M. L. M. Palma. Computational modelling of a large dimension wind farm cluster using domain coupling. *Journal of Physics: Conference Series*, 753 (8):082032, 2016. URL http://stacks.iop.org/1742-6596/753/i=8/a=082032.

V. M. M. G. C. Gomes, J. M. L. M. Palma, and A. S. Lopes. Improving actuator disk wake model. *Journal of Physics: Conference Series*, 524(1):012170, 2014. URL http://stacks.iop.org/1742-6596/524/i=1/a=012170.

V. M. M. G. Costa Gomes and J. M. L. M. Palma. Actuator disk wake model in RaNS. Poster, January 2014. EERA DeepWind'2014, 11th Deep Sea Offshore Wind R&D Conference, 22-24 January 2014, Trondheim, Norway.

R. Gómez-Elvira, A. Crespo, E. Migoya, F. Manuel, and J. Hernández. Anisotropy of turbulence in wind turbine wakes. *Journal of Wind Engineering and Industrial Aerodynamics*, 93(10):797–814, October 2005. doi: 10.1016/j.jweia.2005.08.001. URL https://www.sciencedirect.com/science/article/pii/S016761050500084X?via%3Dihub.

K. S. Hansen and C. Hasager. Validation of wake models for (two) wind farms. Technical Report D5.9, EERA-DTOC, December 2014. URL http://www.eera-dtoc.eu/publications-results/technical-reports/.

K. S. Hansen, R. J. Barthelmie, L. E. Jensen, and A. Sommer. The impact of turbulence intensity and atmospheric stability on power deficits due to wind turbine wakes at Horns Rev wind farm. *Wind Energy*, 15(1):183–196, 2012. ISSN 1099-1824. doi: 10.1002/we.512. URL https://onlinelibrary.wiley.com/doi/full/10.1002/we.512.

K. S. Hansen, P.-E. Réthoré, J. Palma, B. G. Hevia, J. Prospathopoulos, A. Peña, S. Ott, G. Schepers, A. Palomares, M. P. van der Laan, and P. Volker. Simulation of wake effects between two wind farms. *Journal of Physics: Conference Series*, 625(1):012008, 2015. URL http://stacks.iop.org/1742-6596/625/i=1/a=012008.

M. O. L. Hansen. *Aerodynamics of Wind Turbines - Rotors, Loads and Structure*. James & James, 2000.

D. M. Hargreaves and N. G. Wright. On the use of the k-epsilon model in commercial CFD software to model the neutral atmospheric boundary layer. *Journal of Wind Engineering and Industrial Aerodynamics*, 95(5):355–369, 2007. ISSN 0167-6105. doi: 10.1016/j.jweia.2006.08.002. URL https://www.sciencedirect.com/science/article/pii/S016761050600136X?via%3Dihub.

C. B. Hasager and G. Giebel. EERA-DTOC final summary report. Technical report, EERA-DTOC, June 2015. URL http://www.eera-dtoc.eu/publications-results/technical-reports/.

Ulf Högström. Non-dimensional wind and temperature profiles in the atmospheric surface layer: a re-evaluation. *Boundary-Layer Meteorology*, 42(1):55–78, Jan 1988. ISSN 1573-1472. doi: 10.1007/BF00119875. URL https://link.springer.com/article/10.1007%2FBF00119875.

IEC. IEC 61400-12-1 Ed. 1.0 Wind turbines - Part 12-1: Power performance measurements of electricity producing wind turbines, December 2005.

N. O. Jensen. A note on wind generator interaction. Technical report, Risoe, 1983.

A. Jimenez, A. Crespo, E. Migoya, and J. Garcia. Advances in large-eddy simulation of a wind turbine wake. *Journal of Physics: Conference Series*, 75:012041, 2007. doi: 10.1088/1742-6596/75/1/012041. URL https://iopscience.iop.org/article/10.1088/1742-6596/75/1/012041/meta.

A. Jimenez, A. Crespo, E. Migoya, and J. Garcia. Large-eddy simulation of spectral coherence in a wind turbine wake. *Environmental Research Letters*, 3(1):015004, 2008. doi: 10.1088/1748-9326/3/1/015004. URL http://stacks.iop.org/1748-9326/3/i=1/a=015004.

J. Johansen, N. N. Sørensen, J. A. Michelsen, and S. Schreck. Detached-eddy simulation of flow around the NREL phase VI blade. *Wind Energy*, 5(2-3):185–197, 2002. doi: 10.1002/we.63. URL https://onlinelibrary.wiley.com/doi/abs/10.1002/we.63.

A. El Kasmi and C. Masson. An extended k-epsilon model for turbulent flow through horizontal-axis wind turbines. *Journal of Wind Engineering and Industrial Aerodynamics*, 96(1):103–122, 2008. ISSN 01676105. doi: 10.1016/j.jweia.2007.03.007. URL https://www.sciencedirect.com/science/article/pii/S0167610507000943?via%3Dihub.

B.E. Launder and B.I. Sharma. Application of the energy-dissipation model of turbulence to the calculation of flow near a spinning disc. *Letters in Heat and Mass Transfer*, 1(2):131–137, November-December 1974. doi: 10.1016/0094-4548(74)90150-7. URL http://www.sciencedirect.com/science/article/pii/0094454874901507.

B.E. Launder and D.B. Spalding. The numerical computation of turbulent flows. *Computer Methods in Applied Mechanics and Engineering*, 3(2):269–289, 1974. ISSN 0045-7825. doi: 10.1016/0045-7825(74)90029-2. URL http://www.sciencedirect.com/science/article/pii/0045782574900292.

J. Laursen, P. Enevoldsen, and S. Hjort. 3D CFD quantification of the performance of a multi-megawatt wind turbine. *Journal of Physics: Conference Series*, 75(1):012007, 2007.

doi: 10.1088/1742-6596/75/1/012007. URL http://stacks.iop.org/1742-6596/75/i=1/a=012007.

B.P. Leonard. A stable and accurate convective modelling procedure based on quadratic upstream interpolation. *Computer Methods in Applied Mechanics and Engineering*, 19(1): 59–98, 1979. ISSN 0045-7825. doi: 10.1016/0045-7825(79)90034-3. URL http://www.sciencedirect.com/science/article/pii/0045782579900343.

A. S. Lopes, J. M. L. M. Palma, and J. V. Lopes. Improving a two-equation turbulence model for canopy flows using large-eddy simulation. *Boundary-Layer Meteorology*, 149 (2):231–257, 2013. ISSN 0006-8314. doi: 10.1007/s10546-013-9850-x. URL https://link.springer.com/article/10.1007%2Fs10546-013-9850-x.

E. Machefaux, N. Troldborg, G. C. Larsen, J. Mann, and H. A. Madsen. Experimental and numerical study of wake to wake interaction in wind farms. In *EWEA 2012*, 2012.

L. A. H. Machielse, P. J. Eecen, H. Korterink, S. P. van der Pijl, and J. G. Schepers. ECN test farm measurements for validation of wake models. Technical Report ECN-M–07-044, ECN Wind Energy, May 2007. URL https://www.ecn.nl/publications/ECN-M--07-044. Presented at: European Wind Energy Conference 2007, Milan, Italy, 7-10 May 2007.

H. A. Madsen. *A CFD analysis of the actuator disc flow compared with momentum theory results*, page 109–124. Technical University of Denmark. Department of Fluid Mechanics, 1997.

A. Makridis and J. Chick. Validation of a CFD model of wind turbine wakes with terrain effects. *Journal of Wind Engineering and Industrial Aerodynamics*, 123, Part A (0):12–29, 2013. ISSN 0167-6105. doi: 10.1016/j.jweia.2013.08.009. URL http://www.sciencedirect.com/science/article/pii/S0167610513001827.

C. D. Markfort, W. Zhang, and F. Porté-Agel. Turbulent flow and scalar transport through and over aligned and staggered wind farms. *Journal of Turbulence*, 13(1): N33, 2012. doi: 10.1080/14685248.2012.709635. URL http://www.tandfonline.com/doi/abs/10.1080/14685248.2012.709635.

D. Medici and P. H. Alfredsson. Measurements on a wind turbine wake: 3D effects and bluff body vortex shedding. *Wind Energy*, 9(3):219–236, 2006. ISSN 10954244. doi: 10.1002/we.156. URL https://www.scopus.com/record/display.uri?eid=2-s2.0-33745166642&origin=inward&txGid=e9a679a9d620a4154e0cd17abf0c8184. cited By (since 1996) 23.

D. Medici, S. Ivanell, J.-A. Dahlberg, and P. H. Alfredsson. The upstream flow of a wind turbine: blockage effect. *Wind Energy*, 14(5):691–697, 2011. ISSN 1099-1824. doi: 10.1002/we.451. URL https://onlinelibrary.wiley.com/doi/full/10.1002/we.451.

E. Migoya, A. Crespo, J. García, F. Moreno, F. Manuel, Á. Jiménez, and A. Costa. Comparative study of the behavior of wind-turbines in a wind farm. *Energy*, 32(10):1871–1885, 2007. ISSN 0360-5442. doi: 10.1016/j.energy.2007.03.012. URL http://www.sciencedirect.com/science/article/B6V2S-4NVC8VR-1/2/25c8e62afe36344e9b43e5539b7b226e.

R. Mikkelsen. *Actuator Disc Methods Applied to Wind Turbines*. PhD thesis, Technical University of Denmark, Department of Mechanical Engineering Nils Koppels Allé, Building 403 Technical University of Denmark DK-2800 Lyngby, Denmark, June 2003.

R. Mikkelsen, J. N Sørensen, S. Øye, and N. Troldborg. Analysis of power enhancement for a row of wind turbines using the actuator line technique. *Journal of Physics: Conference Series*, 75(1):012044, 2007. doi: 10.1088/1742-6596/75/1/012044. URL http://stacks.iop.org/1742-6596/75/i=1/a=012044.

J.-O. Mo, A. Choudhry, M. Arjomandi, and Y.-H. Lee. Large eddy simulation of the wind turbine wake characteristics in the numerical wind tunnel model. *Journal of Wind Engineering and Industrial Aerodynamics*, 112(0):11–24, 2013. ISSN 0167-6105. doi: 10.1016/j.jweia.2012.09.002. URL http://www.sciencedirect.com/science/article/pii/S0167610512002462.

P. Moriarty, J. S. Rodrigo, P. Gancarski, M. Chuchfield, J. W. Naughton, K. S. Hansen, E. Machefaux, E. Maguire, F. Castellani, L. Terzi, S.-P. Breton, and Y. Ueda Ueda. IEA-Task 31 WAKEBENCH: Towards a protocol for wind farm flow model evaluation. Part 2: Wind farm wake models. *Journal of Physics: Conference Series*, 524(1): 012185, 2014. doi: 10.1088/1742-6596/524/1/012185. URL http://stacks.iop.org/1742-6596/524/i=1/a=012185.

J. M. L. M. Palma, F. A. Castro, L. F. Ribeiro, A. H. Rodrigues, and A. P. Pinto. Linear and nonlinear models in wind resource assessment and wind turbine micro-siting in complex terrain. *Journal of Wind Engineering and Industrial Aerodynamics*, 96(12): 2308–2326, 2008. ISSN 0167-6105. doi: 10.1016/j.jweia.2008.03.012. URL http://www.sciencedirect.com/science/article/pii/S0167610508001037.

E. S. Politis, J. Prospathopoulos, D. Cabezon, K. S. Hansen, P. K. Chaviaropoulos, and R. J. Barthelmie. Modeling wake effects in large wind farms in complex terrain: the problem, the methods and the issues. *Wind Energy*, 15:161–182, 2012. ISSN 10954244. doi: 10.1002/we.481. URL https://onlinelibrary.wiley.com/doi/full/10.1002/we.481. cited By (since 1996) 0; Article in Press.

F. Porté-Agel, Y.-T. Wu, H. Lu, and R. J. Conzemius. Large-eddy simulation of atmospheric boundary layer flow through wind turbines and wind farms. *Journal of Wind Engineering and Industrial Aerodynamics*, 99(4):154–168, 2011. ISSN 0167-6105. doi: 10.1016/j.jweia.2011.01.011. URL http://www.sciencedirect.com/science/article/pii/S0167610511000134.

J. M. Prospathopoulos, E. S. Politis, K. G. Rados, and P. K. Chaviaropoulos. Evaluation of the effects of turbulence model enhancements on wind turbine wake predictions. *Wind Energy*, 14:285–300, 2010. doi: 10.1002/we.419. URL http://onlinelibrary.wiley.com/doi/10.1002/we.419/abstract.

D. C. Quarton and J. F. Ainslie. Turbulence in wind turbine wakes. *Wind Engineering*, 14 (1):15–23, 1990. ISSN 0309524X. URL http://www.scopus.com/inward/record.url?eid=2-s2.0-0025090256&partnerID=40&md5=997e421d22e33db1ed2b82fc1a6ff0b1.

C. M. Rhie and W. L. Chow. Numerical study of the turbulent flow past an airfoil with trailing edge separation. *AIAA Journal*, 21(11):1525–1532, November 1983. doi: 10.2514/3.8284. URL https://arc.aiaa.org/doi/abs/10.2514/3.8284.

P. J. Richards and R. P. Hoxey. Appropriate boundary conditions for computational wind engineering models using the k-epsilon turbulence model. *Journal of Wind Engineering and Industrial Aerodynamics*, 46-47(C):145–153, 1993. doi: 10.1016/0167-6105(93)90124-7. URL https://www.sciencedirect.com/science/article/pii/0167610593901247?via%3Dihub.

C. V. Rodrigues, J. M. L. M. Palma, and A. H. Rodrigues. Atmospheric flow over a mountainous region by a one-way coupled approach based on Reynolds-averaged turbulence modelling. *Boundary-Layer Meteorology*, page 1–31, 2015. ISSN 1573-1472. doi: 10.1007/s10546-015-0116-7. URL https://link.springer.com/article/10.1007%2Fs10546-015-0116-7.

P.-E. Réthoré. *Wind Turbine Wake in Atmospheric Turbulence*. PhD thesis, Aalborg University – Department of Civil Engineering, P.O.Box 49, DK-4000 Roskilde, Denmark, October 2009.

P. E. Réthoré, N. A. Johansen, Sten T. Frandsen, R. Barthelmie, K. S. Hansen, L. E. Jensen, M. A.B. Bækgaard, and J. R. Kristoffersen. Systematic wind farm measurement data reinforcement tool for wake model calibration. In *European Offshore Wind Conference (2009)*, 2009. URL https://orbit.dtu.dk/en/publications/systematic-wind-farm-measurement-data-filtering-tool-for-wake-mod.

P.-E. Réthoré, K.S. Hansen, R.J. Barthelmie, S.C. Pryor, G. Sieros, J. Prospathopoulos, J.M.L.M. Palma, V.C. Gomes, G. Schepers, P. Stuart, T. Young, J.S. Rodrigo, G.C. Larsen, T.J. Larsen, S. Ott, O. Rathmann, A. Pena, M. Gaumond, and C. B.Hasager. Benchmarking of wind farm scale wake models in the EERA-DTOC project. In *ICOWES2013 Conference*, 2013b. URL http://www.eera-dtoc.eu/publications-results/oral-and-poster-presentations/.

P.-E. Réthoré, K.S. Hansen, R.J. Barthelmie, S.C. Pryor, G. Sieros, J. Prospathopoulos, J.M.L.M. Palma, V.C. Gomes, G. Schepers, P. Stuart, T. Young, J.S. Rodrigo, G.C. Larsen, T.J. Larsen, S. Ott, O. Rathmann, A. Peña, M. Gaumond, and C. B. Hasager. Benchmark report on wake models at the wind farm scale. Technical Report D1.3, EERA-DTOC, June 2013a. URL http://www.eera-dtoc.eu/publications-results/technical-reports/.

B. Sanderse. Aerodynamics of wind turbine wakes: Literature review. Technical Report ECN-e2013;09-016, ECN, Energy research Centre of the Netherlands, ECN, P.O. Box 1, 1755 ZG Petten, The Netherlands, 2009. URL http://www.ecn.nl/publications/default.aspx?nr=ECN-E--09-016.

B. Sanderse, S.P. van der Pijl, and B. Koren. Review of computational fluid dynamics for wind turbine wake aerodynamics. *Wind Energy*, 14(7):799–819, 2011. ISSN 1099-1824. doi: 10.1002/we.458. URL https://onlinelibrary.wiley.com/doi/full/10.1002/we.458.

G. Schepers, A. Pena, A. Ely, A. Palomares, A. Attiya, G. Sieros, G. Giebel, H. Svendsen, I. Bastigkeit, I. Karagali, I. Moya, O. A. Lara, P. Ledesma, P. M. F. Correia, V. C. Gomes, and W. He. EERA-DTOC calculation of scenarios. Technical Report D5.12, EERA-DTOC, June 2015. URL http://www.eera-dtoc.eu/publications-results/technical-reports/.

J. G. Schepers and H. Snel. Model experiments in controlled conditions - final report. Technical report, ECN: Energy Research Centre of the Netherlands, 2007. URL https://publications.tno.nl/publication/34628817/8d6E4g/e07042.pdf.

W. Z. Shen, J. H. Zhang, and J. N. Sørensen. The actuator surface model: a new Navier–Stokes based model for rotor computations. *Journal of Solar Energy Engineering*, 131(1):011002, 2009. doi: 10.1115/1.3027502. URL http://solarenergyengineering.asmedigitalcollection.asme.org/article.aspx?articleid=1474410.

A. Silva Lopes, J.M.L.M. Palma, and F.A. Castro. Simulation of the Askervein flow. Part 2: Large-eddy simulations. *Boundary-Layer Meteorology*, 125(1):85–108, 2007. ISSN 00068314. doi: 10.1007/s10546-007-9195-4. URL https://link.springer.com/article/10.1007%2Fs10546-007-9195-4.

D. Simms, S. Schreck, M. Hand, and L.J. Fingersh. NREL unsteady aerodynamics experiment in the NASA-Ames wind tunnel: a comparison of predictions to measurements. Technical report, National Renewable Energy Lab., 6 2001. URL https://www.osti.gov/biblio/783409/.

D. B. Spalding. A novel finite difference formulation for differential expressions involving both first and second derivatives. *International Journal for Numerical Methods in Engineering*, 4(4):551–559, 1972. doi: 10.1002/nme.1620040409. URL https://onlinelibrary.wiley.com/doi/abs/10.1002/nme.1620040409.

J. N. Sørensen and Asger Myken. Unsteady actuator disc model for horizontal axis wind turbines. *Journal of Wind Engineering and Industrial Aerodynamics*, 39(1):139–149, 1992. ISSN 0167-6105. doi: 10.1016/0167-6105(92)90540-Q. URL http://www.sciencedirect.com/science/article/pii/016761059290540Q.

J. N. Sørensen and W. Z. Shen. Numerical modeling of wind turbine wakes. *Journal of Fluids Engineering - - Transactions of the ASME*, 124(2):393–399, 2002. doi: 10.1115/1.1471361. URL http://fluidsengineering.asmedigitalcollection.asme.org/article.aspx?articleid=1429525.

G. J. Taylor. Wake measurements on the Nibe wind turbines in Denmark. Contractor report ETSU WN 5020. Technical report, National Power - Technology and Environment Centre, 1990. URL http://hdl.handle.net/10068/631659.

N. Troldborg, G. C. Larsen, H. A. Madsen, K. S. Hansen, J. N. Sørensen, and R. Mikkelsen. Numerical simulations of wake interaction between two wind turbines at various inflow conditions. *Wind Energy*, 14(7):859–876, 2011. ISSN 1099-1824. doi: 10.1002/we.433. URL http://dx.doi.org/10.1002/we.433.

N. Troldborg, N. N. Sørensen, P.-E. Réthoré, and M. P. van der Laan. A consistent method for finite volume discretization of body forces on collocated grids applied to flow through an actuator disk. *Computers & Fluids*, 119:197–203, 2015. ISSN 0045-7930. doi: 10.1016/j.compfluid.2015.06.028. URL http://www.sciencedirect.com/science/article/pii/S0045793015002194.

J.-J. Trujillo, F. Bingol, G. C. Larsen, J. Mann, and M. Kuhn. Light detection and ranging measurements of wake dynamics. Part II: two-dimensional scanning. *Wind Energy*,

9999(9999):na, 2011. doi: 10.1002/we.402. URL https://onlinelibrary.wiley.com/doi/full/10.1002/we.402.

G. A. M. Van Kuik. *On the Limitations of Froude's Actuator Disc Concept*. PhD thesis, Technical University of Eindhoven, 1991.

N. Vasiljević, J. M. L. M. Palma, N. Angelou, J. Carlos Matos, R. Menke, G. Lea, J. Mann, M. Courtney, L. Frölen Ribeiro, and V. M. M. G. C. Gomes. Perdigão 2015: methodology for atmospheric multi-Doppler lidar experiments. *Atmospheric Measurement Techniques*, 10(9):3463–3483, 2017. doi: 10.5194/amt-10-3463-2017. URL https://www.atmos-meas-tech.net/10/3463/2017/.

L. J. Vermeer, J. N. Sørensen, and A. Crespo. Wind turbine wake aerodynamics. *Progress in Aerospace Sciences*, 39:467–510, 2003. doi: 10.1016/S0376-0421(03)00078-2. URL https://www.sciencedirect.com/science/article/pii/S0376042103000782?via%3Dihub.

R. Wagner, M. Courtney, J. Gottschall, and P. Lindelöw-Marsden. Accounting for the speed shear in wind turbine power performance measurement. *Wind Energy*, 14(8):993–1004, 2011. ISSN 10954244. doi: 10.1002/we.509. URL https://onlinelibrary.wiley.com/doi/full/10.1002/we.509.

A. Witze. World's largest wind-mapping project spins up in Portugal. *Nature*, 542(7641):282–283, February 2017. doi: 10.1038/542282a. URL https://www.nature.com/news/world-s-largest-wind-mapping-project-spins-up-in-portugal-1.21481.

Y.-T. Wu and F. Porté-Agel. Large-eddy simulation of wind-turbine wakes: Evaluation of turbine parametrisations. *Boundary-Layer Meteorology*, 138(3):345–366, 2011. ISSN 00068314. doi: 10.1007/s10546-010-9569-x. URL https://link.springer.com/article/10.1007%2Fs10546-010-9569-x.

Y.-T. Wu and F. Porté-Agel. Simulation of turbulent flow inside and above wind farms: Model validation and layout effects. *Boundary-Layer Meteorology*, 144:1–25, 2012. ISSN 00068314. doi: 10.1007/s10546-012-9757-y. URL https://link.springer.com/article/10.1007%2Fs10546-012-9757-y.

S. Wubow, L. Sitzki, and T. Hahm. 3D simulation of the turbulent wake behind a wind turbine. *Journal of Physics: Conference Series*, 75(012033):na, 2007. doi: 10.1088/1742-6596/75/1/012033. URL https://iopscience.iop.org/article/10.1088/1742-6596/75/1/012033/meta.

D. Yang, C. Meneveau, and L. Shen. Large-eddy simulation of offshore wind farm. *Physics of Fluids (1994-present)*, 26(2):025101, 2014. doi: 10.1063/1.4863096. URL http://scitation.aip.org/content/aip/journal/pof2/26/2/10.1063/1.4863096.

W. Zhang, C. D. Markfort, and F. Porté-Agel. Near-wake flow structure downwind of a wind turbine in a turbulent boundary layer. *Experiments in Fluids*, 52(5):1219–1235, 2012. ISSN 07234864. doi: 10.1007/s00348-011-1250-8. URL https://link.springer.com/article/10.1007%2Fs00348-011-1250-8.